

# **State of the Art Roller Rig for Precise Evaluation of Wheel-Rail**

## **Contact Mechanics and Dynamics**

Sajjad Zeinoddini Meymand

Dissertation submitted to the faculty of the Virginia Polytechnic Institute and State University in partial fulfillment of the requirements for the degree of

Doctor of Philosophy

In

Mechanical Engineering

Mehdi Ahmadian, Chair

Tomonari Furukawa

Muhammad R Hajj

Saied Taheri

Pablo A Tarazaga

December 04, 2015

Blacksburg, VA

Keywords: Roller Rig, Mechanical Design, Wheel-Rail Rolling Contact, Multi-body Dynamic Modeling, Contact Force Measurement System

Copyright© 2015, Sajjad Z Meymand

# State of the Art Roller Rig for Precise Evaluation of Wheel-Rail Contact Mechanics and Dynamics

Sajjad Zeinoddini Meymand

## **ABSTRACT**

The focus of this study is on the development of a state-of-the-art single-wheel roller rig for studying contact mechanics and dynamics in railroad applications. The use of indoor-based simulation tools has become a mainstay in vehicle testing for the automotive and railroad industries. In contrast to field-testing, roller rigs offer a controlled laboratory environment that can provide a successful path for obtaining data on the mechanics and dynamics of railway systems for a variety of operating conditions. The idea to develop a laboratory test rig started from the observation that there is a need for better-developed testing fixtures capable of accurately explaining the complex physics of wheel-rail contact toward designing faster, safer, and more efficient railway systems. A review of current roller rigs indicated that many desired functional requirements for studying contact mechanics currently are not available. Thus, the Virginia Tech Railway Technologies Laboratory (RTL) has embarked on a mission to develop a state-of-the-art testing facility that will allow experimental testing of contact mechanics in a dynamic, controlled, and consistent manner.

VT roller rig will allow for closely replicating the boundary conditions of railroad wheel-rail contact via actively controlling all the wheel-rail interface degrees of freedom: cant angle, angle of attack, and lateral displacement. Two sophisticated independent drivelines are configured to precisely control the rotational speed of the wheels, and therefore their relative slip or creepage. A novel force measurement system, suitable for steel on steel contact, is configured to precisely measure the contact forces and moments at the contact patch. The control architecture is developed based on the SynqNet data acquisition system offered by Kollmorgen, the motors supplier. SynqNet provides a unified communication protocol between actuators, drives, and data acquisition system, hence eliminating data conversion among them. Various design analysis indicates that the rig successfully meets the set requirements: additional accuracy in measurements, and better control on the design of experiments. The test results show that the rig is capable of conducting various contact mechanics studies aimed for advancing the existing art.

Beyond developing the experimental testing fixture for studying contact mechanics, this study provides a comprehensive review of the contact models. It discusses the simplifying assumptions for developing the models, compares the models functionality, and highlights the open areas that require further experimental and theoretical research. In addition, a multi-body dynamic model of the entire rig, using software package SIMPACK, is developed for conducting modal analysis of the rig and evaluating the performance of the rig's components. A MATLAB routine is also developed that provides a benchmark for developing creep curves from measurements of the rig and comparing them with existing creep curves.

*To my family*

## ACKNOWLEDGEMENTS

I would like to thank my advisor, Professor Mehdi Ahmadian, for his advice and support during this study. I have been very pleased to have the chance to work with him during the last three and half years and his support and guidance throughout my research have been the most valuable gift. I will never be able to express the level of my gratefulness for all the things I learned from him. Those are not just limited to the research matters; I have learned many general things from him, which I will be using in my life.

I would also like to thank the members of my committee, Dr. Saied Taheri, Dr. Mohammad Hajj, Dr. Pablo Tarazaga, and Dr. Tomonari Furukawa for their advice and for being kind enough to serve on my graduate committee. I would like to especially thank Dr. Saied Taheri for his friendship and for his great help in different aspects throughout my study at Virginia Tech.

I would like to thank the Federal Railroad Administration for the funding they have provided for this work. In particular, I would like to thank Mr. Ali Tajaddini for his great support and help throughout the project.

I am sincerely thankful to the CVeSS family; my dear friends and colleagues. I would like to thank Sara Vallejo, Andrew Peterman, Mehdi Taheri, Masoud Taheri, Abdullah Abdullah, Tarek Shalaby, Yunbo Hou, and Zebo Zhu for providing me with a friendly and productive work environment. I am thankful to Milad Hosseinipour for his contributions to the design and configuration of the power electronic part of the roller rig. I am also very thankful to Mr. Michael Craft, CVeSS past research scientist and lab manager for his friendship and for all his great help during the early stages of the project.

My time at Virginia Tech would not be this enjoyable without my good friends who enriched every moment of my life with their kind friendship, help and enthusiasm. I would like to particularly thank Mehran Tehrani, Ayoub Yari, Fatemeh Yazdandoost, Meysam Khaleghian, Ali Yeylaghi, Pedram Hatami, and Mehran Motamedi who all made my life at Blacksburg more enjoyable.

Most importantly, I would like to thank my parents, Forouzandeh and Atallah, for their great support and care in my entire life, without whom I would never achieve anything I have achieved. I am also very thankful to my beloved brothers, Saeed and Vahid, and my beautiful sister, Sahar, and sister-in-law, Roshanak, for the meaning they add to my life. Thank you all for everything.

Sajjad Zeinoddini Meymand

December 2015

Blacksburg, VA

# Contents

---

<b>1</b>	<b>INTRODUCTION .....</b>	<b>1</b>
1.1	MOTIVATION .....	1
1.2	OBJECTIVES .....	2
1.3	APPROACH .....	2
1.4	CONTRIBUTIONS .....	2
1.5	OUTLINE .....	3
<b>2</b>	<b>LITERATURE REVIEW .....</b>	<b>5</b>
2.1	INTRODUCTION AND BACKGROUND .....	5
2.2	REVIEW OF DESIGN AND FUNCTIONALITY OF ROLLER RIGS .....	6
2.2.1	<i>History</i> .....	6
2.2.1.1	The Chengdu Roller Rig, China, 1995 .....	7
2.2.1.2	The Naples Roller Rig, Italy, 1992 .....	9
2.2.1.3	The Tokyo Roller Rig, Japan, 1957 .....	10
2.2.1.4	The Pueblo Roller Rig, USA, 1978 .....	11
2.2.1.5	The DB AG Roller Rig, Munich, Germany, 1977 .....	12
2.2.1.6	NRC Rigs, Canada .....	13
2.2.1.7	The DLR Rig, Germany, 1984 .....	15
2.2.1.8	The MMU Rig, England, 1992 .....	16
2.2.1.9	The INRET Rig, France, 1984 .....	17
2.2.1.10	Full-Car Roller Rig, Czech, 1990's .....	17
2.2.1.11	MDM Test Rig, Italy, 2003's .....	18
2.2.1.12	Full-Car Roller Rig, Korea, 2011 .....	18
2.2.1.13	Full-Scale Test Rig, Austria, 2000's .....	19
2.2.1.14	Single Wheelset Scaled Roller Test Stand, Japan, 2000's .....	19
2.2.1.15	SUROS Twin Disk, Sheffield, UK, 1995 .....	20
2.2.1.16	The Rolling Contact Testing Machine, Japan, 1984 .....	21
2.2.1.17	IIT - GMEMD Wheel-Rail Simulation Facility, Chicago, 1990's .....	21
2.2.1.18	The Adhesion Test Equipment, Japan, 2000's .....	22
2.2.1.19	Roller Rig Testing Machines, Japan, 2004's .....	22
2.2.1.20	JD-1 Wheel/Rail Tribological Simulation Apparatus, China, 2000's .....	23
2.2.1.21	The Twin Disc Rig, UK, 2000's .....	24
2.2.1.22	Scaled Roller Rig, Italy, 2000's .....	24
2.3	REVIEW OF STUDIES CONDUCTED BY ROLLER RIGS .....	25
2.3.1	<i>Wheel-Rail Contact Mechanics</i> .....	25

2.3.2	<i>Operational Safety</i> .....	26
2.3.3	<i>Wear and RCF</i> .....	26
2.3.4	<i>Design Improvement</i> .....	26
2.4	REVIEW OF SCALING STRATEGIES.....	27
2.4.1	<i>MMU's Strategy</i> .....	29
2.4.2	<i>DLR's Strategy</i> .....	34
2.4.3	<i>INRET's Strategy</i> .....	36
2.5	DIFFERENCES BETWEEN ROLLER AND TANGENT TRACK.....	38
2.6	ROLLING CONTACT MECHANICS.....	40
2.7	IN SUMMARY .....	42
<b>3</b>	<b>CONFIGURATION AND LAYOUT DEVELOPMENT .....</b>	<b>45</b>
3.1	ROLLER RIG DESIGN CONCEPTS.....	45
3.1.1	<i>Vertical Plane Roller, (Typical Roller Rig)</i> .....	45
3.1.1.1	Concept Benefits .....	46
3.1.1.2	Concept Drawbacks .....	46
3.1.2	<i>Perpendicular Roller</i> .....	46
3.1.2.1	Concept Benefits .....	47
3.1.2.2	Concept Drawbacks .....	47
3.1.3	<i>Tangent Roller, Internal</i> .....	47
3.1.3.1	Concept Benefits .....	48
3.1.3.2	Concept Drawbacks .....	48
3.1.4	<i>Drum Roller</i> .....	48
3.1.4.1	Concept Benefits .....	49
3.1.4.2	Concept Drawbacks .....	49
3.2	ROLLER RIG ALTERNATIVE DESIGNS.....	49
3.2.1	<i>Short Stroke Oscillating Rail</i> .....	50
3.2.1.1	Concept Benefits .....	50
3.2.1.2	Concept Drawbacks .....	50
3.2.2	<i>High Speed Shooting Rail</i> .....	51
3.2.2.1	Concept Benefits .....	51
3.2.2.2	Concept Drawbacks .....	51
3.2.3	<i>Modified Rail (Crown and Gauge Face)</i> .....	51
3.2.3.1	Concept Benefits .....	52

3.2.3.2	Concept Drawbacks .....	52
3.3	ROLLER RIG TEST SPECIMENS.....	53
3.3.1	<i>Single Wheel</i> .....	53
3.3.1.1	Potential Advantages.....	53
3.3.1.2	Potential Limitations .....	53
3.3.1.3	Suggested Application .....	54
3.3.2	<i>Single Wheelset</i> .....	54
3.3.2.1	Potential Advantages.....	54
3.3.2.2	Potential Limitations .....	55
3.3.2.3	Suggested Application .....	55
3.3.3	<i>Full Truck</i> .....	56
3.3.3.1	Potential Advantages.....	56
3.3.3.2	Potential Limitations .....	56
3.3.3.3	Suggested Application .....	57
3.4	CONFIGURATION DESIGN .....	57
3.5	BRIEF DESCRIPTION OF VIRGINIA TECH ROLLER RIG.....	60
3.6	RIG'S CAPABILITIES .....	62
3.6.1	<i>Precise Measurement of Creep-Creepage Curves</i> .....	62
3.6.2	<i>Accurate Measurement of Contact Geometry</i> .....	64
3.6.3	<i>Precise Evaluation of Third Body Layers</i> .....	64
3.6.4	<i>Dynamic Creepage Analysis</i> .....	64
3.6.5	<i>Wheel-rail Vibration Analysis</i> .....	65
3.6.6	<i>Wheel-Rail Wear Analysis</i> .....	65
3.6.7	<i>Derailment Mechanics</i> .....	66
3.6.8	<i>Hardware-in-the-loop (HIL) Operation</i> .....	66
<b>4</b>	<b>HARDWARE DEVELOPMENT.....</b>	<b>68</b>
4.1	FLOOR PLATE .....	68
4.1.1	<i>Floor Plate Design</i> .....	68
4.1.2	<i>Floor Plate Functionality</i> .....	71
4.2	LOAD FRAME .....	72
4.2.1	<i>Frame Design</i> .....	72
4.2.2	<i>Structural and Modal Analysis</i> .....	74
4.2.3	<i>Functionality</i> .....	77

4.3	POSITIONING SYSTEMS .....	77
4.3.1	<i>Angle of Attack (AoA) Positioning System</i> .....	78
4.3.1.1	Component Design and Functionality .....	78
4.3.1.2	Component Sizing .....	80
4.3.2	<i>Lateral Positioning System</i> .....	84
4.3.2.1	Component Design and Functionality .....	84
4.3.2.2	Component Sizing .....	85
4.3.3	<i>Cant Angle Positioning System</i> .....	86
4.3.3.1	Component Design and Functionality .....	87
4.3.3.2	FEM analysis .....	88
4.3.4	<i>Vertical Positioning System</i> .....	89
<b>5</b>	<b>POWERTRAIN .....</b>	<b>91</b>
5.1	MAIN DRIVELINE .....	91
5.1.1	<i>Design Considerations</i> .....	91
5.1.1.1	Independent Drives .....	92
5.1.1.1.1	Concept .....	92
5.1.1.1.2	kinematics and dynamics analysis .....	92
5.1.1.2	Differential Driveline .....	96
5.1.1.2.1	Concept .....	96
5.1.1.2.1.1	Zero Creepage Mode .....	97
5.1.1.2.1.2	Braking Mode .....	97
5.1.1.2.1.3	Traction Mode .....	97
5.1.1.2.2	Power Analysis and Creepage Calculations .....	99
5.1.2	<i>Selected Configuration and Functionality</i> .....	100
5.1.3	<i>Component Selection</i> .....	102
5.2	ROTATIONAL BODIES .....	112
5.3	LINEAR ACTUATORS .....	116
<b>6</b>	<b>INSTRUMENTATION AND CONTROL ARCHITECTURE .....</b>	<b>120</b>
6.1	FORCE-TORQUE MEASURING SYSTEM .....	120
6.1.1	<i>Introduction</i> .....	120
6.1.2	<i>Design Considerations</i> .....	122
6.1.3	<i>Component Sizing and Selection</i> .....	126
6.1.4	<i>Flexural Dynamic Modeling</i> .....	132

6.1.5	<i>Force-Moment Calculations</i> .....	135
6.1.6	<i>Calibration</i> .....	141
6.1.7	<i>Conclusions</i> .....	147
6.2	CONTACT GEOMETRY INSTRUMENTATION .....	148
6.2.1	<i>Additional Sensors</i> .....	150
6.3	CONTROL ARCHITECTURE .....	151
<b>7</b>	<b>TECHNICAL SURVEY OF CONTACT MODELS</b> .....	<b>157</b>
7.1	THE LAW OF COULOMB-D'AMONTONS .....	158
7.2	GENERAL STATEMENT OF WHEEL-RAIL ROLLING CONTACT PROBLEM.....	159
7.3	NORMAL CONTACT.....	162
7.3.1	<i>Hertz's Theory</i> .....	162
7.3.2	<i>Non-Hertzian Models</i> .....	166
7.3.2.1	Kalker's Non-Hertzian Models .....	167
7.3.2.2	Approximate multi-Hertzian models.....	168
7.3.2.3	Approximate virtual penetration models .....	170
7.4	TANGENTIAL CONTACT .....	173
7.4.1	<i>Creepage definition and formulation</i> .....	173
7.4.2	<i>Creep-Creepage relation models</i> .....	175
7.4.2.1	Kalker's linear theory.....	176
7.4.2.2	Kalker's coeffocients .....	178
7.4.2.3	Johnson & Vermuelen theory.....	182
7.4.2.4	Normalized longitudinal and lateral coefficients.....	184
7.4.2.5	Kalker's empirical theory.....	185
7.4.2.6	Shen-Hedrik-Elkins models .....	187
7.4.2.7	Polach contact model .....	187
7.4.2.8	FASTSIM algorithm .....	190
7.4.2.9	CONTACT algorithm .....	195
7.5	EXPERIMENTAL VALIDATION OF CONTACT MODELS .....	198
7.5.1	<i>Velocity dependent friction coefficient</i> .....	201
7.5.2	<i>Effect of contamination and surface roughness</i> .....	204
7.6	RESULTS .....	208
7.7	DISCUSSION AND CONCLUSIONS .....	212

<b>8</b>	<b>MULTI-BODY DYNAMIC MODELING AND CONTACT MECHANICS</b>	
<b>SIMULATIONS</b>		<b>214</b>
8.1	COUPLED MULTI-BODY DYNAMIC MODELING	214
8.1.1	<i>SIMPACK</i>	214
8.1.2	<i>Multibody Modeling</i>	215
8.1.2.1	Bodies and Joints	216
8.1.2.2	Force Elements	218
8.1.3	<i>Simulations and results</i>	220
8.1.4	<i>Conclusions</i>	227
8.2	CONTACT MODULE; A MATLAB ROUTINE	228
8.2.1	<i>Flowchart</i>	228
8.2.2	<i>ANALYN+FaStrip Algorithm</i>	231
8.2.2.1	ANALYN Algorithm	232
8.2.2.2	FaStrip Algorithm	234
8.2.3	<i>Results</i>	236
8.2.4	<i>Conclusions</i>	252
<b>9</b>	<b>SUMMARY AND CONCLUSION</b>	<b>254</b>
9.1	SUMMARY	254
9.2	STRENGTHS AND LIMITATIONS OF THE RIG	258
9.3	FUTURE STUDIES	259
<b>10</b>	<b>REFERENCES</b>	<b>260</b>
<b>APPENDIX A</b>	<b>: KINEMATIC AND DYNAMIC DNALYSES OF A DIFFERENTIAL DRIVELINE</b>	<b>281</b>
A.1	GRAPHICAL METHOD	281
A.2	FREE BODY DIAGRAM	284
A.3	DRIVELINE DYNAMICS AND KINEMATICS ANALYSIS	285
A.3.1	<i>Kinematics Analysis</i>	286
A.3.2	<i>Dynamics Analysis</i>	286
A.3.3	<i>Creepage Calculation</i>	289
A.3.4	<i>Power Calculation</i>	290
A.4	CASE STUDY	290

---

<b>APPENDIX B</b>	<b>: THE MATLAB CODE FOR THE CONTACT MODULE.....</b>	<b>298</b>
THE INITIALIZATION CODE AND MAIN ROUTINE FOR RUNNING SIMULATIONS .....		298
THE CODE FOR SOLVING RIGID GEOMETRY CONTACT MODULE .....		299
THE CODE FOR CALCULATING THE SEPARATION CURVE .....		303
THE CODE FOR CALCULATING KALKER’S COEFFICIENTS .....		304
THE CODE FOR SOLVING NORMAL CONTACT PROBLEM BASED ON ANALYN ALGORITHM....		306
THE CODE FOR CALCULATING THE CREEPAGES.....		308
THE CODE FOR SOLVING TANGENTIAL CONTACT PROBLEM BASED ON FASTRIP ALGORITHM		308
THE CODE FOR CALCULATING HERTZ THEORY’S COEFFICIENTS.....		312

# List of Figures

---

FIGURE 2-1: FULL-SCALE TEST FACILITY AT CHENGDU, CHINA [18] .....	8
FIGURE 2-2: SCHEMATIC DRAWING OF THE DRIVELINE OF THE CHENGDU RIG [18] .....	8
FIGURE 2-3: TEST FACILITY AT NAPLES, ITALY [18] .....	9
FIGURE 2-4: THE FULL-SCALE TEST FACILITY IN TOKYO, JAPAN [18].....	10
FIGURE 2-5: THE ROLL DYNAMIC UNIT (RDU) IN PUEBLO, USA [18] .....	12
FIGURE 2-6: THE DB AG TEST FACILITY AT MUNICH, GERMANY [19].....	12
FIGURE 2-7: TRAVERSE SECTION OF ONE AXLE FOR THE CURVED TRACK SIMULATOR SUPPORT STAND [31] ..	14
FIGURE 2-8: THE NRC WHEEL, BEARING, AND BRAKING TEST FACILITY IN CANADA [36].....	15
FIGURE 2-9: THE 1/5 SCALE DLR ROLLER RIG IN GERMANY [19] .....	16
FIGURE 2-10: THE TEST FACILITY AT MANCHESTER METROPOLITAN UNIVERSITY [42].....	16
FIGURE 2-11: THE INRET TEST FACILITY AT GRENOBLE (LEFT) [19], AND ITS LARGE FLYWHEEL (RIGHT) [44] .....	17
FIGURE 2-12: THE MDM TEST FACILITY AT FLORENCE, ITALY [46] .....	18
FIGURE 2-13: THE FULL-SCALE TEST FACILITY AT VOESTALPINE SCHIENEN GMBH [8] .....	19
FIGURE 2-14: THE SCALED TEST FACILITY IN JAPAN [11] .....	20
FIGURE 2-15: THE SOROS TEST FACILITY AT THE SHEFFIELD UNIVERSITY, UK [52].....	20
FIGURE 2-16: THE ROLLING CONTACT TESTING MACHINE IN JAPAN [53].....	21
FIGURE 2-17: THE IIT-GMEMD TEST FACILITY IN CHICAGO, USA [54] .....	22
FIGURE 2-18: THE ADHESION TEST EQUIPMENT IN JAPAN [56] .....	22
FIGURE 2-19: THE SINGLE-WHEELSET TEST FACILITY IN CHINA [59].....	23
FIGURE 2-20: THE SQUEAL TESTING FACILITY IN UK [12].....	24
FIGURE 2-21: SCALED FULL BOGIE ROLLER RIG IN ITALY [60] .....	25
FIGURE 2-22: SCHEMATIC DRAWING OF PURE SLIDING CONTACT (LEFT) AND ROLLING CONTACT (RIGHT) [74] .....	41
FIGURE 2-23. CREEP CURVE SHOWING THE RELATIONSHIP BETWEEN CREEP FORCE AND CREEP AS WELL AS DIVISION OF CONTACT PATCH TO SLIP AND STICK AREAS [74].....	41
FIGURE 3-1: DIAGRAM OF A VERTICAL PLANE ROLLER RIG AND PRODUCT DESIGN [12] .....	46
FIGURE 3-2: A ROLLER RIG DESIGN WITH HORIZONTAL ROLLER CONFIGURATION .....	47
FIGURE 3-3: A ROLLER RIG DIAGRAM WITH INTERNAL TANGENT ROLLER .....	48
FIGURE 3-4: SIMPLE DIAGRAM OF A WHEELSET ON A DRUM ROLLER AND PRODUCT DESIGN [36].....	49
FIGURE 3-5: OSCILLATING RAIL RIG DIAGRAM AND PRODUCED DESIGN [8].....	50
FIGURE 3-6: STATIONARY TRUCK, TRACK IN MOTION .....	51
FIGURE 3-7: ROLLER RIGS DIAGRAMS WITH MODIFIED RAIL CROWN .....	52
FIGURE 3-8: CONCEPT OF A SINGLE WHEEL ROLLER TEST RIG .....	54

FIGURE 3-9: CONCEPT OF A SINGLE WHEELSET ROLLER TEST RIG.....	55
FIGURE 3-10: CONCEPT OF A FULL TRUCK ROLLER TEST RIG.....	57
FIGURE 3-11: SOLID MODEL OF VIRGINIA TECH ROLLER RIG .....	61
FIGURE 3-12: THE VIRGINIA TECH ROLLER RIG .....	63
FIGURE 4-1: T-SLOTTED FLOOR PLATE AND ITS SOLID MODEL SHOWING BI-DIRECTIONAL T-SLOTS ON TOP SURFACE AND REINFORCED RIBBING STRUCTURE AT THE BOTTOM .....	69
FIGURE 4-2: LEFT: 28H12 T-SLOTS AND CLAMPING HARDWARE INCLUDING T-NUTS, STUD, NUT, TRIANGULAR LOCK, AND CLAMP STRAP FOR MOUNTING COMPONENTS ON THE FLOOR PLATE. RIGHT: PRECISION BUBBLE LEVELER USED FOR LEVELING THE FLOOR PLATE .....	69
FIGURE 4-3: VRC WEDGE-MOUNT PRECISION LEVELERS MANUFACTURED BY AIRLOC [77] .....	70
FIGURE 4-4: STRUCTURAL ANALYSIS OF THE MOUNTING PLATE FOR EVALUATING THE PERFORMANCE (STATIC DEFLECTION OF PLATE) OF WEDGE-MOUNTS USING ABAQUS .....	71
FIGURE 4-5: FINITE ELEMENT ANALYSIS OF THE FLOOR PLATE USING ABAQUS .....	72
FIGURE 4-6: SOLID MODEL AND FABRICATED REACTION LOAD FRAME .....	74
FIGURE 4-7: THE WIRE FRAME MODEL OF REACTION LOAD FRAME IN ABAQUS USING BEAM ELEMENTS .....	75
FIGURE 4-8: THE ANGULAR POSITION OF THE WHEEL RELATIVE TO THE RAIL KNOWN AS ANGLE OF ATTACK (AOA) .....	78
FIGURE 4-9: SCHEMATIC DRAWING OF THE CROSS ROLLER RING MANUFACTURED BY THK [79].....	79
FIGURE 4-10: SOLID MODEL OF THE AOA AND LATERAL POSITIONING SYSTEMS, AND THEIR ACTUATION MECHANISMS. GREEN ARROWS INDICATE THE LATERAL AND AOA DEGREES OF FREEDOM .....	80
FIGURE 4-11: LEFT: SOLID MODEL OF THE RIG. RIGHT: SCHEMATIC DRAWING OF THE RIG THAT SHOWS HOW THE CONTACT FORCES ARE REACTED AT THE LATERAL POSITIONING SYSTEM, AOA POSITIONING SYSTEM, AND VERTICAL POSITIONING SYSTEM .....	81
FIGURE 4-12: FREE BODY DIAGRAM OF AOA AND LATERAL POSITIONING SYSTEMS .....	82
FIGURE 4-13: THE LINEAR POSITION OF THE WHEEL RELATIVE TO THE RAIL KNOWN AS LATERAL DISPLACEMENT .....	84
FIGURE 4-14: SCHEMATIC DRAWING OF THE CAGED BALL LM GUIDES [79].....	85
FIGURE 4-15: THE VERTICAL INCLINATION OF THE WHEELSET RELATIVE TO THE RAIL IS KNOWN AS CANT ANGLE .....	86
FIGURE 4-16: SCHEMATIC DRAWING OF THE DESIGNED CRADLE AND ROTATING MECHANISM FOR PROVIDING THE CANT ANGLE MOTION. GREEN ARROWS INDICATE THE VERTICAL AND CANT DEGREES OF FREEDOM .....	88
FIGURE 4-17: THE WIRE FRAME MODEL OF THE CRADLE IN ABAQUS USING BEAM ELEMENTS .....	88
FIGURE 4-18: FRONT (LEFT) AND REAR (RIGHT) VIEWS OF THE RIG SHOWING HARDWARE DEVELOPMENT AND ASSEMBLY .....	90

FIGURE 5-1: DIFFERENT CONFIGURATIONS FOR THE INDEPENDENT DRIVELINE .....92

FIGURE 5-2: LEFT: WHEEL AND ROLLER SHAFTS IN THE INDEPENDENT DRIVES CONFIGURATION. TOP-RIGHT: FREE BODY DIAGRAM OF THE WHEEL. BOTTOM-RIGHT: FREE BODY DIAGRAM OF THE ROLLER. ....93

FIGURE 5-3: SCHEMATIC DRAWING OF THE INDEPENDENT DRIVES CONFIGURATION .....95

FIGURE 5-4: SCHEMATIC DRAWING OF THE DIFFERENTIAL DRIVELINE CONFIGURATION IN WHICH A DIFFERENTIAL GEARBOX IS EMPLOYED FOR PRODUCING CREEPAGE AT THE CONTACT.....96

FIGURE 5-5: SCHEMATIC OF DIFFERENT DIFFERENTIAL DRIVE FUNCTIONALITY: LEFT: ZERO CREEPAGE MODE. MIDDLE: BRAKING MODE. RIGHT: TRACTION MODE. ....98

FIGURE 5-6: SCHEMATIC DRAWING OF ENERGY FLOW CHART FOR DIFFERENTIAL DRIVELINE: A) TRACTION MODE, B) BRAKING MODE.....99

FIGURE 5-7: PROPOSED CONFIGURATION FOR IMPLEMENTING THE DIFFERENTIAL DRIVELINE.....100

FIGURE 5-8: SCHEMATIC DRAWING OF BASIC DRIVE CIRCUIT FOR AC SERVOMOTORS [81].....102

FIGURE 5-9: KEY DESIGN FEATURES OF KOLLMORGEN’S PERMANENT MAGNET SYNCHRONOUS MACHINE [82] .....103

FIGURE 5-10: EXPLODED VIEW OF THE AC SYNCHRONOUS SERVOMOTOR [82].....104

FIGURE 5-11: PERFORMANCE CURVE FOR AKM84T SERVOMOTOR [82].....104

FIGURE 5-12: PICTURE OF S772 SERVO DRIVE OFFERED BY KOLLMORGEN [83].....106

FIGURE 5-13: LEFT) WIRING DIAGRAM OF THE S772 SERVO DRIVES [83]. RIGHT) INSTALLED S772 SERVO-DRIVES CONTROLLING THE SERVOMOTORS THAT DRIVE THE WHEEL AND ROLLER DRIVELINES .....107

FIGURE 5-14: BDB330 PRECISION GEARBOX OFFERED BY MIJNO [84].....108

FIGURE 5-15: UNIQUE FEATURES OF THE UT018-005 TRUE PLANETARY GEARHEAD OFFERED BY MICRON [85] .....109

FIGURE 5-16: LEFT) DOUBLE ROW SPHERICAL ROLLER BEARING. MIDDLE) PILLOW BLOCK SPHERICAL ROLLER BEARING FSYE SERIES SELECTED FOR THE RIG AND OFFERED BY SKF [86]. RIGHT) INSTALLED ROLLER DRIVELINE’S BEARING .....110

FIGURE 5-17: SCHEMATIC OF CONCENTRA MOUNTING DESIGN CONFIGURATION [86].....110

FIGURE 5-18: THE DETAILED DRAWING OF AREMA 136-LBS RE RAIL SECTION [87] .....112

FIGURE 5-19: LEFT: FENNER DRIVE KEYLESS LOCKING DEVICE FUNCTIONS AS A MECHANICAL INTERFERENCE FIT. RIGHT: A SIMPLE WEDGE PRINCIPAL USED TO APPLY A UNIFORM PRESSURE DISTRIBUTION [88] .....113

FIGURE 5-20: ROLLER DRIVELINE DURING ASSEMBLY PROCESS .....114

FIGURE 5-21: LEFT) THE DETAILED DRAWING OF AAR-1B WIDE-FLANGE WHEEL PROFILE [89]. RIGHT) FABRICATED WHEELS WITH FLAT CYLINDRICAL AND AAR-1B PROFILES.....115

FIGURE 5-22: SOLID MODEL (TOP) AND INSTALLED HARDWARE (BOTTOM) OF THE ROLLER (LEFT) AND WHEEL (RIGHT) DRIVELINES .....115

FIGURE 5-23: LEFT) EC4 ELECTRIC CYLINDER INCORPORATES AN AKM SERVOMOTOR AND A BALLSCREW TO PRECISELY CONTROL THE LINEAR MOTION. RIGHT) INSTALLED AKD SERVO DRIVES CONTROLLING SIX ELECTRIC CYLINDERS THAT CONTROL THE MOTION OF POSITIONING SYSTEMS .....117

FIGURE 5-24: CUT-AWAY DRAWING OF THE EC SERIES ELECTRIC CYLINDERS WITH THE KEY DESIGN FEATURES [90].....117

FIGURE 5-25: THE THRUST-SPEED PERFORMANCE CURVE FOR THE AKM52G SERVOMOTORS [90].....118

FIGURE 5-26: HALL-EFFECT END-OF-TRAVEL SENSORS FOR SIGNALING THE END OF STROKE FOR EC4 CYLINDERS [90]. RIGHT) INSTALLED HALL-EFFECT SENSOR IN ACTION .....119

FIGURE 6-1: DIFFERENT OPTIONS FOR PLACEMENT OF THE F/T PLATFORM IN THE EXPERIMENTAL SETUP ...123

FIGURE 6-2: THE PRIMARY F/T PLATFORM (WHEEL DYNAMOMETER) IS PLACED ON THE CRADLE FRAME IN-PLANE WITH THE CONTACT PATCH .....123

FIGURE 6-3: THE LOAD-PATH FROM THE CONTACT PATCH TO THE GROUND INCLUDES TWO ROUTES: ONE THAT PASSES THROUGH THE PRIMARY F/T PLATFORM, AND THE OTHER ONE, WHICH GOES THROUGH THE DRIVELINE AND MOTOR CASING (FORCE SHUNT).....124

FIGURE 6-4: TOP VIEW OF THE RIG SHOWING WHEEL AND MOTOR DYNAMOMETERS INSTALLED UNDER THE WHEEL DRIVELINE .....124

FIGURE 6-5: MULTI-COMPONENT SENSOR SET TYPE 9026C4 CONSISTS OF FOUR SIMILAR SENSORS, TWO PAIRS OF 9027C AND 9028C FORMING A F/T PLATFORM [101] .....126

FIGURE 6-6: RECOMMENDED TOLERANCES FOR MOUNTING THE SENSOR TYPE 9027C OR 9028C [101] .....128

FIGURE 6-7: SIX COMPONENT DYNAMOMETERS CONSIST OF FOUR TRIAXIAL SENSORS PRELOADED BETWEEN TWO PLATES. LEFT) FOUR TRIAXIAL SENSORS ARE ALIGNED AND INSTALLED ON THE BASE PLATE. THE COVER PLATE AND PRETENSIONING SET ARE INSTALLED TO PRELOAD THE SENSORS FOR THE MOTOR DYNAMOMETER (MIDDLE) AND THE WHEEL DYNAMOMETER (RIGHT).....129

FIGURE 6-8: INTERCONNECTION OF 12 SENSOR OUTPUTS FOR THE 6-COMPONENT FORCE MEASURING DYNAMOMETER [101].....129

FIGURE 6-9: KISTLER DYNAMOMETER ACCESSORIES: PRE-TENSIONING SET (LEFT), SUMMING BOX (MIDDLE), AND MULTICHANNEL CHARGE AMPLIFIER (RIGHT) [101] .....130

FIGURE 6-10: LEFT) KiTORQ SYSTEM CONSISTING OF A KiTORQ ROTOR MEASURING UNIT AND A KiTORQ STATOR EVALUATION UNIT [102]. RIGHT) TORSION-PROOF MULTI-DISK COUPLING ESPECIALLY DESIGNED FOR USE WITH THE KiTORQ FLANGE [103].....131

FIGURE 6-11: STRUCTURAL ANALYSIS OF THE COVER PLATE FOR THE WHEEL (TOP) AND MOTOR (BOTTOM) DYNAMOMETERS IN ABAQUS FOR UNDEFORMED (LEFT) AND DEFORMED (RIGHT) STATES DUE TO MAXIMUM LOADING CONDITIONS .....133

---

FIGURE 6-12: MODE SHAPES FOR THE FIRST FIVE NATURAL FREQUENCIES OF THE TOP PLATE FOR THE MOTOR DYNAMOMETER .....	135
FIGURE 6-13: FREE BODY DIAGRAM OF THE LOADCELLS AND CONTACT PATCH WHEN THE CONTACT PATCH IS LOCATED INLINE AND CENTERED RELATIVE TO THE IMAGINARY PLANE DEFINED BY THE LOAD CELLS SENSING ORIGINS .....	135
FIGURE 6-14: FREE BODY DIAGRAM OF THE LOADCELLS AND CONTACT PATCH WHEN THE CONTACT PATCH IS LOCATED OFF-PLANE AND NOT CENTERED RELATIVE TO THE IMAGINARY PLANE DEFINED BY THE LOAD CELLS SENSING ORIGINS.....	140
FIGURE 6-15: FREE BODY DIAGRAM OF THE WHEEL DRIVELINE FOR DYNAMIC MEASUREMENT OF THE CONTACT FORCES .....	141
FIGURE 6-16: CALIBRATION SETUP FOR THE DYNAMOMETERS .....	142
FIGURE 6-17: QUASI-STATIC CALIBRATION AND CROSS-SENSITIVITY CURVES OF THE WHEEL DYNAMOMETER FOR INPUT FORCE IN X-DIRECTION .....	143
FIGURE 6-18: QUASI-STATIC CALIBRATION AND CROSS-SENSITIVITY CURVES OF THE MOTOR DYNAMOMETER FOR INPUT FORCE IN X-DIRECTION .....	143
FIGURE 6-19: QUASI-STATIC CALIBRATION AND CROSS-SENSITIVITY CURVES OF THE WHEEL DYNAMOMETER FOR INPUT FORCE IN Y-DIRECTION .....	144
FIGURE 6-20: QUASI-STATIC CALIBRATION AND CROSS-SENSITIVITY CURVES OF THE MOTOR DYNAMOMETER FOR INPUT FORCE IN Y-DIRECTION .....	144
FIGURE 6-21: QUASI-STATIC CALIBRATION AND CROSS-SENSITIVITY CURVES OF THE WHEEL DYNAMOMETER FOR INPUT FORCE IN Z-DIRECTION .....	145
FIGURE 6-22: QUASI-STATIC CALIBRATION AND CROSS-SENSITIVITY CURVES OF THE MOTOR DYNAMOMETER FOR INPUT FORCE IN Z-DIRECTION .....	145
FIGURE 6-23: IMPACT FREQUENCY RESPONSE OF THE WHEEL DYNAMOMETER FOR AN IMPACT INPUT IN X,Y,Z-DIRECTIONS .....	146
FIGURE 6-24: IMPACT FREQUENCY RESPONSE OF THE MOTOR DYNAMOMETER FOR AN IMPACT INPUT IN X,Y,Z-DIRECTIONS .....	147
FIGURE 6-25: THE PROVISIONAL DESIGN OF THE CRADLE FOR ACCOMMODATING VISION SYSTEM (LEFT) AND SCHEMATIC DRAWING OF THE PROPOSED VISION CONFIGURATION FOR ESTIMATING THE CONTACT AREA (RIGHT).....	150
FIGURE 6-26: THE SCHEMATIC DRAWING OF THE PROPOSED CONFIGURATION OF LASER SENSORS FOR MEASURING THE RELATIVE DISPLACEMENTS BETWEEN THE ROTATING BODIES .....	151
FIGURE 6-27: SCHEMATIC DIAGRAM OF THE CONTROL ARCHITECTURE CONFIGURED FOR THE ROLLER RIG. THE HOST COMPUTER THAT INCLUDES ZMP-SYNQNET CARD CONNECTS TO TWO S772 DIGITAL DRIVES	

IN SERIES, THEN CONNECTS TO 6 AKD DRIVES IN SERIES, THEN CONNECTS TO FOUR SQIO-SQID CARDS IN SERIES, AND FINALLY CONNECTS BACK TO THE HOST COMPUTER.....	153
FIGURE 6-28: BLOCK DIAGRAM OF THE CONTROL ARCHITECTURE OF THE RIG .....	154
FIGURE 6-29: SYNQNET SUPPORTS VARIOUS MOTION CONTROLLERS [109] .....	154
FIGURE 6-30: THE CONTROL CABINET OF THE RIG INCLUDING S700 DRIVES, AKD DRIVES, REGENERATIVE AND DYNAMITIC BRAKE RESISTORS, SAFETY/CONTROL CIRCUITS, ETC. ALL THE COMPONENTS ARE PLACED INSIDE A FARADAY CAGE AND ARE CONTROLLED THROUGH OPERATOR INTERFACE PANEL....	156
FIGURE 7-1: SCHEMATIC DRAWING OF A WHEEL ROLLING OVER A RAIL SHOWING THE FIXED AND MOVING COORDINATE SYSTEMS .....	158
FIGURE 7-2: SCHEMATIC DRAWING OF THE INTERFACE OF TWO ELASTIC BODIES IN CONTACT SHOWING DEFORMED AND UNDEFORMED STATES OF THE INTERFACE. THE INTERPENETRATION REGION AND THE CONTACT AREA ARE SHOWN IN THE BOTTOM (ADAPTED FROM [119]). .....	160
FIGURE 7-3: WHEEL-RAIL INTERFACE FOR PLANE $X=0$ IN THE UNDEFORMED STATE.....	163
FIGURE 7-4: SEMI-ELLIPSOID NORMAL PRESSURE DISTRIBUTION .....	166
FIGURE 7-5: HERTZIAN VS NON-HERTZIAN NORMAL PRESSURE DISTRIBUTION.....	168
FIGURE 7-6: DETERMINATION OF MULTIPLE ELLIPSES USING MULTI-HERTZIAN METHODS AND REPRESENTING THEM BY AN EQUIVALENT ELLIPSE (ADAPTED FROM [112]).....	170
FIGURE 7-7: DISCRETIZATION OF THE CONTACT AREA BY STRIPS (ADAPTED FROM [112]) .....	173
FIGURE 7-8: SCHEMATIC DRAWINGS FOR DEFINITION OF CREEPAGE .....	174
FIGURE 7-9: TRACTION DISTRIBUTION WITHIN CONTACT AREA BASED ON KALKER'S LINEAR THEORY. EXTREME CONDITION WHEN $m$ IS LARGE (RIGHT) [118] .....	177
FIGURE 7-10: COMPARISON BETWEEN AYASSE MODEL AND PROPOSED POLYNOMIAL MODEL FOR ESTIMATING $c_{11}$ KALKER COEFFICIENT: TOP PLOT SHOWS ESTIMATED COEFFICIENTS FOR BOTH THE MODELS AS A FUNCTION OF $G$ FOR A CONSTANT POISSON RATIO ( $\nu = 0.25$ ), AND BOTTOM PLOT PRESENTS THEIR RESIDUAL FROM TABULATED VALUES. ....	181
FIGURE 7-11: SLIP AND ADHESION AREAS INSIDE THE CONTACT PATCH DEFINED IN VERMUELEN AND JOHNSON THEORY [146] .....	183
FIGURE 7-12: TOTAL TANGENTIAL FORCE COMPARISON BETWEEN KALKER'S EMPIRICAL MODEL, AND VERMUELEN & JOHNSON MODEL .....	186
FIGURE 7-13: NORMAL AND TANGENTIAL STRESS DISTRIBUTION OVER THE CONTACT AREA FOR SLIP AND ADHESION AREAS [154] .....	188
FIGURE 7-14: THE AREA OF CONTACT SLICES AND STRIPS ACCORDING TO FASTSIM ALGORITHM. ....	193
FIGURE 7-15: ADHESION-SLIP BORDER PREDICTION BY FASTSIM WITH PARABOLIC AND ELLIPTICAL TRACTION BOUNDS COMPARED WITH CONTACT. ....	194

FIGURE 7-16: LEFT) CREEP CURVES COMPARISON BETWEEN FASTSIM WITH PARABOLIC AND ELLIPTICAL TRACTION BOUNDS WITH CONTACT ALGORITHM. RIGHT) CREEP FORCE ESTIMATION ERROR FOR FASTSIM WITH PARABOLIC AND ELLIPTICAL TRACTION BOUNDS AS COMPARED WITH CONTACT ALGORITHM .....194

FIGURE 7-17: THE SLIP AND ADHESION AREAS FOR THE CASE OF PURE SPIN CREEPAGE ( $\phi_1 < \phi_2 < \phi_3$ ) SHOWING THE AREA IN THE VICINITY OF SPIN POLE IS OFTEN MARKED BY GREAT STRESS CHANGES [157] .....195

FIGURE 7-18: TWO ELASTIC BODIES IN CONTACT: UNDEFORMED AND DEFORMED STATES .....196

FIGURE 7-19: DISCREPANCIES BETWEEN THEORETICAL CREEP FORCE CALCULATIONS AND MEASUREMENTS [171, 188]. CONTACT PROGRAM IS EXTENDED TO ACCOUNT FOR VELOCITY DEPENDENT FRICTION COEFFICIENT, SURFACE ROUGHNESS, AND THIRD BODY LAYER [158]. .....201

FIGURE 7-20: COMPARISON OF TANGENTIAL STRESS DISTRIBUTION FOR A STRIP IN THE ROLLING DIRECTION UNDER DIFFERENT METHODS IMPLEMENTED IN THE FASTSIM ALGORITHM. TRACTION CURVES SHOWN HERE ARE SCHEMATIC .....203

FIGURE 7-21: SCHEMATIC MODEL OF THE TANGENTIAL WHEEL-RAIL CONTACT FOR (A) CLEAN AND SMOOTH, AD (B) FOR ROUGH AND CONTAMINATED SURFACES [51].....205

FIGURE 7-22: SCHEMATIC DRAWING OF THE INTERFACIAL LAYER MODELING IN CONTACT PROGRAM [206] .....205

FIGURE 7-23: ELASTIC-PLASTIC MATERIAL PROPERTIES OF THE THIRD BODY LAYER (ADAPTED FROM [211]) .....208

FIGURE 7-24: COMPARISON OF DIMENSIONLESS LONGITUDINAL CREEP FORCE-CREEPAGE CURVE FOR DIFFERENT CONTACT MODELS: KALKER’S LINEAR THEORY, KALKER’S EMPIRICAL THEORY, VERMEULEN’S THEORY, SHEN’S MODEL, AND CONTACT ALGORITHM (LEFT), AS WELL AS FASTSIM ALGORITHM, POLACH’S, AND CONTACT ALGORITHM (RIGHT). .....210

FIGURE 7-25: COMPARISON OF LATERAL CREEP-CREEPAGE CURVE FOR COMBINED LONGITUDINAL AND SPIN CREEPAGE CONDITION (LEFT) AND FOR PURE SPIN CREEPAGE CONDITION (RIGHT) FOR DIFFERENT CONTACT THEORIES. ....211

FIGURE 7-26: COMPARISON OF VARIOUS VELOCITY DEPENDENT FRICTION COEFFICIENT LAWS (LEFT) AND THEIR IMPLEMENTATION IN POLACH MODEL (RIGHT) .....212

FIGURE 8-1: MULTI-BODY DYNAMIC MODEL OF VIRGINIA TECH ROLLER RIG IMPLEMENTED IN SIMPACK SOFTWARE PACKAGE .....216

FIGURE 8-2: AAR1B AND FLAT CYLINDRICAL WHEEL PROFILES AND 136R RAIL HEAD PROFILE USED FOR THE ROLLER RIG. ....217

FIGURE 8-3: MULTI-BODY DYNAMIC SIMULATION SAMPLE RESULTS FOR ESTIMATING THE MAXIMUM CONTACT FORCES IN LONGITUDINAL, LATERAL, AND NORMAL DIRECTIONS .....222

FIGURE 8-4: DESIRED SPEED PROFILE INPUT FOR THE ROLLER SHAFT .....222

FIGURE 8-5: MULTI-BODY DYNAMIC SIMULATION RESULTS FOR ESTIMATING THE CONTACT FORCES IN LONGITUDINAL (TOP), LATERAL (MIDDLE), AND VERTICAL (BOTTOM) DIRECTIONS. RESULTS SHOW THAT INDIVIDUAL FORCE READINGS FROM EITHER ONE OF THE WHEEL OR MOTOR DYNAMOMETERS ARE NOT ABLE TO ESTIMATE THE CONTACT FORCES. HOWEVER, THE READINGS FROM BOTH THE DYNAMOMETERS CAN ESTIMATE THE CONTACT FORCES ACCURATELY. ....224

FIGURE 8-6: MULTI-BODY DYNAMIC SIMULATION RESULTS FOR THE DISCREPANCIES BETWEEN THE ESTIMATED CONTACT FORCES FROM DYNAMOMETERS AND ACTUAL CONTACT FORCES WITH CONSIDERING THE INERTIA TERMS (USING ACCELEROMETERS’ READINGS) AND WITHOUT CONSIDERING THE INERTIA TERMS IN LONGITUDINAL (TOP), LATERAL (MIDDLE), AND VERTICAL (BOTTOM) DIRECTIONS. ....225

FIGURE 8-7: FLOWCHART FOR THE CONTACT MODULE IMPLEMENTED IN MATLAB .....229

FIGURE 8-8: CONTACT GEOMETRY SUBROUTINE CALCULATES THE LOCATION OF THE CONTACT POINTS BASED ON GIVEN CONTACT CONDITIONS (LATERAL SHIFT=0, CANT ANGLE=0°, ANGLE OF ATTACK=0°) .....230

FIGURE 8-9: CONTACT GEOMETRY SUBROUTINE CALCULATES THE LOCATION OF THE CONTACT POINTS BASED ON GIVEN CONTACT CONDITIONS (LATERAL SHIFT=2, CANT ANGLE=5°, ANGLE OF ATTACK=3°) .....230

FIGURE 8-10: SEPARATION CURVE AND CORRESPONDING CURVATURE CURVE OF WHEEL-ROLLER CONTACT FOR DIFFERENT LATERAL DISPLACEMENTS; FROM TOP TO BOTTOM  $Y = 0.0$ ,  $Y = 0.4$ ,  $Y = 0.8$ , AND  $Y = 1.2\text{MM}$  (CANT ANGLE=0°, ANGLE OF ATTACK=0°) .....238

FIGURE 8-11: CONTACT AREA AND NORMAL PRESSURE DISTRIBUTION ALONG LINE  $X = 0.0$  FOR WHEEL-ROLLER CONTACT FOR DIFFERENT LATERAL DISPLACEMENTS; FROM TOP TO BOTTOM  $Y = 0.0$ ,  $Y = 0.4$ ,  $Y = 0.8$ , AND  $Y = 1.2\text{MM}$  (CANT ANGLE=0°, ANGLE OF ATTACK=0°) .....239

FIGURE 8-12: CONTACT AREA AND NORMAL PRESSURE DISTRIBUTION ALONG LINE  $X = 0.0$  FOR WHEEL-ROLLER CONTACT FOR DIFFERENT LATERAL DISPLACEMENTS; FROM TOP TO BOTTOM  $Y = -0.5$ ,  $Y = -1$ ,  $Y = -2\text{MM}$  (CANT ANGLE=0°, ANGLE OF ATTACK=0°).....240

FIGURE 8-13: CONTACT AREA PREDICTED BY DIFFERENT NORMAL CONTACT THEORIES FOR INCREASED NORMAL LOADING CONDITION AT THE INTERFACES (LATERAL SHIFT=0.8, CANT ANGLE=0°, ANGLE OF ATTACK=0°) .....241

FIGURE 8-14: GEOMETRY OF WHEEL-ROLLER CONTACT FOR DIFFERENT CANT ANGLES SHOWING THE CONTACT POINT LOCATION AND NORMAL VECTOR AT THE CONTACT POINT; FROM TOP TO BOTTOM CANT ANGLE IS  $-5^\circ$ ,  $0^\circ$ , AND  $5^\circ$ , RESPECTIVELY (LATERAL SHIFT=0MM, ANGLE OF ATTACK=0°) .....242

FIGURE 8-15: CONTACT AREA AND NORMAL PRESSURE DISTRIBUTION ALONG LINE  $x = 0.0$  FOR WHEEL-ROLLER CONTACT FOR DIFFERENT CANT ANGLES; FROM TOP TO BOTTOM CANT ANGLE IS  $-5^\circ$ ,  $0^\circ$ , AND  $5^\circ$ , RESPECTIVELY (LATERAL SHIFT=0MM, ANGLE OF ATTACK= $0^\circ$ ).....244

FIGURE 8-16: CONTACT AREA PREDICTION WITH AND WITHOUT CONSIDERING THE ANGLE OF ATTACK (LATERAL SHIFT=0MM, CANT ANGLE= $0^\circ$ , ANGLE OF ATTACK= $3^\circ$ , NORMAL LOADING=40600N) .....245

FIGURE 8-17: CONTACT AREA PREDICTION WITH AND WITHOUT CONSIDERING THE ANGLE OF ATTACK FOR A FLANGE CONTACT CONDITION (LATERAL SHIFT=2MM, CANT ANGLE= $0^\circ$ , ANGLE OF ATTACK= $1.5^\circ$ , NORMAL LOADING=10600N).....245

FIGURE 8-18: THREE-DIMENSIONAL NORMAL PRESSURE DISTRIBUTION PREDICTED BY ANALYN (TOP) AND CONTACT (BOTTOM) ALGORITHMS (LATERAL SHIFT=0MM, CANT ANGLE= $0^\circ$ , ANGLE OF ATTACK= $0^\circ$ , NORMAL LOADING=10600N).....246

FIGURE 8-19: CONTACT AREA AND ITS DIVISION TO ADHESION AND SLIP AREAS (TOP), LONGITUDINAL SHEAR STRESS CURVE (MIDDLE), AND LATERAL SHEAR STRESS DISTRIBUTION (BOTTOM) ALONG ROLLING DIRECTION  $Y = 2.5$  FOR PURE LONGITUDINAL CREEPAGE CONDITION;  $V_x = 0.2\%$  (LEFT) AND COMBINED CREEPAGE CONDITION  $V_x = V_y = 0.2\%$  (RIGHT).....247

FIGURE 8-20: CONTACT AREA AND ITS DIVISION TO ADHESION AND SLIP AREAS (TOP), LONGITUDINAL SHEAR STRESS CURVE (MIDDLE), AND LATERAL SHEAR STRESS DISTRIBUTION (BOTTOM) ALONG ROLLING DIRECTION  $Y = 3$  FOR PURE SPIN CREEPAGE CONDITIONS;  $\phi = -0.01$  (LEFT) AND  $\phi = -0.001$  (RIGHT). .....248

FIGURE 8-21: CONTACT AREA AND ITS DIVISION TO ADHESION AND SLIP AREAS (TOP), LONGITUDINAL SHEAR STRESS CURVE (MIDDLE), AND LATERAL SHEAR STRESS DISTRIBUTION (BOTTOM) ALONG ROLLING DIRECTION  $Y = 3$  (LEFT) AND  $Y = 2.5$  FOR COMBINED CREEPAGE CONDITIONS;  $V_x = V_y = 0.2\%$  AND  $\phi = -0.001$ .....249

FIGURE 8-22: THREE-DIMENSIONAL LONGITUDINAL (LEFT) AND LATERAL (RIGHT) SHEAR STRESS DISTRIBUTION PREDICTED BY ANALYN-FASTIP (TOP) AND CONTACT (BOTTOM) ALGORITHMS FOR COMBINED CREEPAGE CONDITIONS;  $V_x = V_y = 0.2\%$  AND  $\phi = -0.001$ .....250

FIGURE 8-23: CONTACT AREA AND ITS DIVISION TO ADHESION AND SLIP AREAS (TOP), LONGITUDINAL SHEAR STRESS CURVE (MIDDLE), AND LATERAL SHEAR STRESS DISTRIBUTION (BOTTOM) ALONG ROLLING DIRECTION  $Y = 3$  (LEFT) AND  $Y = 2.5$  FOR COMBINED CREEPAGE CONDITIONS;  $V_x = 0.2\%$  AND  $\phi = -0.001$ . .....251

FIGURE 8-24: COMPARISON OF LONGITUDINAL CREEP FORCE-CREEPAGE CURVE FOR DIFFERENT CONTACT THEORIES; CONTACT, FASTSIM, AND FASTRIP.....252

---

FIGURE 8-25: COMPARISON OF LATERAL CREEP FORCE-CREEPAGE CURVE FOR COMBINED LONGITUDINAL AND SPIN ( $\phi = -0.001$ ) CREEPAGE (LEFT) AND PURE SPIN CREEPAGE (RIGHT) CONDITIONS AT THE CONTACT .....	252
FIGURE 9-1: VIRGINIA TECH ROLLER RIG TESTING FACILITY .....	256
FIGURE A-1: PLANETARY DIFFERENTIAL GEARBOX. ....	281
FIGURE A-2: GRAPHICAL METHOD TO ANALYZE A) VELOCITY B) FORCE C) TORQUE, IN PLANETARY GEARBOX. ....	282
FIGURE A-3: FREE-BODY DIAGRAM FOR ASSEMBLY NUMBER 4. ....	284
FIGURE A-4: CONFIGURATION REPRESENTING THE BIGGER TORQUE SUN GEAR IS CONNECTED TO INPUT GEARBOX .....	285
FIGURE A-5: CONFIGURATION REPRESENTING THE BIGGER TORQUE SUN GEAR IS CONNECTED TO WHEEL ..	286
FIGURE A-6: DIFFERENT SHAFT ELEMENTS IN THE DIFFERENTIAL DRIVELINE. ....	287
FIGURE A-7: FREE-BODY DIAGRAM FOR CARRIAGE (SHAFT NUMBER 1) .....	287
FIGURE A-8: FREE-BODY DIAGRAM FOR SHAFT NUMBER 2.....	287
FIGURE A-9: FREE-BODY DIAGRAM FOR SHAFT NUMBER 3.....	288
FIGURE A-10: FREE-BODY DIAGRAM FOR SHAFT NUMBER 4.....	288
FIGURE A-11: FREE-BODY DIAGRAM FOR ROLLER AXLE (SHAFT NUMBER 6) .....	289
FIGURE A-12: MAXIMUM REQUIRED POWER FOR THE DRIVE MOTORS IN THE DIFFERENTIAL DRIVELINE VERSUS THE REDUCER GEAR RATIO. ....	292
FIGURE A-13: MAXIMUM REQUIRED POWER FOR THE DRIVE MOTORS IN THE DIFFERENTIAL DRIVELINE VERSUS THE SIMULATED SPEED. ....	293

# List of Tables

---

TABLE 2-1: MAIN CHARACTERISTICS OF THE CHENGDU RIG [18].....	9
TABLE 2-2: MAIN CHARACTERISTICS OF THE NAPLES RIG.....	10
TABLE 2-3: THE MAIN CHARACTERISTICS OF THE TOKYO RIG [18].....	11
TABLE 2-4: LIST OF THE ROLLER RIGS THAT HAVE BEEN USED FOR STUDYING ADHESION BEHAVIOR AND THEIR MAIN CHARACTERISTICS. DOFS COLUMN PRESENTS THE NUMBER RELATIVE DISPLACEMENTS THAT THE RIG ALLOWS BETWEEN THE CONTACTING BODIES AT THE INTERFACE, AND CREEPAGE CONTROL COLUMN INDICATES THE METHOD BY WHICH CREEPAGE IS PROVIDED AT THE INTERFACE; CONTROLLING THE ROTATIONAL SPEED OF THE CONTACTING BODIES INDEPENDENTLY OR USING A DIFFERENTIAL GEARBOX.....	42
TABLE 3-1: THE SCALING FACTORS FOR THE PHYSICAL QUANTITIES OF THE RIG.....	59
TABLE 4-1: COMPARISON TABLE FOR FEM RESULTS OF THE LOAD FRAME.....	76
TABLE 4-2: MAXIMUM ESTIMATED CREEP FORCES AT THE CONTACT PATCH.....	80
TABLE 4-3: REQUIRED SPECIFICATIONS FOR THE AoA POSITIONING SYSTEM.....	82
TABLE 5-1: MAIN SPECIFICATIONS FOR AKM84T (480 V) AC SERVOMOTOR [82].....	105
TABLE 5-2: MAIN CHARACTERISTICS OF THE BDB330 PRECISION GEARBOX MANUFACTURED BY MIJNO ...	108
TABLE 5-3: MAIN SPECIFICATIONS OF THE UT018-005 TRUE PLANETARY GEARHEAD OFFERED BY MICRON [85].....	109
TABLE 5-4: REQUIRED SPECIFICATIONS FOR THE BEARINGS.....	111
TABLE 5-5: DESIGN CALCULATION OF LOAD AND LIFE IN HOURS FOR DRIVELINE BEARINGS.....	111
TABLE 5-6: INERTIA AND MASS SPECIFICATIONS OF THE DRIVELINES.....	114
TABLE 5-7: SYSTEM SPECIFICATIONS FOR KOLLMORGEN EC4 ELECTRIC CYLINDER.....	118
TABLE 5-8: SELECTED EC4 ELECTRIC CYLINDERS FOR DIFFERENT POSITIONING SYSTEMS.....	119
TABLE 6-1: MAXIMUM MOMENTS REACTED AT THE F/T SENSOR (FORCE PLATE).....	123
TABLE 6-2: TECHNICAL SPECIFICATION OF FORCE MEASURING ELEMENTS (TYPE 9027C AND 9028C) [101] .....	127
TABLE 6-3: TECHNICAL SPECIFICATION OF KiTORQ TORQUE MEASURING SYSTEM (INCLUDING A ROTOR TYPE 4550A AND A STATOR TYPE 4540A) [102].....	131
TABLE 6-4: TECHNICAL SPECIFICATION OF STEEL TORSION-PROOF MULTI-DISK COUPLING (TYPE 2305A) [103].....	132
TABLE 6-5: FEM RESULTS FOR THE WHEEL FORCE DYNAMOMETER'S TOP/COVER PLATE.....	134
TABLE 6-6: FEM RESULTS FOR THE MOTOR FORCE DYNAMOMETER'S TOP/COVER PLATE.....	134
TABLE 7-1: COEFFICIENTS M, AND N FOR DIFFERENT VALUES OF $\theta$ [121].....	164
TABLE 7-2: KALKER'S COEFFICIENTS FOR VARIOUS POISSON RATIOS AND VARIOUS CONTACT ELLIPSE ASPECT RATIO (IN THIS TABLE $\Sigma$ REPRESENTS POISSON RATIO) [120].....	178

---

TABLE 7-3: COMPARISON TABLE OF PROPOSED MODELS FOR ESTIMATING $c_{11}$ KALKER COEFFICIENT.....	179
TABLE 7-4: COMPARISON TABLE OF PROPOSED MODELS FOR ESTIMATING $c_{11}$ KALKER COEFFICIENT.....	180
TABLE 7-5: THE VALUES OF $\Phi$ , AND $\Psi$ AS FUNCTIONS OF POISSON RATIO AND CONTACT ELLIPSE ASPECT RATIO ( $\Sigma$ IN THIS TABLE REPRESENTS POISSON RATIO) [148] .....	185
TABLE 7-6: TYPICAL MODEL PARAMETERS FOR DIFFERENT SURFACE CONDITIONS OF WHEEL-RAIL CONTACT, ADAPTED FROM [197] .....	202
TABLE 7-7: WHEEL-RAIL CONTACT PARAMETERS USED IN SIMULATIONS .....	209
TABLE 8-1: SIMPACK BUILT-IN CONTACT THEORIES .....	215
TABLE 8-2: LIST OF BODIES AND JOINTS IMPLEMENTED IN THE ROLLER RIG'S SIMPACK MODEL .....	218
TABLE 8-3: LIST OF FORCE ELEMENTS IMPLEMENTED IN THE ROLLER RIG'S SIMPACK MODEL .....	219
TABLE 8-4: WHEEL-RAIL/ROLLER CONTACT PARAMETERS.....	220
TABLE 8-5: SPECIFICATIONS OF FORCE ELEMENTS IMPLEMENTED IN THE RIG'S MULTIBODY DYNAMIC MODEL .....	221
TABLE 8-6: PREDICTED MAXIMUM CONTACT LOADINGS AT THE WHEEL-RAIL INTERFACE .....	221
TABLE 8-7: RESULTS OF THE EIGENVALUES ANALYSIS OF THE ROLLER RIG'S SIMPACK MODEL .....	226
TABLE 8-8: WHEEL-RAIL CONTACT MATERIAL PROPERTIES AND GEOMETRY PARAMETERS USED IN SIMULATIONS.....	237
TABLE A-1: SPECIFICATIONS FOR THE PLANETARY DIFFERENTIAL GEARBOX.....	291
TABLE A-2: DESIRED SPECIFICATIONS FOR THE CASE-STUDY EXPERIMENTAL RIG .....	291

# 1 Introduction

## 1.1 Motivation

The wheel-rail contact mechanics and dynamics is one of the most complex aspects of railroading. Contact mechanics plays a crucial role in the behavior of railcars. Accurate determination of contact points and contact forces between wheel and rail play an important role in the dynamic study of rail vehicles. Full understanding of the physics behind the contact phenomenon provides a fundamental foundation for the vehicle performance study, both in terms of modeling the train dynamics and in terms of reducing operational costs in the long-term. While many researches have been conducted to deepen the understanding of the contact mechanics at the interface of wheel and rail, further studies are still highly desirable to shed more light on the understanding of the physics behind the contact phenomenon. Although there is a broad, high-level understanding of what happens at the wheel-rail interface, much of the science behind why it happens is lacking.

In contrast to field-testing, indoor-based simulation tools such as roller rigs offer a controlled laboratory environment that can provide a successful path for obtaining data on the mechanics and dynamics of railway systems for a variety of operating conditions. Roller rigs have proved to be useful for the study of various aspects of railway vehicle systems. While vast improvements in roller rigs have significantly increased their ability to replicate and study wheel-rail dynamics, further improvements are still highly desirable. The idea to develop a laboratory test rig started from the observation that there is a need for better developed testing fixtures capable of accurately explaining the unknown physics behind wheel-rail contact as well as designing faster, safer, and more efficient railway systems. In addition, a review of current roller rigs indicated that many desired functional requirements for studying contact mechanics were not available. For these reasons, the Virginia Tech Railway Technologies Laboratory (RTL) has set out to develop a state-of-the-art testing facility that will allow experimental testing for contact mechanics in a dynamic, controlled, and consistent manner. The specific functional requirements that are elected to include in the design are:

- Relatively high bandwidth data measurements (~1000 Hz)
- Real-time high precision control of creepage (slip) at the contact (~0.01 % creepage)

- Real-time high precision measurement of contact forces ( $\sim 2\%$  FSO)
- Allow for real time adjustment of all the boundary conditions: cant angle, angle of attack, lateral displacement, and normal loading
- Allow for contact geometry measurements
- Allow for hardware in the loop studies

## 1.2 Objectives

The primary objectives of this study are summarized as:

- Provide the means for more accurate measurement of the wheel-rail contact mechanics and dynamics
- Enable access to more accurate test data, often needed for rail vehicle dynamic studies
- Design and build a state of the art roller rig test facility that can achieve the need for accurate measurements of the wheel-rail contact under controlled laboratory conditions
- Incorporate measurement methods congruent with the with the design for effective, precise, and seamless measurements

## 1.3 Approach

The following approach is taken to fulfill the objectives of this study:

- Investigate the possibility of developing a roller rig to contribute to the current knowledge of contact mechanics
- Design the layout and configuration of the rig for primarily studying the contact mechanics
- Survey the contact mechanics literature for potential open research areas
- Design and develop the experimental rig from a paper concept to a finished product
- Provisional design of the rig for conducting Hardware-in-the-Loop simulations
- Characterize the roller rig through modeling and simulation

## 1.4 Contributions

The potential contributions of the current study are summarized as:

- Designing of an exceedingly complex test rig with limited resources
- Establishing a railroad test facility with the following unique features:

- High level of precision for controlling the speed and measuring the forces
- Capable of controlling all the 4 DoFs between wheel and rail with high level of precision
- Capable of performing Hardware-in-the-Loop (HiL) simulations due to its unified communication protocol between actuators, drives, and data acquisition
- Providing a comprehensive survey on the contact mechanics models
- Development of a comprehensive multi-body dynamics model of the rig for vibration analysis
- Advancing the state of the art for studying the contact mechanics and science of railroad wheels and rails

## 1.5 Outline

Chapter 1 provides the introduction and an overview of the objectives and approach for the current study.

Chapter 2 provides the background and literature review for the study. A comprehensive study of the past and existing roller rig is presented. The overall design layout and functionality for each roller rig is discussed.

Chapter 3 investigates the layout and configuration of the roller rig. Different design concepts are presented and compared.

Chapter 4 details the development of hardware and structure of the rig. Chapter 5 discusses the electromechanical design of the roller rig. The component selection and functionality of the parts are discussed. Chapter 6 continues to present the details on the design of the instrumentation and control architecture of the rig.

In chapter 7, a comprehensive survey of all the railway contact models is presented. The simplifying assumptions for each model are discussed. In order to compare the performance and functionality of the models, the models are implemented in MATLAB. Open areas in contact mechanics that require further research for developing better models to represent the wheel-rail interaction are discussed.

Chapter 8 details the multibody dynamic model of the rig using software package SIMPACK. It also includes the computer program for developing creep curves from experimental results of the rig.

The work performed in this research project is summarized and concluded in chapter 9.

## 2 Literature Review

The following chapter provides a literature survey of commonly well-known roller rigs. Technical background and history of each roller rig along with a review of their design and functionality are presented. An overview of the studies conducted using roller rigs is also presented. After a review of the roller rigs, the scaling strategies for scaling down a full rail car to a laboratory rig are reviewed. Technical background necessary for understanding the differences between behavior of a railcar wheel on a roller and a tangent track are presented. The chapter is concluded with a discussion on the evolution of the contact models and theories.

### 2.1 Introduction and Background

Roller rigs have proved to be useful for the study of various aspects of railway vehicle systems [1] [2]. They have been used to validate the existing theories regarding railway vehicle dynamics or to examine new designs of railway vehicles [1] [2] [3] [4]. The purpose of roller test rigs has consistently been to improve rail vehicle performance, yet the specific focus of individual rigs has varied widely. Some rigs are designed to test brake and propulsion systems while others are designed to refine and improve dynamic models of wheel-rail interactions on the wheelset, truck, and car body systems [5] [6]. While vast improvements in roller rigs have significantly increased their ability to replicate and study wheel-rail dynamics, further improvements are still highly desirable.

The prevalent use of roller rigs began from the desire to test locomotive systems in a laboratory environment at the Great Western Railway in 1904 [7]. Since then, railway roller test rigs have been in service throughout the world in both full-scale [8] [9] [10] and scaled versions [5] [11] [12]. Rigs have been used for a variety of purposes, including but not limited to: the study of high-speed track conditions, braking, turning, wheel and rail geometry, derailling, etc. [5] [13] [14]. One of the important advantages of roller rig systems is that they offer a repeatable environment for the study of wheel-rail dynamics and allow for the use of multiple sensors and data acquisition equipment either difficult or impossible to use in the field on a train or with a conventional track.

The use of laboratory test rigs for automotive applications has similarly been developed over the course of decades, yet these testing systems are at much greater maturity than railroad testing systems [15] [16]. Manufacturers of these systems have gone to great lengths to closely approximate the dynamics of the ground vehicle or system components in a real world environment. While some differences from the real world are always inherent, a well-designed rig would allow that most of these differences negligible. For instance, automotive roller designs are specifically manufactured to replicate the road surface for the study of noise, vibration, and harshness (NVH), yet these rigs are typically not satisfactory for precise tuning of suspensions or tires [17].

In a similar manner, a railroad wheel-rail interface test rig must adequately simulate the real world environment in which it serves to study. It needs to maximize the benefit of the experimental studies when applying them to the understanding of vehicle dynamics in the field. For this reason, a considerable amount of effort should always be spent on the development of the test rig design and the constraint system of the trucks, wheelsets or wheels, with respect to the moving track or roller.

## 2.2 Review of Design and Functionality of Roller Rigs

In this section, a comprehensive review of the past and current roller rigs is presented. Worldwide well-known roller rigs that are reviewed in great detail by Zhang et al [18], as well as Jaschinski et al [19] are briefly presented. In addition, other roller rigs around the world that have been used for studying the railway vehicle behavior are reviewed. A brief description of each roller rig and their key design elements are reviewed. The functionality of the roller rig and the studies conducted using the rig are also presented.

### 2.2.1 History

One of the earliest roller rigs was built at the Swindon Works of the Great Western Railway in Britain in 1904. It was used for the investigation of the performance of steam locomotives, specifically, their pulling power at different speeds [7].

Carter [19] used model tests on a scaled tangent track rig to conduct experiments in rail vehicle dynamics in 1920. The Railway Technical Research Institute in Japan during 1950's developed two 1/10<sup>th</sup> and 1/5<sup>th</sup> scaled roller rigs to support design efforts for rail vehicle's suspension [4].

In the early 1950's, the C&O – B&O railroad in the United States developed a 1/10<sup>th</sup> scaled roller rig to study lightweight passenger trains and freight cars [19].

A 1/5<sup>th</sup> scaled roller rig was built at Princeton University for experimenting the mechanics of derailment for typical three-piece trucks in 1970's. Forces in the model were carefully scaled according to similarity laws [20] [14].

During two decades of 1960's and 1970's, multiple roller rigs were developed in Europe. In 1960's, British Railways have constructed a number of roller rigs, both scaled and full-size, to conduct multiple studies of vehicle dynamics. A 1/5<sup>th</sup> scaled roller rig and a full-scale two-axle rig were built to demonstrate the instabilities experienced by rolling stock. Another 4-axle roller rig was built in 1969. It, however, was not used, because of availability of a more advanced test track [21]. In 1964, CAFL Company in France built a roller rig for studying the vertical, lateral, and yaw vibration frequencies and amplitudes. It was equipped with hydraulic actuators to control the lateral and vertical motions [18]. In 1967, a roller rig that was mainly intended for studying traction and braking equipment was developed in Germany. In 1970's, the RWTH in Aachen, Germany developed a scaled roller rig [22].

The application of roller rigs for studying rail vehicle dynamics and development of high-speed trains has become more widespread in recent decades. Many full-scale and scaled roller rigs have been constructed during the past few decades. Some of the most recent or most influential rigs are discussed here:

#### **2.2.1.1 The Chengdu Roller Rig, China, 1995**

In 1995, the State Key Laboratory of Traction Power in Southwest Jiantong University at Chengdu, china developed a four-axle roller rig for studying the optimum design of rail vehicles [18]. The rig was upgraded with two additional axles for studying locomotives in 2002. Figure 2-1 shows the test facility at Chengdu. The new modified rig is capable of running two rollers of each roller set at different speeds.

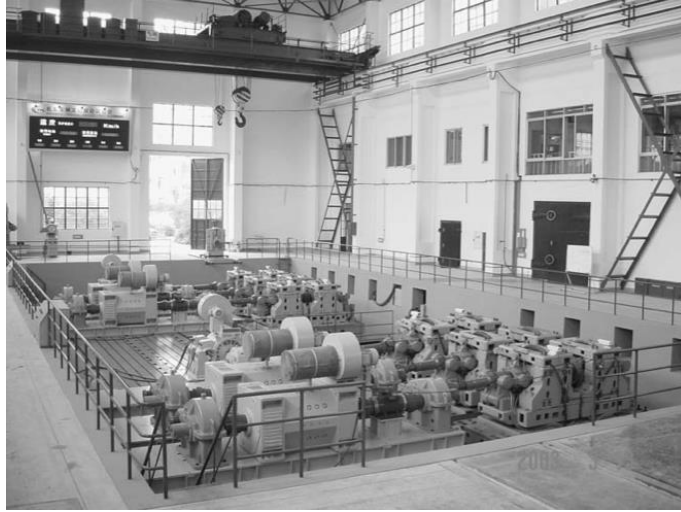


Figure 2-1: Full-scale test facility at Chengdu, China [18]

Hydraulic actuators provide the movements of the two rollers in vertical and lateral directions, independently. The rig is also capable of controlling yaw angle of each rollers as well as cant angle of each roller set. So, the rig is capable of simulating straight track and circular track with track irregularities. A differential gearbox is employed to simulate the speed differential between left and right rollers during curving. A flywheel is used to maintain the running stability of the rollers and to simulate the inertia of the vehicle. 6 DC motors are used to drive the roller sets via double-articulated universal joints. A schematic drawing of the driveline is depicted in Figure 2-2.

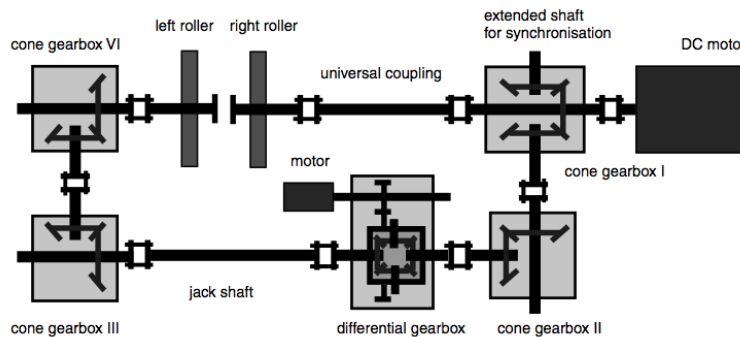


Figure 2-2: Schematic drawing of the driveline of the Chengdu rig [18]

The rig's data acquisition and monitoring system can measure and monitor various variables such as signals of displacement, velocity, acceleration, strain, pressure, temperature, voltage, current,

etc. The accuracy of speed control for rotating rollers is 0.5%. The main characteristics of the rig are listed in Table 2-1. The rig has been used to conduct basic research on wheel-rail creep theory, derailment mechanism, hunting stability, braking and traction effort, wheel-rail wear, vibration analysis, and among others. Creep curves were studied for different longitudinal velocities, different axle loads, and different contact surface conditions, as well as for different surface condition at the contact [9] [23].

**Table 2-1: Main characteristics of the Chengdu rig [18]**

Exciting in Vertical		Exciting in Lateral	
Maximum Frequency $f_{vmax}$	30 Hz	Maximum Frequency $f_{vmax}$	30 Hz
Maximum Amplitude $A_{vmax}$	$\pm 10$ mm	Maximum Amplitude $A_{hmax}$	$\pm 10$ mm
Maximum Acceleration $a_{vmax}$	$\pm 4$ g	Maximum Acceleration $a_{hmax}$	$\pm 5$ g
Maximum traction force per axle $F_e$	10 T	Maximum axle load $M_w$	25 T
Maximum motor power/brake $W$	1200/1500 kW	Maximum speed $V$	450 km/h
Maximum cant angle $\phi_{max}$	$7^\circ$	Distance between bogies $L$	4 ~ 22 m
Bogie wheelbase $l$	1600 ~ 3500 mm	Range of gauge $A_0$	1000 ~ 1676 mm
Minimum curve radius $R$	200 m	Maximum wheelset numbers $N_z$	6

### 2.2.1.2 The Naples Roller Rig, Italy, 1992

The Ansaldo Transport Research Center in Naples, Italy developed a full-scale four-axle roller rig [18]. The rig was later upgraded to accommodate six axles. Figure 2-3 shows the test facility at Naples. The rig does not allow for speed differential between two rollers in a roller set. It is designed to simulate running in a straight track. The drive motor is connected to the roller directly without a gearbox or braking system. The accuracy of speed control for rotating rollers is 0.1%.



**Figure 2-3: Test facility at Naples, Italy [18]**

The characteristics of the rig are summarized in Table 2-2. A sophisticated data acquisition system that can receive up to 400 signals is designed to monitor and process the system. The rig is mainly intended for traction simulation of locomotives. It also used to study traction effort during transients, start up tests, braking tests, etc.

**Table 2-2: Main characteristics of the Naples rig**

Wheel diameter	500-1400 mm
Maximum traction effort per axle	100 kN
Maximum speed	300 km/h
Range of gauges	600-1700 mm
Bogie wheelbase	1400-3500 mm
Distance between bogies	5200-22000 mm
Maximum continuous power at the axle	1500 kW
Total weight	100,00 kg

### 2.2.1.3 The Tokyo Roller Rig, Japan, 1957

The Railway Technical Research Institute in Japan developed a full-scale, two-axle roller rig that contributed greatly to the railroad industry for more than 30 years [18] [24]. The rig used an eccentric roller to create sinusoidal excitation for simulating track irregularities, and made a great contribution in studies related to hunting, derailment, regenerative braking and the development of Shinkansen bolsterless high-speed bogies [5]. In 1989, the rig was renewed for inducing vibrations using hydraulic actuators. Figure 2-4 shows the test facility at Tokyo.

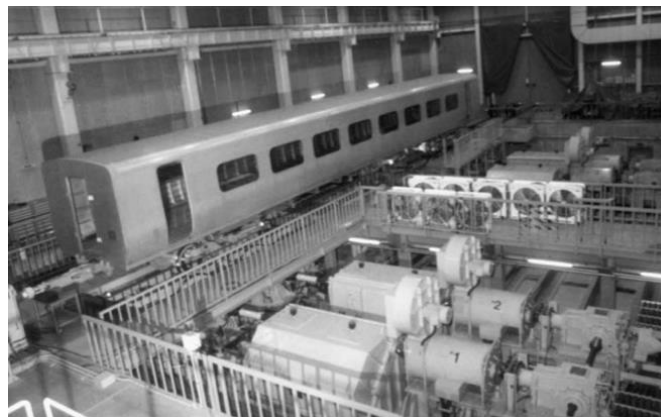


**Figure 2-4: The full-scale test facility in Tokyo, Japan [18]**

The rig is equipped with hydrostatic bearings, hydrostatic couplings, and actuators for lateral vibrations. A DC motor of 500 kW drives each roller set. Table 2-3 summarizes the main characteristics of the Tokyo roller rig.

**Table 2-3: The main characteristics of the Tokyo rig [18]**

Gauge	1,000 ~ 1676 mm(variable)
Minimum wheelbase	1600 mm
Maximum test speed	500 km/h
Maximum axle load	200 kN
Diameter of roller	1500 mm
Lateral displacement	0 ~ 1 Hz Max. $\pm 30$ mm 3 Hz Max. $\pm 10$ mm 10 Hz Max. $\pm 2$ mm Maximum acceleration 10 m/sec <sup>2</sup>
Vertical displacement	0 ~ 1.8 Hz Max. $\pm 12$ mm 25 Hz Max. $\pm 0.4$ mm Maximum acceleration 10 m/sec <sup>2</sup>
Rolling displacement	0 ~ 2 Hz Max. $\pm 0.011$ rad 15 Hz Max. $\pm 0.0006$ rad Maximum acceleration 5 rad/sec <sup>2</sup>

#### 2.2.1.4 The Pueblo Roller Rig, USA, 1978

A full-size, four-axle roller rig, called the Roll Dynamics Unit (RDU), was developed in Pueblo, Colorado, USA [25] [25] [26]. Auxiliary support stands are used to accommodate six or eight-axle locomotives for testing on the roller rig. Figure 2-5 shows the facility at TTCi, in Pueblo. The unit was used to test different railcars such as non-powered vehicles, passenger cars, and locomotives [18]. The rig was used for simulating vehicles on tangent track with no lateral or vertical irregularities or simulation of flat curve geometry.

The rig was equipped with four 600-hp drivetrains. The maximum simulated vehicle speed of 60-inch rollers was 230 km/h. The rig was equipped with two actuators to apply lateral forces to the side frame of the tested bogie, and flywheels to simulate inertia associated with the vehicle during braking or acceleration. RDU, which is decommissioned now, was used to test locomotive's traction motors, as well as to study general vehicle-track dynamics [27].



Figure 2-5: The Roll Dynamic Unit (RDU) in Pueblo, USA [18]

#### 2.2.1.5 The DB AG Roller Rig, Munich, Germany, 1977

In 1970's, German Federal Minister of Research and Technology constructed the Deutsche Bahn AG roller rig in Munich [28] [29]. The test bench is a full-size, four-axle roller rig capable of achieving speeds of up to 500 km/h and allowing the simulation of various track irregularities using hydraulic actuators. Figure 2-6 shows the test facility at Munich.

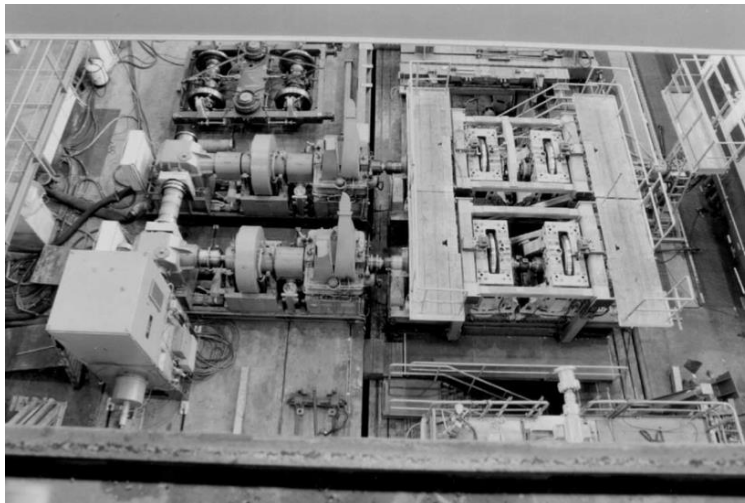


Figure 2-6: The DB AG test facility at Munich, Germany [19]

Two DC shunt motors drive the four roller sets. Each driveline comprises a disk brake, an eddy-current brake, a bevel gearbox, and a Cardan shaft. Two rollers rotate at the same speed. A data acquisition system capable of receiving up to 120 signals is configured to measure and monitor multiple variables of both the roller rig and test object. Some of the main characteristics of the rig are:

- Steel rollers of 1400 mm diameter profiled according to UIC 60 rail profile
- Separately moved in the lateral and normal directions within  $\pm 10$  mm and turned about the longitudinal and normal axis within  $\pm 1$  degree by hydraulic actuators
- The rollers can be tilted up to  $7^\circ$  about a common longitudinal axis for simulating cant deficiency
- Wheelsets with gauges of 1435 to 1676 mm
- Wheel loads of 125 kN for a roller with a speed of up to 400 km/h and 100 kN up to the maximum roller speed of 500 km/h

The commercial rig has been used for conducting multiple tests including investigation into the relation between force and slip, vibration, ride comfort and stability, failure tests, testing of actively controlled bogie, etc. [28] [29] [30] [13].

#### 2.2.1.6 NRC Rigs, Canada

The National Research Council in Canada has developed several rigs throughout the years. In Ottawa, a full-scale roller rig called the Curved Track Simulator was developed in 1980's [2] [31]. It was a two-axle roller rig allowing for yaw angle. Hydrostatic bearings were used for floating the frame (Figure 2-7). The rig was used for studying bogie designs, wear tests, and has been dismantled since [32] [33].

In addition, NRC has developed a very small twin disk rig called Amsler twin disk for studying rolling contact fatigue. This machine has been used for study of tribological properties of friction modifiers at the wheel-rail interface [34,35].

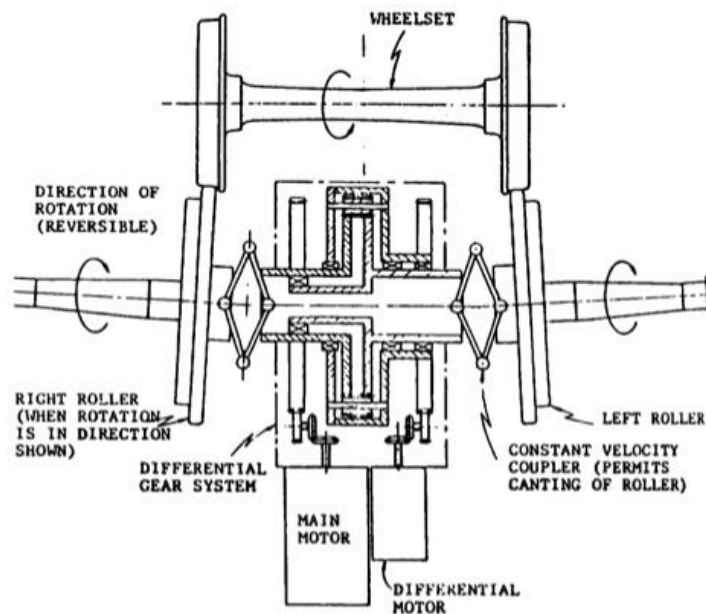


Figure 2-7: Traverse section of one axle for the curved track simulator support stand [31]

A Wheel, Bearing, and Brake facility was also developed by NRC. The full-scale single wheelset rig consists of a pair of large rollers, which simulate rails, on a driveline that is fixed in a loading frame. Full-size railway wheelsets are mounted atop the rollers. The rig's features are listed below:

- Equivalent longitudinal speed: 80 mph (135 km/h)
- Equivalent vertical wheel load: 350 kN which is twice that of a loaded 125-ton car
- Maximum wheelset yaw angle: approximately  $2^\circ$
- Contamination effects: water, grease, oil, etc.
- Partial, normal or emergency braking

The rig has been used for studying wheel-rail wear, performance tests of brakes and bearings, and rail-wheel contact patch.



Figure 2-8: The NRC wheel, bearing, and braking test facility in Canada [36]

NRC has also developed a dual disc on disc testing facility. It is a one-axle 1/8<sup>th</sup> scaled rig with following features [37] [38]:

- The bottom disc representing the roller set is driven by a 20 H P variable speed.
- The rig is equipped with a yaw angle adjustment mechanism
- Two bi-axial load cells are employed for measuring vertical and lateral contact load components
- The longitudinal components of tread forces are measured by two load cells placed in the flexure arms
- The rig is equipped with an instrument capable of tracing the worn rail and wheel profiles with an accuracy of  $\pm 2$  micrometer.

The rig has been mostly used for wheel-rail wear studies.

#### 2.2.1.7 The DLR Rig, Germany, 1984

In 1980's, a 1/5<sup>th</sup> scaled, two-axle roller rig was developed at DLR in Oberpfaffenhofen [39] [40] [2]. A DC motor was used to drive the roller sets via a toothed belt. The maximum speed of the rollers was between 900 to 1100 RPM. Rollers with diameter of 360mm were rigidly connected together using a thick tube (Figure 2-9). The two-axle test bench was used for developing simulation software of railway vehicle dynamics; SIMPACK. It was used for conducting research on bogie model and limit cycle behavior, as well as different designs of the bogie and independent wheels. The scaling strategy used for DLR rig is discussed in great detail in scaling section.



**Figure 2-9: The 1/5 scale DLR roller rig in Germany [19]**

#### **2.2.1.8 The MMU Rig, England, 1992**

In 1992, the Rail Technology Unit of the Manchester Metropolitan University developed a 1/5 scale, two-axle roller rig [2] [41] [42]. The rig is capable of driving the rollers at a scale speed of up to 250 mph. An electric motor is used to drive the roller via belt and pulleys. Two roller of each roller set are connected using splined and hooked joint shaft. The rig is equipped with hydraulic actuators for controlling the linear motion of the rollers laterally and their rotation around vertical axis. The rig has been used for studying suspension designs, wheel-rail wear, and independent wheels design. The scaling strategy used for MMU rig is discussed in great detail in scaling section [42].

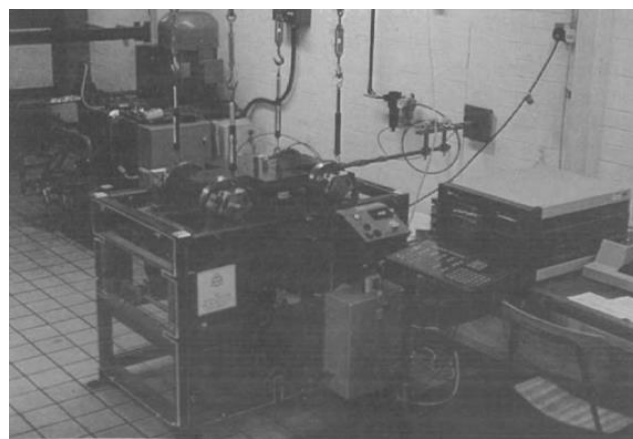


**Figure 2-10: The test facility at Manchester Metropolitan University [42]**

### 2.2.1.9 The INRET Rig, France, 1984

In 1980's, the "Institut National de Recherche sur les Transports et leur Securite" (INRETS) turned a big flywheel test facility for linear motors to a roller rig in Grenoble, France (Figure 2-11). The unique feature of the rig was the large diameter rollers (13 m), which could be driven at speeds up to 250 km/h (Figure 2-11-right). The track on the roller was composed of UIC60 rails. Pneumatic jack was used for applying the vertical load. A test bogie of 1/4<sup>th</sup> scaled was used for testing. The wheel-roller condition was very similar to those on tangent track, because of the large diameter of the rollers [43]. From 1984 to 1992, the test unit was used for conducting numerous experiments such as hunting stability and measuring Kalker's coefficients [3]. The results of the rig supported development of the simulation software VOCO. The scaling strategy used for INRET rig is discussed in great detail in scaling section.

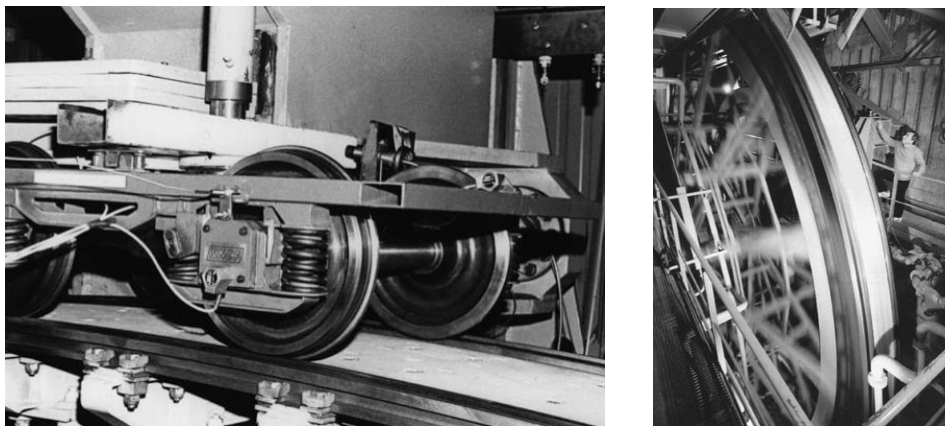


Figure 2-11: The INRET test facility at Grenoble (left) [19], and its large flywheel (right) [44]

### 2.2.1.10 Full-Car Roller Rig, Czech, 1990's

The roller rig at Czech Technical University (CTU) was initially built in the years 1988-9 [45]. It was originally a single wheelset rig, but the rig has been improved many times throughout years. The current state of the rig is a 1/3.5 scaled two-axle roller rig. The rollers have a diameter of 0.5 m and a railhead profile of R65. A 5.5 kW asynchronous motor drives the rollers and a planetary differential gearbox located in between two rollers of a roller set actively control the differential speed between two rollers for curve simulations. The maximum speed of rollers is 700 RPM. The rig is equipped with a servo drive system for actively control the yaw angle of a wheel set. 16

strain gauges installed radially on the roller are used for measuring the contact forces. The rig has been used for studying new design of actuated steering mechanism for wheelsets.

#### *2.2.1.11 MDM Test Rig, Italy, 2003's*

In 2010's, the Research Centre of Firenze Osmannoro, Italy developed two roller rigs; a full-scale two-axle rig and its scaled version [46] [47]. The rigs simulate degraded adhesion conditions to test rail vehicles' response; rather than physically introducing a contaminant at the interface, its presence is being simulated by controlling angular speeds of the rollers. In the scaled version, two electric motors drive the two roller sets, and two additional motors are designed for testing of bogies with independent wheels (Figure 2-12). The roller diameter is 0.5 m. The rig has been used for conducting Hardware in the Loop testing of various safety relevant on-board subsystems like wheel slide protection systems, traction and stability controls, odometry and automatic train protection and control [47] [46].

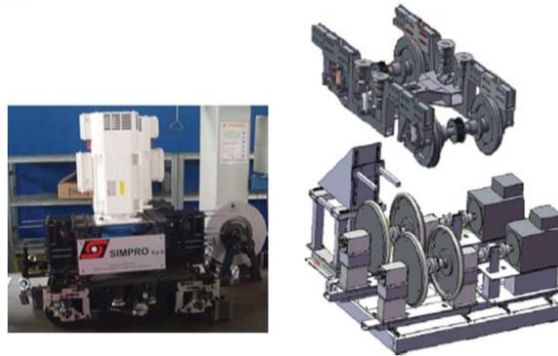


**Figure 2-12: The MDM test facility at Florence, Italy [46]**

#### *2.2.1.12 Full-Car Roller Rig, Korea, 2011*

The Railway Safety Research Center in Seoul National University of Science & Technology, Korea developed a small-scaled roller rig called derailment simulator in 2010's [48] [49]. A 1/5<sup>th</sup> scaled bogie is designed for testing on the two axle derailment simulator. A 3.7 kW AC motor is used for driving the rollers via belt pulley mechanism. The rig is equipped with cant angle, angle of attack and wheel base adjustment mechanisms. The maximum velocity of the motor is 1150 RPM. The roller diameter is 0.45 m and wheel diameter is 0.18 m. The derailment simulator has been used to investigate the dynamic stability of railway vehicles.

### 2.2.1.13 Full-Scale Test Rig, Austria, 2000's

The Voestalpine Schienen GmbH in Linz, Austria developed a full-scale single wheel roller rig [8]. This rig utilizes a short (1.5-m) piece of rail, rather than a roller, for simulating the track (Figure 2-13). The rig is equipped with hydraulic cylinders for moving the carriage, which is attached to the short rail, back and forth up to a maximum speed of 0.5 m/s. Vertical loads up to 100 tons and lateral loads up to 10 tons can be applied to the rail wheel contact. The cant angle and angle of attack can be adjusted for simulating the curve. Forces are calculated from measured pressures within the hydraulic cylinders. The rig has a nozzle for spraying water or friction modifier at the contact. The rig is mainly used to investigate rail wear and rolling contact fatigue.

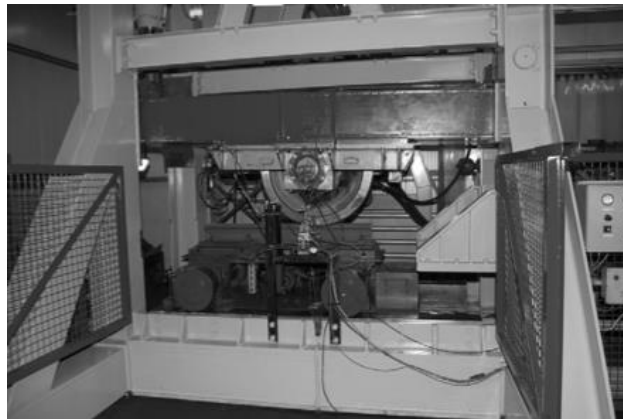


Figure 2-13: The full-scale test facility at voestalpine Schienen GmbH [8]

### 2.2.1.14 Single Wheelset Scaled Roller Test Stand, Japan, 2000's

Matsumoto et al. developed a 1/5th scaled single wheelset test setup in Japan [11]. Vector-controlled AC induction motors are used to drive the rollers and the wheels independently. The maximum roller speed is 312.5 RPM with a minimum resolution precision of 0.03125rpm. The driving torque at each roller (diameter of 860mm) is 700 Nm. The rig is equipped with cant angle and angle of attack adjustment mechanisms (Figure 2-14). Rollers comprise a spoke-rim design and are gauged to measure the lateral and vertical forces. The rig has been used to investigate the creep force characteristics between roller and wheel at varied contact conditions [11].

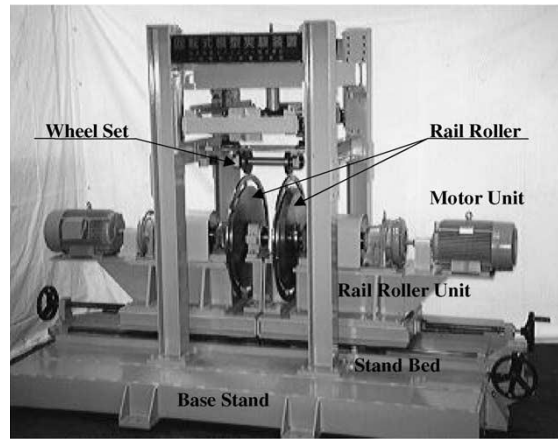


Figure 2-14: The scaled test facility in Japan [11]

**2.2.1.15 SUROS Twin Disk, Sheffield, UK, 1995**

The Sheffield University Rolling Sliding (SUROS) twin disc experimental device became operational in 1995 [50] [51]. It is basically two disks rotating on each other and being driven independently (7.5 kW AC induction motor). Discs were cut from railroad rail and wheel with a diameter 47.0 mm and a width of 10 mm. The maximum speed of the disk is 1600RPM. The discs are hydraulically loaded together up to 29 kN [52]. The unit does not allow for any cant or yaw angle adjustment. The setup is equipped with a chute for applying contaminant at the contact (leaves, sand), and with crack detection mechanism by a noncontact eddy current method. The setup has been used for conducting fatigue and wear tests, as well as surface condition (water, oil, etc.) studies. In addition, basic creep analyses were done using this test machine. Test stand is capable of producing just longitudinal creepage.

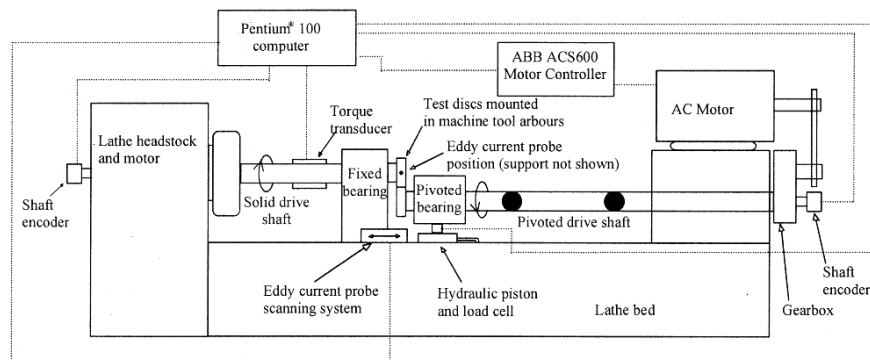


Figure 2-15: The SUROS test facility at the Sheffield University, UK [52]

### 2.2.1.16 The Rolling Contact Testing Machine, Japan, 1984

Ohyama [53] has investigated the adhesion phenomenon using a rolling contact machine. The single wheel test setup has two steel wheels with diameters of 730 and 910 mm. Normal load between the two wheels is applied by a hydraulic actuator controlling desired contact pressure between 588 and 784 MPa. A hydraulic motor was used to drive one disk to a desired rotational speed, then a braking torque was applied for a short time on the driven disk for producing longitudinal creepage. Using this device, the adhesion phenomenon at high speeds was investigated. Water-lubricated condition for the contact patch is also examined.

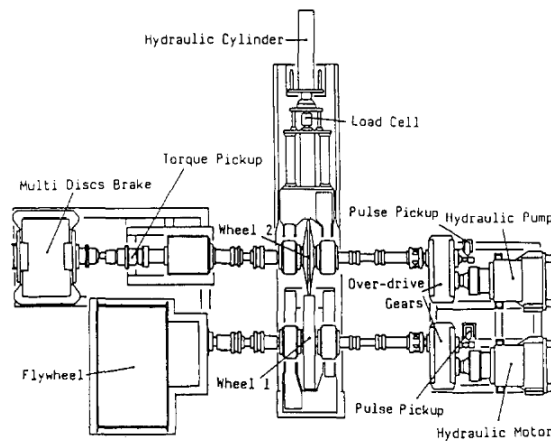


Figure 2-16: The rolling contact testing machine in Japan [53]

### 2.2.1.17 IIT - GMEMD Wheel-Rail Simulation Facility, Chicago, 1990's

In 1990's, a 1/4<sup>th</sup> scaled test facility was used for investigating the effects of axle load, surface condition, angle of attack, and mode of operation (braking and traction) on the contact mechanics [54] [55]. Two 1000 hp and 300 hp DC motors were used for driving the wheel (8 inch diameter) and roller (36 inch diameter), respectively. The setup was equipped with two actuators for controlling the normal load and yaw motion. A three dimensional load cell mounted between the small wheel and the supporting spindle was used for measuring the normal, lateral, and longitudinal contact forces.

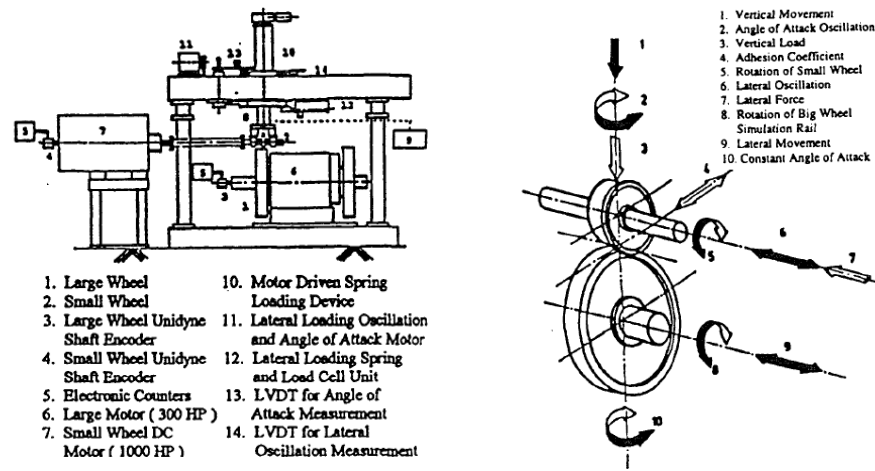


Figure 2-17: The IIT-GMEMD test facility in Chicago, USA [54]

### 2.2.1.18 The Adhesion Test Equipment, Japan, 2000's

The adhesion test equipment, in Japan, has been used for studying adhesion in railway vehicles [56]. It consists of two discs simulating wheel and rail with a scaling factor of 1/8th. Two 7.5 kW electric motors are used for driving both wheel and roller independently. The 1:8 reduction gearbox is installed in the roller driveline. No friction modifier was experimented. Maximum linear speed capability of the device is 40 km/h. The diameter of the wheel and roller are 107.5 and 537.5 mm, respectively. Tractive coefficient for different slip ratio is measured and used to develop anti-slip control algorithms.

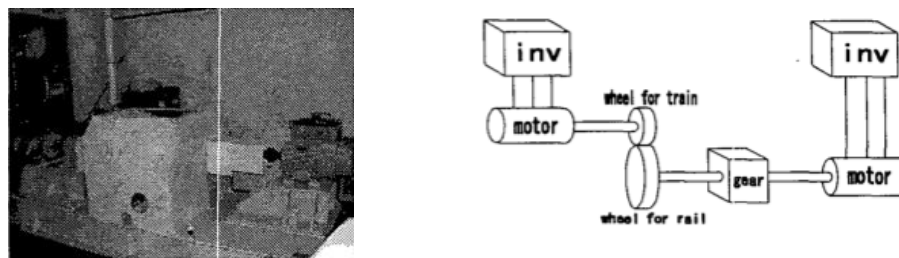
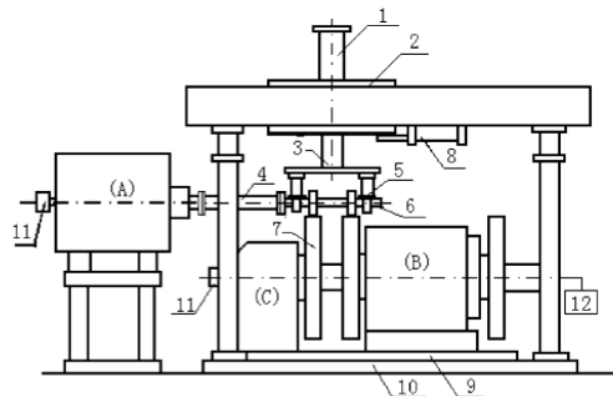


Figure 2-18: The adhesion test equipment in Japan [56]

### 2.2.1.19 Roller Rig Testing Machines, Japan, 2004's

Matsumoto et.al. [57] [58] developed two experimental setups for studying control of friction between rail and wheel using friction modifier. A 1/10<sup>th</sup> scaled full bogie model riding on a 3 m

curved track test equipment is designed and experimented. In addition, a single wheel 1/10<sup>th</sup> scaled roller rig testing machine is designed. The testing machine can produce small slip accurately between two rollers and measure creep forces generated by the slip. The diameters of both the rollers are 172 mm. Profile of the wheel is cylindrical and that of the roller has 100mm convex single arc. These profiles of two rollers are designed considering the contact face ellipse and the contact pressure for simulating actual wheel/rail contact. The setup is equipped with a spraying mechanism for applying friction modifier at the contact. The amount of friction and timing between each spraying of friction modifier and their effect on the contact mechanics has been investigated experimentally [58].



JD-1 wheel/rail tribological simulation apparatus: (1) vertical loading oil cylinder; (2) loading carriage; (3) spindle and yoke; (4) universal shaft; (5) 3D load cell; (6) small wheel; (7) big wheel or rolling rig; (8) lateral loading oil cylinder; (9) turning plate; (10) base plate; (11) optical shaft encoder; and (12) speed measuring.

**Figure 2-19: The single-wheelset test facility in China [59]**

#### 2.2.1.20 JD-1 Wheel/Rail Tribological Simulation Apparatus, China, 2000's

Tribology Research Institute of Southwest Jiaotong University in Chengdu, China developed a single wheelset tribological simulation apparatus [59]. The experimental setup mainly consists of a larger wheelset serving as rail, and a smaller wheelset serving as locomotive or rolling stock wheel. The diameter of the roller is 1070 mm. According to the scale of 1/4<sup>th</sup>, the diameter of the smaller wheel is about 200 mm. The setup is equipped with hydraulic actuators for applying normal load and electric motors for driving the wheel and roller, independently. Rollers and

wheelset were powered by electric motors. The test setup has been used for studying wheel-rail wear and corrugation by optical and scanning electron microscopy.

#### *2.2.1.21 The Twin Disc Rig, UK, 2000's*

The twin disc rig, shown below, was developed in UK for investigating the squeal phenomenon due to unstable friction force [12]. Wheel disc, which is driven by an external motor via pulley and timing belt mechanism, has a diameter of 310 mm. Roller disc, which rotates freely, has a diameter of 290 mm. The rig is equipped with a lever arm for applying the normal force between the discs, and a turntable under the roller for providing the angle of attack between two discs. The rig is instrumented with loadcell and strain gauges for measuring the contact forces.

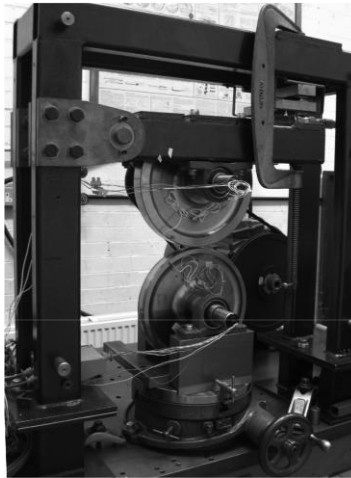


**Figure 2-20: The squeal testing facility in UK [12]**

#### *2.2.1.22 Scaled Roller Rig, Italy, 2000's*

Bosso et.al. developed a 1/5<sup>th</sup> scaled roller rig at Politecnico di Torino in Italy [60] [61]. The two-axle rig is equipped with permanent magnet synchronous motors for driving the rollers, independently. The rig has been modified to a single wheelset roller rig for studying single wheelset behavior. The rig is instrumented with:

- two longitudinal and two lateral laser displacement sensors;
- three encoders to measure the angular velocity (one for the wheelset and one on each roller);

- two torsionmeters;
- six load cells (one for each spring); and
- three accelerometers applied on each axle-box.

The test setup is equipped with a water jet mechanism for spraying water into the interface between the wheelset and rollers. The rig has been used for studying wheel-rail wear and dynamic analysis of rail vehicles.

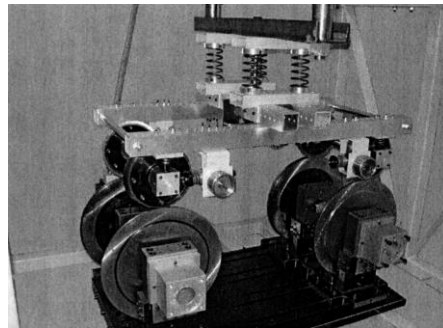


Figure 2-21: Scaled full bogie roller rig in Italy [60]

## 2.3 Review of Studies Conducted by Roller Rigs

Typically, roller rigs are used by researchers and railway organizations around the world to assist in understanding the behavior of railway vehicles and to develop faster, safer, and more efficient railways. The application of roller rigs to study of vehicle system dynamics, development of higher speed trains, the study of power or braking ability, or similar studies has been most common for decades. Roller rigs have contributed to many current railway vehicle designs. Following, a brief review of studies conducted using roller rigs is presented.

### 2.3.1 Wheel-Rail Contact Mechanics

A large number of studies have addressed adhesion characteristics in railway applications [43] [57] [51] [62] [56]. Contact mechanics plays a crucial role in the behavior of railcars. Accurate determination of contact points and contact forces between wheel and rail play an important role in the dynamic study of rail vehicles. Many rigs have been built to deepen the understanding of physics behind the contact mechanics at the interface of wheel and rail [3] [11] [57]. Some have investigated the creep forces trying to validate existing theories [3] [51] or introduce new

characteristics for wheel-rail adhesion [9] [11] [62]. Some experimental research has been conducted on the contact patch regarding the geometry of the contact patch [63] [64]. While vast improvements in roller rigs have significantly increased their ability to replicate and study rolling tock behavior, further improvements especially for studying wheel-rail contact mechanics and dynamics are still highly desirable. For example, there is no known roller rig that is equipped with a contact patch geometry measurement system.

### 2.3.2 Operational Safety

In addition to contact mechanics studies, operational safety of railcars has been the focus of many experimental studies. Experimental rigs are developed to examine the effect of many parameters on dynamic stability of railcars and key dynamic parameters such as derailment coefficient and critical speed [25] [65]. Conditions under which the wheel can climb the rail and derailment may occur have been investigated [7] [8] [9]. The lateral dynamic stability or hunting has been investigated for high speed trains [5]. Moreover, the curving dynamics and performance has been studied [66].

### 2.3.3 Wear and RCF

Rail wear and fracture due to rolling contact fatigue (RCF) has been the subject of many investigations, since surface conditions at the contact greatly affects the ride quality and safety of railcar systems [8]. The effect of various parameters (loading, adhesion coefficient, angle of attack, etc.) on wheel-rail wear is determined for optimizing maintenance strategies and for reducing total life cycle costs [50,54]. Many researchers have studied the mechanisms by which RCF cracks initiate and grow that are strictly related to the wear of railway wheels [10] [50]. Additionally, rail corrugation, wave-like wear on top of rail, is investigated in terms of its formation mechanism and influence of key parameter on its extent [11] [59].

### 2.3.4 Design Improvement

Other studies such as curve squeal [12], characteristics of different third body-layers at the contact (friction modifier, water, leaves, wear debris, etc.) [9] [57] [62], and traction effort [56] have been conducted experimentally. The performance of new designs such as suspension [4],

brake [5], and steering mechanisms [6] have been investigated using proper roller rigs with less effort and cost compared with field tests.

Despite these wide range of studies conducted on railway vehicles using roller rigs and vast improvements in roller rigs' design and functionality, there is still a need for better developed testing fixtures especially capable of accurately explaining the unknown physics behind wheel-rail contact.

## 2.4 Review of Scaling Strategies

Both full scale and scaled test rigs have been used to validate existing theories or to investigate new designs of railway vehicles. While these two systems vary significantly in size and cost, their goals are the same. The use of scaled designs will require much lower investments and simpler logistics than is required for a full-scale test facility, mostly driven by simpler facility requirements, safety systems, load actuators, and constraint systems. The sensors required, however, will be similar—sometimes identical—to those used on a full-scale rig, offering little savings over a full-scale rig testing facility. The major drawback of a scaled system is that it eliminates the ability to directly test fielded and standard components, such as off-the-shelf wheels, wheelsets, and rail segments.

To minimize the effects of scaling down the dimensions, a proper scientific scaling strategy must be adopted according to the purpose of the scaled rig. A similitude relation (scaling factor) for all the desired quantities involved in the physical system needs to be developed between the scaled and full-scale model. Based on laws relating the physical quantities to each other as well as length scaling factor, other scaling factors will be obtained. In general, all the scaling factors might not satisfy all the physical laws, since the laws are not linear [2]. The development of similarity laws dates back to the work of Reynolds [67]. Analogous to Reynolds' approach, similarity laws of scaled roller rigs in regard with their dynamic behavior and elastic deformation have been defined for various testing purposes [1] [2]. Two approaches have been most commonly used for developing scaling strategies: 1- Based on the method of dimensional analysis, several dimensionless parameters and groups are established for deriving scaling factors for various quantities. 2- Based on the equations of motion governing the system, scaling factors are

calculated to maintain the similarity among various terms in the equation. This requires a good understanding of physics of the system.

Material properties and consequently material selection could be the most challenging part of the scaling strategy. As opposed to the most of the quantities involved in the system (e.g. length), there is not a continuous chart of various materials representing scaled material properties. As a result, maintaining the similarity of all the quantities between the scaled and full-scale systems could get challenging, sometimes impossible.

In another words, the similarity rules could lead to scaling (reducing) of some parameters such as the modulus of elasticity for the material and acceleration of gravity. Since these parameters are not scalable, it may get impossible to make perfect similarity between full scale and scaled models.

The starting point for defining dynamic similarity of railway vehicles is the geometric scaling [2], which is defined as ratio of characteristical length of the full scale ( $l_f$ ) to characteristical length of the scaled model ( $l_s$ ):

$$\mathcal{S}_l = \frac{l_f}{l_s} \quad (2-1)$$

Similarly, time scaling factor can be defined as:

$$\mathcal{S}_t = \frac{t_f}{t_s} \quad (2-2)$$

Based on these definitions, scaling factor for other geometry and kinematic quantities are defined:

$$\text{area: } \mathcal{S}_A = \frac{A_f}{A_s} = \mathcal{S}_l^2 \quad (2-3)$$

$$\text{volume: } \mathcal{S}_V = \mathcal{S}_l^3 \quad (2-4)$$

$$\text{velocity: } \mathcal{S}_v = \frac{\mathcal{S}_l}{\mathcal{S}_t} \quad (2-5)$$

$$\text{acceleration: } \mathcal{S}_a = \frac{\mathcal{S}_l}{\mathcal{S}_t^2} \quad (2-6)$$

Based on the definition of density scaling factor as  $\mathcal{S}_\rho = \frac{\rho_f}{\rho_s}$ , scaling factor for inertia quantities are defined:

$$\text{mass: } \mathcal{S}_m = \frac{m_f}{m_s} = \mathcal{S}_\rho \mathcal{S}_l^3 \quad (2-7)$$

$$\text{moment of inertia: } \mathcal{S}_I = \mathcal{S}_m \mathcal{S}_l^2 = \mathcal{S}_\rho \mathcal{S}_l^5 \quad (2-8)$$

$$\text{Force: } \mathcal{S}_F = \frac{F_f}{F_s} = \frac{m_f a_f}{m_s a_s} = \frac{\mathcal{S}_\rho \mathcal{S}_l^4}{\mathcal{S}_t^2} \quad (2-9)$$

For railway vehicles applications, scaling factor of creep forces ( $\mathcal{S}_{F_{creep}}$ ), friction coefficient ( $\mathcal{S}_\mu$ ), and contact patch area ( $\mathcal{S}_{ab}$ ) need to be defined. In addition, material properties scaling factor like Young's modulus ( $\mathcal{S}_E$ ), Poisson's modulus ( $\mathcal{S}_\nu$ ), stiffness ( $\mathcal{S}_c$ ), and damping ( $\mathcal{S}_d$ ) need to be defined.

Jaschinski et al. [2] discussed three most commonly-used similitude approaches, which are discussed here:

#### 2.4.1 MMU's Strategy

The roller rig at Manchester Metropolitan University (MMU) was primarily intended to study rail vehicles' dynamics rather than just creepage forces [18] [41] [42]. Therefore, the strategy used on this rig was based on the similarity of equation of motion [68] [69].

The roller rig has been built 1/5<sup>th</sup> scaled, so the length scaling factor is  $\mathcal{S}_l = 5$ . Since the most common measurements in dynamic studies are conducted in time histories or frequency spectra, the scaling factor of time is considered unity ( $\mathcal{S}_t = 1$ ). Based on the time and displacement scaling factors, scaling factor for frequency, linear velocity, and acceleration are calculated:

$$\text{frequency: } \mathcal{S}_{freq} = \frac{1}{\mathcal{S}_t} = 1 \quad (2-10)$$

$$\text{velocity: } \mathcal{S}_v = 5 \quad (2-11)$$

$$\text{acceleration: } \mathcal{S}_a = 5 \quad (2-12)$$

In order to allow a reasonably practical wear life of the wheels and rollers, the same material (steel), which is normally used in railroad industry, was used for wheels and rollers. This makes the material properties scaling factor unity:

$$\mathcal{S}_E = \mathcal{S}_\rho = \mathcal{S}_\mu = \mathcal{S}_v = 1 \quad (2-13)$$

Scaling factor for mass and mass moment of inertia are:

$$\mathcal{S}_m = 5^3 \quad (2-14)$$

$$\mathcal{S}_I = 5^5 \quad (2-15)$$

Once the general scaling factors are defined, the translational and rotational equations of motion for a dynamic system are considered:

$$m\ddot{x} + d\dot{x} + cx = F \quad (2-16)$$

$$I\ddot{\theta} + d_T\dot{\theta} + c_T\theta = T \quad (2-17)$$

Where  $m$  is the mass,  $I$  is the mass moment of inertia,  $d$  and  $d_T$  are damping coefficients,  $c$  and  $c_T$  are stiffnesses,  $F$  is applied force, and  $T$  is applied torque to the system. Substituting the scaling factors, these equations for the scale model become:

$$m\ddot{x}(\mathcal{S}_m\mathcal{S}_a) + d\dot{x}(\mathcal{S}_d\mathcal{S}_v) + cx(\mathcal{S}_c\mathcal{S}_l) = F(\mathcal{S}_F) \quad (2-18)$$

$$I\ddot{\theta}(\mathcal{S}_I\mathcal{S}_t^{-2}) + d_T\dot{\theta}(\mathcal{S}_d\mathcal{S}_t^{-1}) + c_T\theta(\mathcal{S}_c) = T(\mathcal{S}_T) \quad (2-19)$$

In order to maintain similarity, all the terms in the equations must have the same scaling factor:

$$(\mathcal{S}_m \mathcal{S}_a) = (\mathcal{S}_d \mathcal{S}_v) = (\mathcal{S}_c \mathcal{S}_l) = (\mathcal{S}_F) \quad (2-20)$$

$$(\mathcal{S}_l \mathcal{S}_t^{-2}) = (\mathcal{S}_d \mathcal{S}_t^{-1}) = (\mathcal{S}_c) = (\mathcal{S}_T) \quad (2-21)$$

Therefore, the scaling factor for force and torque are:

$$\mathcal{S}_F = \mathcal{S}_l^4 = 5^4 \quad (2-22)$$

$$\mathcal{S}_T = \mathcal{S}_l^5 = 5^5 \quad (2-23)$$

In order to include the equations governing the forces at the wheel-rail interface, linear approximations for the motion of a wheelset using Kalker's linear theory are considered. Detailed derivation of the equations of motion for a railway vehicle can be found in [41]. The lateral and yaw equations of motion for a wheelset on track are:

$$m\ddot{y}_w + 2f_{22}\left(\frac{\dot{y}_w}{v_{ref}} - \psi_w\right) + 2f_{23}\left(\frac{\dot{\psi}_w}{v_{ref}} - \frac{\varepsilon_0}{l_0 r_0}\right) + \frac{F_z \varepsilon_0 y_w}{l_0} + d_y(\dot{y}_w - \dot{y}_b - a\dot{\psi}_b + h\dot{\theta}_b) + c_y(y_w - y_b - a_0\psi_b + h\theta_b) = 0 \quad (2-24)$$

$$I_z \ddot{\psi}_w + 2f_{11}\left(\frac{l_0^2 \dot{\psi}_w}{v_{ref}} - \frac{l_0 \lambda y_w}{r_0}\right) - 2f_{23}\left(\frac{\dot{y}_w}{v_{ref}} - \psi_w\right) + 2f_{33}\left(\frac{\dot{\psi}_w}{v_{ref}}\right) + c_\psi(\psi_w + \psi_b) = 0 \quad (2-25)$$

Where

- $m$  is the wheelset mass,
- $y_w$  the wheelset lateral displacement,
- $y_b$  the bogie lateral displacement,
- $\psi_w$  the wheelset yaw angle,
- $\psi_b$  the bogie yaw angle,
- $\theta_b$  the bogie roll angle,

$d_y$	the wheelset/bogie lateral damping,
$c_y$	the wheelset/bogie lateral stiffness,
$c_\psi$	the wheelset/bogie yaw stiffness,
$F_z$	the axle load,
$\lambda$	the effective conicity,
$l_0$	the semi gauge,
$a_0$	half the bogie wheelbase,
$h$	the height of the bogie center of gravity above the wheelset axis,
$v_{ref}$	the forward velocity of the vehicle,
$\varepsilon_0$	the rate of change of contact angle with $y_w$ ,
$r_0$	the rolling radius with the wheelset central,
$f_{11}, f_{22}, f_{23}, f_{33}$	Kalker's linear creep coefficients.

Based on linear theory of Kalker [70], the equations governing the linear creep coefficients are:

$$f_{11} = (ab)Gc_{11} \quad f_{23} = (ab)^{\frac{3}{2}}Gc_{23} \quad (2-26)$$

$$f_{22} = (ab)Gc_{22} \quad f_{33} = (ab)^2Gc_{33}$$

Using Hertz theory [71], the size of contact patch can be related to geometry and mechanical properties of the wheel and roller as [70]:

$$ab = mn \left[ 3\pi N \frac{(k_1 + k_2)}{4k_3} \right]^{\frac{3}{2}} \quad (2-27)$$

$$k_1 = \frac{1 - \nu_W^2}{E_W}, k_2 = \frac{1 - \nu_R^2}{E_R}$$

$$k_3 = \frac{1}{2} \left( \frac{1}{r_1} + \frac{1}{r'_1} + \frac{1}{r_2} + \frac{1}{r'_2} \right) \frac{1 - \nu_W^2}{E_W}, k_2 = \frac{1 - \nu_R^2}{E_R}$$

Where  $m$  and  $n$  are elliptical contact constants,  $N$  is normal force at the contact [70]. The scaling factor for the contact area constants are:

$$\mathcal{S}_{k_1} = \mathcal{S}_{k_2} = \frac{1}{\mathcal{S}_E} = 1 \quad (2-28)$$

$$\mathcal{S}_{k_3} = \frac{1}{\mathcal{S}_l} = 5^{-1}$$

Taking the scaling factor for the normal force same as other force elements (Equation(2-22)), the contact patch area scaling factor will be:

$$\mathcal{S}_{ab} = \left( \mathcal{S}_N \frac{\mathcal{S}_{k_1}}{\mathcal{S}_{k_3}} \right)^{\frac{2}{3}} = \left( \frac{\mathcal{S}_F}{\mathcal{S}_{k_3}} \right)^{\frac{2}{3}} = 5^{3.33} \quad (2-29)$$

Based on the contact geometry scaling factor, the scaling factor for the linear creep coefficients are calculated as:

$$\mathcal{S}_{f_{11}} = \mathcal{S}_{f_{22}} = \mathcal{S}_E \mathcal{S}_{ab} = 5^{3.33}$$

$$\mathcal{S}_{f_{23}} = \mathcal{S}_E (\mathcal{S}_{ab})^{\frac{3}{2}} = 5^5 \quad (2-30)$$

$$\mathcal{S}_{f_{33}} = \mathcal{S}_E (\mathcal{S}_{ab})^2 = 5^{6.66}$$

Since the gravitational acceleration cannot be scaled, the vehicle weight scaling factor, which is the multiplication of mass and acceleration, is:

$$\mathcal{S}_{F_z} = \mathcal{S}_m \mathcal{S}_g = 5^3 \quad (2-31)$$

A conflict can be detected between normal force scaling factor (Equation(2-22)) and weight scaling factor (Equation(2-31)). The problem is solved by the use of vertical actuators to support a proper portion of vehicle weight on each axle.

Considering the Equations (2-24), and (2-25), by substituting pertinent scaling factors, all the terms agree with the scaling strategy (Equation (2-22) for force scaling factor, and Equation (2-23) for torque scaling factor), except for the following terms:

$$\begin{aligned}
 2f_{22} \left( \frac{\dot{y}_w}{v_{ref}} - \psi_w \right) & \text{ gives a force scaling factor of } 5^{3.33} \\
 2f_{23} \left( \frac{\dot{\psi}_w}{v_{ref}} - \frac{\varepsilon_0}{l_0 r_0} \right) & \text{ gives a force scaling factor of } 5^{4.1} \\
 2f_{11} \left( \frac{l_0^2 \dot{\psi}_w}{v_{ref}} - \frac{l_0 \lambda y_w}{r_0} \right) & \text{ gives a torque scaling factor of } 5^{4.4} \\
 2f_{33} \left( \frac{\dot{\psi}_w}{v_{ref}} \right) & \text{ gives a torque scaling factor of } 5^{5.8}
 \end{aligned}
 \tag{2-32}$$

#### 2.4.2 DLR's Strategy

Since the test rig at the German Aerospace Center (Deutsches Zentrum für Luft- und Raumfahrt; DLR) was primarily intended for studying hunting oscillations and consequently developing simulation software for railway vehicle dynamics, the scaling strategy adopted for this rig was based upon similarity of nonlinear lateral equation of motion for a suspended wheelset [19] [39] [69]. Detailed differential equation for the nonlinear lateral dynamical behavior of a wheelset is derived in [2]. For a suspended dicone, representing a wheelset, the equation is derived as:

$$\frac{m}{\chi} \ddot{y}_w = \frac{I_y \Gamma v_{ref}}{\chi r_0} \dot{\psi}_w - \frac{m g b_0}{\chi} y_w - \frac{c_y}{\chi} y_w + F_y + F_x \psi_w
 \tag{2-33}$$

Where,  $m$  is wheelset mass,  $c_y$  is lateral stiffness,  $v_{ref}$  is full-scale system volume,  $I_y$  is wheelset's rotational inertia around y-axis,  $F_x$  and  $F_y$  are longitudinal and lateral creepage forces,  $\Gamma$  is a geometric parameter defined as:

$$\Gamma = \frac{\gamma}{l_0} - r_0\gamma \quad (2-34)$$

Where  $l_0$  is half-gauge,  $\chi$  is leading angle defined as:

$$\chi = \frac{\Gamma l_0}{\gamma} \quad (2-35)$$

And  $b_0$  is a geometric quality defined as:

$$b_0 = 2\Gamma + \Gamma^2(r_0 + R_R) \quad (2-36)$$

Where  $R_R$  is the profile radius of the railhead. Substituting the pertinent scaling factors, Equation (2-33) will result in:

$$\begin{aligned} \frac{m}{\chi} \ddot{y}_w \frac{\mathcal{S}_m \mathcal{S}_l}{\mathcal{S}_t^2} &= \frac{I_y \Gamma v_{ref}}{\chi r_0} \dot{\psi}_w \frac{\mathcal{S}_m \mathcal{S}_l^2 \mathcal{S}_l}{\mathcal{S}_t^2 \mathcal{S}_l^2} - \frac{m g b_0}{\chi} y_w \mathcal{S}_m - \frac{c_y}{\chi} y_w \mathcal{S}_l \mathcal{S}_c + f_y \mathcal{S}_T \\ &+ f_x \psi_w \mathcal{S}_T \end{aligned} \quad (2-37)$$

In order to maintain similarity between scaled (Equation (2-33)) and full-scale (Equation (2-37)) models, the following conditions need to hold:

$$\frac{\mathcal{S}_l}{\mathcal{S}_t^2} = 1 \xrightarrow{\text{velocity scaling}} \mathcal{S}_v = \sqrt{\mathcal{S}_l} \quad (2-38)$$

$$\frac{\mathcal{S}_c \mathcal{S}_t^2}{\mathcal{S}_m} = 1 \xrightarrow{\text{stiffness scaling}} \mathcal{S}_c = \mathcal{S}_\rho \mathcal{S}_l^2 \quad (2-39)$$

$$\frac{\mathcal{S}_F \mathcal{S}_t^2}{\mathcal{S}_m \mathcal{S}_l} = 1 \xrightarrow{\text{creep force scaling}} \mathcal{S}_F = \mathcal{S}_\rho \mathcal{S}_l^3 \quad (2-40)$$

Therefore, the scaling factor for time and acceleration is:

$$\mathcal{S}_t = \sqrt{\mathcal{S}_l}, \quad \mathcal{S}_a = 1 \quad (2-41)$$

Since acceleration scaling factor is unity, unlike MMU's strategy, the scaling factor for gravitational force and creep forces are the same:

$$\mathcal{S}_{F_z} = \mathcal{S}_{mg} = \mathcal{S}_m \mathcal{S}_g \xrightarrow{\mathcal{S}_g = \mathcal{S}_a = 1} \mathcal{S}_{mg} = \mathcal{S}_m = \mathcal{S}_\rho \mathcal{S}_l^3 = \mathcal{S}_T \quad (2-42)$$

From contact linear theory, the scaling factor for creep forces is:

$$\mathcal{S}_F = \mathcal{S}_{f_{11}} = \mathcal{S}_{f_{22}} = \mathcal{S}_{ab} \quad (2-43)$$

Where based on the Hertz theory, the scaling factor for contact ellipse mean radius is defined as:

$$\mathcal{S}_e = \sqrt{\mathcal{S}_{ab}} = \sqrt{(\mathcal{S}_{F_z} \mathcal{S}_l)^{2/3}} \xrightarrow{\mathcal{S}_{F_z} = \mathcal{S}_\rho \mathcal{S}_l^3} \mathcal{S}_e^3 = \mathcal{S}_\rho \mathcal{S}_l^4 \quad (2-44)$$

In order to maintain geometry similarity between length and contact ellipse mean radius ( $\mathcal{S}_e = \mathcal{S}_l$ ), the scaling factor for density must be:

$$\mathcal{S}_\rho = 1 / \mathcal{S}_l \quad (2-45)$$

Since achieving density scaling factor of  $\mathcal{S}_\rho = 1 / \mathcal{S}_l$  could get challenging, Jaschinski [2] proposes an approach to select a density scaling factor that can be reached much easier (*e.g.*  $\mathcal{S}_\rho = 2 * 1 / \mathcal{S}_l$ ). It could be justified as the contact patch is mostly saturated for limit cycle analysis, and the area of the contact patch has the least influence on the saturated creep forces. The compromise for the density scaling factor results in a rather good approximation for dynamical similarity of limit cycle analysis.

### 2.4.3 INRET's Strategy

The main purpose of the test rig at the National Institute of Research on Transportation and Security (INRETS) in Grenoble was the study of wheel-rail contact patch and its elasticity in order to gain Kalker's creep forces [43]. As a result, the scaling strategy chosen for this rig was based upon the similarity of stresses everywhere in the system, including contact patch and elastic components [19] [18]. So, the starting point for the INRET scaling strategy is to set the stress scaling factor to unity:

$$\mathcal{S}_\sigma = \frac{\mathcal{S}_F}{\mathcal{S}_A} = \frac{\mathcal{S}_F}{\mathcal{S}_l^2} = 1 \quad (2-46)$$

It ensures similarity of creep forces at the contact. Based on the stress scaling factor, the stiffness scaling factor is defined as:

$$\mathcal{S}_c = \frac{\mathcal{S}_F}{\mathcal{S}_l} = \mathcal{S}_l \quad (2-47)$$

In order to maintain the similarity of elastic forces, as well as gravitational forces, the following condition must hold:

$$\mathcal{S}_c \mathcal{S}_l = \mathcal{S}_m \mathcal{S}_g \quad (2-48)$$

Assuming a unity scaling factor for density ( $\mathcal{S}_\rho = 1$ ), Equation (2-48) results in the following scaling factor for the gravitational scaling factor:

$$\mathcal{S}_g = 1 / \mathcal{S}_l \quad (2-49)$$

Since the gravitational acceleration cannot be scaled, it can be compensated by the use of vertical actuators to control the normal loading at the contact. Scaling factor for normal loading should be:

$$\mathcal{S}_{F_z} = \mathcal{S}_{m.g} = \mathcal{S}_l^2 \quad (2-50)$$

The scaling factor frequency will be:

$$\mathcal{S}_f = \sqrt{\frac{\mathcal{S}_c}{\mathcal{S}_m}} = \frac{1}{\mathcal{S}_l} \quad (2-51)$$

And consequently, scaling factor for time, velocity, and acceleration will be:

$$\mathcal{S}_t = \frac{1}{\mathcal{S}_f} = \mathcal{S}_l \quad (2-52)$$

$$\mathcal{S}_v = 1 \quad (2-53)$$

$$\mathcal{S}_a = \frac{1}{\mathcal{S}_l} \quad (2-54)$$

INRET scaling strategy ensures similarity of contact forces, as well as vertical dynamics.

## 2.5 Differences Between Roller and Tangent Track

Since a roller rig employs a rotating round rail instead of a stationary tangent track, the geometry of the contact between wheel and rail at the interface and consequently the dynamic behavior of the roller rig differ. In order to accurately evaluate roller rig's experimental data for studying actual rail vehicle's behavior, it is important to consider the extent to which the motion of the vehicle on the rig represents the motion of the same vehicle on the track. Many researches have investigated differences between dynamic behavior of a railway vehicle on a roller rig versus tangent track. De Pater [72] developed the detailed equations of motion for a wheelset supported by rollers as compared with the motion along a tangent track. Both non-linear and linearized equations of motion are derived. From de Pater's analysis it is possible to see the differences between the linearized equations of motion for a wheelset on rollers and those for a wheelset on track. Bosso et.al. [73] developed a systematic approach to obtain analytical model of a wheelset motion on a roller rig and tangent track. The model investigates kinematics and dynamics of the wheel based on the intrinsic differences between roller and rail. The differences between creepages and contact point location due to the roller curvature are studied.

Keylin [69] introduced correction factors for various parameters between roller rig contact data and track data. Based on the finite longitudinal radius of the roller, he worked on the Hertz theory to develop the correction factors for the contact geometry (area, radii). Then, he continued to develop the correction factors for creep forces and creepages according to both Kalker's linear theory and Johnson and Vermuellen's theory. He studied the effect of the roller diameter on the correction factors. His results show that creep forces and creepages in a roller rig and tangent track vary by less than 10% as long as the radius of the roller is 5 times or larger than the radius of the wheel.

Zhang et.al. [18] investigated the differences between roller and track in great detail. They developed the relations for geometry differences between wheel-rail and wheel-roller contact, and continued to find the differences between creep forces analytically. To this end, they used Kalker linear theory. They discussed the differences in stability and vibration response of the vehicle on a tangent track versus a roller.

Jashniski et.al. [19] categorized the differences involved in roller rig simulations. He discussed five principal differences between roller rig and tangent track [2]:

1. The longitudinal creepage is modified because of the variation of the rolling radius of the rollers as the point of contact is displaced laterally. The longitudinal creep is modified because as the contact point between the vehicle wheel and the roller moves laterally, the roller longitudinal velocity varies whereas, the corresponding rail velocity is, of course, zero. Matsudaira [5] introduced an equivalent conicity to incorporate the effect of longitudinal creepage modification to critical speed of the vehicle. Bosso [73] incorporated it directly into the longitudinal creepage formulation.
2. The spin creepage is modified because the roller angular velocity has a component resolved along the common normal at the point of contact. Many researchers have directly incorporated it directly to the formulation of spin creepage.
3. As the rollers possess curvature in the longitudinal vertical plane the geometry of the Hertzian contact areas is different. In the case of a tangent track, the longitudinal radius of curvature for the track is infinity whereas the longitudinal radius of curvature for a roller rig is finite. Using Hertz theory, Kaylin [69] investigated the contact geometry modifications due to the finite longitudinal radius of the roller.
4. When the wheelset yaws on the rollers the contact plane rotates in both pitch and yaw relative to the rollers. This pitch rotation will affect the effective conicity of the wheel as well as the angle of contact. However, these differences for the small values of yaw angle and hence very small values of pitch angle could be negligible.
5. The lateral and vertical stiffness of rollers may be different from the track stiffness. Change in the stiffness can influence the behavior of the wheel on the rig. From a contact mechanics standpoint, this could be neglected, although it could considerably affect the lateral dynamic and stability of the vehicle.

As a result, the contact mechanics and overall dynamic behavior of a railway vehicle could be considerably different on a roller rig compared with on a track. These modifications need to be

carefully considered for the design of a roller rig as well as for conducting any experimental research that a roller rig is intended for.

## 2.6 Rolling Contact Mechanics

In rail vehicles, the contact forces that roll and carry the load of train happen in the tiny contact area (roughly 1 cm<sup>2</sup>), where steel wheel meets steel rail. As a result, the wheel rail contact is extremely complex. A broad interdisciplinary research is needed to understand, model and optimize the contact mechanics and dynamics problem. The contact stress distribution prediction is the key to many wheel-rail related problems such as wear, rolling contact fatigue (RCF), plastic deformation, etc. Additionally, the accurate prediction of creep forces at the contact is fundamental requirement of any rail vehicle model. The multi-body simulation methods, widely used for studying rail vehicle dynamic behavior, require an accurate and fast contact model to predict the creep forces between wheel and rail.

As wheel and rail come into contact due to external force, deformations of microscopic asperities happen at the interface. Due to relative motion between the bodies, contact forces between two bodies appear. The tangential force at the contact is known as adhesion force or creep force. Adhesion or creep is different from (sliding) friction (Figure 2-22) [74]. Figure 2-22-Left shows a block sliding on a stationary surface with a velocity of  $v_s$ . The free-body diagram of the block includes a normal force ( $F_N$  usually is the weight of the block) and horizontal friction force ( $F_f$ ). The horizontal force is equal to kinetic friction force, which is generally lower than static friction force. The static friction force is the force required to initiate sliding of the block against the surface, whereas the kinetic friction force is the force required to maintain sliding. The ratio between the static or kinetic friction force and the normal force is called the static or kinetic friction coefficient:

$$\mu_f = \frac{F_f}{F_N} \quad (2-55)$$

Figure 2-22-Right shows a wheel or roller rolling along a surface/rail with an angular velocity of  $w$  and a forward velocity of  $v$ , like a locomotive wheel rolling on a rail. The wheel is subjected to a driving torque ( $T$ ) and normal force ( $F_N$ ). The torque maintains the angular velocity of the wheel and also causes a reactive tangential force ( $F_t$ ). The tangential force is the creep/adhesion

force at the interface and propels the wheel along the rail. The ratio between the tangential (adhesion) force and normal force is called the adhesion (rolling friction) coefficient:

$$\mu_r = \frac{F_t}{F_N} \tag{2-56}$$

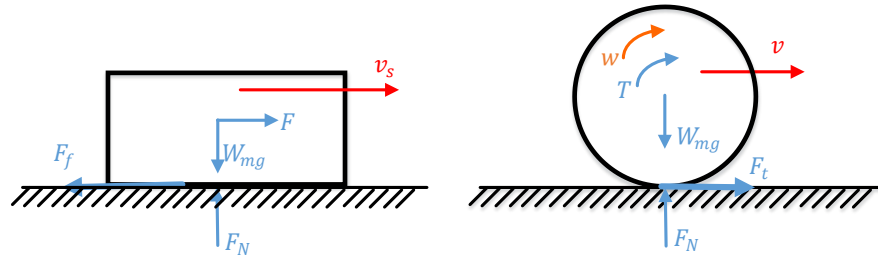


Figure 2-22: Schematic drawing of pure sliding contact (left) and rolling contact (right) [74]

To maintain a constant velocity of the wheel or accelerating the wheel, the circumferential velocity of the wheel at the interface ( $wR$ ) for a driven wheel will always be greater than its forward velocity ( $v$ ). During deceleration, the circumferential velocity is always smaller than the forward velocity. The normalized differential speed at the interface, which is the difference between the circumferential velocity and the forward velocity, is called creepage or creep:

$$\xi = \frac{v - wR}{(v + wR)/2} \tag{2-57}$$

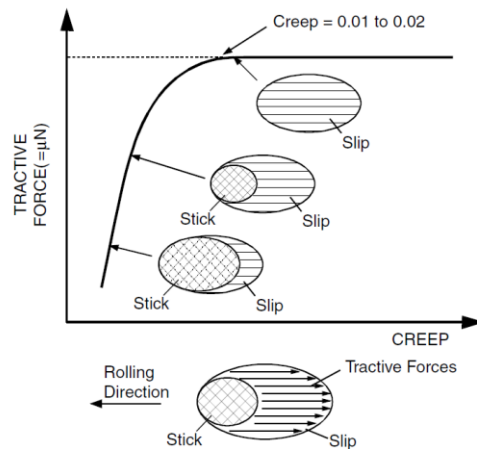


Figure 2-23. Creep curve showing the relationship between creep force and creepage as well as division of contact patch to slip and stick areas [74]

The tangential force due to this differential speed is called creep force, and it is a function of material properties of the contacting bodies, creepage/creep, and contact geometry.

Figure 2-23 shows the relationship between creep force and creep/creepage for a typical dry wheel-rail contact, which is known as a creep curve. Note that this plot can also be called traction versus slip curve. The figure shows that as the creep increases, the tractive/creep force at the wheel is also increased in an approximately linear fashion. The creep curve merges to a saturation line at typically 1-2% creep. At this point the adhesion equals the friction force of two bodies identical to the wheel and rail in pure sliding under identical contact conditions. Figure 2-23 also shows that the contact patch between the wheel and rail is divided into stick and slip regions. Longitudinal creep and tangential forces arise due to the slip that occurs in the trailing region of the contact patch. With increasing tangential force, the slip region increases and the stick region decreases, resulting in a rolling and sliding contact. When the tangential force reaches its saturation value, the stick region disappears, and the entire contact is in a state of pure sliding. The maximum level of tangential force depends on the capacity of the contact patch to absorb the adhesion, which is expressed in the form of the coefficient of friction.

During past century and even earlier, many researches have investigated the rolling contact phenomenon and developed various contact models. The contact problem is usually divided into two categories:

- i. Normal contact problem that investigates the geometry of the contact (shape and area) and formulating the normal pressure distribution inside the contact patch.
- ii. Tangential contact problem that studies the relationship between creepage and creep force, particularly the tangential stress distribution throughout the contact patch.

The contact phenomenon and well-known contact theories are extensively discussed in chapter 7.

## 2.7 In Summary

Since Virginia Tech roller rig is primarily intended for studying contact mechanics and dynamics, a list of roller rigs that have conducted adhesion studies is tabulated in Table 2-4.

**Table 2-4: List of the roller rigs that have been used for studying adhesion behavior and their main characteristics. DOFs column presents the number relative displacements that the rig allows between the**

contacting bodies at the interface, and creepage control column indicates the method by which creepage is provided at the interface; controlling the rotational speed of the contacting bodies independently or using a differential gearbox

Roller rig	Layout	Wheel radius (m)	Roller radius (m)	Analysis	DOFs	Creepage control
Chengdu	Full truck	----	---	Creep curves for different long. Speed, axle load, and surface condition studies (water, oil)	All DOFs	Independent
Full car rig, Japan	Full	0.75	1.2	Long. and lat. Creep characteristics	All DOFs	Independent
SUROS	Single wheel	0.047	0.047	Fatigue and wear testing and creep curves for different contact conditions	0 DOF	Independent
Rolling Contact Testing Machine, Japan	Single wheel	0.73	0.91	Creep curve for water lubricated surface and adhesion coefficient for different long. speed	0 DOF	Independent (braking)
The Adhesion Test Equipment, Japan	Single wheel	0.30	0.53	Tractive coefficient for different slip ratio is measured and used to develop anti-slip control algorithms	0 DOF	Independent
Scaled roller rig (Italy, 2012)	wheelset	0.094	0.15	Wheel-rail adhesion and surface condition studies (dry, wet )	All DOFs	Independent
The Twin Disc Rig, UK,	Single wheel	0.290	0.310	Railway wheel squeal	AoA, Lateral	No creepage control

---

Two-roller- rig testing machine, Japan	Single	0.172	0.172	Effect of friction modifier	0 DOF	Differential
---	--------	-------	-------	--------------------------------	-------	--------------

---

A large number of roller rigs have addressed adhesion characteristics in railway applications [75]. Zhang et.al. [9], using a full scale roller rig, studied the adhesion characteristics for various contact conditions (various speeds, axle-loads, contaminations). Although the full-scale rig is beneficial in terms of replicating the same conditions in the actual wheel-rail contact, it sacrifices the accuracy of the speed control, and force measurements due to the size of the equipment. The Sheffield University Rolling Sliding (SUROS) twin disc experimental device [50] [51] has been used for conducting creep-creepage model and velocity dependent friction coefficient studies. The rig, however, is capable of providing solely longitudinal creepage. Same is true for other twin disc test machines [53] [56] [58]. Matsumoto et.al. [11], using a 1/5<sup>th</sup> scaled single wheelset test setup, investigated the creep force characteristics between roller and wheel at varied contact conditions. The gauged spoke-rim design of the roller for measuring contact forces (due to cross-talk), and vector controlled AC induction motors that are employed to control the speed of the roller would not produce the highest precision data points.

A review of current roller rigs indicated that many desired functional requirements for studying contact mechanics were not available. There is no known roller rig that is equipped with a contact patch geometry measurement system and hence non elliptical contact experimental studies is lacking. A thorough experimental study on the velocity dependency of the friction coefficient, which could help explaining the physics behind the falling friction phenomena of the creep-creepage curve, is lacking. A comprehensive experimental study using roller rigs for explaining the influence of contamination on the adhesion characteristics (third body layer studies) is lacking. In conclusion, a dedicated contact mechanics roller rig that is equipped with proper instrumentation is needed for accurately explaining the unknown physics behind wheel-rail contact. Thus, the Virginia Tech Railway Technologies Laboratory (RTL) has embarked on a mission to develop a state-of-the-art testing facility that will allow experimental testing for contact mechanics in a dynamic, controlled, and consistent manner.

# 3 Configuration and Layout Development

(This chapter was published in part in proceedings of ASME 2013 Rail Transportation Division Fall Technical Conference [75]. Reproduced with permission.)

In this chapter, different design concepts for railroad's test rigs are explained. These are based on past or existing research facilities (as provided by literature, council with industry, or industrial suppliers), and test rigs used in other industries. Each concept is reviewed in terms of suitability for conducting research; hence the design benefits and drawbacks are presented [75]. Based on the various design concepts reviewed and intended functionality for our test rig, the final design solution for the Virginia Tech Roller Rig (VTRR) is introduced. At the end, the testing capabilities of VTRR are presented.

## 3.1 Roller Rig Design concepts

### 3.1.1 Vertical Plane Roller, (Typical Roller Rig)

This type of roller rig has been used for testing railway vehicles as early as the turn of 20th century. There are various implementations of this concept; the simplest and most common of these is the single-wheel roller (Figure 3-1). In this configuration, the wheel is placed on one roller that has a profile similar to that of a rail. Typically, this setup can allow adjustment of the simulated weight of the train on the test wheel, the angle of attack, the rail cant, or other parameters. The rolling rail is usually powered to rotate the wheel up to a specified speed where steady-state testing is performed. Some rigs have the ability to perform dynamic vibration actuation while taking measurements using various sensors. A wide range of literature is available for this configuration in the chapter two of this dissertation [18] [19]. This design configuration can be used for simulating curving dynamics, although the differential speeds of the rollers would require extremely precise control for accurate slip measurements. Also, wheelset hunting tests may be possible but the constraint system must be designed to allow such a test. This design suffers from having different contact geometry from conventional rail due to contact patch distortion. Roller diameter, however, plays a significant role in contact patch distortion [see section 2.5].

### 3.1.1.1 Concept Benefits

- Most common design of rail test rigs
- Fielded wheels and other components may be used as test specimens
- Flexibility for accommodating various configurations
- Capable of high speeds
- Roller strain gauges may be used for wheel force measurements (wheel may be mounted to a wheel force transducer)
- Curvature testing is possible, although angle of attack (AoA) may cause more instability due to geometric effects of the rail-roller radius
- Many options available for constraining the test article

### 3.1.1.2 Concept Drawbacks

- Fielded rails cannot be tested
- Rail profile not easily altered
- Test data obtained from roller rig experiments have to be correlated to straight rail via mathematical models, they are not precise replications of conventional track

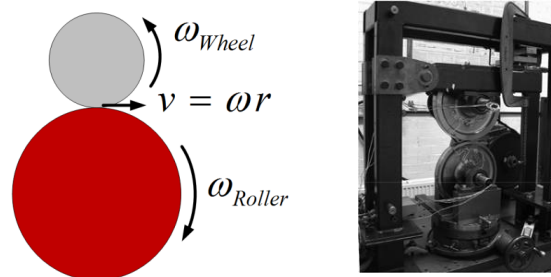


Figure 3-1: Diagram of a vertical plane roller rig and product design [12]

### 3.1.2 Perpendicular Roller

Another alteration of the roller rig design is when the rollers are in the horizontal plane, as shown in Figure 3-2. In this configuration, the wheel is placed on one roller that has a profile similar to that of a rail but travels in a circular path perpendicular to a typical roller rig. Similar to other roller rigs, this setup can allow adjustment of the simulated weight of the train on the test wheel, the angle of attack, the rail cant, or other parameters. The rolling rail is usually powered to rotate the wheel up to a specified speed where steady-state testing is performed. Unlike conventional roller rig design, there is no known literature available directly pertaining to this particular design

concept from either mathematical modeling or experimental viewpoints. For this reason, more design work will be required to ensure a successful design. While this concept is an untested design, it may offer some key advantages over a typical roller rig.

### 3.1.2.1 Concept Benefits

- Real rail crown may be used in this configuration, although this will depend on desired top speeds, power availability, operating costs, and other aspects
- “Flat” rail profile is expected to reduce the result differences from conventional rail. Typical roller rigs suffer from having creep behavior that varies from flat track due to the curvature of the rolling rail
- Underside of rail roller below the contact patch may be supported by bearings that may be able to allow real-time adjustments of the vertical stiffness of the simulated track
- Differential speeds needed for curving studies will be possible

### 3.1.2.2 Concept Drawbacks

- Large moments are created due to the large radius of the roller. This implies auxiliary bearings will be required to counteract these forces
- Concept has never been implemented and no known literature exists concerning this design
- Differential speed systems will likely require two separate drive systems (rather than the use of a differential drive)

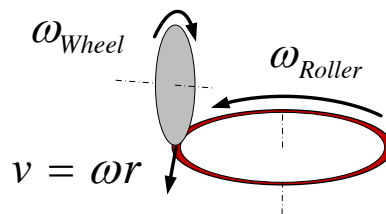


Figure 3-2: A roller rig design with horizontal roller configuration

### 3.1.3 Tangent Roller, Internal

In this variation of the roller rig design, the wheel is internally contacting the roller, as shown in Figure 3-3. While one example of this design has been found for rail transit use [76], it is similar to automotive test rigs used in the tire and braking dynamometer industry. While similar to a

typical roller rig, it is important to note that, unlike a conventional roller, this rig is naturally stabilizing due to the geometric effects of the rail radius.

### 3.1.3.1 Concept Benefits

- More stable than the external roller configuration
- Single-wheel designs have been used in automotive and rail transit studies and industry

### 3.1.3.2 Concept Drawbacks

- Axle constraint system unfeasible for most truck designs
- Test data obtained from roller rig experiments have to be correlated to straight rail via mathematical models, there are discrepancies because of roller diameter
- Large roller (cylinder) will have very large mass
- Not common design
- Bearing placement not ideal for taking high normal loads

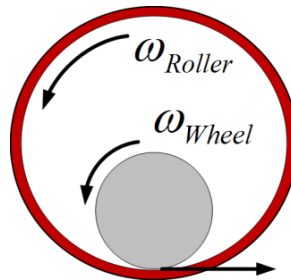


Figure 3-3: A roller rig diagram with internal tangent roller

### 3.1.4 Drum Roller

A variation of the vertical plane roller is where the rail rollers rotate at the same angular velocity (no differential speeds). These types of rigs have been used for truck or full car test rigs, but usually for hunting or braking test rigs, not to study curving or contact mechanics (Figure 3-4). The advantage of this type of rig is primarily reduced cost and complexity when compared with the individual vertical plane roller. This setup could allow to make adjustments of the simulated loading and the angle of attack, but will not be able to make adjustments for rail cant. This design of rig could not reproduce curving dynamics. Wheelset hunting tests may be possible but the constraint system must be designed to allow for such a test. This system design

still suffers from having contact mechanics variation from conventional rail, just as the other typical roller concepts.

#### 3.1.4.1 Concept Benefits

- Simple variation of the most common design of rail testing rig
- Fielded wheels and other components may be used as test specimens
- Can be coupled with inertial elements to simulate various loading conditions
- Flexibility for accommodating various configurations
- Capable of high speeds
- Wheel may be mounted to a wheel force transducer
- Roller strain gauges may be used for wheel force calculations

#### 3.1.4.2 Concept Drawbacks

- Fielded rails cannot be tested
- Rail profile not easily altered
- Test data obtained from this design have to be correlated to straight rail via mathematical models
- Differential speed testing (curving) is not possible
- AoA tests introduce instability due to geometric effects of the rail-roller radius



Figure 3-4: Simple diagram of a wheelset on a drum roller and product design [36]

## 3.2 Roller Rig Alternative Designs

To avoid some of the problems associated with conventional roller rigs (such as the longitudinal and spin creep dissimilarity to conventional rail), researchers considered the design of a test rig

that utilizes a section of conventional rail instead of the rotating rail (roller) for the repeatable laboratory testing:

### 3.2.1 Short Stroke Oscillating Rail

The most feasible concept of flat rail testing rigs utilizes a short length of rail, which is passed underneath a railroad wheel. This rail section is moved forward and back under the wheel to simulate track conditions. Oscillating test machines such as these have been built and are in use; however, they have primarily been used for testing rail strength or joint bar fatigue. The oscillating rail concept considers the use of a short length of rail on the bearing platform, longitudinally displaced beneath a wheel. While antiquated versions of this concept rely on mechanical actuators to oscillate the rail, at least one modern version of this concept has been created that uses hydraulic actuators to apply normal loading on the wheel and positioning the rail (Figure 3-5). However, no known full truck or single wheelset testing machines of this type have been designed or produced.

#### 3.2.1.1 Concept Benefits

- Equivalent behavior to conventional rail
- Single wheel versions have been previously implemented
- Depending on design, differential speeds possible
- Superelevation and rail cant are possible

#### 3.2.1.2 Concept Drawbacks

- Low speeds only
- Steady-state testing not possible without expensive actuators
- Huge loads required to accelerate the track to high speeds
- Constraining the rail would be difficult depending on the speeds and conditions required

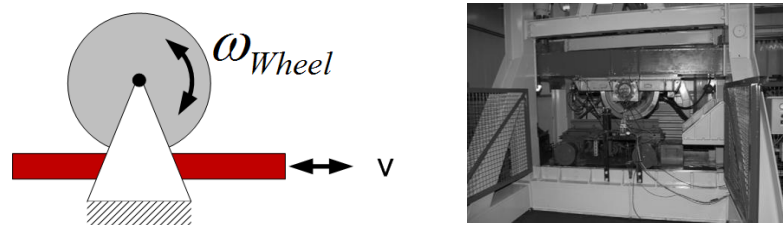


Figure 3-5: Oscillating rail rig diagram and produced design [8]

### 3.2.2 High Speed Shooting Rail

As an alternative to the oscillating rail idea, a high-speed shooting rail rig could take advantages of the contact similarities of using flat rail yet also be capable of reaching high speeds. This design would utilize a length of rail and pass that rail along adjustable guides that constrain the rail under the wheel assembly (Figure 3-6). The greatest limiting factor of this type of design, as with the previous design, is the difficulty associated with the acceleration of the rail up to elevated test speeds. For example, consider the acceleration of 115 lb/yd rail (very light rail) to a speed of 220 mph. Neglecting the weight of guide bearings or other necessary components for such a device, and assuming a constant acceleration of the rail, it is found that regardless of the length of rail, the force required to reach that test speed is 60 kip. If a 50ft section of rail was chosen, the acceleration of the rail needed (just to reach 220 mph) is 31 times the acceleration of gravity. For this reason, high speed testing on such a rig is exceedingly impractical.

#### 3.2.2.1 Concept Benefits

- Contact mechanics equivalent to typical
- Differential speeds theoretically possible

#### 3.2.2.2 Concept Drawbacks

- Huge loads required to accelerate the track to high speeds
- Constraining the rail would be difficult regardless of the speeds and conditions required

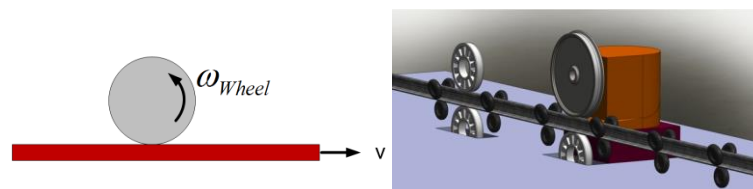


Figure 3-6: Stationary truck, track in motion

### 3.2.3 Modified Rail (Crown and Gauge Face)

Another design rig that has never been implemented in the rail industry is the modified rail roller (continuous rail band), although the concept is very common in automotive tire testing rigs. This design would have the ability to produce contact mechanics equivalent to the flat-rail test testing,

yet allow the capability of obtaining higher test speeds. In this configuration, a modified rail crown would be used as the rail and it would be passed under the rail wheel, such as an automotive rolling road tester performs (Figure 3-7). Although this configuration uses modified rail crown, the band must be thick enough to allow deflection of the rail elastic region.

### 3.2.3.1 Concept Benefits

- Continuous, steady-state testing of wheels
- May use standard rail crown for testing. This would allow for investigating the wheel-rail interaction under real operating conditions

### 3.2.3.2 Concept Drawbacks

- Possible plastic deformation of the rail crown will greatly reduce the time between belt replacement of the test machine
- Stress on rail may exceed the limits of the material at higher loads and speeds
- Rail band placement and control expected to be difficult

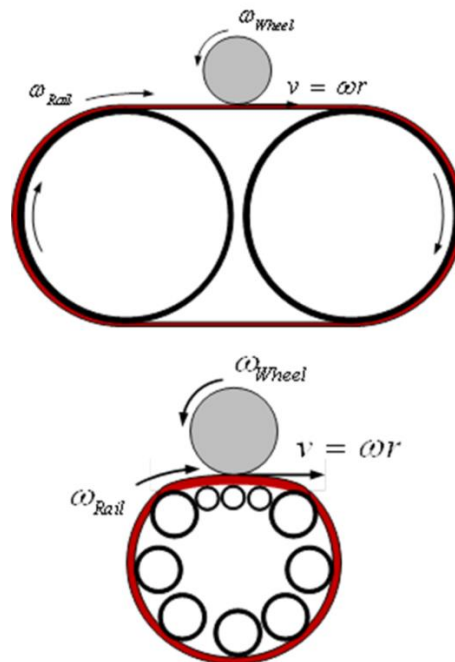


Figure 3-7: Roller rigs diagrams with modified rail crown

### 3.3 Roller Rig Test Specimens

In addition to the various design configurations discussed earlier, roller rigs can be categorized as single wheel, single wheelset, and full truck (expandable to full car). Each aforementioned design concept may be implemented in any of these layouts. These different design layouts are investigated and their potential advantages and limitations for conducting railway studies are discussed.

#### 3.3.1 Single Wheel

Single wheel test rigs are designed to test a single wheel on a rail setup (Figure 3-8). The single wheel setup is the simplest overall system but lacks the ability to study behavioral interactions associated with a complete suspension setup or the interaction of stick-slip of a single axle during cornering operations. Primarily, the testing constraints of the single wheel testing rigs will be used to verify computer simulations at various AoA, speed, and slip conditions.

##### 3.3.1.1 Potential Advantages

- Single wheel design may make integration with wheel load transducers the most feasible
- Single rail-roller reduces system cost and complexity
- Optical sensors may get best vantage point to test specimen as compared with wheelset and truck test rigs
- Advanced constraint system may allow the most precise control and data collection of angle of attack testing
- This design may make independent evaluation of lateral positioning and AoA the most feasible
- Single wheel design may provide the most accurate contact mechanics studies (creep forces, contact patch geometry, surface conditions) because of better control over the parameters

##### 3.3.1.2 Potential Limitations

- Wheel constraint and loading systems will likely vary significantly from fielded components to the point where the study of those components (side frames, bearings, suspensions, etc) will be limited or not possible
- Hunting studies that minimally constrain the test article are not possible
- Wheels may require modification for fitment on to a wheel force transducer

- Curving dynamics and suspension compliance studies are not possible

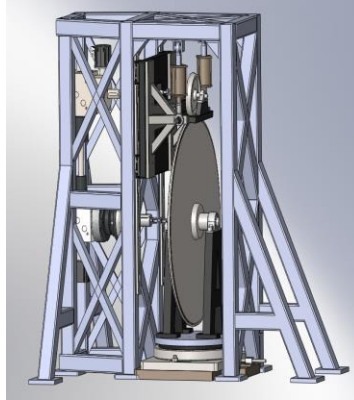


**Figure 3-8: Concept of a single wheel roller test rig**

### **3.3.1.3 Suggested Application**

For characterizing and expanding on the current understanding of the phenomena affecting the contact ellipse behavior under various conditions, only a dedicated single wheel rig will suffice. A single wheel test rig with the proper instrumentation will allow for the precision control and sensing needed to improve upon models that are currently employed. While not being able to study suspensions or other various truck components, a single wheel test rig would be the least complex platform for providing the accurate measurements needed for contact mechanics studies.

### **3.3.2 Single Wheelset**

Wheelset test rigs are designed to test a single wheelset on a rail setup (Figure 3-9). The single wheelset setup significantly increases system complexity over the single wheel design, but offers significant advantages such as the ability to study behavioral interactions associated with a complete suspension setup or the interaction of stick-slip of a single axle during cornering operations, although hunting studies may not be possible. Primarily, the testing constraints of a single wheelset test rig will allow verification of computer simulations at various angle-of-attack, speed, and slip conditions, yet may also allow testing of fielded axles and bearings to quantify their behavior.

#### **3.3.2.1 Potential Advantages**

- Wheelset design may allow for curvature studies

- Wheelset rig may be used to test complete suspension compliance (if truck is still one unit)
- Wheel constraint and loading systems may be designed to closely replicate that of fielded components, giving the rig ability to accurately study those components (side frames, bearings, suspensions, etc)

### 3.3.2.2 Potential Limitations

- Wheelset test rig requires additional rolling rail, significantly increasing the cost and control system complexity
- Single wheelset design will greatly increase complexity of wheel force transducer integration
- Optical sensors may get less beneficial vantage point to monitor the test specimen as compared with a single wheel rig
- Constraint system must have increased complexity to allow precise control and data collection of angle of attack testing
- Hunting studies that minimally constrain the test article may not be possible
- Wheels may require modification for fitment on to a wheel force transducer

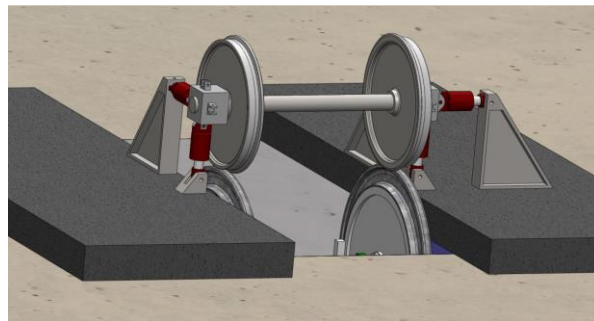


Figure 3-9: Concept of a single wheelset roller test rig

### 3.3.2.3 Suggested Application

For component-focused studies, the use of a wheelset roller rig is most commonly employed. Wheelset rigs typically test the performance of brake systems, friction modifiers, wear, fatigue (RCF), wheel loading and resultant forces. However, because of the difficulty in obtaining precise measurements or maintaining precise control over the test conditions, these rigs are typically inadequate for improving the understanding of the contact ellipse behavior other than adhesion characteristic studies.

### 3.3.3 Full Truck

Full truck test rigs are designed to test a fully assembled truck on a track setup. Testing an assembled truck significantly increases system complexity over both the single wheel or wheelset designs, but potentially offers the advantage of studying the complete system interaction with regard to friction studies, stick-slip of a wheelset during cornering operations, and hunting studies. Constraining the test article may allow for testing of the bearings, sideframes, springs, friction wedges, bolster, center plate, and the interaction of these assemblies at various angle-of-attacks, speeds, and slip conditions, but will increase the difficulty of performing precise studies of the wheel-rail interface and contact ellipse. Additionally, the full truck roller setup may be replicated multiple times to allow the testing of an entire car or locomotive.

#### 3.3.3.1 Potential Advantages

- Truck assemblies allow for curvature studies
- Truck testing rig may be used to test complete suspension compliance
- Full-scale rigs may be used to test fielded trucks or any subassemblies
- Truck constraint and loading systems may be designed to closely replicate that of those in the field, giving the rig ability to accurately study those components and assemblies (side frames, bearings, suspensions, etc.)
- Full truck design may make railway dynamics studies (hunting, derailment) the most feasible

#### 3.3.3.2 Potential Limitations

- Full truck test rigs requires multiple rolling rails (depending on the design), significantly increasing the cost and control system complexity
- Facilities must be able to accommodate large test equipment and test specimens, adding to facility requirements
- Large power requirement are likely required for drivetrain systems
- Truck assembly will greatly increase complexity of wheel force transducer integration
- Optical sensors may get a less beneficial vantage point for monitoring the test specimen as compared with a single wheel rig
- Constraint system must have increased complexity to allow precise control and data collection of angle of attack testing (less accurate contact mechanics studies)
- Wheelsets may require modification for fitment on to a wheel force transducer

- The roller diameters are limited. Wheelset spacing determines the spacing and allowable diameter of the rollers
- Constraining the bolster for test article placement will allow significant compliance of the assembly, possibly leading to poor test results

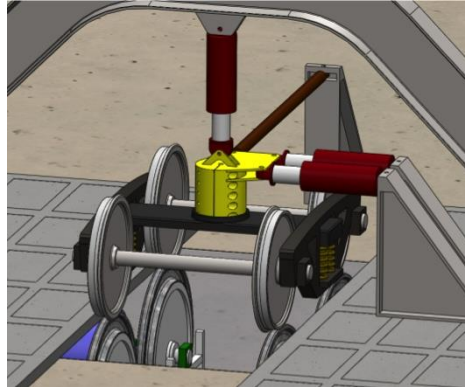


Figure 3-10: Concept of a full truck roller test rig

### 3.3.3.3 Suggested Application

For macro-scale dynamics, such as car-body rocking, car-body hunting, braking performance, locomotive power, or truck suspension performance, full car-body or full truck rigs are most desirable. These rigs may be designed to handle such tests with versatile rollers that may be equipped with brakes, powertrain systems, or vertical displacement actuators. However, because of the limitations on the roller diameters, the lack of precise control over the inputs, the difficulty of making precision measurements, and the operating cost of performing tests, these rigs are not designed for studying contact fatigue, wheel wear, contact forces, or wheel-rail contact on a precise scale.

## 3.4 Configuration Design

According to above review study of the roller rig designs, the Virginia Tech Roller Rig (VTRR) is designed to be a single-wheel test rig with a vertical plane roller (typical roller rig) configuration. It is the least complex configuration that will allow for the precision control and sensing needed to improve upon contact models that are currently employed [75], as the rig is primarily intended for the contact mechanics and dynamics studies. Provision designs, however,

are incorporated that makes the rig a viable platform for studying many other aspects of the rail vehicles. The rig's capabilities are detailed in the next section (Section 3.6).

Since having a roller instead of a tangent track imposes a finite longitudinal radius to the contact geometry, careful consideration must be taken for developing the most accurate contact results (Section 2.5). Keylin [69] showed that creep forces and creepages in a roller rig and tangent track vary by less than 10% as long as the radius of the roller is 5 times or larger than the radius of the wheel. A ratio of  $\sim 5$  between diameters of the roller and wheel is selected to keep the contact patch distortion to a minimum. It ensures that the contact data from the roller rig is in the area that could be compensated and compared with the actual rail vehicle's contact data.

For repeatable laboratory testing, a roller rig is the most practical piece of test equipment for the study of rail vehicle dynamics. The scaling factor, however, could have a considerable influence on the validity of the experimental data. In this regard, a very small scaled rig, which would make the rig very affordable and more controllable, could possibly add not much to the current science of the wheel-rail contact. On the other hand, a full-scale rig would exponentially add to the complexity of the design and its implementation. For example, since the ratio of 5 is chosen between the diameters of the roller and wheel, a full-scale rig requires a roller with a diameter of 200 in. To spin such a large roller, a gigantic electric motor is needed that reduces the accuracy of speed control significantly; hence reduces the accuracy of slip (differential speed at the contact). As a result, after a great deal of discussions with suppliers and rail experts, considering available components in the market, and conducting many design calculations, a length scaling factor of  $\sim 4$  is selected; the diameter of the full-scale wheel (actual train wheel) to the diameter of the rig's wheel is  $\sim 4$ .

According to the selected scaling factor and the roller to wheel diameter ratio, the rig's wheel and roller diameters are designed to be 10 and 45 inch, respectively. The wheel has a 1/4th scaled down version of wheel profile AAR-1B wide-flange for freight car wheels, and a 1/4th scaled down version of AREMA 136-lbs RE rail section is machined on a locomotive wheel to function as a rotating rail.

Since the rig is a contact mechanics rig, the INRET similitude strategy is employed for calculating scaling factors for other quantities (Section 2.4). Based on the INRET similarity

formulation and rig's length scaling factor of 4, the scaling factor for the other physical quantities are developed. The scaling results are listed in Table 3-1.

**Table 3-1: The scaling factors for the physical quantities of the rig**

Physical quantity	Symbol	Scaling factor
Length	$\mathcal{S}_l$	4
Area	$\mathcal{S}_A$	16
Stiffness	$\mathcal{S}_c$	4
Density	$\mathcal{S}_\rho$	1
Force	$\mathcal{S}_F$	16
Velocity	$\mathcal{S}_v$	1
Acceleration	$\mathcal{S}_a$	$\frac{1}{4}$
Time	$\mathcal{S}_t$	4
Frequency	$\mathcal{S}_f$	$\frac{1}{4}$
Mass	$\mathcal{S}_m$	64
Friction coeff.	$\mathcal{S}_\mu$	1

The main practical consequences of these scaling factors are summarized here:

- Both the rolling speed and the vibration velocity of the wheel are not modified by similarity.
- The modal frequencies of the wheel should multiply by  $\frac{1}{4}$  to correspond to modal frequency of the full-scale system.
- The scaling factor for mass is 64, whereas the scaling factor for force, including gravitational force, is 16. In order to maintain the similarity of the stresses at the contact, the scaling factor for the normal loading at the contact is kept 16 using linear actuators.
- Although the stresses at the contact are kept the same as the full scale, however, the similarity could not perfectly ensured in the local conditions of the contact, which affect the size of the contact patch and the friction law.

The rig is designed for simulating a freight rail car with an average speed of 10 mph (16k/m). The typical weight of a freight railcar is around 300,000 lbs, and it will be taken by four wheelsets in a typical freight railcar. Therefore the gravitational loading on each wheel is:

$$(F_z)_{full\ scale} = \frac{300000}{8} = 37500\ lb \quad (3-1)$$

Based on the force scaling factor of 16 (Table 3-1), the gravitational force at the contact patch in the designed roller rig will be:

$$(F_z)_{roller\ rig} = \frac{37500}{16} = 2343\ lb \approx 10664\ N \quad (3-2)$$

In order to estimate the contact forces, a friction coefficient of 0.4 is assumed. Therefore, for the maximum longitudinal and lateral friction forces, based on the Coulomb's law, we have:

$$(F_x)_{max} = (F_y)_{max} = F_z \mu = 0.4 \times 10664 = 4265.6\ N \quad (3-3)$$

Similarly, based on the scaling factor for velocity and the intended tangential speed of 10 mph for the full-scale system, the linear velocity at the contact, and consequently the rotational speeds for the wheel and roller are calculated:

$$(v_{ref})_{roller\ rig} = \frac{(v_{ref})_{full\ scale}}{\mathcal{S}_v} = 10\ mph = 4.4\ m/s \quad (3-4)$$

$$\omega_{wheel} = \frac{v_{ref}}{r_{wheel}} = 34.65 \frac{rad}{sec} = 330.8\ RPM \quad (3-5)$$

$$\omega_{roller} = \frac{v_{ref}}{r_{roller}} = 7.7 \frac{rad}{sec} = 73.5\ RPM \quad (3-6)$$

### 3.5 Brief Description of Virginia Tech Roller Rig

The Virginia Tech Roller Rig project is a state of the art testing fixture for experimental investigation of wheel-rail contact mechanics and dynamics. It is a single-wheel roller rig with vertical plane roller configuration for studying wheel-roller adhesion characteristics. The rig is a one-fourth scaled version of a railroad wheel on a roller (rotating rail), as shown in Figure 3-11 and

Figure 3-12. The roller is five times larger than the scaled wheel, in order to keep the contact patch distortion that is inevitable for such a setup to a minimum. The rig also includes the latest technology in motor control to control the relative speed between the wheel and roller to a high degree of precision. Similarly, a specially designed load platform is used to measure the contact forces and moments, accurately.

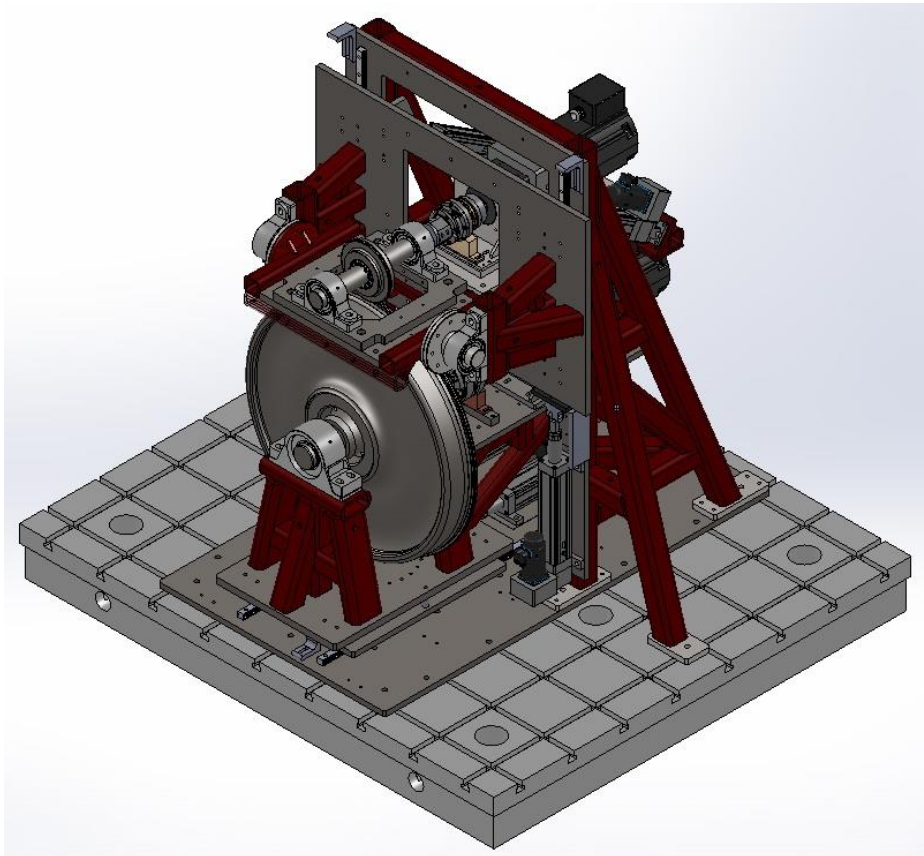


**Figure 3-11: Solid model of Virginia Tech roller rig**

The rig is equipped with two independent, direct drivelines, which provide the required power to drive the wheel and roller, while precisely control the differential speed at the contact (creepage). The setup is equipped with positioning mechanisms to replicate boundary conditions of real railway vehicles. Linear actuators are employed to actively control:

- Contact pressure (normal loading)
- Angle of attack (AoA)

- Lateral displacement
- Cant angle

The rig is equipped with an instrumentation system to monitor all the required variables. It incorporates various sensors, such as force, torque, speed, displacement sensors and vision system. A novel force measurement system is configured to accurately acquire contact forces and moments. It consists of four triaxial load cells that are placed in line with the contact patch, and another set of four triaxial load cells that are able to measure any reaction loading components due to the driveshaft.

A sophisticated powering scheme and control architecture—manufactured by motor supplier, Kollmoregn—is configured to actively drive all the components. It integrates multiple sub-systems such as power distribution, safety, motion control, data acquisition. It provides a unified command and feedback network between all the components with high update rate.

The mechanical and electromechanical design, analysis, calculations, and simulations of the rig are discussed in detail in chapters four, five, and six.

## 3.6 Rig's Capabilities

The wheel-rail contact mechanics and dynamics is one of the most complex aspects of railroading. Although there is a broad, high-level understanding of *what* happens at the wheel-rail interface, much of the science behind *why* it happens is lacking. The roller rig that is designed and fabricated by Virginia Tech's Railway Technologies Laboratory (RTL) is intended to provide a better understanding of the physics of the wheel-rail interface through its unique electro-mechanical configuration and highly precise instrumentation. Some of the studies that are possible with the roller rig include:

### 3.6.1 Precise Measurement of Creep-Creepage Curves

This includes measuring the:

- Influence of angle-of-attack (AoA), rail cant angle, and rail lateral shift
- Velocity-dependent coefficient of friction

The test rig is capable of controlling the differential speed (creepage) at the wheel-rail interface with a high level of precision. In addition, a novel force measurement system is configured to accurately read the contact (creep) forces and moments. Therefore, the rig is capable of conducting precise creepage-creep force studies both on straight and curved tracks, for developing new models or improving the existing ones. The contact studies will be generalized to investigate the effect of angle of attack, cant angle, and lateral shift in creep models. The rig will also shed more light on the spin creepage studies and creep forces due to spin creepage.



**Figure 3-12: The Virginia Tech Roller Rig**

Furthermore, the rig will allow verifying theories related to velocity-dependent friction coefficient. In particular, the falling friction phenomenon (friction forces reducing at higher speeds) could be investigated extensively. Since both the rotating bodies (wheel and roller) are

actively controlled, both positive and negative creepage values could be studied, and the resulting creepage-creep curves could be compared.

### **3.6.2 Accurate Measurement of Contact Geometry**

The test rig can accurately measure the wheel-rail contact geometry to a high degree of precision that surpasses all other rigs that currently exist, worldwide. It will be equipped with a state-of-the-art vision system that is able to provide a precise image of the interface between the wheel and rail. This high-definition imaging system is capable of precisely investigating the contact geometry using advanced image-processing methods and extracting measurements from every frame. Therefore, the area and shape of the contact patch could be recorded at every instant in time. The major and minor axes for the elliptical contact patch can then be measured from the recorded data. This also enables studying the conditions under which double-point contact occurs. Other sensory measurements will be synchronized with the vision data to accurately measure the resulting forces from the single- or double-point contact geometry.

### **3.6.3 Precise Evaluation of Third Body Layers**

Third body layers refer to any material that is placed in between the wheel and rail at the interface as a third layer to the wheel and rail surfaces. These include:

- Friction modifier
- Surface conditioning elements, such as water, oil, sand, leaves, etc.

Test rig has the ability to accommodate the equipment necessary for studying the effect of surface condition and friction modifiers. The rig is also capable of studying the characteristics of surface roughness and different interfacial layers at the wheel-rail contact surface, to an accuracy that is unmatched among any other equipment that is currently in existence. Other aspects of the wheel-rail contact dynamics that can be measured precisely include the slope reduction phenomenon in contact curve models and wheel/rail damage due to contaminant at the interface.

### **3.6.4 Dynamic Creepage Analysis**

The test rig is capable of performing a full range of dynamic creepage studies that will allow the scientists and engineers to get a better understanding of the fundamental aspects of the wheel-rail

contact physics. The unique design that is used for the rig enables easily controlling the cant angle, angle of attack, and lateral displacement, among other critical parameters. A state-of-the-art instrumentation system provides precise measurement of the forces and moments that occur as a result of the changes. This enables accurately measuring the critical aspects of wheel-rail dynamics that has not been studied in the past (due to limitations of the past roller rigs), such as the time-varying spin creepage (perceived as an important factor in generation of squeal noise) and a broad range of combined creepage studies.

### 3.6.5 Wheel-rail Vibration Analysis

The stick-slip dynamics at the wheel-rail interface can result in excessive wheel/rail wear, noise, and vibrations that are difficult to measure in the field. This is particularly true at high AoA, high adhesion, and flanging conditions. The strategic instrumentation of the rig provides for scientific analysis of this phenomenon to unmatched accuracies, specifically as it relates to:

- Vibration analysis of wheel and rail
- Longitudinal and lateral contact stiffness

Different stick-slip conditions can be emulated for performing lateral, longitudinal, and rotational vibration analyses. The test rig has a provisional design for installing multiple accelerometers for studying wheel-roller vibrations. Modal analysis studies for finding the natural frequencies can also be conducted. The accurate load cell platform of the rig also allows for precisely measuring the lateral and longitudinal contact stiffness of the wheel.

### 3.6.6 Wheel-Rail Wear Analysis

Wear is a major source of concern to the U.S. railroads and their suppliers because of its high economic impact and also the effect it has on efficient operation of rolling stock. Better understanding of

- Rolling contact fatigue (RCF)
- Plastic flow of material under high traction, high loads

will shed light on better understanding the causes and remedies of wear at the wheel-rail interface. The unique design of the rig and the ability to precisely change the wheel-rail contact conditions enables performing design of experiments that are necessary for better understanding

wear in more realistic conditions, as compared with abstract equipment such as four- ball test machines that are often used.

The design of the rig enables accurately studying the effect of various parameters including loading, adhesion coefficient, angle of attack, flanging, etc. The results of such studies will lead to better rail safety and also allow the U.S. railroads to optimize their maintenance practices for reducing total life cycle costs. Other wear effects such as rail corrugation, wave-like wear at the top of the rail, can also be analyzed in terms of their formation mechanisms and influence of the key parameters. Mechanisms by which RCF-induced cracks initiate and grow, which are strongly related to wheel and rail wear, can also be determined through a state of the art vision system that will be installed on the rig. The vision system will also allow for studying other effects, including the plastic flow of material at the contact patch.

### **3.6.7 Derailment Mechanics**

Benefiting from the modern force, torque, acceleration, and displacement sensors, the Virginia Tech's roller rig enables investigating the dynamics of the wheel prior, during, and after derailment. Because it is possible to control the wheel-rail relative motion and constraints in real time, the rig allows studying

- Derailment coefficient
- Wheel-climb derailment

Each parameter can be changed precisely and its effect on the forces and moments that cause derailment will be studied. Such design of experiments will allow scientists and practitioners get a better understanding of some of the track and wheel conditions that can result in derailment.

### **3.6.8 Hardware-in-the-loop (HIL) Operation**

One of the features of the roller rig is the ability to perform Hardware-in-the-Loop (HiL) studies. This allows merging the rig with rail vehicle dynamic simulation models, to bring an unprecedented level of accuracy to the models. HiL allows using the rig in synchronization with rail vehicle simulation models, such that the output of the rig becomes the input to the model and, conversely, the output of the model serves as input to the rig. HIL represents the state of the art

in representing complex dynamics, such as wheel-rail interface, in high fidelity simulation models.

The immediate benefits of HiL are research and engineering development in

- Advanced train control algorithms
- Traction and braking studies

A unified communication protocol between actuators, drives, and data acquisition system eliminates data conversion between these units; hence, facilitating online high-speed measurements and control. The rig will serve as a unique platform for studying advanced train control algorithms, whereby instantaneous measurements from the rig are fed into the analytical model of the entire train to control the motion of the wheel relative to the rail in real time. The state-of-the-art measurement and control network used in the rig, makes the sense-to-act process as fast as the sensors' update rate.

## 4 Hardware Development

(This chapter was published in part in proceedings of ASME 2015 Joint Rail Conference [77]. Reproduced with permission.)

In this chapter the engineering approach to the hardware design and construction of the Virginia Tech Roller Rig is discussed. The design specifications and functionality of each major component are detailed. It begins with the design of the load frame and base frame. Following, are detailed discussions of the rig's structure and positioning systems. The chapter discusses alternative designs for each component and how the design is optimized.

### 4.1 Floor Plate

In order to have the most control over the laboratory environment, the dynamics and behavior of the testing facility must not be influenced by external noise and vibration. To this end, a very rigid basement is needed to isolate the rig from surrounding equipment in the laboratory. In addition, the basement must provide a very flat base for accommodating the rig.

#### 4.1.1 Floor Plate Design

Virginia Tech Roller Rig has a footprint of approximately 91 x 80 inch. A one-inch thick steel plate, which is sitting underneath all the components, functions as a base for the lateral linear guides that is discussed in positioning systems section. Therefore, the deflection of this plate is limited by the manufacturer's permissible error for the linear guides' mounting plate. In addition, the floor plate should function as a rigid basement for the entire rig. It should take all the loadings and preferably isolate the rig from the surroundings.

A cast iron T-slotted plate is designed to make a rigid, multipurpose basement for the rig (Figure 4-1). It is a resin-sand casted plate made of iron HT250. It is a purpose-built plate with 2200 x 2500 x 250 mm dimensions and top-surface flatness accuracy of +/- 0.03 mm manufactured by Cangzhou Kuntai Machinery & Equipment Co., Ltd, China. It weighs approximately 5000 kg. The plate is hollow with a stiffening rib structure on the underside (Figure 4-1).

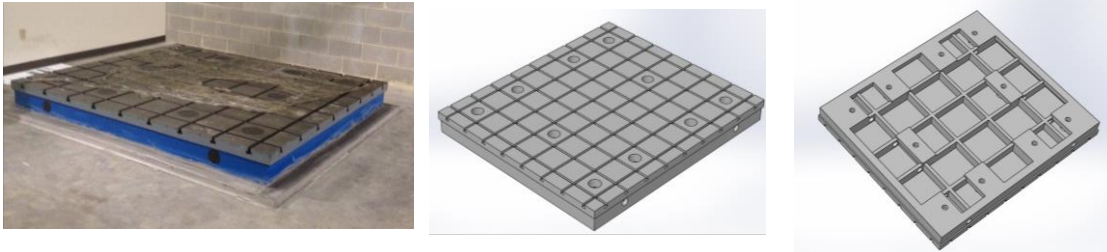


**Figure 4-1: T-slotted floor plate and its solid model showing bi-directional t-slots on top surface and reinforced ribbing structure at the bottom**

The working surface of the plate has cast-in 28H12 T-slots in both directions with 250 mm spacing. Casted T-slots enable the basement to insert or remove T nuts for mounting the specimen in different configurations. The load frame and linear guides' plate are secured to the base plate using the T-slots and the appropriate hardware shown in Figure 4-2-Left. Because of the massive weight of the plate, it ensures a very rigid basement for the rig.



**Figure 4-2: Left: 28H12 T-slots and clamping hardware including T-nuts, stud, nut, triangular lock, and clamp strap for mounting components on the floor plate. Right: Precision bubble leveler used for leveling the floor plate**

The base plate is anchored to floor via ten 1 inch anchors, one for each hole of the plate. The laboratory floor was marked for the exact location of the anchors. The 1-inch all-thread anchors were secured to the 5-inch thick concrete floor with epoxy. With the epoxy cured, the base plate was lowered down over the anchors. Using shimming method, the plate was leveled within 0.04 inch tolerance in all the directions (Figure 4-2-Right). Once the plate was leveled, jam nuts fixed

the position of the plate to the anchors. With the plate fixed in place, it was then filled with a non-shrinking grout. The grout filled the underside completely and allows the plate to distribute loads over its entire footprint on to the floor. The fully anchored plate is actually an extension of the concrete floor (Figure 4-1).

It must be noted that an alternative method of using anti-vibration wedge-mounts for mounting the rig to ground was considered. The AirLoc anti vibration mounts include a vibration absorber pad, and function as a precision leveler under heavy loads (Figure 4-3). Although the mounts could serve as a leveler to precisely level the rig, and could isolate the vibration of the entire rig through the anti vibration pads, finite element analysis showed that they failed to provide a rigid basement for the rig. Results show that the deflection of lateral linear guides' plate would be more than what the manufacturer recommends, as shown in Figure 4-4.

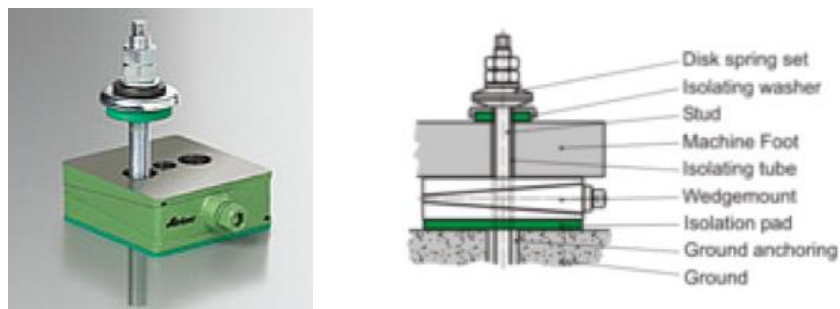


**Figure 4-3: VRC wedge-mount precision levelers manufactured by AirLoc [78]**

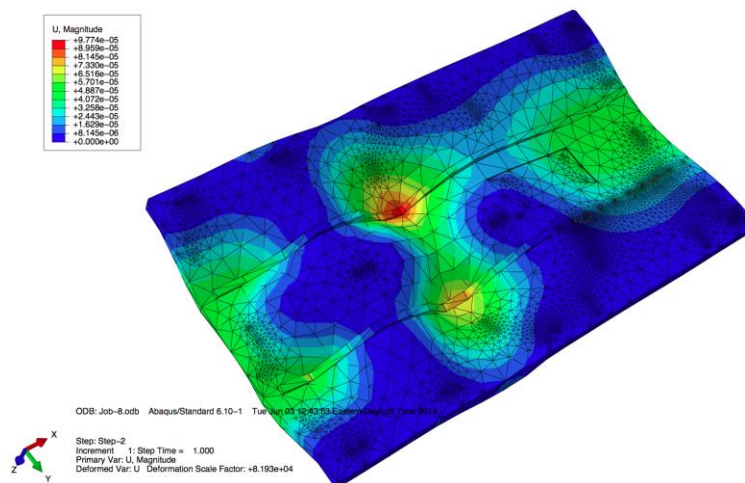


**Figure 4-4: Structural analysis of the mounting plate for evaluating the performance (static deflection of plate) of wedge-mounts using ABAQUS**

#### 4.1.2 Floor Plate Functionality

The reinforced ribbing structure of the plate makes it extremely heavy and rigid. Since grout could not fill out the entire underside of the plate due to lacking of air holes to let the air out of the gap, finite element analysis is conducted to ensure the rigidity and strength of the plate. The solid model of the plate was imported to ABAQUS software package. The loading from the weight of the rig and the contact forces was applied to the top surface of the plate. For the boundary conditions, all the mounting holes of the underside of the plate in the model were rigidly fixed in all 6 directions, as the holes are bolted down to the concrete floor using epoxy anchors. A mesh type of tetrahedron with 2,116,674 elements was used for static and modal analyses of the plate (Figure 4-5). The results show that the maximum deflection of the plate is *0.01 mm*, and the first natural frequency is *313 Hz*. The deflection is well below the manufacturer recommended value (0.12 mm). The modal analysis ensures that the plate has much higher natural modes than the test specimen, which helps to reduce error in tests. The plate is leveled within desirable accuracy to ensure that the forces being introduced into the system are well defined. Misalignment/tilting of the rig would introduce undefined forces at the contact patch; the weight of the components would not be along the vertical axis. This could decrease the accuracy of force estimation at the contact. In summary, T-slotted base plate secures the rig in place and ensures a rigid basement for the rig to reduce unwanted noise in test signals.

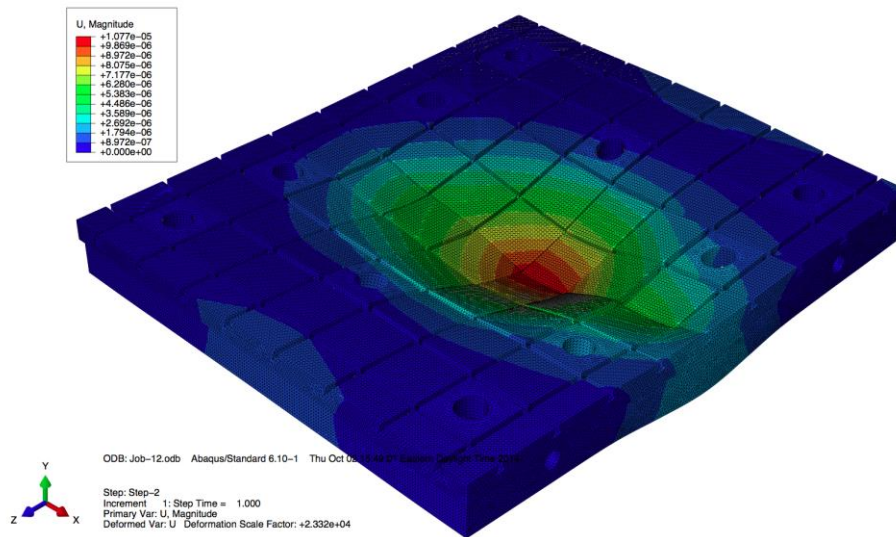


**Figure 4-5: Finite element analysis of the floor plate using ABAQUS**

## 4.2 Load Frame

In addition to the base plate, the reaction load frame needs to be extremely strong. It should be able to take all the contact force loading with minimized deflection to avoid generation of any unwanted vibration. In another words, the dynamics of the frame should not affect the dynamics of the test specimen. Together, the reaction load frame, and the base plate should provide an excellent rigid structure for conducting the contact mechanics tests with minimized external noise and vibration. Additional functionality of the frame lies in the ability to accommodate all the powertrain and positioning components. The frame should make enough room for placing two drivelines.

### 4.2.1 Frame Design

In order to meet all the required specifications for the frame, different design solutions were investigated. The advantages and disadvantages of these solutions were discussed, and the best cost effective solution was selected. The first step in the design of the rig was deciding on the frame's construction material. Extruded aluminum and low carbon steel tubing were compared. Aluminum frames assembled using bolts, nuts, and brackets can result in unwanted flexibility in the structure. The flexibility could result in unwanted vibrations and deflections, which would possibly ruin the accuracy level of measurements and control capabilities of the rig. The goal is to

reduce excitations from outside sources including rig's structure in order to have maximized precision level for sensor measurements and speed regulations. Hence, low carbon steel tubing was chosen for fabricating the load frame.

Next, different design layouts for the structure of the frame were investigated. Most importantly, triangular and rectangular shaped frames were considered. Rectangular frame would result in a larger footprint without adding considerable rigidity to the structure. Triangular frame could provide better access to the rotating bodies for maintenance and allow for easy replacement of the wheel or roller in future. Therefore, a triangular structure was chosen for the frame. Based on engineering intuition, several modifications were made to strengthen the reaction load frame: sidebars, cross bars, gusset plates. Two sidebars were designed on each side of the structure to strengthen it in side directions. By doing so, the frame was fortified against longitudinal creep force at the contact.

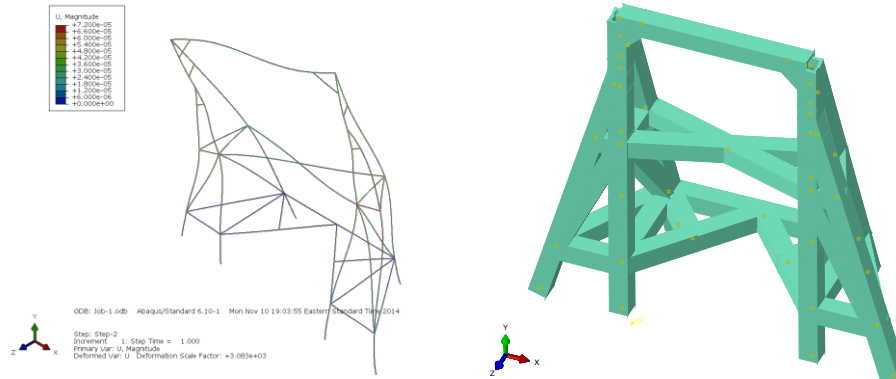
Once the frame structure is designed, different steel tubing sizes were considered. Finite element analysis, detailed below, indicated that 4 x 4 inch steel square tubing with a 3/8-inch wall thickness resulted in a better trade off between mass and rigidity. Other overall dimensions were designed based on the size of rig's drivelines and other major components. A 1-inch thick steel plate is added in front of the frame for mounting the vertical positioning system, as well as strengthening the frame. Furthermore, provisional holes were adapted on the steel tubings for filling inside the tubes with some sort of expandable foam for further attenuating any unwanted vibrations in the system (increasing the natural frequency of the frame), if needed in the future. Figure 4-6 shows the finalized design of the frame.



Figure 4-6: Solid model and fabricated reaction load frame

#### 4.2.2 Structural and Modal Analysis

In order to optimize the rigidity and strength of the load frame, finite element analysis was conducted using ABAQUS package. To this end, a finite element model of the frame was created using beam elements. A grid system using 3D deformable wires was adopted to describe the location of the structural elements (steel tubings). The model adequately represented all the main structural elements in the load frame. However, some simplifications were taken into account. The weldments in the structure were not modeled as the entire structure was modeled as a one piece. This could be justified with the proper welding of the frame that could even make a stronger connection than the steel tubing. Moreover, the front steel plate and gusset plates were not modeled in the FE model. This could underestimate the strength of the load frame, as welding the gusset plates and a solid steel plate in front would strengthen the structure. So, it merely added a safety factor to the analysis. Figure 4-7 shows the wire frame and beam element model of the frame in ABAQUS. For the boundary conditions, all six frame feet in the model were rigidly fixed in all 6 directions, since the frame feet are bolted down to the base plate, which is anchored down to floor.



**Figure 4-7: The wire frame model of reaction load frame in ABAQUS using beam elements**

After modeling the frame in ABAQUS, two types of analyses were conducted to study the design of the structure. First, static analysis was conducted to predict the deflections of the frame due to contact forces. The contact forces on the wheel are reacted at the frame through the cradle-bearing assembly. The contact forces on the roller are reacted directly at the base plate through the AoA weldment frame. The FEM analysis was just to ensure the strength of the load frame under maximum operating loading conditions. In order to minimize the deflections, as well as maximize the first natural frequency, different tubing sizes for the structure were studied. Minimizing the deflection of the frame was necessary to reduce friction created by vertical bearing rails, which mount directly to the frame. The results of the simulations for different tubing sizes are shown in Table 4-1. Maximum deflection, maximum stress, and maximum strain are compared.

In addition to static deflection analysis, modal analysis for estimating the natural frequencies of the structure was investigated with finite element ABAQUS package. Using the same beam model and boundary conditions as before, a free vibration modal analysis was performed. The results of the analysis are summarized in Table 4-1 for different tube sizing. The first vibration mode of the frame is the first side-bending mode. The longitudinal contact force could excite this mode of vibration. The second mode is the first bending mode in the direction of front and aft. The lateral contact force could excite this mode of vibration. The third vibration mode is the first torsional mode around vertical axis.

**Table 4-1: Comparison table for FEM results of the load frame**

Design (cross section)	Max. stress (Mpa)	Max. defl. (mm)	Modal freq. (Hz)	Weight (kg)
No side bar ( $4 \times 4 \times \frac{3}{8} in$ )	15.6	0.23	75, 139, 157, 181, 216	636
Half-length side bar ( $4 \times 4 \times \frac{3}{8} in$ )	19.8	0.13	89, 141, 161, 196, 222	690
Full-length side bar ( $4 \times 4 \times \frac{3}{8} in$ )	15.9	0.072	96, 135, 159, 206, 216	735
Full-length side bar ( $4 \times 4 \times \frac{1}{2} in$ )	12.8	0.057	94, 135, 157, 201, 212	980
Full-length side bar ( $4 \times 4 \times \frac{1}{4} in$ )	22.4	0.101	97, 136, 160, 212, 221	490
Full-length side bar ( $3 \times 3 \times \frac{3}{8} in$ )	29.5	0.126	85, 128, 145, 164, 178	531
Full-length side bar ( $5 \times 5 \times \frac{3}{8} in$ )	45.5	0.126	106, 140, 170, 249, 250	938

In order to optimize the structure in terms of rigidity, overall mass, and first natural frequency, the finite element results presented in Table 4-1 were compared together. The comparison showed that 4 x 4 inch steel square tubing with a 3/8 in wall thickness would result in the best compromise between maximizing the stiffness (minimizing the deflection) and minimizing the mass (maximizing the first natural frequency).

The result for 4 x 4 inch steel square tubing with a 3/8 in wall thickness shows that the first natural frequency is 95 Hz. This is comparable to the first natural frequency of another load frame similar to our roller rig's frame [79]. The resonant frequencies of the frame could be well above all the resonances of interest for studying vehicle dynamics and contact mechanics. However, squeal noise frequency, which commonly happens in railway vehicles specially while negotiating a curve, could be in the same range. In addition, the results indicated that the deflection of the frame is less than 0.07 mm due to extreme loading condition, which is significantly below the allowable misalignment of 375µm/500mm (rail length) for vertical linear bearings, specified by

the bearing manufacturer (THK). This could ensure proper bearing operation under different loading conditions.

### 4.2.3 Functionality

A triangular reaction load frame, made of low carbon steel tubing, is designed to serve as a rigid structure for the rig. The frame is optimized to accommodate all the drivetrains' components, as well as to be rigid enough for minimizing unwanted vibrations. The FEM results indicated that the frame is very rigid compared with the rest of the components. This guarantees that sensor noise from excitation of the load frame would be minimal. To make the frame fully functional, small steel pads (1 in thickness) were welded to the bottom of each foot. These pads are used to clamp the fixture to the base plate and floor plate.

A steel plate was welded in front of the frame to serve as a suitable platform for mounting the vertical linear guides. After the frame was fully welded, the entire load frame was machined as a unit. The feet were all milled to within 0.005 inch flatness of one another. The level of machining precision, as well as the rigid floor plate ensure that the rig is very stable and does not flex, as it is anchored down to the concrete floor. Next, the front 1 inch plate was milled to within 0.001 in flatness (the allowable misalignment of the bearing rails per the manufacturer). Also, the front face was milled to within 0.005 in perpendicularity of the bottom feet.

## 4.3 Positioning Systems

Virginia Tech Roller Rig is equipped with various positioning systems to actively control the relative angular and linear displacements between the two rotating wheels. These relative displacements are angle of attack (AoA), cant angle, lateral shift, and vertical displacement. The setup allows for real-time positioning of these relative displacements to closely replicate boundary conditions of actual railway vehicles. For each one of the degrees of freedom, multiple design solutions were considered. The advantage and disadvantages were compared, and the best cost-effective solution was selected.

### 4.3.1 Angle of Attack (AoA) Positioning System

The angular attitude of the wheel relative to the rail (or to the roller in a roller rig) is commonly known as angle of attack (Figure 4-8). The angle of attack of the rolling stock wheels and rails/rollers is one of the main indices of the interaction between the rolling stock and railroad. It has a primary and determining role related to lateral creepage and spin creepage. As a result, it is a key parameter for contact mechanics, wear, and safety against derailing studies.

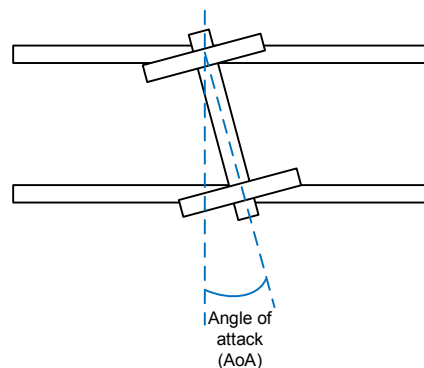


**Figure 4-8: The angular position of the wheel relative to the rail known as angle of attack (AoA)**

The roller rig is equipped with a AoA positioning system capable of actuating in real-time. A suitable cost-effective mechanism was designed such that it can meet all the requirements in terms of accuracy and rigidity.

#### 4.3.1.1 Component Design and Functionality

In order to configure the AoA positioning system, different design options were investigated. Various mechanisms such as two sliding plates with a circular guidance groove, a sliding post in which components pivot around the post, and off-the-shelf turntables (slewing ring or cross roller ring) were thoroughly discussed. Rigidity, ease of implementation, rotation around the contact patch center, cost, and required actuation force were among design criteria. Considering a vast number of vendors and manufacturers, as well as consulting the application engineers, a cross roller ring offered by THK was selected. It is capable of highly accurate rotational motion, as well as taking all the required loading in the system. As depicted in Figure 4-9, cross roller ring consists of inner and outer rings, which are in rolling contact via cylindrical roller that are arranged perpendicular to the adjacent roller. As a result, the cross roller ring can take loads in all

directions including radial, axial, and moment loads. The spacer retainer keeps the roller in place and prevents them from skewing. It allows a bigger contact area between rollers and the rings, thus significantly increase the load capacity. In addition, since inner and outer rings are designed to be separable, a preload can be applied to the bearing for adjusting the clearance [80].

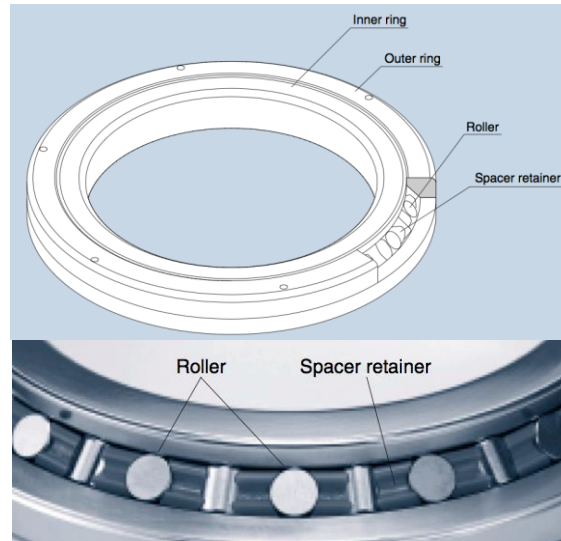


**Figure 4-9: Schematic drawing of the cross roller ring manufactured by THK [80]**

Figure 4-10 shows a schematic view of the cross roller ring implemented in the roller rig. The cross roller ring is bolted down to the upper and lower plates via two circular hole-patterns. The upper plate, which is bolted to inner ring, is welded to the roller bearing posts. The bottom plate functions as an intermediate mounting plate between the cross roller ring (AoA positioning system) and linear guides (lateral positioning system). This mechanism provides the AoA degree of freedom for the roller relative to the wheel. The design is such that the pivot point (center of rotation) is set exactly underneath the contact patch. This provides two advantages: i. When the roller rotates around the vertical axis (AoA changes), other displacements (lateral, cant) are kept fixed. ii. The rotation requires minimum moment around the vertical axis, since the moment arm is kept minimal. Finally, the rotational motion of the cross roller ring is controlled via a linear actuator, which is discussed in the linear actuator section (Section 5.3).

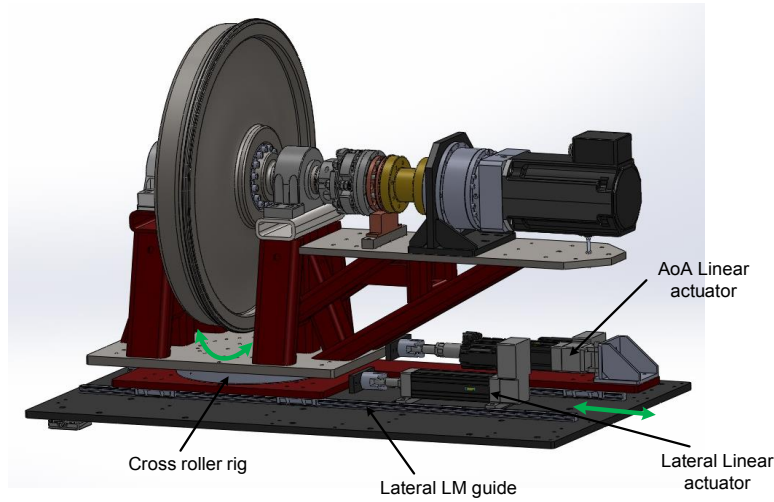


**Figure 4-10: Solid model of the AoA and lateral positioning systems, and their actuation mechanisms. Green arrows indicate the lateral and AoA degrees of freedom**

#### 4.3.1.2 Component Sizing

In addition to accuracy requirement, the positioning system should be capable of taking all the required loadings in the system. Maximum forces and torques that react at each positioning system are calculated based on the contact forces (Section 3.4). Table 4-2 shows the maximum creep forces at the contact.

**Table 4-2: Maximum estimated creep forces at the contact patch**

Unit	Longitudinal ( $F_x$ )	Lateral ( $F_y$ )	Vertical ( $F_z$ )
Newton (N)	+/- 4265	+/- 4265	-10664

The contact forces are reacted at the positioning systems. Figure 4-11 shows how the contact creep forces are reacted at the positioning systems.

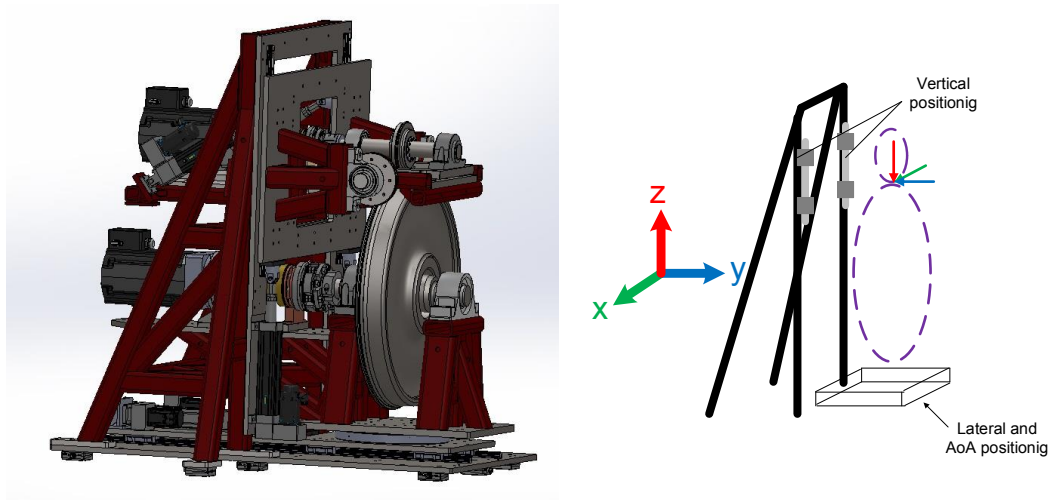


**Figure 4-11: Left: Solid model of the rig. Right: Schematic drawing of the rig that shows how the contact forces are reacted at the lateral positioning system, AoA positioning system, and vertical positioning system**

Beside the contact forces, AoA positioning system needs to take the gravitational forces and moments applied by the weight of components. Taking all into consideration, Figure 4-12 presents the free body diagram of the AoA positioning system, and Table 4-3 shows all the required dimensions and weights.

The cross roller ring was selected and sized with assistance from THK America corporation engineers and product documentation [80]. Following assumptions are made to calculate the safety factor:

- Perfect system rigidity including the mounting surface for the inner and outer ring
- No contamination
- Adequate lubrication
- No induced loads due to misalignment
- The acceleration due to gravity  $g = 9.81 \text{ m/s}^2$

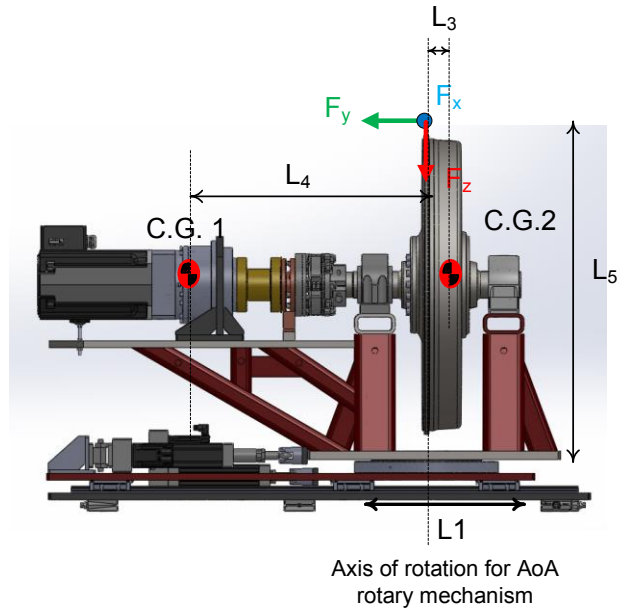


Figure 4-12: Free body diagram of AoA and lateral positioning systems

Table 4-3: Required specifications for the AoA positioning system

Parameter	Magnitude
L <sub>1</sub> (in)	21.5
L <sub>2</sub> (in)	16.5
L <sub>3</sub> (in)	1
L <sub>4</sub> (in)	25
L <sub>5</sub> (in)	50
W <sub>C.G.1</sub> (lb)	1500
W <sub>C.G.2</sub> (lb)	2000

Following the standard sizing practice recommended by THK, the safety factor of the cross roller ring is calculated. The equivalent loading ( $Q_0$ ) is calculated as follows:

$$Q_0 = X_0 \cdot \left( F_{radl} + \frac{2M}{dp} \right) + Y_0 \cdot F_{axl} \quad (4-1)$$

Where  $F_{radl}$ ,  $F_{axl}$ , and  $M$  are radial force, axial force, and moments applied to the cross roller ring, respectively. For the maximum loading capabilities, the biggest available cross roller ring (RU445) is selected. For RU445,  $X_0$ ,  $Y_0$ ,  $C_0$ , and  $dp$  are 1.0, 0.44, 447 kN, and 445.4 mm, respectively. According to Figure 4-12, Table 4-2, and Table 4-3, we have:

$$F_{radl} = F_x + F_y = 4963 + 4456 = 9419N$$

$$F_{axl} = F_z + W_{C.G.1} + W_{C.G.2} = 12103 + 4448 + 8896 = 25447 N \quad (4-2)$$

$$M = (W_{C.G.1} \cdot L_2 - W_{C.G.2} \cdot L_1) + (F_x \cdot L_3) + (F_y \cdot L_3) = 14334.7 Nm$$

Therefore, the safety factor ( $f_s$ ) for the cross roller ring is:

$$Q_0 = 1 * \left( 9419 + \frac{2 * 14334.7}{.4455} \right) + 0.44 * 25447 = 84983 N \quad (4-3)$$

$$f_s = \frac{C_0}{Q_0} = 5.56$$

The cross roller ring (RU445G) has an outer ring with 540 mm outer diameter (OD) and 445.5 mm inner diameter (ID), and an inner ring with 445.5 mm OD and 350 mm ID. For the rotational accuracy grade of P4, selected for the roller rig, the axial and radial run-out tolerances are 12  $\mu$ m for the inner ring, and 16  $\mu$ m for the outer ring. This could minimize the rattle space between the rings, hence could minimize the parasitic vibrations during tests. In order to increase the rigidity, preload class of CC0 is selected. The preload class adds between 25 to 50 N.m torque to the running torque of the cross roller ring, according to the manual. The running torque of the designed cross roller ring will be the summation of preload torque, frictional torque, and moment torque. The frictional torque is the multiplication of the rolling friction coefficient ( $\sim 0.01$ ), radial and axial loadings on the bearing ( $\sim 20$  kN), and the effective radius ( $\sim 0.2227$ m), which will be around 44 N.m, and the moment torque is the torque due moment (M) created due to off-center loading. According to manual, the moment torque is calculated as  $1.15 * M * \mu$ , where  $\mu$  is the friction of coefficients of the ball guides ( $\sim 0.003$ ). As a result, the total running moment for the designed cross roller ring is around 100 Nm. This information is used for multibody modeling of the rig in SIMPACK (Chapter 8).

The cross roller ring is designed such that the static and dynamic friction coefficient does not differ considerably. As a result, closed loop force controlling of these bearings becomes a much easier task.

### 4.3.2 Lateral Positioning System

The linear position of the wheel relative to the rail/roller is called lateral displacement (Figure 4-13). Wheelset displacement is the main manifestation of wheel/rail dynamic interaction when a train is running on railway track. Lateral displacement is of great importance in railway vehicles dynamics, since when the wheelset is displaced to one side, the diameters of the regions of contact and hence the (linear) velocities of the wheels, are different (due to the conical design of wheel profile).

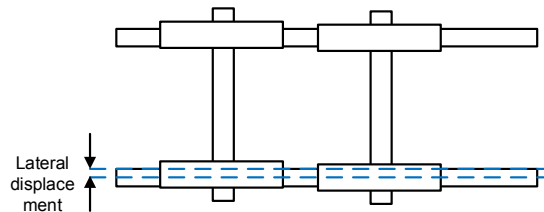


**Figure 4-13: The linear position of the wheel relative to the rail known as lateral displacement**

The setup is equipped with a lateral positioning system capable of actuating in real-time. To this end, a suitable cost-effective mechanism was designed such that it can meet all the requirements in terms of accuracy and rigidity.

#### 4.3.2.1 Component Design and Functionality

Similar to the AoA positioning system, different design options for lateral positioning system were investigated. Different mechanisms were considered, such as two sliding plates, off-the-shelf linear bearings, and a tapered bushing, which goes in between the roller and axle, and allows for lateral shift of roller against the axle. Rigidity, ease of implementation, cost, active control possibility, and required actuation force were among design criteria. Contacting a vast number of vendors and manufacturers, a caged ball linear motion guide offered by THK was selected. It is suitable for highly accurate linear motion, as well as taking all the required loading in the system.

As depicted in Figure 4-14, caged ball linear motion (LM) guide model SHS consists of LM blocks and LM rails that has a recirculating ball bearing design. Balls roll in four rows of raceways precision-ground on an LM block and an LM rail. The LM block incorporates ball cages and endplates that allow the ball to recirculate. Ball rows are placed at a contact angle of 45 degree. As a result, the LM block can take equal load for both lateral and radial directions. Moreover, a preload can be applied to the LM guide for increasing the rigidity in all directions, while maintaining a constant low friction coefficient [80].

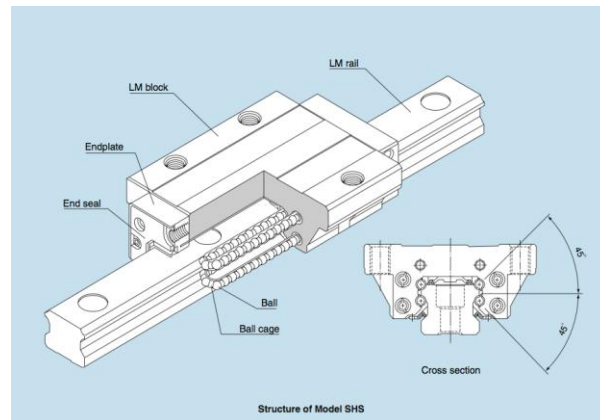


Figure 4-14: Schematic drawing of the caged ball LM guides [80]

Figure 4-10 shows a schematic view of the lateral LM guides implemented in the roller rig. The LM blocks are bolted down to the intermediate plate, which is bolted to the cross roller ring from the top side. The LM rails are bolted down to 1-inch thick bottom plate, which is mounted to the t-slotted base plate. This configuration provides the lateral degree of freedom for the roller relative to the wheel. Similar to other degrees of freedom, the lateral motion of the LM guide is controlled via a linear actuator that is discussed in linear actuator section (Section 5.3).

#### 4.3.2.2 Component Sizing

In order to select the proper sizing of linear guides, the standard sizing practice recommended by THK was followed. The reaction loadings of the lateral positioning system are similar to AoA positioning system (Figure 4-12, and Table 4-3) except the weight of the cross roller ring should be added. Factor of safety for lateral linear guides is calculated similar to cross roller ring, and calculation shows that the factor of safety for the lateral LM guide is 5.55.

The lateral LM guide has two rails: one with lengths of 1160 mm that carries two LM blocks, and the other one with length of 1960 mm that carries three LM blocks. Two rails operate parallel to each other and provide a smooth linear motion between the roller and wheel. For the accuracy grade of SP (super precision grade), running parallelism value for LM rail of length 1160 mm is  $5\ \mu\text{m}$ , and for length of 1960 is  $5.5\ \mu\text{m}$ . This could minimize the rattle space between the rail and block, hence would minimize the parasitic vibrations during tests. A preload grade of C0 is selected for lateral LM guides. The dynamic friction force due to preload is 33.3-39.1 N per block. This is used in multibody dynamic modeling of the rig (Chapter 8).

Similar to cross roller ring, the LM guides are designed such that the static and dynamic friction coefficient does not differ considerably. As a result, closed loop force controlling of these bearings becomes a much easier task.

#### 4.3.3 Cant Angle Positioning System

Cant angle of a railway track is the difference in elevation (height) between the two rails. This results in an inclination of moving wheelset from vertical line with respect to the rail (Figure 4-15). Cant angle (also known as superelevation) has a considerable effect on the dynamic behavior of railway vehicles in negotiation of a curved track. In addition, the vertical inclination of the wheel relative to the roller distorts the contact patch and produces spin creepage. Therefore, In order to test real-life conditions for the contact, the rig needed to be equipped with the cant angle degree of freedom.

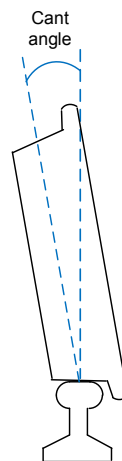


**Figure 4-15: The vertical inclination of the wheelset relative to the rail is known as cant angle**

#### 4.3.3.1 *Component Design and Functionality*

One of the most challenging parts of the design was configuring the cant angle rotation mechanism. The fact that the rotation needed to be around the contact point, as well as needed to be implemented in real-time made it a very challenging task. After considering many different design solutions, a very rigid and quite simple mechanism is configured. This mechanism consists of a cradle that embraces the wheel (Figure 4-16). The cradle is attached to two separate shafts that are inline with the wheel-roller interface patch. Two bearings hold the two aligned shafts. Therefore, the configuration of shafts and cradle can easily rotate around the centerline of the shafts, which is inline with the contact patch. This provides the cant angle degree of freedom for the wheel relative to the roller. Since the pivot point (center of rotation) is closest to the contact patch, this provides two advantages: i. When the wheel rotates around the cant angle axis solely the cant angle changes, and the other displacements (lateral, AoA) are kept fixed. ii. The cant rotation requires minimum moment, since the moment arm is kept minimal.

All the wheel driveline components (servomotor, gearhead, coupling, torque-sensor), as well as force dynamometers mount on the cradle. In order to obtain enough rigidity and strength, 3 x 3 inch steel square tubing with a 3/8 inch wall thickness were used. Two linear actuators are used to actively control the motion of cant positioning system. The actuators mount to the rear side of the cradle from one side and on the other side, they mount to the back plate of vertical positioning system (Figure 4-16).

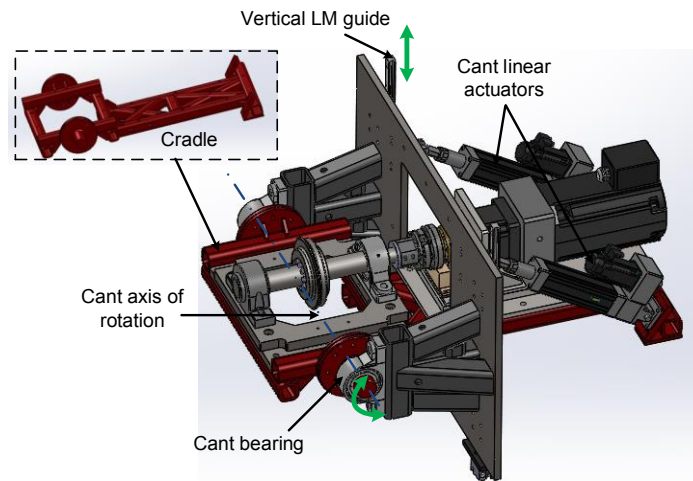


Figure 4-16: Schematic drawing of the designed cradle and rotating mechanism for providing the cant angle motion. Green arrows indicate the vertical and cant degrees of freedom

#### 4.3.3.2 FEM analysis

Similar to FE model for the load frame, a finite element model of the cradle was created using beam elements. Figure 4-17 shows the wire frame and beam element model of the cradle in ABAQUS. For the boundary conditions, the linear actuators' mounting surfaces were rigidly fixed in all 6 directions, and the aligned shafts were fixed in all 5 directions, except for the cant rotation.

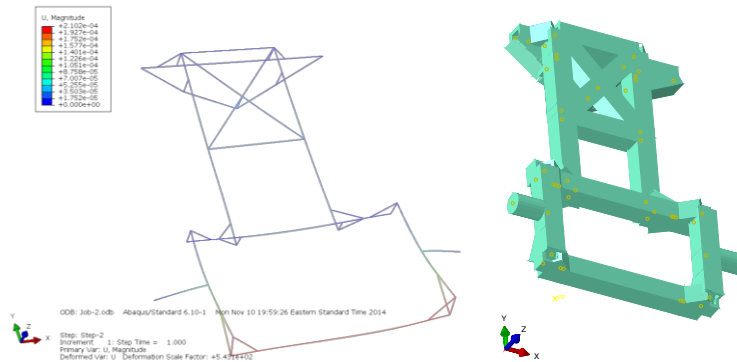


Figure 4-17: The wire frame model of the cradle in ABAQUS using beam elements

After modeling the frame in ABAQUS, two types of analyses were conducted to study the design of the structure. First, static analysis was conducted to predict the deflections of the frame due to

contact forces and driveline loadings. The contact forces on the wheel are reacted at the cradle. In addition to static deflection analysis, modal analysis for estimating the natural frequencies of the structure was investigated. The results show that for the extreme loading conditions the maximum deflection of the cradle is less than 0.2 mm, and the first natural frequency is 127 Hz. It must be noted that the FE model of the cradle does not include the dynamometers' base plate that is bolted down to the cradle. The FEM analysis could underestimate the strength of the cradle, as the thick steel dynamometer plates would strengthen the structure.

#### 4.3.4 Vertical Positioning System

In addition to AoA, cant angle, and lateral displacement degrees of freedom, the rig is equipped with a vertical degree of freedom between the wheel and roller (Figure 4-18). This would provide the ability to control the normal force (contact normal pressure) between two rotating bodies. Moreover, because of conical shape of the wheel profile, the vertical and lateral motion of the wheel are coupled. In another words, as the wheel shifts laterally with respect to the roller, it shifts vertically as well. Therefore, the vertical positioning system needed to accommodate the lateral shift.

In order to set up the rig with this degree of freedom, a proper sizing LM guides from THK is designed. Similar to lateral LM guides, SHS35 is selected for vertical positioning system. Following the THK recommended sizing practice; the safety factor for the LM guide is calculated as 8.55. Two linear actuators are employed to simulate the required normal loading at the contact based on the INRET scaling strategy.

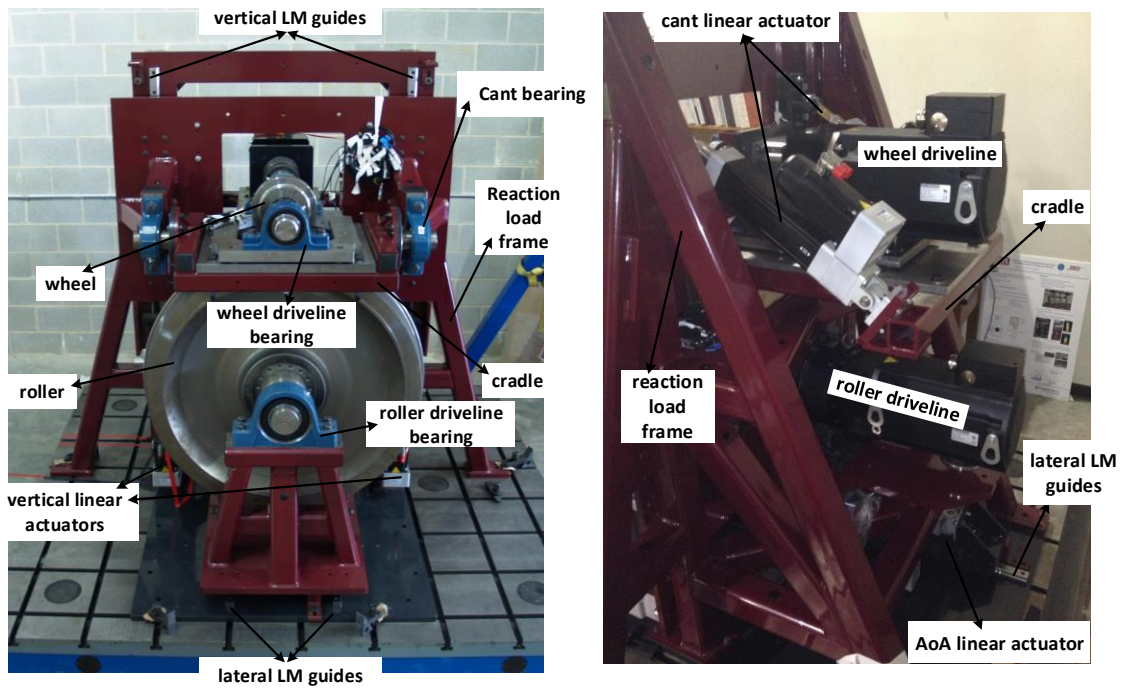


Figure 4-18: Front (left) and rear (right) views of the rig showing hardware development and assembly

## 5 Powertrain

(This chapter was published in part in proceedings of ASME 2015 Joint Rail Conference [77]. Reproduced with permission.)

Virginia Tech Roller Rig is equipped with a unique actuation system capable of actively control all the degrees of freedom. A highly compatible, and exclusive electro-mechanical system is configured for powering the rotational motion of the wheel and roller, as well as the motion of all the positioning systems. Since the rig is primarily intended to study the contact mechanics, accuracy of creepage regulation (accuracy in controlling the differential speed at the wheel-roller interface) is one of the most important key factors towards successful operation and achieving the goals of the rig. To this end, two drivelines, one powering the wheel and the other one powering the roller, are configured to precisely regulate the rotational speed of the rotating bodies; hence control the creepage with a high level of precision. In addition, linear actuators are designed to control the relative displacements between the wheel and roller. In this section, the design concepts used for powering the drivelines are thoroughly discussed. The required specifications in terms of accuracy and operating range are presented. Finally, the best cost-effective solutions are selected.

### 5.1 Main Driveline

#### 5.1.1 Design Considerations

Two different design concepts for providing and controlling slip at the contact between the wheel and roller are studied: i. independent drives, ii. differential driveline. Kinematic and dynamic analyses are conducted for each design concept. Moreover, the required power and speed regulation accuracy for the driving motors in each configuration are compared with each other. Finally, based on the analysis, the best cost-effective design is proposed.

### 5.1.1.1 Independent Drives

#### 5.1.1.1.1 Concept

To produce slip at the contact, one wheel should be driven by an external power source like an electric motor and the other wheel should brake. In another words, energy flows into one of the wheels and is dissipated at the other wheel. In the independent drive configuration, one motor drives the roller, while a braking system resists the rotation of the wheel to produce slip at the interface (in braking mode). In traction mode, however, the motor drives the wheel while the braking system operates on the roller. Therefore, to simulate both braking and traction modes, either two motors (Figure 5-1-A) or a motor, a braking mechanism and a switching system are needed (Figure 5-1-B). For the former configuration, at any given time, one motor functions as an electric motor while the other one functions as a generator. For the latter configuration, in the braking mode, the motor should be connected to the roller and the braking system should be connected to the wheel. Using the switching mechanism, the motor can be switched to the wheel and the braking to the roller to simulate the traction mode.

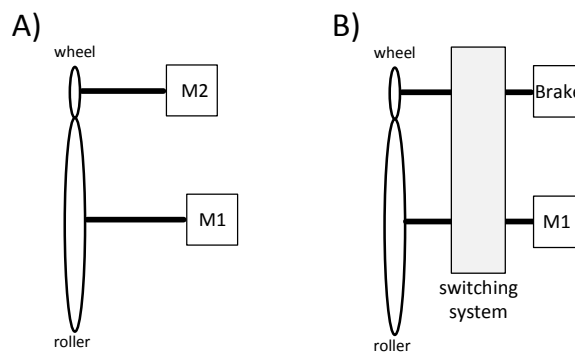


**Figure 5-1: Different configurations for the independent driveline**

#### 5.1.1.1.2 kinematics and dynamics analysis

This section develops kinematical and dynamical relations for the independent drives system in which two separate motors are connected to each shaft (Figure 5-1-A). Similarly, the same procedure should be repeated to analyze the independent drive system, which includes motor, brake and switching mechanism (Figure 5-1-B). Calculations based on free-body diagram obtain power and torque requirements for the system. Following, creepage analysis is presented.

To analyze the governing dynamics of the system, free-body diagram for each shaft is developed in the braking mode and accordingly Newton’s second law is applied:

$$\begin{cases} T_{M1} = R_r F_{creep,2/1} \\ T_{M2} = -R_w F_{creep,1/2} \end{cases} \quad (5-1)$$

Where  $T_{M1}$  and  $T_{M2}$  are roller and wheel torques, respectively.  $R_r$  and  $R_w$  are the roller and wheel radii,  $F_{creep,2/1}$  and  $F_{creep,1/2}$  are the creep forces acting on the roller and wheel, respectively. It must be noted, the system is analyzed as it is operating in the steady state motion (all the velocities are constant).

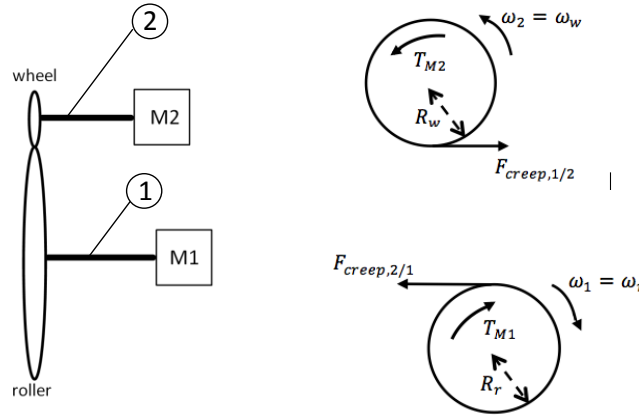


**Figure 5-2: Left: Wheel and roller shafts in the independent drives configuration. Top-right: Free body diagram of the wheel. Bottom-right: Free body diagram of the roller.**

Similarly, for the traction mode, we will have:

$$\begin{cases} T_{M1} = -R_r F_{creep,2/1} \\ T_{M2} = R_w F_{creep,1/2} \end{cases} \quad (5-2)$$

Hence, for the power of motor  $M1$  and  $M2$ , we will have:

$$\begin{cases} P_{M1} = T_{M1} \omega_r \\ P_{M2} = T_{M2} \omega_w \end{cases} \quad (5-3)$$

Where  $\omega_R$  and  $\omega_w$  are angular velocities of the roller and wheel, respectively. So, the difference between power for motor  $M1$  and  $M2$  is the power dissipated at the contact due to friction as heat:

$$P_{hl} = -|P_{M1} - P_{M2}| = -|T_{M1}\omega_r - T_{M2}\omega_w| \quad (5-4)$$

Sign convention: In this report, negative sign for power means the element is dissipating energy from the system (like a generator), and positive power sign means the element is injecting energy to the system (like an electric motor).

In order to have creep forces at the contact, there must be a small apparent slip between the wheel and the rail at their interface. If this slip is normalized against wheel and rail's absolute velocities, it is called creepage. Based on the definition, the creepage in terms of absolute circumferential velocities of the wheel and rail/roller at the point of contact is calculated, as follows:

$$creepage = \frac{V_w - V_R}{(V_w + V_R)/2} = \frac{R_w\omega_w - R_r\omega_r}{(R_w\omega_w + R_r\omega_r)/2} \quad (5-5)$$

In order to produce creepage, the roller speed considered constant and the wheel speed varies according to the percentage of creepage. For example, -10% creepage (braking mode) results in the following wheel speed (based on the desired specifications of the rig listed in Section 3.4):

$$\begin{aligned} creepage &= \frac{R_w\omega_w - R_r\omega_r}{(R_w\omega_w + R_r\omega_r)/2} \Rightarrow -0.1 = \frac{5\omega_w - 22.5 * 73.5}{(5\omega_w + 22.5 * 73.5)/2} \Rightarrow \omega_w \\ &= 299 \text{ RPM} \end{aligned} \quad (5-6)$$

Hence, for the power, we will have:

$$\begin{cases} P_{M1} = T_{M1}\omega_R = 4265 * 22.5 * 0.0254 * 7.7 = 18768 \text{ Watt} = 25.2 \text{ hp} \\ P_{M2} = T_{M2}\omega_w = -4265 * 5 * 0.0254 * 31.4 = 17016 \text{ Watt} = -22.8 \text{ hp} \\ P_{hl} = -|P_{M1} - P_{M2}| = -2.4 \text{ hp} \end{cases} \quad (5-7)$$

Similarly, for the +10% creepage (traction mode), the angular velocity of the wheel is 365 RPM, and for the power, we will obtain:

$$\begin{cases} P_{M1} = T_{M1}\omega_R = 4265 * 22.5 * 0.0254 * 7.7 = 18768 \text{ Watt} = 25.2 \text{ hp} \\ P_{M2} = T_{M2}\omega_w = -4265 * 5 * 0.0254 * 38.3 = 20725 \text{ Watt} = -27.8 \text{ hp} \\ P_{hl} = -|P_{M1} - P_{M2}| = -2.6 \text{ hp} \end{cases} \quad (5-8)$$

In order to calculate creepage resolution, variation analysis is conducted:

$$\begin{aligned} Creep &= \frac{R_w\omega_w - R_r\omega_r}{(R_w\omega_w + R_r\omega_r)/2} \approx \frac{\frac{R_w}{R_r}\omega_w - \omega_r}{\omega_r} \Rightarrow \partial creep \\ &= \frac{(\partial\omega_w * \frac{R_w}{R_r} - \partial\omega_r) * \omega_r - \partial\omega_r * (\frac{R_w}{R_r}\omega_w - \omega_r)}{\omega_r^2} \\ &\approx (|\partial\omega_r * \frac{R_w}{R_r}| + |\partial\omega_r|)/\omega_r \end{aligned} \quad (5-9)$$

This means, for example, a creepage resolution of 0.01% requires speed resolution of 0.006 RPM for both M1 and M2.

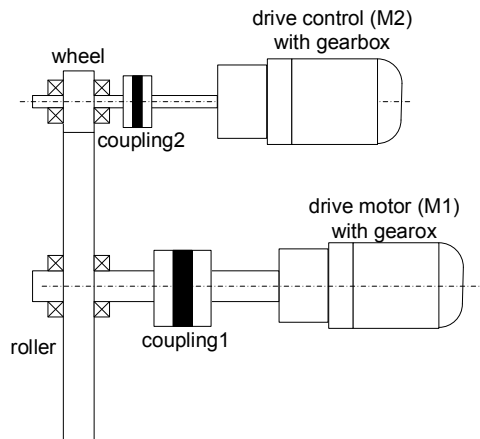


Figure 5-3: Schematic drawing of the independent drives configuration

### 5.1.1.2 Differential Driveline

The differential driveline works based on the fact that the friction force at the contact between the roller and wheel resists the motion of one of the wheels, however, helps to drive the other wheel. So, a differential gearbox can be designed such that the driven energy of the driven wheel transfers back into the driveline mechanically.

#### 5.1.1.2.1 Concept

In addition to the independent drives, an alternative driveline, which works based on a differential gearbox was considered. In this powertrain, the desired slip between wheel and roller is controlled using a differential gearbox. Friction force at the contact between the roller and wheel resists the motion of the roller, however, helps to drive the wheel, in the braking mode. Similarly, the contact friction force resists the rotation of the wheel; however, helps to rotate the roller, in the traction mode. Therefore, a differential gearbox can be designed such that the driven energy of the driven wheel transfers back into the driveline mechanically, as shown in Figure 5-4.

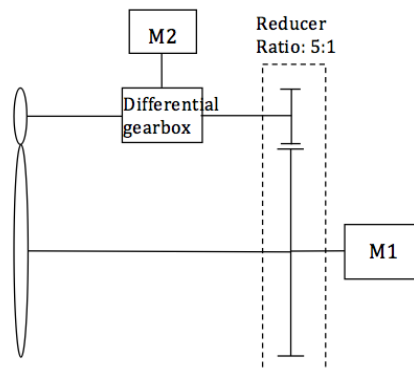


**Figure 5-4: Schematic drawing of the differential driveline configuration in which a differential gearbox is employed for producing creepage at the contact**

In the differential configuration, two electric motors are employed: creep control motor ( $M2$ ) and drive motor ( $M1$ ). An input gearbox (reducer) is designed such that its gear ratio is exactly equal to the ratio of the roller diameter to the wheel diameter ( $5:1$ ). The gear ratio of  $5:1$  is chosen to explain the concept of differential driveline. Later, it is explained how the gear ratio can affect the

required power. Based on the speed of motor  $M2$ , the differential gearbox can function as a reducer or a multiplier or a neutral gearbox (ratio 1:1):

#### 5.1.1.2.1.1 Zero Creepage Mode

This mode simulates zero creepage condition at the contact between the wheel and roller (Figure 5-5-Left). To this end, speed of  $M2$  is set such that the output speed of the differential gearbox is equal to input speed (differential gearbox function as a gearbox with ratio 1:1). Since the ratio of input reducer is the same as the ratio of the wheel to roller diameter, this configuration results in zero creepage (no slip between the roller and wheel). We will have:

$$\left\{ \begin{array}{l} \text{direct drive} \Rightarrow \omega_r = \omega'_r \\ \text{differential gear ratio } 1:1 \Rightarrow \omega_w = \omega'_w \Rightarrow \omega_r = 5 \times \omega_w \text{ (no slip)} \\ \text{reducer ratio } 5:1 \Rightarrow \omega'_r = 5 \times \omega'_w \end{array} \right. \quad (5-10)$$

#### 5.1.1.2.1.2 Braking Mode

This mode simulates the braking condition at the contact between the wheel and roller (Figure 5-5-Middle). To this end, speed of  $M2$  is set such that output speed of the differential gearbox is greater than input speed (differential gearbox function as a multiplier with ratio 1:q,  $q>0$ ). Since the ratio of input reducer is the same as the ratio of the wheel to roller diameter, this configuration results in a bigger tangential speed for the roller than the wheel, hence simulating braking forces (negative creepage). We will have:

$$\omega_r = 5 \times q \times \omega_w > 5 \times \omega_w \text{ (negative creepage)} \quad (5-11)$$

#### 5.1.1.2.1.3 Traction Mode

This mode simulates the traction condition at the contact between wheel and roller (Figure 5-5-Right). To this end, speed of  $M2$  is set such that output speed of the differential gearbox is less than input speed (differential gearbox function as a reducer with ratio  $q:1$ ,  $q>0$ ). Since the ratio of input reducer is the same as the ratio of the wheel to roller diameter, this configuration results in a bigger tangential speed for the wheel than the roller, hence simulating traction forces (positive creepage). We will have:

$$\omega_r = \left(\frac{5}{q}\right) \times \omega_w < 5 \times \omega_w \text{ (positive creepage)} \quad (5-12)$$

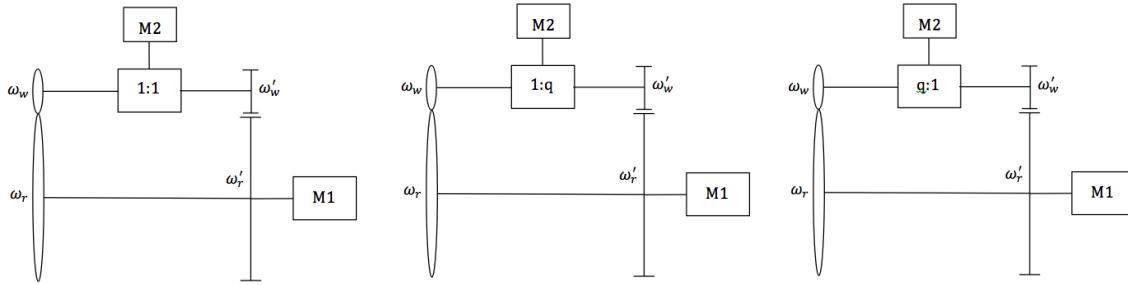


**Figure 5-5: Schematic of different differential drive functionality: Left: zero creepage mode. Middle: braking mode. Right: traction mode.**

In the traction mode, the power of the rotating wheel is bigger than the rotating roller, since wheel speed is more than roller speed while the friction force interacting at the contact patch is equal for both the wheel and roller (based on Newton's third law). Therefore, in the contact patch, energy flows from the wheel to the roller, which means the roller is the driven body and the wheel is the driver body, as shown in Figure 5-6-A. In other words, the driving energy of the wheel partially goes to the driven body (roller) and the remaining dissipates at the contact patch as heat (proportional to linear speed difference at the contact).

In the braking mode, however, the power of the rotating roller is bigger than the rotating wheel since roller speed is more than the wheel speed while the friction force interacting at contact patch is equal for both wheel and roller (based on Newton's third law). Therefore, in contact patch, energy flows from roller to wheel meaning roller is driver body and wheel is driven body, as shown in Figure 5-6-B. So, the driving energy of the roller partially goes to the driven body (wheel) and the remaining dissipates at the contact patch as heat (proportional to differential linear speed at the contact).

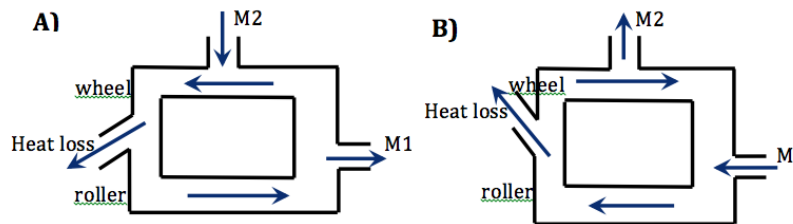
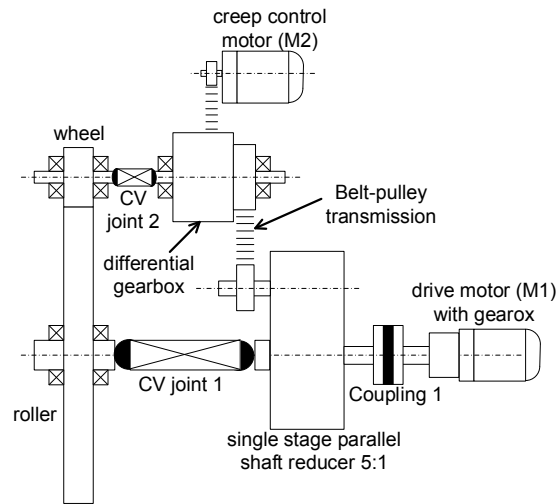


Figure 5-6: Schematic drawing of energy flow chart for differential driveline: A) traction mode, B) braking mode

5.1.1.2.2 Power Analysis and Creepage Calculations

For the sake of brevity of power-train section, the detailed kinematics and dynamic analysis of the differential driveline for calculation of power and creepage is presented in appendix A. The results show that the required motor powers for the differential driveline greatly depends on the reducer gear ratio and planetary differential gear sizes. For the desired speed and loading specifications of the roller rig, the required power of the two motors for producing +/- 10 percent creepage could be as low as 0.5 and 3.33 hp. Moreover, The variational analysis shows that the speed resolution of 0.5 RPM for both the motors results in 0.009 % creepage resolution.

Using a differential gearbox to drive the system could allow running the system in both braking and traction modes. This type of driveline could save a lot of power for driving the system compared with the independent driveline in case a proper gear ratio for the designed reducer is chosen. In addition to power consumption savings, this differential driveline could provide the advantage of requiring just one precisely controllable motor to be able to control creepage (adjust differential speed), precisely. So, the creepage at the contact can be controlled in a much higher level of precision using the differential driveline compared with the independent drives.



**Figure 5-7: Proposed configuration for implementing the differential driveline**

### 5.1.2 Selected Configuration and Functionality

In order to design the proper powering system, both the driveline concepts (differential and independent) were thoroughly discussed. The advantages and disadvantageous of both the driveliens were fully discussed with application engineers from multiple differential gearbox manufacturers, as well as multiple electrical motor manufacturers. In addition to power and creepage requirements, feasibility of implementation of the concepts, ease of installation, cost, and time were deeply taken into account. Finally, the best cost-effective solution was proposed.

Initially the differential concept looked a much better configuration for the rig’s drivelines. It needs much lower power-rated drive motors and produces much higher resolution for the creepage control. However, consultation with the application engineers shed more light on the concept and revealed some problems implementing the concept. One of the major problems with differential concept is that it requires flexible power transmission lines. The rig is equipped with positioning systems, and two rotating wheels change their relative displacements (cant, AoA, lateral) relative to each other. As a result, the transmission line requires compliant connections such as CV joints to accommodate these relative displacements (Figure 5-7). Compliant connections such as CV joints in the driveline could produce axial vibrations due to shudder motion and rotational delay between driver and driven components [81]. Direct driveline, however, delivers maximum accuracy in speed control from a electric motor. After many

discussions with the motor supplier, a direct driveline was highly recommended to mount the rotational bodies (roller and wheel) to the motors directly, without any joint compliance.

In the differential driveline, flexible transmission lines such as belt or chain from reducer to differential gearbox is inevitable to accommodate the exact distance between the two wheel and roller drive-shafts. Two rotational bodies could get worn out due to friction at the interface. This causes the distance between the drive-shafts to reduce. A flexible transmission line is needed to accommodate the variable distance between the drive-shafts. In addition to inefficiencies associated with flexible transmission line, it superimposes nonlinearities such as backlash to the driveline that could drastically affect the accuracy of the velocity regulation.

Moreover, the rated power of the drive motors in the differential driveline configuration greatly depends on the reducer gear ratio. A specific gear ratio for the reducer would lead to the minimized needed power of the drive motors. However, based on the diameters of the rotating bodies, and the available off-the-shelf differential gearboxes, the calculated optimum gear ratio (5.74) for the reducer with required loading specification was not commercially available. Made-to-specification (customized) gearbox could cost as high as three times the available ones.

On the other hand, independent driveline concept supports mounting the rotational bodies (roller and wheel) to the motors directly, without any joint compliance. This eliminates axial vibrations and rotational delay between driver and driven components. In order to get the desired creepage regulation, servo drives are selected such that the differential speed between two servo-motors (which drive the wheel and roller) would be controlled using electric gearing (digital master-slave mode) with a high level of precision.

All in all, independent driveline is designed for powering the rotational bodies, and producing the slip at the interface. Although the differential concept looks beneficial in terms of power consumption, it has the disadvantage of employing compliant joints that alarmingly influence the performance of servomotors.

### 5.1.3 Component Selection

The desired speed profile against time varying load for both the rotational bodies is supplied via two independent three-phase permanent magnet servomotors. To this end, various electrical motor suppliers and products have been considered and carefully compared. Manufacturers such as Kollmorgen, Baldor, Parker, Yaskawa, and Marathon, as well as products such as vector duty AC induction motor, permanent magnet servomotor, and DC motor are among the long list of discussed options. After consultation with the application engineers and reviewing their solutions for the rig’s powertrain, AKM84T AC synchronous servomotor offered by Kollmorgen is selected. Servomotors give the best performance in motion control applications. They outperform other type of motors in terms of accuracy in speed regulation. The largest standard Kollmorgen shafted brushless servomotor (AKM84T) meets all the required power specifications for the powertrain.

AC servomotors with permanent magnets are intended for up-to-date electronically controlled electric drives with a wide control range, good dynamical properties, a high level of precision. The servomotors are three-phase synchronous motors with excitation by permanent magnets on the rotor operating as brushless DC electric motors. This function of the motors is ensured by transistor converters with DC intermediate circuit and feedback control by a position sensor (e.g. resolver) embedded in the servomotor. Basic diagram of the drive with an AC servomotor is shown in Figure 5-8.

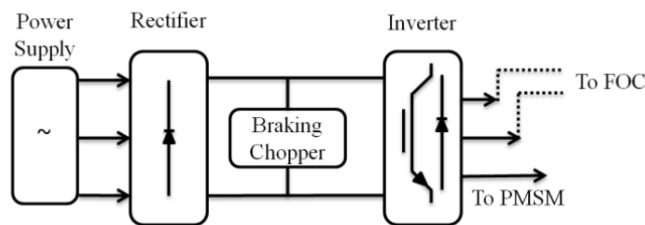


**Figure 5-8: Schematic drawing of basic drive circuit for AC servomotors [82]**

The three-phase rectifier, braking chopper, three-phase inverter, field-oriented controller (FOC), and speed controller are the main parts of the drive [82]. The permanent magnet synchronous machine (PMSM) and the position sensor are the main parts inside the motor housing. An

optional mechanical brake may also be added. The PMSM has permanent magnets mounted on the surface of the rotor, with a uniform air gap and no saliency. Figure 5-9 shows the key design features of the permanent magnet synchronous machine, and Figure 5-10 shows the exploded view of the machine [83].

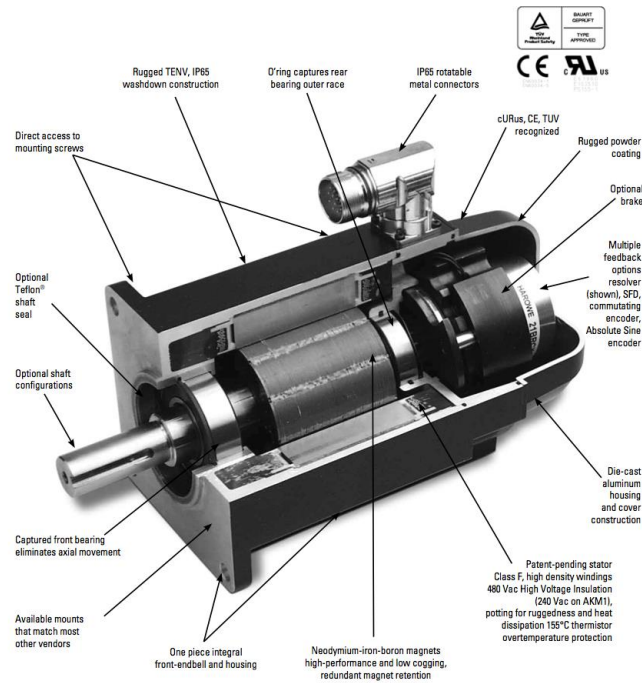
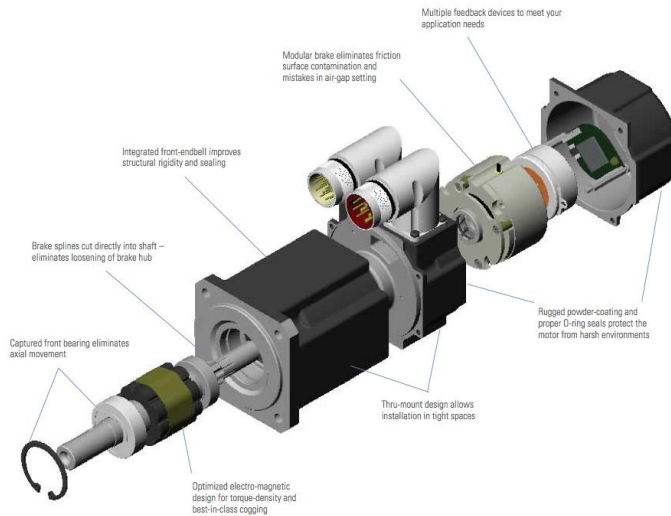


Figure 5-9: Key design features of Kollmorgen’s permanent magnet synchronous machine [83]



**Figure 5-10: Exploded view of the AC synchronous servomotor [83]**

Table 5-1 shows specifications of the AKM84T motor, and the performance curve of the motor is presented in Figure 5-11. The AKM84T servomotor outputs continuous power of 19.5 kW for a rated speed of 2500 RPM. The servo-machine is equipped with a single turn absolute sine encoder (DA).



**Figure 5-11: Performance curve for AKM84T servomotor [83]**

Table 5-1: Main specifications for AKM84T (480 V) AC servomotor [83]

<b>Max speed:</b>	2500 RPM
<b>Rated power (max. continuous):</b>	19.5 kWatts
<b>Sinusoidal Commutation</b>	
<b>Continuous torque (stall):</b>	180.0 N-m
<b>Cont. Tq. (stall) @ 60°C rise:</b>	140.0 N-m
<b>Peak torque (stall):</b>	668.0 N-m
<b>Continuous current (stall):</b>	67.0 amps
<b>Peak current (stall):</b>	335.0 amps
<b>Torque sensitivity (stall):</b>	2.75 N-m/A
<b>Back EMF constant:</b>	1.69 V/rad/s
<b>Rated ambient temp.:</b>	40 °C
<b>DC resistance:</b>	0.058 ohms
<b>Inductance:</b>	2.46 mH
<b>Rotor inertia:</b>	0.0495 kg-m <sup>2</sup>
<b>No. of poles:</b>	10
<b>Static friction:</b>	2.34 N-m
<b>Viscous damping:</b>	1.6 N-m/kRPM
<b>Thermal time constant:</b>	116.0 min
<b>Thermal resistance:</b>	0.183 °C/watt
<b>Motor weight:</b>	97.0 kg(m)
<b>Industry standards:</b>	UR, cUR, CE
<b>Sealing standard:</b>	IP54
<b>Brake derating @ 100°C rise:</b>	6.0 N-m
<b>Encoder derating @ 100°C rise:</b>	18.0 N-m
<b>Brake w/ encoder derating @ 100°C rise:</b>	28.0 N-m

AkM84T servomotors are controlled by a digital servo drive (S772) offered by Kollmorgen (Figure 5-12). Kollmorgen servo drive is specifically designed with the versatility, communications, and power needed to expand machine performance and increase integration speeds. Motor set-up is plug-and-play and multiple Ethernet connectivity options provide both open and closed protocols. Online troubleshooting and data verification enable faster, bug-proof programming. And a broad power range in a smaller, compact design allows using these robust drives with a single interface while experiencing industry-leading, high-performance servo loops [84].



**Figure 5-12: Picture of S772 servo drive offered by Kollmorgen [84]**

The S700, which is based on the SERVOSTAR® 300 architecture and features the same kind of processor, is a fully digital servo amplifier that is ideal for complex drive tasks. It incorporates onboard Ethernet connectivity for use with EtherCAT® and SynqNet™, and the optional MMC memory card enables parameter records and firmware to be easily backed up in the field. A Safe Torque Off function is standard, and other safety functions can be added. The S772 integrates a Safe Torque Off function. A digital input disables the amplifier's power output stage, thereby implementing the Safe Torque Off function (safe stop). Advanced safety functions such as safety limited speed could be implemented by means of a safety expansion card. The S772 can read data from a wide range of feedback systems (including encoder, resolver, hall effect sensor, etc) and evaluate up to three of them in parallel. This feature ensures a high level of flexibility where integration of the S772 into different applications is concerned. The S772 really stands out on account of the high level of flexibility that it offers when integrated into network environments. Virtually all of the most popular fieldbus connections can be accommodated (RS232, EtherCat, CAN standard ISO 11898), thereby enabling the servo amplifier to communicate with any standard controller [84]. The wiring diagram of the components of the servo drive is depicted in Figure 5-13.

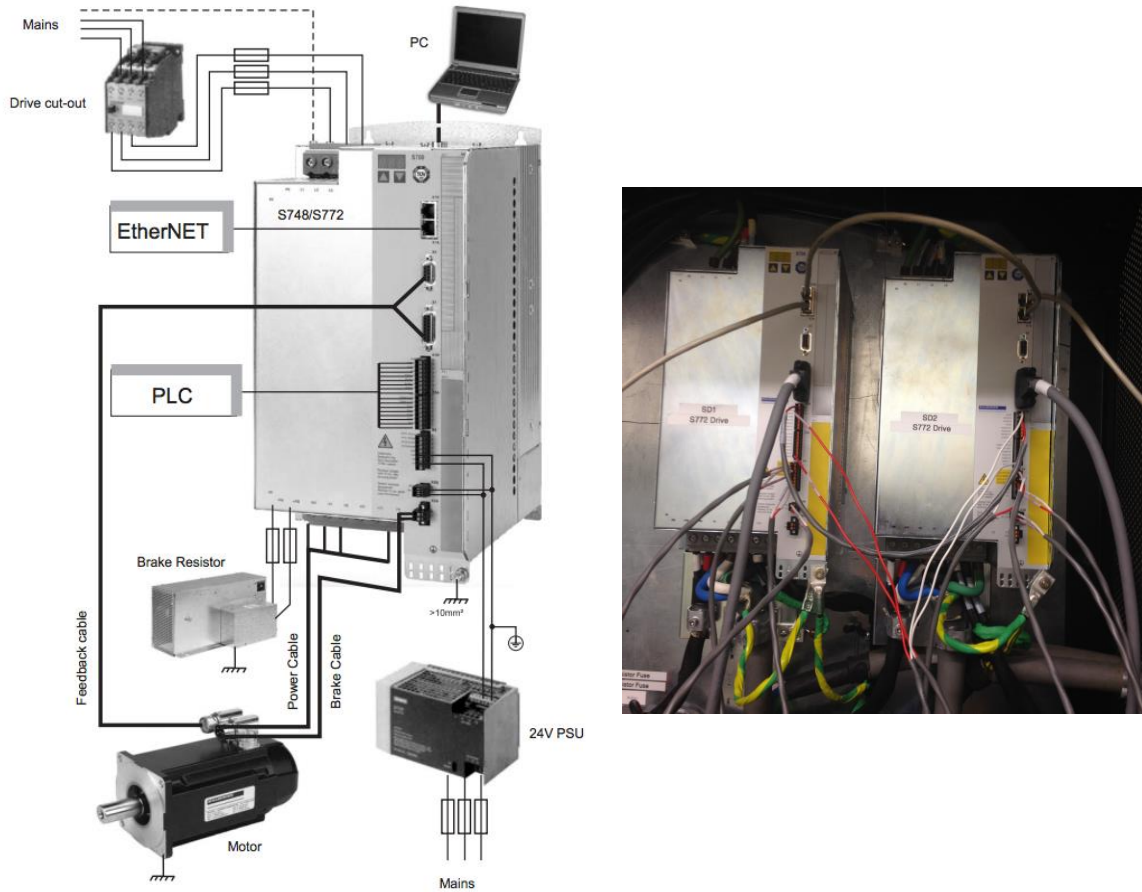


**Figure 5-13: Left) Wiring diagram of the S772 servo drives [84]. Right) Installed S772 servo-drives controlling the servomotors that drive the wheel and roller drivelines**

In order to deliver the needed torque to the rotating body, a proper-size gearbox is designed to transmit power from the servomotor to the roller. Different vendors (products) are considered including Micron (UT022), Stober (PHQ932, C812), Wittenstein (TP 500S, TP 300S)), Mijno (BDB330), and Apex (AE235). Comparing all the available options, BDB330 precision gearbox manufactured by Mijno offers the best cost-effective solution that meets all the required specifications (Figure 5-14).



**Figure 5-14: BDB330 precision gearbox offered by Mijno [85]**

Table 5-2 shows the technical characteristics of gearbox BDB330-028. BDB planetary gearbox is a high rated-torque gearhead suitable for heavy duty, low backlash, high rigidity servo applications. It has a rotating output flange instead of traditional output shaft. It is supported by two angular contact bearings or tapered roller bearings for maximal radial and axial load acceptance. Satellite gear is double-supported on hardened and ground shaft with full complement needle bearings for increased torsional stiffness [85]. The gearhead comes with an adaptor that is compatible with Kollmorgen servo-motor (AKM84T) for direct face mounting.

**Table 5-2: Main characteristics of the BDB330 precision gearbox manufactured by Mijno**

Type	Ratio	Weight (kg)	Inertia Kg.cm <sup>2</sup>	Tors. Stiffness Nm/(arc-min)	Max speed : Continuous (cycl.)- RPM	Efficiency %
Planetary (inline)	28	80	40	1969.7	2000 (3000)	>94
Backlash (arc-min)	Rated Output torque-Nm	Max accel. Torque-Nm	E-stop Torque-Nm	Output type	Axial Load (N)	Radial Load (N)
<3	6250	8950	15000	flange	25000	55000

Similar to roller driveline, for the wheel driveline, identical servomotor and S772 digital servo drive offered by Kollmorgen are employed based on the selection of independent drive configuration. However, since the nominal speed of the wheel driveline is almost five times faster than the roller driveline, a proper gearhead offered by Thomson Linear is selected. Similar to Mijno gearhead, UT018-005 precision gearhead comes with a standard adaptor compatible with Kollmorgen motor for direct face mounting. UT018-005 incorporates helical crowned true

planetary gearing, which offers high torque capacity, low backlash, smooth operation, gearer load sharing, and whisper quiet. Figure 5-15 shows the unique features of the Ultra True geaheads. Table 5-3 shows the performance specifications of the UT018-005 planetary precision gearhead.



**Figure 5-15: Unique features of the UT018-005 true planetary gearhead offered by Micron [86]**

**Table 5-3: Main specifications of the UT018-005 true planetary gearhead offered by Micron [86]**

Type	Ratio	Weight (kg)	Inertia Kg.cm <sup>2</sup>	Tors. Stiffness Nm/(arc-min)	Max speed : Continuous (cycl.)- RPM	Efficiency %
True Planetary (inline)	5	40	20	150	2000 (5000)	95
Backlash (arc-min)	Rated Output torque (1000 RPM)-Nm	Rated Output torque (5000 RPM)-Nm	Peak Torque-Nm	Output type	Axial Load (N)	Radial Load (N)
<4	1333	1058	2654	shaft	16000	16500

In order to hold the rotating shaft in each one of the drivelines, two bearing sets are designed. Spherical roller bearing offered by SKF is selected as the best cost-effective solution for the roller rig project. Spherical roller bearings have two rows of rollers, a common sphered outer ring raceway, and two inner ring raceways inclined at an angle to the bearing axis. The center point of the sphere in the outer ring raceway is at the bearing axis. Therefore, the bearings are self-

aligning and insensitive to misalignment of the shaft relative to the housing, which can be caused, for example, by shaft deflection. Spherical roller bearings are designed to accommodate heavy radial loads, as well as heavy axial loads in both directions. Symmetrical rollers self-adjust and provide optimal load distribution along the roller length. This keeps stresses low under all load conditions and extends bearing service life. In addition, the rollers in an SKF spherical roller bearing are manufactured to extremely tight tolerances. Each roller is virtually identical in size and shape to the other rollers in the set. This optimizes load distribution over the rollers to maximize bearing service life.

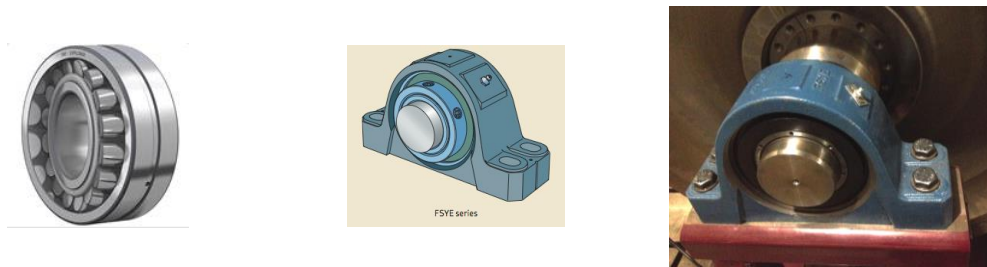


**Figure 5-16: Left) Double row spherical roller bearing. Middle) Pillow block spherical roller bearing FSYE series selected for the rig and offered by SKF [87]. Right) Installed roller driveline's bearing**

The SKF ConCentra locking concept is based on two sets of inclined planes (serrations): one set in the bearing bore, the other on the stepped sleeve. When the set (grub) screws in the mounting collar are tightened, the bearing is displaced axially, forcing the inner ring to expand. This does two things: it sets the correct internal clearance within the bearing and it exerts pressure on the stepped sleeve, forcing it to contract around the circumference of the shaft for a true concentric, tight fit (Figure 5-17). On the opposite side of the bearing, set (grub) screws for dismounting are located [87].

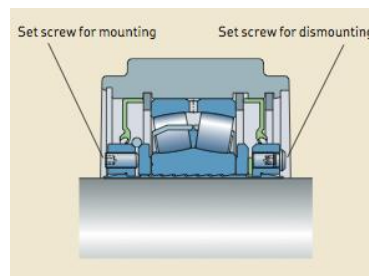


**Figure 5-17: Schematic of ConCentra mounting design configuration [87]**

The selected pillow block bearings allow for 1.5° degree misalignment. In order to accommodate any potential thermal expansion of the shaft, on each axle one bearing is designed to be floating unit. The heat loss at the contact patch due to the friction between wheels at the interface is about 3 hp. Unlike tapered roller bearing, spherical roller bearing allow for float mounting configuration.

The SKF bearings were selected and sized with assistance from SKF engineers and product documentation [87]. Following the standard sizing practice recommended by SKF, the bearing life is calculated. The loading conditions for the bearings are tabulated in Table 3.

**Table 5-4: Required specifications for the bearings**

Item	Shaft diameter (in)	Axial loading (kN)	Radial loading (kN)	Max speed (RPM)	Mounting option	Quantity
Roller axle bearing	4	6	12	70	Pillow block	2
Wheel axle bearing	3	6	8	385	Pillow block	2
Cant angle bearing	3	6	8	20	Pillow block	2

The spherical roller bearing with pillow block mounting (FSYE-4-N, FSYE-4-NH) is selected for the roller driveline. Similar bearings with 3-inch inner diameter (SYE-3-N, SYE-3-NH) are selected for the wheel driveline. According to the SKF catalog, static and dynamic basic loadings for the bearings are determined. Based on the calculated parameters, and the given formula, the basic rating life for the bearings are calculated. The results are tabulated in Table 5-5. Another bearing set is designed for the cant angle positioning system to allow for the relative angular displacement between the wheel and roller. Since the loading condition of the cant bearings is very similar to the wheel driveline’s bearings, similar bearing set is selected for the cant axis.

**Table 5-5: Design calculation of load and life in hours for driveline bearings**

Bearing	Wheel/Cant	Roller
	axis	
Type	SYE 3 NH	FSYE 4 NH
Dynamic basic load ratings (kN) - C	212	425



A rotating shaft made of 1045 carbon steel is machined to the required specifications for mounting to the bearings and torque-sensor’s coupling, as shown in Figure 5-20. Finite element analysis is conducted to optimize the diameter of the shaft for taking the required loadings. Different mounting methods such as interference fit (shrink and press), key and keyway, and splines are considered for mounting/locking the wheel to the shaft. A keyless locking device offered by Fenner Drives offers the most efficient way of mounting the roller to the shaft, as it optimizes the productivity while minimizing material and cost. Fenner Drive Keyless Locking Device functions as mechanical interference fit with a uniform pressure distribution similar to a shrink or press fit. It is a true zero backlash shaft-to-hub connection. Additionally, the keyless bushing offers simple and easy installation, adjustment, and removal, even in the field. This allows to easily replacing the wheel or roller due to fatigue/wear or testing various wheels with different head profiles. The keyless locking device operates using simple wedge principle. A series of annular screws apply axial force to engage circular steel rings with mating tapers, as depicted in Figure 5-19. The resulting wedge action creates a radial force on the tapered rings, one of which squeezes the shaft while the other presses into the wheel hub [89].

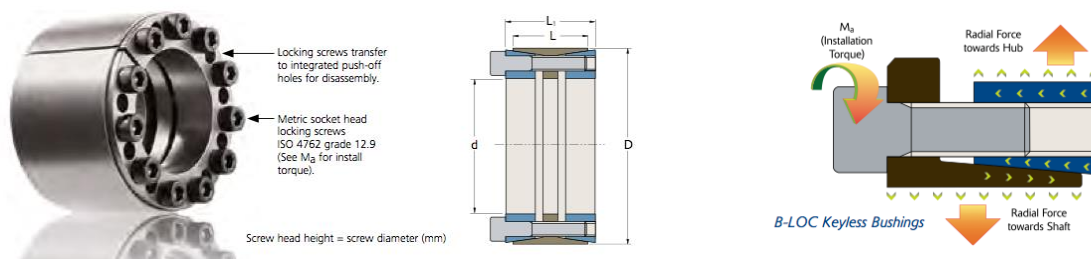


**Figure 5-19: Left: Fenner Drive Keyless Locking Device functions as a mechanical interference fit. Right: A simple wedge principal used to apply a uniform pressure distribution [89]**

The product of the radial force applied to the shaft, the radius of the shaft, and the coefficient of friction between the joined surfaces determines the rated torque capacity of the connection. According to the dimensions and the required loading capacities, two heavy-duty keyless bushings (B122300, B122700) are selected. B122700, which has a bore diameter of 7-inch, is able to take a maximum torque of 90619 ft.lb, and a maximum trust force of 310695 lbs. This is employed to mount the rig’s roller to its shaft, as shown in Figure 5-20. Similarly, B122300,

which has a bore diameter of 3-inch, is able to take a maximum torque of 10252 ft.lb, and a maximum trust force of 82017 lbs. This locking device mounts the wheel to its shaft.

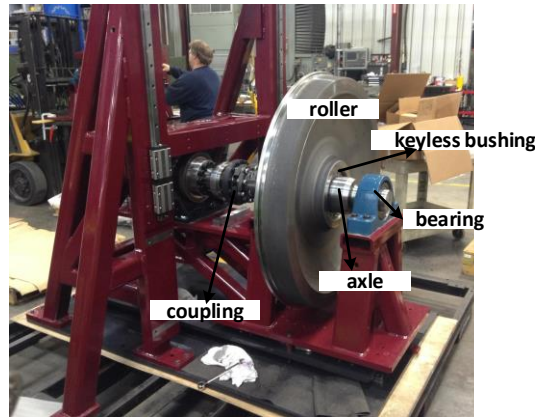


**Figure 5-20: Roller driveline during assembly process**

According to the designed scale factor, a custom made disc that is a cutout from railroad axles donated by Standard Steel, functions as the wheel in the rig, shown in Figure 5-21-right. The wheel has a 1/4th scaled down version of the wheel profile AAR-1B wide-flange for freight car wheels. In order to initialize the experimental tests, another wheel with a flat cylindrical profile is also machined from railroad axle, and is temporarily assembled to the rig (the cylindrical wheel is replaced by the AAR-1B wheel to study the railroad wheel-rail contact mechanics). Similar to roller’s axle, a shaft made of steel carbon 1045 is machined to the required tolerances for mounting the bearings and locking collar. Figure 5-21 shows the detailed drawing of AAR-1B wide-flange wheel profile of which the scaled down version is machined to the rig’s wheel. The mass and mass moment of inertia’s specifications of the wheel and roller and their axles are tabulated in Table 5-6.

**Table 5-6: Inertia and mass specifications of the drivelines**

Part	Mass (kg)	Mass moment of inertia (kg.m <sup>2</sup> )
Roller	669.5	96.3
Roller axle	83.1	0.25
Wheel	15.6	0.13
Wheel axle	12.4	0.01

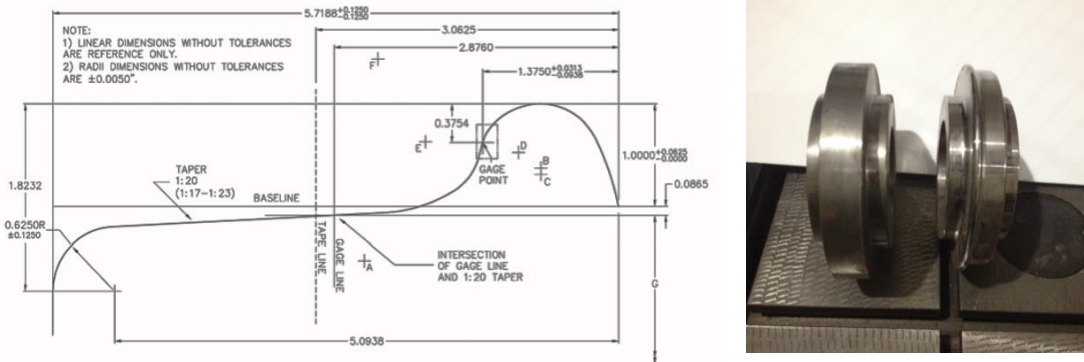


Figure 5-21: Left) The detailed drawing of AAR-1B wide-flange wheel profile [90]. Right) Fabricated wheels with flat cylindrical and AAR-1B profiles

Figure 5-22 shows the detailed drawings of the roller and wheel drivelines. The servomotor-gearhead assembly is bolted to a mounting bracket. A jackscrew mechanism (anti-vibration leveler offered by Advanced Anti-vibration Components) is designed for supporting all the cantilever beam weight of the face-mounted assembly of the motor and gearhead.

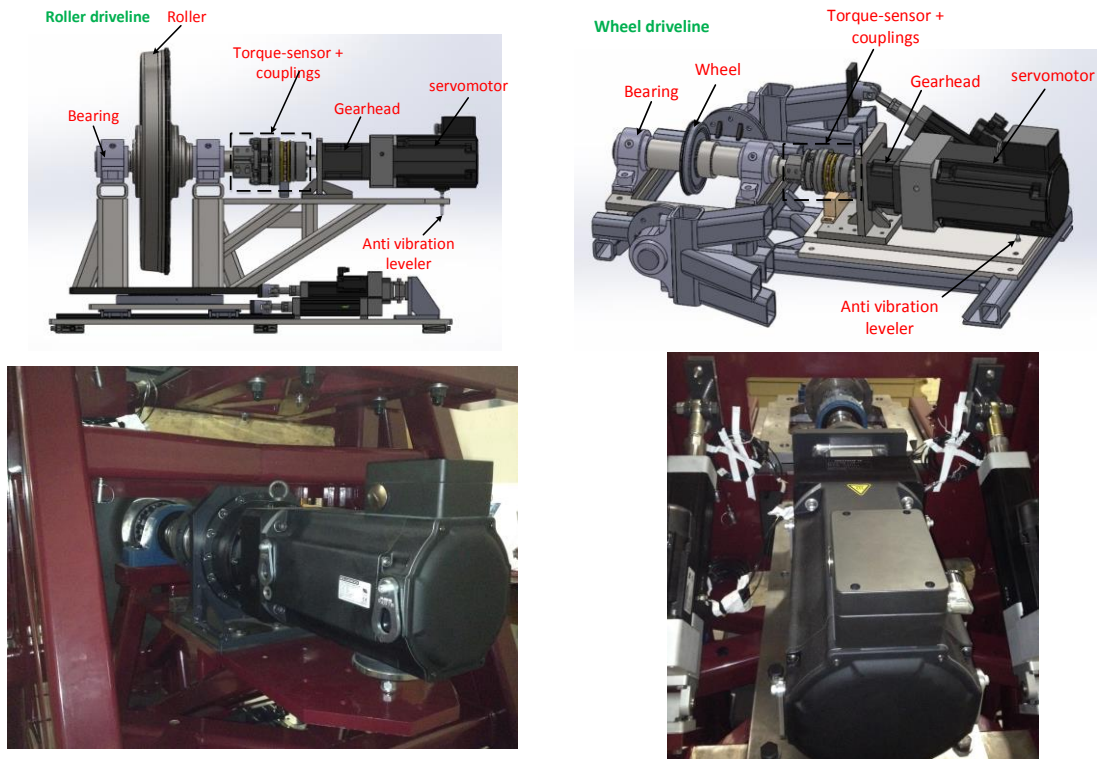
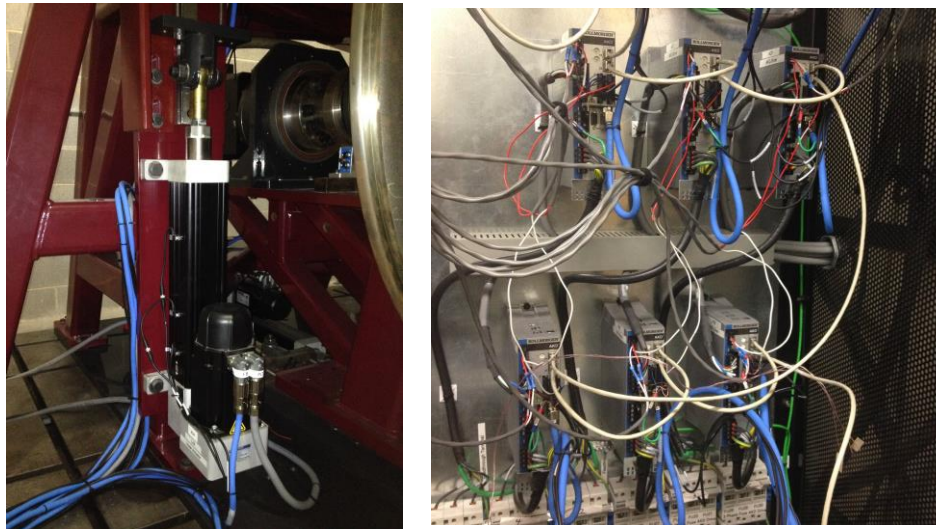


Figure 5-22: Solid model (top) and installed hardware (bottom) of the roller (left) and wheel (right) drivelines

### 5.3 Linear Actuators

As discussed, in order to closely replicate boundary conditions of actual railway vehicles, Virginia Tech Roller Rig is equipped with different positioning systems to actively control the relative angular and linear displacements between the two rotating wheels. These relative displacements are angle of attack (AoA), cant angle, lateral shift, and normal contact loading (vertical displacement). For each one of these degrees of freedom, a linear actuator is designed for real-time positioning of the displacements. Different actuation methods (electric, hydraulic, and pneumatic) were considered. In addition to possessing many of the same unique design characteristics of hydraulic and pneumatic cylinders, electric cylinders benefit from a cleaner and simpler power transmission. As opposed to hydraulic or pneumatic actuators, electric cylinders do not require compressed air or hydraulic pump. Electric linear actuators offer direct power transmission and electronic control, maximum thrust efficiency and superior mounting flexibility, low maintenance performance including the ability to isolate the motor and main cylinder body from the work area. Moreover, the electric cylinders offered by Kollmorgen are highly compatible with the rest of powertrain, as well as with SynqNet data acquisition system selected for the rig.

Kollmorgen offers EC4 electric cylinder drive mechanisms designed around ballscrews. Ballscrews, being more efficient than lead screw, utilize ball-nuts riding on recirculating ball bearings resulting in higher speeds, loads and cycle rates. However, the design of ballscrew technology is backdriven when power is removed. As a result, precautions such as electric brakes or counter loading need to be taken, if needed [91].



**Figure 5-23: Left) EC4 electric cylinder incorporates an AKM servomotor and a ballscrew to precisely control the linear motion. Right) Installed AKD servo drives controlling six electric cylinders that control the motion of positioning systems**

Figure 5-24 shows a cut-away drawing of the EC series electric cylinders with its key design features. The EC4 Series provides robust electric cylinders for heavy-duty thrust loads. Precision-rolled ball screw types yield quiet operation, low backlash and high accuracy, with a selection of motor-to-screw reduction types. The selected cylinders include exceptionally durable bearing and drive housings. The special design of these cylinders minimizes the need for routine maintenance.

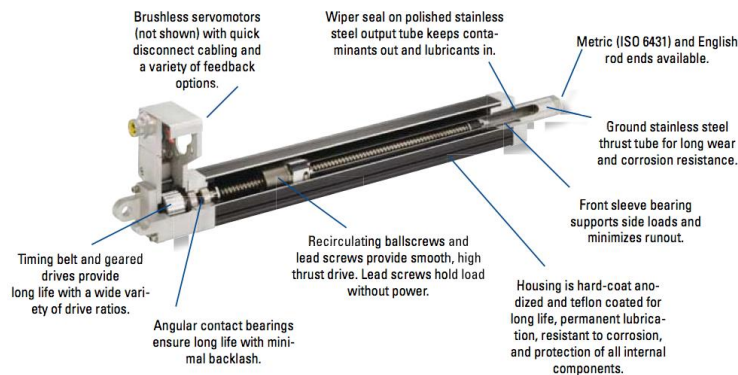


**Figure 5-24: Cut-away drawing of the EC series electric cylinders with the key design features [91]**

AKM52H servomotor with AKD-B00607 digital servo drive provides a robust, precise servo drive system for the selected EC4 electric cylinders. Figure 5-25 shows the thrust-speed performance curve for the AKM52G servomotors. The power of motor is transmitted to the ball screw mechanism using a belt/pulley system with a reduction ratio of 2:1. A lead of 10 mm per revolution is selected for the actuators. The system specifications for the EC4 electric cylinders are presented in Table 5-7. Different mounting options and stroke lengths are selected for various positioning axes. The list of employed actuators for different positioning systems is tabulated in Table 5-8.

**Table 5-7: System specifications for Kollmorgen EC4 electric cylinder**

Lead (mm/rev)	10	Repeatability (mm)	+/- 0.013
Backlash (mm/rev)	0.30	Max thrust (lbs)	2698
Lead Accuracy (mm/300mm)	+/- 0.05	Continuous thrust (lbs) at speed of 5.3 in/s	1396

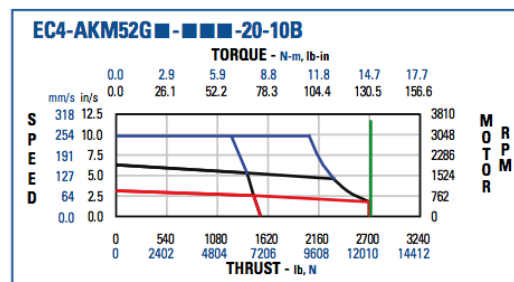


**Figure 5-25: The thrust-speed performance curve for the AKM52G servomotors [91]**

The electric cylinders are equipped with motor brakes. The electrically released, spring set brake prevents backdriving when the unit is at rest, or in case of a power failure. When power is applied, the brake releases and the cylinder is free to move. When power is off, springs engage the brake to hold the load in position. The brake torque is multiplied by the belt reduction ratio. However, if the belt fails, the brake will be inoperative. The brake applies a torque of 14.5 N.m, which is equivalent to a holding force of 36 kN for the electric cylinder.

**Table 5-8: Selected EC4 electric cylinders for different positioning systems**

Positioning axis	Stroke length (mm)	Mounting option	Rod end type	# of EC
Lateral	100	MS2 Side Lugs Parallel	FS2 Spherical Joint Dimensions	1
Cant angle	100	MP3 Clevis Mount with Pivot Base and Pin	FS2 Spherical Joint Dimensions	2
Angle of attack	100	MP3 Clevis Mount with Pivot Base and Pin	FS2 Spherical Joint Dimensions	1
Vertical	200	MS2 Side Lugs Parallel	FS2 Spherical Joint Dimensions	2

In order to maximize cylinder life, end-of-travel “limit switches” (position sensors) are used for all the cylinders. The purpose of an hall-effect end-of-travel sensor is to signal the controller that the cylinder is about to travel beyond its normal safe operating region, and is nearing its physical end of stroke. The controller brings the cylinder to a stop to prevent physical contact, and to avoid damage to the cylinder or the machine. The sensors must be located such that an adequate stopping distance is provided between the sensing position and the physical end of stroke [91].



**Figure 5-26: Hall-effect end-of-travel sensors for signaling the end of stroke for EC4 cylinders [91]. Right Installed hall-effect sensor in action**

## 6 Instrumentation and Control Architecture

(This chapter was published in part in Measurement journal [92]. Reproduced with permission.)

In this chapter, the instrumentation system and control architecture of the Virginia Tech Roller Rig is discussed. The rig is equipped with a sophisticated instrumentation system including a custom design force measuring system, torque sensors, and velocity sensors. In addition, the rig will be equipped with a vision system for accurately looking at the interface between the wheel and rail for conducting contact geometry studies. One of the unique features of the rig is its unified communication protocol between actuators, drives, and data acquisition system eliminates data conversion between these units; hence, facilitating online high-speed measurements and control. The state-of-the-art measurement and control network used in the rig, makes the sense-to-act process as fast as the sensors' update rate. Following is the details on the instrumentation design and control scheme of the rig.

### 6.1 Force-Torque Measuring System

In addition to the hardware and powertrain of the rig, Virginia Tech's Roller Rig is equipped with a custom-designed instrumentation system that is capable of measuring the contact forces and other dynamic variables with high level of precision. Since the rig is primarily intended to study the contact mechanics, accuracy of contact force measurements is one of the most important key factors towards successful operation and achieving the goals of the rig. In this section, the novel force measurement system configured for the rig and capable of measuring the contact forces with the desired level of accuracy is thoroughly discussed. The design concept used for measuring the creep forces is introduced. The required specifications in terms of accuracy and operating range are presented.

#### 6.1.1 Introduction

In order to study the creep characteristic of the wheel-rail contact, the normal and tangential forces at the contact patch should be measured accurately. To this end, a proper real-time measurement of forces ( $F_x$ ,  $F_y$ , and  $F_z$ ) and moments ( $M_x$ ,  $M_y$ , and  $M_z$ ) acting on the wheel/roller under dynamic conditions needs to be conducted.

Reviewing the past experimental studies, as well as consultation with the experts and industrial suppliers indicated that two approaches for measuring the contact forces have been mostly used:

- Using off-the-shelf wheel force transducers (WFT)
- Customized instrumentation of wheel or roller

Wheel force transducers have been vastly employed in the automotive industry [93]. The compliance of the rubber at the contact in ground vehicles functions as a filter and hence eliminates the high frequency content of the readings. However, the interface of the wheel and rail in railway vehicles does not retain as much compliance, inherent to steel on steel contact. For this reason, using automotive WFT for measuring contact forces can capture high frequency chatters at the contact and superimpose them to the force sensor measurements. In addition, all off-the-shelf WFTs are designed to be mounted on one end of the spindle. This is why these transducers are not suitable for motorcycle applications. Similarly, Virginia Tech Roller Rig is a single wheel test machine with a through axle (central axle) held by two bearings on the sides of the wheel.

On the other hand, instrumenting a wheel or a wheelset for measuring the contact forces of railway vehicles would be a very costly, and time-consuming task. It also needs a proper calibration process to ensure preventing any cross-talk between force measuring elements. Consultation with industrial suppliers showed that an instrumented wheelset could cost as high as 3 times an automotive WFT.

For all these reasons, Virginia Tech has designed a novel force measurement system using multi component force platforms (dynamometers). The concept of using dynamometers for measuring forces is not new; Dynamometers have been widely used to measure forces and moments in metal cutting devices [94,95,96], deadweight force standard machines [97], robotic systems [98], etc. Various designs and configurations of dynamometers have been studied for measuring the forces. Dynamometers have been designed based on multiple principles such as parallel beam type [99], identical T-shaped bars [100], strain gauge based octagonal ring [95], piezo-electric [101], etc.

This section outlines a piezo-electric based dynamometer design and implementation for measuring contact forces in the rig. Compared with strain-gauge based dynamometers, piezo-electric force sensors provide increased rigidity and improved dynamic range. The designed

dynamometer is capable of measuring all the six contact force and moment components with a desired level of accuracy.

### 6.1.2 Design Considerations

Based on the scaling strategy (INRET) and scale factor (1/4th) designed for the Virginia Tech Roller Rig, the maximum tangential, and normal forces at the contact patch are tabulated in Table 4-2. A force platform is needed to accurately measure these forces. The force platform should be placed in a position that reacts to all the contact forces. Different locations for placing the platform were thoroughly investigated. The position that minimizes the reaction moments of the contact forces and simplifies resolving the contact forces from the sensor readings is highly desirable. Figure 6-1 shows four different options to install the force plate. All these locations sit in the load-path of the contact forces from the wheel-roller interface to the ground. According to the position of force platform relative to the contact patch (Figure 6-1), moments taken by the transducer are calculated (Table 6-1). Calculations show that the third proposed location results in smaller moments reacted at the load cells due to closeness of the contact patch and force plate. It is notable here that option four does not provide any information for the vertical force. As shown in the following section, the third configuration defines the complete loading at the contact patch, as well as reduces the magnitude of the force couples due to cant moment. Therefore, placing the force platform in the contact patch's plane seems to be beneficial (Figure 6-2).

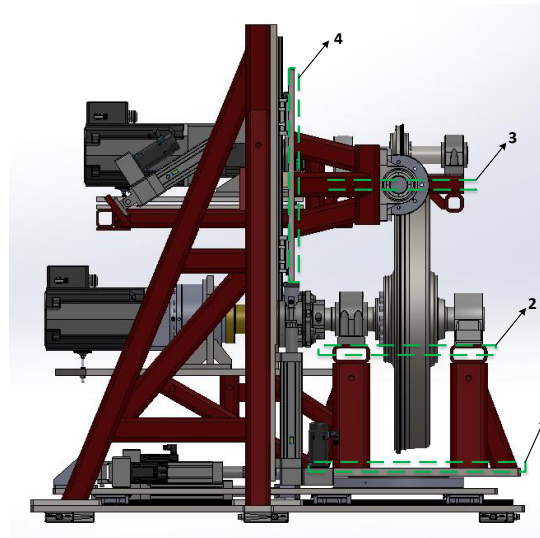


Figure 6-1: Different options for placement of the F/T platform in the experimental setup

Table 6-1: Maximum moments reacted at the F/T sensor (force plate)

	$M_x$	$M_y$	$M_z$
Mounting option 1	5	5	0.3
Mounting option 2	2.5	2.5	0.3
Mounting option 3	0	0	0.3
Mounting option 4	0	0	2

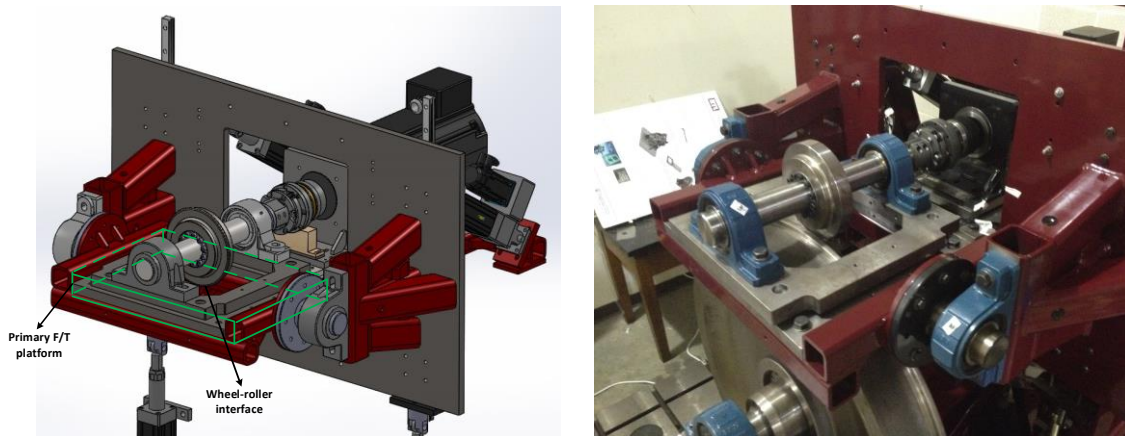
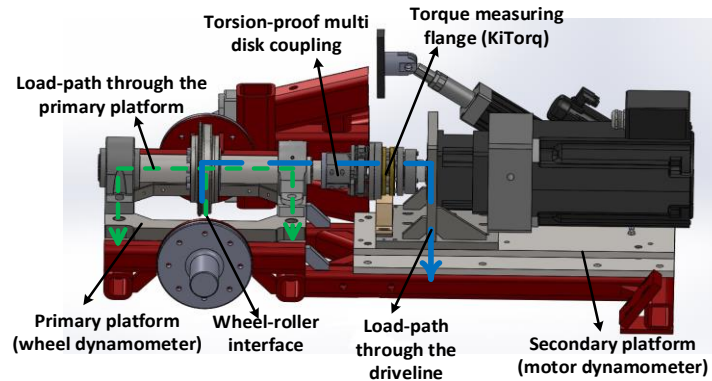
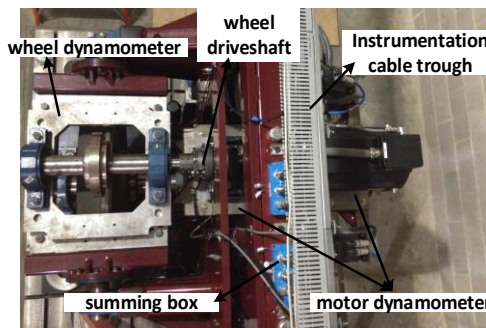


Figure 6-2: The primary F/T platform (wheel dynamometer) is placed on the cradle frame in-plane with the contact patch

As discussed in powertrain chapter, a direct driveline is designed to mount the rotational bodies (roller and wheel) to the motors directly, without any joint compliance, as direct driveline delivers maximum accuracy in speed control. This causes a load-path to ground (force shunt) that exists through the driveshaft connected to the small wheel i.e. the load path of the small wheel to ground is not solely through the load cells. The up/down, fore/aft, and lateral plunge forces are reacted through the driveshaft assembly. Unless compensated for, direct driveline, however, allows for loadcell readings to be affected by the force shunt. Different designs were investigated in order to counteract this effect.



**Figure 6-3: The load-path from the contact patch to the ground includes two routes: one that passes through the primary F/T platform, and the other one, which goes through the driveline and motor casing (force shunt)**



**Figure 6-4: Top view of the rig showing wheel and motor dynamometers installed under the wheel driveline**

The load-path from the contact patch to the ground includes two routes: one that passes through the primary force platform (wheel dynamometer), which is in line with the contact patch. Another load-path goes through the driveline and motor casing (force shunt), as depicted in Figure 6-3. The loading component that passes through the driveline needs to be measured and compensated

in the sensor readings for obtaining accurate contact forces. To this end, a secondary force platform (motor dynamometer) is implemented under the motor casing (Figure 6-3). The secondary force platform measures any axial loading component that passes through the driveline. The motor supplier guaranteed minimized motor vibrations, since the servomotor is balanced to the highest level of precision (balancing quality grade of G 2.5). This ensures that motor would not apply any considerable vibration-loading component during operation. If there are any other components such as shear loading that passes through the driveline, the secondary platform will be able to resolve them from the sensor readings. Secondary platform's sensors measure the motor torque in addition to the force shunt components. Assuming the motor is mounted exactly between left and right sensors, the motor torque can be resolved to the left and right sensors as a force couple. Therefore, it can be subtracted from the sensor readings and we would be able to resolve all the force shunt components of the driveline from the secondary platform's sensor readings.

A notable point about the dynamic measurements is that a big inertia has been introduced on the sensing (i.e. non-ground) side of the sensors, especially in motor dynamometer that can affect the measurements. In other words, the dynamic response of the loadcell could be different from the static or quasi-static responses.

In addition to the two force platforms, a rotating torque-sensor is embedded in the wheel driveline (Figure 6-3). It is located upstream in the driveshaft between the motor and the wheel measuring the applied torque to the wheel for overcoming the creep forces. Another torque-sensor is implemented in the roller driveshaft. The difference between the driveshaft torque-sensor's readings and pillow block bearings' friction torque is the actual torque of the wheel/roller shaft at the wheel/roller hub.

Finally, a coupling is employed for connecting the torque-sensor flange to the shaft (Figure 6-3). Although the driveline is designed with no compliant joint, this coupling allows for minor misalignments. This would potentially minimize any loading component through the driveline, provided that the axial and radial misalignment capacities of the coupling are more than the deflections of the cradle and axle. The cradle deflections (including bearing housing and shaft) would be imposed to the system due to the contact loadings.

### 6.1.3 Component Sizing and Selection

The force platform consists of four triaxial (3-component) loadcells preloaded between common base and cover plates; hence jointly ground to the same height, configuring a multi-component dynamometer or multicomponent force plate [102]. Each 3-component loadcell (Kistler, type 9027C and 9028C) is capable of conducting dynamic and quasi-static measurements of the three orthogonal components of any force acting on the sensor. The preloading of the sensors between the base and cover plates would ensure that tensile forces are measured as a relief of the preloaded sensor, shear forces are transmitted between sensor and plates, and micro-gaps are closed ensuring high rigidity and a wide frequency range.

Based on the loading requirements, the multi-component set (type 9026C4) consisting of four similar sensors (two pairs of 9027C and 9028C) is selected. The connectors of the four sensors are all directed inwards (Figure 6-5). The sensor types 9027C and 9028C differ only in the position of the connector in relation to the coordinate system. Otherwise, technical specifications of both types are identical.

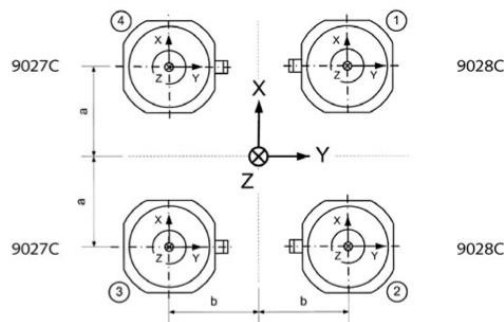


**Figure 6-5: Multi-component sensor set type 9026C4 consists of four similar sensors, two pairs of 9027C and 9028C forming a force platform [103]**

Each 3-component load cell (type 9027C and 9028C) is a quartz force sensor capable of measuring the three perpendicular components of a dynamic or quasi-static force in any direction. The force measurement of the sensor is based on the piezoelectric principle; application of a force results in a charge proportional to the force. This is picked off by built-in electrodes and is transferred to the corresponding connector.

The contact faces of the sensor are covered with ceramic discs to facilitate ground-isolated mounting of the sensor. The straightforward and vibration-resistant design of the sensor produces a very rigid structure. The resulting high natural frequency makes highly dynamic force measurements possible over a large frequency range. The cable connection of the sensors is made of a 3-pole connector V3neg (design patented by Kistler). Table 6-2 shows specifications for sensor type 9027C and 9028C.

The surfaces of the plates must be flat and rigid so that the force on the platform is evenly distributed among the sensors. Uneven bearing surfaces induce internal stresses that substantially increase the loading on the individual force links and can increase the crosstalk. The base and cover plates are designed and precision machined according to manufacturer recommendations in terms of tolerances and material. Plates are made of carbon steel 1045 and sensor's mounting holes are machined to the tight tolerances of Figure 6-6.

**Table 6-2: Technical specification of force measuring elements (type 9027C and 9028C) [103]**

Range	$F_x, F_y$	kN	-4 ... 4
	$F_z$	kN	-8 ... 8
Sensitivity	$F_x, F_y$	pC/N	$\approx -7.8$
	$F_z$	pC/N	$\approx -3.8$
Overload	$F_x, F_y$	kN	-5/5
	$F_z$	kN	-10/10
Linearity, each axis		%FSO	$\leq \pm 0.25$
Hysteresis, each axis		%FSO	$\leq 0.25$
Cross talk	$F_z \rightarrow F_x, F_y$	%	$\leq \pm 0.5$
	$F_x \leftrightarrow F_y$	%	$\leq \pm 2$
	$F_x, F_y \rightarrow F_z$	%	$\leq \pm 2$
	$F_z$		
Weight		g	30
Operating range	temperature	$^{\circ}\text{C}$	-40... 120

The base and cover plate for the wheel dynamometer are designed as rectangular frames for placing the dynamometer in-line with the wheel-roller interface, as depicted in Figure 6-7. The base plate is bolted to the rig presenting the groundside of the platform, and the cover plate is mounted to the wheel driveline's bearings functioning as the sensing side of the platform (Figure 6-7). Similarly, two base and cover plates are precision machined for the motor dynamometer (Figure 6-7).

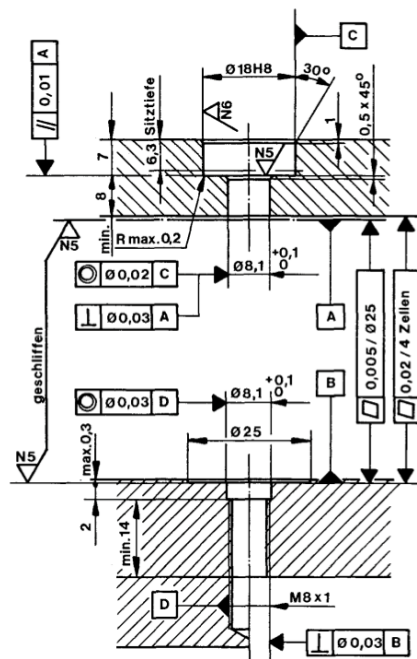
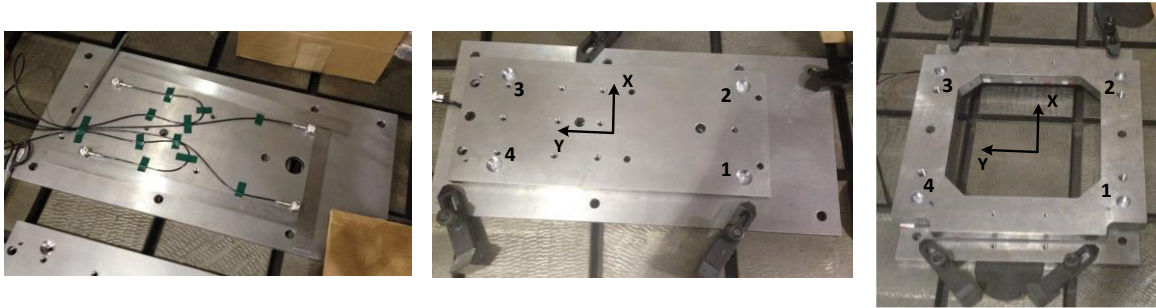


Figure 6-6: Recommended tolerances for mounting the sensor type 9027C or 9028C [103]

A set of pre-tensioning elements consists of a pre-tensioning bolt (high-strength made of stainless tool steel), a centering sleeve, an anti-friction washer, and a nut for pre-tensioning the sensors (Figure 6-9). It allows the shear forces to be transferred by static friction from the base and cover plates to the surfaces of the force sensor.



**Figure 6-7: Six component dynamometers consist of four triaxial sensors preloaded between two plates. Left) Four triaxial sensors are aligned and installed on the base plate. The cover plate and pretensioning set are installed to preload the sensors for the motor dynamometer (middle) and the wheel dynamometer (right).**

In the dynamometer, the four quartz force links are mechanically paralleled [103]. The measuring signals (electric charge) of the four sensors can also be paralleled (summed). The summated signal corresponds to the algebraic total of the individual forces (Figure 6-8). Summing box (Kistler, type 5417) facilitates the simple and reliable interconnection of measuring signals (Figure 6-9). As depicted in Figure 8, the x-component of sensors 1 & 2 (same for x-component of sensors 3 & 4) and y-component of sensors 1 & 4 (same for y-component of sensors 2 & 3) would be summed together. By doing so, the number of output channels is decreased to 8 instead of 12.

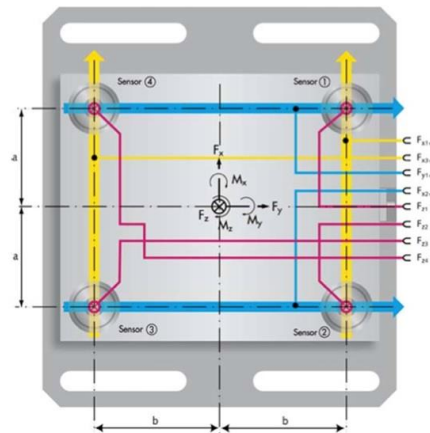


**Figure 6-8: Interconnection of 12 sensor outputs for the 6-component force measuring dynamometer [103]**

A multichannel charge amplifier (Kistler, type 5070A) is selected for converting the eight measuring signals (charge) of the summation box into a voltage. The value that is output is

exactly proportional to the force. Type 5070A multichannel charge amplifier was built specifically for the multicomponent force measuring system (Figure 6-9). The graphics-capable LCD shows all settings including the instantaneous, minimum and maximum values of a charge amplifier channel. The output signals of the charge amplifier connect to the SynqNet data acquisition system, discussed in detail below, for real-time measurement of the contact forces.



**Figure 6-9: Kistler dynamometer accessories: Pre-tensioning set (left), Summing box (Middle), and multichannel charge amplifier (right) [103]**

In addition to the force platforms, a torque-sensor is designed in the driveline for measuring the driving torque of each one the rotating bodies. KiTorq measuring unit (Kistler, type 4550A) is selected for both the wheel and roller drivelines. The KiTorq torque measuring system consists of a KiTorq rotor torque measuring unit (Kistler, Type 4550A) [104] and a KiTorq stator torque evaluation unit (Kistler, Type 4540A) [104], as depicted in Figure 6-10. KiTorq rotor captures the torque using strain gages at a high sampling rate (35 kS/sec). The analog and digital signals are transmitted without contact to the evaluation unit (via induction). Similarly, the torque evaluation unit supplies power to the KiTorq rotor and amplifies the generated signals. The evaluation unit has an integrated speed-measuring unit and provides various signal outputs. The specifications for the Kitorq units are tabulated in Table 6-3. Based on the driveline's maximum torque, 4550A1k0 is selected for the wheel driveline, and 4550A5k0 is selected for the roller driveline.

In order to install the Kitorq flange in the driveline, torsion-proof multi disk couplings (Kistler, type 2305A) are used. They are especially designed for use with the torque measuring unit KiTorq rotor type 4550 (Figure 6-10). The coupling allows for minor axial, radial, and angular misalignments when incorporating the measuring flange into the shaft assembly [105]. These misalignments' compensations are always needed to avoid measurement error and damage to the

sensor. Based on the driveline’s maximum torque, 2305A64H is selected for the wheel driveline, and 2305A500 H is selected for the roller driveline. The specifications for the steel multi-disk coupling (type 2305A) are tabulated in Table 6-4.

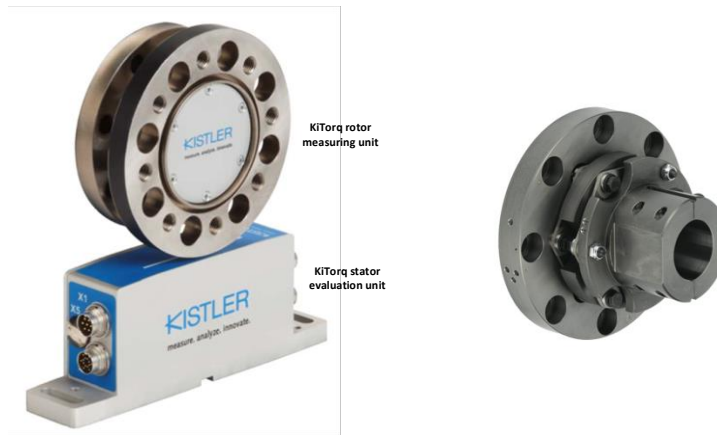


Figure 6-10: Left) KiTorq System consisting of a KiTorq rotor measuring unit and a KiTorq stator evaluation unit [104]. Right) Torsion-proof multi-disk coupling especially designed for use with the KiTorq flange [105]

Table 6-3: Technical specification of KiTorq torque measuring system (Including a rotor Type 4550A and a stator Type 4540A) [104]

Accuracy class		0.05
Temperature influence on the zero point TK0	% FSO/10k	0.05
Temperature influence on the nominal value TKC	% FSO/10k	0.05
Linearity	% FSO	0.03
Hysteresis	% FSO	0.03
Limit Frequency -3 dB	kHz	10
Operating temperature range	°C	10... 60
Scanning rate	kS/Sec	35
Protection class		IP54

### 6.1.4 Flexural Dynamic Modeling

Two base and two cover plates preload the four triaxial force sensors for each dynamometer. Uneven bearing surfaces of the dynamometer induce internal stresses on the sensors that could substantially increase the loading on the individual force links and consequently could increase the crosstalk. Similarly, structural integrity of the dynamometer could influence its performance. Deformation of bearing surfaces due to application forces can result in crosstalk and uneven distribution of force. For all these reasons, the base and cover plates need to be especially designed to be rigid enough and meet manufacturer’s recommendations in terms of tolerances and material.

**Table 6-4: Technical specification of steel torsion-proof multi-disk coupling (type 2305A) [105]**

Driveline		Wheel	Roller
Rated measuring torque	Nm	1000	5000
Permitted axial offset	mm	0.4	0.5
Permitted radial offset	mm	0.1	0.1
Permitted angle offset	°	0.2	0.2
Max. speed	rpm	6000	3600
Moment of inertia	kg.cm <sup>2</sup>	2.12	16.4
Mass	kg	7.9	25.8

In order to optimize the rigidity and strength of the dynamometers, flexural dynamic modeling and structural analysis are conducted using ABAQUS package. The solid model of the cover plate for both the dynamometers are imported to ABAQUS package and a mesh type of tetrahedron was used. Figure 6-11 shows the FE model of the cover plate for both the dynamometers in ABAQUS. For the boundary conditions, all the mounting holes of the triaxial loadcells in the model are rigidly fixed in all 6 directions. This could be a valid assumption for the boundary conditions, since the cover plate is bolted down to the sensors via pre-tensioning elements, and the sensors are bolted down to the dynamometers’ base plates and cradle frame.

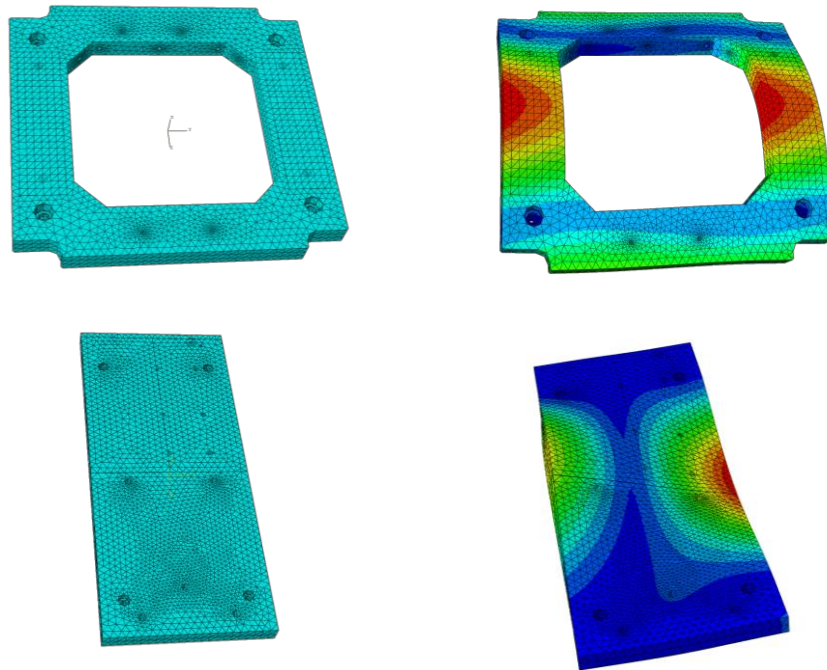


**Figure 6-11: Structural analysis of the cover plate for the wheel (top) and motor (bottom) dynamometers in ABAQUS for undeformed (left) and deformed (right) states due to maximum loading conditions**

After modeling the plate in ABAQUS, two types of analyses are conducted to study the design of the plate, as well as to optimize its structure in terms of rigidity, overall mass, and first natural frequency. Static analysis is conducted to predict the deflections of the cover plates due to contact forces and weight of components. The contact forces on the wheel are reacted at the bearings through the wheel shaft. These bearings are mounted on top of the wheel dynamometer's cover plate. The reaction torque from servomotor, and the cantilever beam weight of the motor-gearhead assembly are applied to the cover plate of the motor dynamometer. The analyses are conducted to ensure the strength of the plates under maximum loading conditions. In order to minimize the deflections, as well as maximize the first natural frequency, different plate's thickness and various distances between sensors (various sizing of the sensing rectangle) are studied. Minimizing the deflection of the plate is necessary to reduce any cross talk between the triaxial loadcells. The results of the simulations for different plate designs (different thickness, and different sensing rectangle's sizes) are shown in Table 6-5 and Table 6-6. Number of mesh elements, maximum deflection, and maximum stress are compared.

**Table 6-5: FEM results for the wheel force dynamometer’s top/cover plate**

	# of mesh elements	Max Stress [Pa]	Max Deflection [m]	Modal Analysis [Hz]
Version 1 (Thickness: 1.5 in, sensing rectangle: 14.5 in X 18 in)	1,357,770	$1.6 \times 10^8$	$4.007 \times 10^{-5}$	401, 441, 587, 772, 886
Version 1	44184	$8.7 \times 10^7$	$2.87 \times 10^{-5}$	440,505, 694, 851, 982
Version 2 (1 in added width on each side)	45738	$6.75 \times 10^7$	$2.16 \times 10^{-5}$	435,502,687,836,948,

In addition to static deflection analysis, modal analysis for estimating the natural frequencies of the structure is investigated with finite element ABAQUS package. The triaxial sensors are modeled as three dimensional spring/dashpot elements. Using the same FE model for the plates, a free vibration modal analysis is performed. The results of the analysis are summarized in Table 6-5 and Table 6-6 for different plate designs. Mode shapes for the first five natural frequencies of the cover/top plate for the motor dynamometer are shown in Figure 6-12.

**Table 6-6: FEM results for the Motor force dynamometer’s top/cover plate**

	# of mesh elements	Max Stress [Pa]	Max Deflection [m]	Modal Analysis [Hz]
Version 1 (Thickness: 0.875 in, Rectangle size: 8in X 28.25 in)	12256	$1.66 \times 10^8$	$3.17 \times 10^{-5}$	265, 769, 845, 1145, 1676
Version 1	506172	$1.71 \times 10^8$	$1.54 \times 10^{-4}$	138, 356, 432, 771, 862
Version 2 (Thickness: 1.125 in, Rectangle size: 8 in X 19.5 in)	84113	$2.83 \times 10^7$	$1.33 \times 10^{-5}$	313, 752, 888, 1039, 1225

The results show that the first natural frequency of the wheel dynamometer’s plate is 435 Hz and for the motor dynamometer’s plate is 321 Hz. These resonant frequencies are much higher than those of interest in railway vehicle dynamics and contact mechanics. This ensures a relatively high bandwidth for evaluating the dynamics at the wheel-rail interface. These modal frequencies are also higher than the modal frequencies for the other components of the rig (load frame, cradle, etc.).

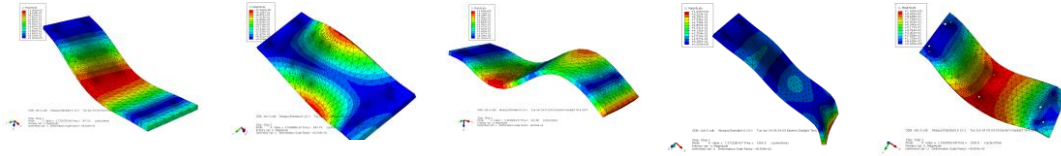


Figure 6-12: Mode shapes for the first five natural frequencies of the top plate for the motor dynamometer

### 6.1.5 Force-Moment Calculations

In order to resolve the contact forces and moment from triaxial sensors’ readings, equilibrium equations of the dynamometer are considered. Equilibrium equations result in the calculation of net platform forces and moments from four sensors’ readings (Figure 6-3). These net platform forces and moments are related to the contact creep forces and moments using free body diagram of the platform.

Initially, a non-rotating platform in which the reaction point of the forces (contact point) is located right at the center of the sensing rectangle, as depicted in Figure 6-13, is considered. For this simplified case, net triaxial platform forces are:

$$\begin{aligned}
 F_x &= F_{x_A} + F_{x_B} + F_{x_C} + F_{x_D} \\
 F_y &= F_{y_A} + F_{y_B} + F_{y_C} + F_{y_D} \\
 F_z &= F_{z_A} + F_{z_B} + F_{z_C} + F_{z_D}
 \end{aligned}
 \tag{6-1}$$

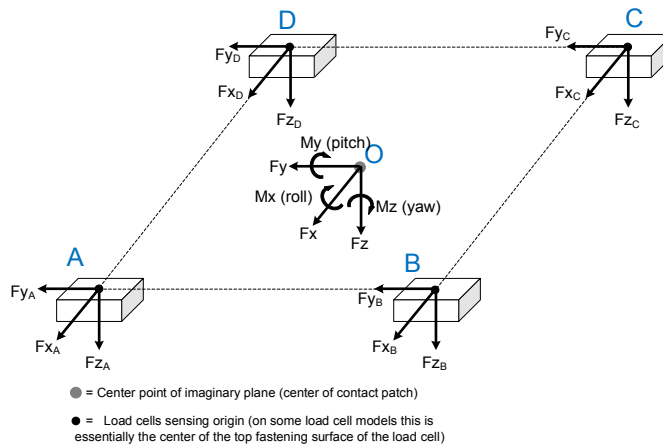


Figure 6-13: Free body diagram of the loadcells and contact patch when the contact patch is located inline and centered relative to the imaginary plane defined by the load cells sensing origins

A coordinate system is located at the center point of the imaginary plane defined by the load cells sensing origins. The net triaxial platform moments about this coordinate system are:

$$\begin{aligned}
 M_x &= \frac{W}{2} (F_{z_A} - F_{z_B} - F_{z_C} + F_{z_D}) \\
 M_y &= \frac{L}{2} (-F_{z_A} - F_{z_B} + F_{z_C} + F_{z_D}) \\
 M_z &= \frac{W}{2} (-F_{x_A} + F_{x_B} + F_{x_C} - F_{x_D}) + \frac{L}{2} (F_{y_A} + F_{y_B} - F_{y_C} - F_{y_D})
 \end{aligned} \tag{6-2}$$

However, because of the conical shape of the wheel profile and lateral motion of the wheel relative to the roller, the contact patch is not stationary, and relocates both vertically and laterally with very minor displacements. Moreover, the rig is equipped with cant positioning mechanism that allows for changing the relative angle (vertical inclination) of the wheel with respect to the roller. Therefore, the contact point is not necessarily located at the center of the sensing rectangle.  $H$  denotes the vertical distance between the contact patch and the imaginary plane defined by the loadcells sensing origins, and  $\alpha$  denotes the cant angle (Figure 6-14). As such, the net platform forces at the general case are calculated as:

$$\begin{aligned}
 F_x &= F_{x_A} + F_{x_B} + F_{x_C} + F_{x_D} \\
 F_y &= F_{y_A} \cos \alpha + F_{z_A} \sin \alpha + F_{y_B} \cos \alpha + F_{z_B} \sin \alpha + F_{y_C} \cos \alpha + F_{z_C} \sin \alpha \\
 &\quad + F_{y_D} \cos \alpha + F_{z_D} \sin \alpha \\
 F_z &= F_{z_A} \cos \alpha - F_{y_A} \sin \alpha + F_{z_B} \cos \alpha - F_{y_B} \sin \alpha + F_{z_C} \cos \alpha - F_{y_C} \sin \alpha \\
 &\quad + F_{z_D} \cos \alpha - F_{y_D} \sin \alpha
 \end{aligned} \tag{6-3}$$

Similarly, net platform moments at the contact patch are:

$$\begin{aligned}
& \{(w \times \cos \alpha \times (F_{z_A} \cos \alpha - F_{y_A} \sin \alpha + F_{z_D} \cos \alpha - F_{y_D} \sin \alpha) - (W - w) \\
& \quad \times \cos \alpha \times (F_{z_B} \cos \alpha - F_{y_B} \sin \alpha + F_{z_C} \cos \alpha - F_{y_C} \sin \alpha)\} \\
& - \{(H - w \times \sin \alpha)(F_{y_A} \cos \alpha + F_{z_A} \sin \alpha + F_{y_D} \cos \alpha \\
& + F_{z_D} \sin \alpha) + \{H + (W - w) \times \sin \alpha\} \\
& \quad \times (F_{y_B} \cos \alpha + F_{z_B} \sin \alpha + F_{y_C} \cos \alpha + F_{z_C} \sin \alpha)\} \\
& = -(H \cos \alpha) \times (F_{y_A} + F_{y_B} + F_{y_C} + F_{y_D}) + (w - H \times \sin \alpha) \\
& \quad \times (F_{z_A} + F_{z_D}) - (W - w + H \times \sin \alpha) \times (F_{z_B} + F_{z_C})
\end{aligned} \tag{6-4}$$

$$\begin{aligned}
M_z = & \{-(w + H \sin \alpha) \times \cos \alpha\} (F_{x_A} + F_{x_D}) + \{(W - w - H \sin \alpha) \times \cos \alpha\} \\
& \quad \times (F_{x_B} + F_{x_C}) \\
& + \{(L - l)(F_{y_A} \cos \alpha + F_{z_A} \sin \alpha + F_{y_B} \cos \alpha + F_{z_B} \sin \alpha) - l \\
& \quad \times (F_{y_C} \cos \alpha + F_{z_C} \sin \alpha + F_{y_D} \cos \alpha + F_{z_D} \sin \alpha)\}
\end{aligned} \tag{6-5}$$

$$\begin{aligned}
M_z = & \{-(w + H \sin \alpha) \times \cos \alpha\} (F_{x_A} + F_{x_D}) + \{(W - w - H \sin \alpha) \times \cos \alpha\} \\
& \quad \times (F_{x_B} + F_{x_C}) \\
& + \{(L - l)(F_{y_A} \cos \alpha + F_{z_A} \sin \alpha + F_{y_B} \cos \alpha + F_{z_B} \sin \alpha) - l \\
& \quad \times (F_{y_C} \cos \alpha + F_{z_C} \sin \alpha + F_{y_D} \cos \alpha + F_{z_D} \sin \alpha)\}
\end{aligned} \tag{6-6}$$

It must be noted that the structural stiffness of the platform assembly should be such that each load cell is only subjected to forces and not subjected to any localized moments individually. In other words, all platform moments should be completely reacted by the triaxial forces.

As mentioned above, the four loadcells in a dynamometer are mechanically paralleled. As depicted in Figure 6-8, the x and y components of in-line sensors' readings are summated. The summated signals (outputs of the summing box) are defined as:

$$\begin{aligned} F_{xAD} &= F_{xA} + F_{xD} \quad \& \quad F_{xBC} = F_{xB} + F_{xC} \\ F_{yAB} &= F_{yA} + F_{yB} \quad \& \quad F_{yDC} = F_{yD} + F_{yC} \end{aligned} \quad (6-7)$$

Using the summated signals, the net platform forces and moments at the contact patch are:

$$\begin{aligned} F_x &= F_{xAD} + F_{xBC} \\ F_y &= F_{yAB} \cos \alpha + F_{yDC} \cos \alpha + F_{zA} \sin \alpha + F_{zB} \sin \alpha + F_{zC} \sin \alpha + F_{zD} \sin \alpha \\ F_z &= -F_{yAB} \sin \alpha - F_{yDC} \sin \alpha + F_{zD} \cos \alpha + F_{zA} \cos \alpha + F_{zB} \cos \alpha + F_{zC} \cos \alpha \end{aligned} \quad (6-8)$$

$$\begin{aligned} M_x &= -(H \cos \alpha) \times (F_{yAB} + F_{yDC}) + (w - H \times \sin \alpha) \times (F_{zA} + F_{zD}) \\ &\quad - (W - w + H \times \sin \alpha) \times (F_{zB} + F_{zC}) \end{aligned}$$

$$\begin{aligned} M_y &= \{-(L - l)(F_{zA} \cos \alpha - F_{yAB} \sin \alpha + F_{zB} \cos \alpha) + l \\ &\quad \times (F_{zC} \cos \alpha - F_{yDC} \sin \alpha + F_{zD} \cos \alpha)\} \\ &\quad + \{(H - w \times \sin \alpha)(F_{xAD}) + \{H + (W - w) \times \sin \alpha\} \\ &\quad \times (+F_{xBC})\} \end{aligned} \quad (6-9)$$

$$\begin{aligned} M_z &= \{-(w + H \sin \alpha) \times \cos \alpha)(F_{xAD}) + \{(W - w - H \sin \alpha) \times \cos \alpha\} \\ &\quad \times (F_{xBC})\} \\ &\quad + \{(L - l)(F_{yAB} \cos \alpha + F_{zA} \sin \alpha + F_{zB} \sin \alpha) - l \\ &\quad \times (F_{yDC} \cos \alpha + F_{zC} \sin \alpha + F_{zD} \sin \alpha)\} \end{aligned}$$

In order to compensate for any driveline-loading component (force shunt via motor casing), the motor dynamometer is designed and placed underneath the motor and gear-head assembly. As depicted in Figure 6-3, the motor dynamometer reacts to the driveline-loading components, weight of the motor-gearhead assembly, and any loads that are imposed by the motor like

rotational torque. Since the motor is balanced to the highest level of precision, any axial load imposed by the motor is minimized, and hence ignored in the calculations. The motor rotational torque (measured by the torque-sensor) is resolved to a pair of vertical forces reacted at left and right sensors. Since these vertical forces are equal and opposite sign for the left and right sensors, the net vertical force would diminish. Therefore, the net driveline loading components are calculated as:

$$\begin{aligned}
 F_{x\_dr} &= F_{x_{AD\_s}} + F_{x_{BC\_s}} \\
 F_{y\_dr} &= F_{y_{AB\_s}} \cos \alpha + F_{y_{DC\_s}} \cos \alpha + F_{z_{A\_s}} \sin \alpha + F_{z_{B\_s}} \sin \alpha + F_{z_{C\_s}} \sin \alpha + F_{z_{D\_s}} \sin \alpha \\
 W_{m\_g} + F_{z\_dr} &= -F_{y_{AB\_s}} \sin \alpha - F_{y_{DC\_p}} \sin \alpha + F_{z_{D\_p}} \cos \alpha + \\
 &\quad + F_{z_{A\_s}} \cos \alpha + F_{z_{B\_s}} \cos \alpha + F_{z_{C\_s}} \cos \alpha
 \end{aligned} \tag{6-10}$$

Where  $F_{x\_dr}$ ,  $F_{y\_dr}$ , and  $F_{z\_dr}$  are driveline loading components in  $x$ ,  $y$ , and  $z$  directions, respectively.  $W_{m\_g}$  is the static weight of motor and gearhead assembly reacted at the motor dynamometer. Subscript “s” denotes secondary platform sensors.

The net driveline loading components ( $F_{x\_dr}$ ,  $F_{y\_dr}$ , and  $F_{z\_dr}$ ) are subtracted from the net primary platform’s sensor readings ( $F_x$ ,  $F_y$ , and  $F_z$ ) to obtain the total creep forces at the contact

$$\begin{aligned}
 F_{x\_creep} &= F_x - F_{x\_dr} \\
 F_{y\_creep} &= F_y - F_{y\_dr} \\
 F_{z\_creep} &= F_z - F_{z\_dr}
 \end{aligned} \tag{6-11}$$

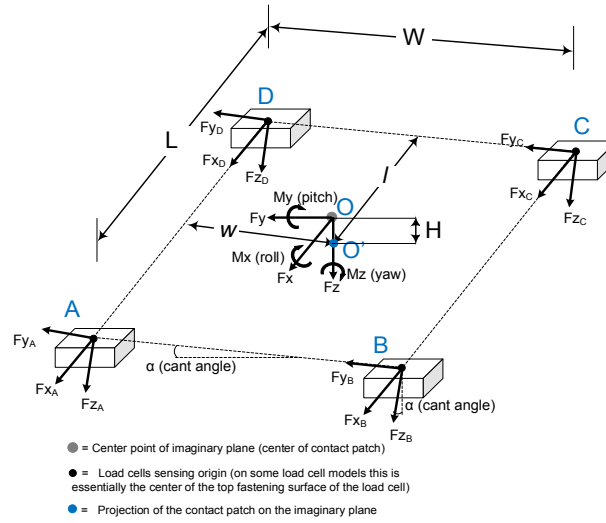


**Figure 6-14: Free body diagram of the loadcells and contact patch when the contact patch is located off-plane and not centered relative to the imaginary plane defined by the load cells sensing origins**

In order to compensate for the inertia contributions of the driveline components for dynamic measurements, acceleration and mass of the major drivelines components need to be measured. To this end, multiple triaxial piezoelectric accelerometers from PCB Piezotronics Inc. will be installed on the major drivelines components. According to the free body diagram of the wheel driveline (all the components that are sitting on the dynamometers), presented in Figure 6-15, we will have:

$$\mathbf{F}_{creep\_dyn} = \sum_{j=1}^n m_j \mathbf{a}_j + \mathbf{F}_{creep} \quad (6-12)$$

Where  $\mathbf{F}_{creep\_dyn}$  is the vector of creep forces,  $\mathbf{F}_{creep}$  is the vector of static creep forces from Equation (6-11) and  $m_j \mathbf{a}_j$  is the acceleration times the mass for all the driveline components. Equation (6-12) is in vector notation and can be broken to three  $x$ ,  $y$ , and  $z$  directions ( $n$  is the number of driveline components). Multibody dynamic simulation results, discussed in detail in Chapter 8, show that the acceleration terms can have considerable effect on the accuracy of the estimated contact forces. The accelerometers' readings are used for polishing the estimated contact forces according to Equation (6-12).

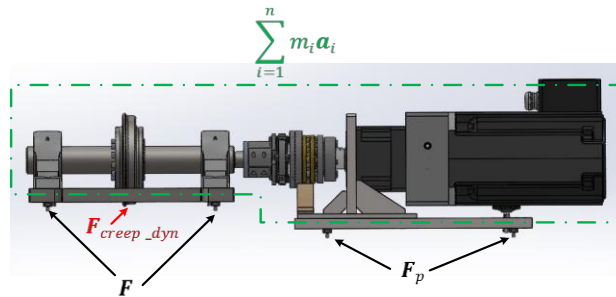


Figure 6-15: Free body diagram of the wheel driveline for dynamic measurement of the contact forces

### 6.1.6 Calibration

The individual triaxial force sensors are calibrated by Kistler. The platform, however, needs to be calibrated after the assembly of the dynamometer; because preloading of the sensors in the dynamometer may not be exactly the same as the preloading that factory uses to calibrate the individual sensors. In addition, depending on the structural integrity of the dynamometer, the actual application of force on the dynamometer can slightly deform the bearing surfaces, which can result in crosstalk and uneven distribution of forces. Temperature could also influence the sensitivity of the dynamometer. For all these reasons, quasi-static and dynamic calibrations of the dynamometers are conducted to minimize assembly errors. To this end, a calibration setup is developed that is used for both the dynamometers and in all three directions, as depicted in Figure 6-16.

The quasi-static calibration was made in three directions using weight blocks. To do so, the charge amplifier was set to read quasi-static measurements. The inherent electrical drift of the piezoelectric sensors is approximately  $\pm 0.05 \frac{\mu\text{C}}{\text{s}}$ , which leads to discharge time of several minutes and hence allows for long calibration periods. Weight blocks in 2.5 lbs intervals were applied to the dynamometer up to 350 lbs for each direction, and the summated signals for all three directions were recorded. In order to examine the repeatability, the procedure was repeated three times for each direction. The repeated measurements were very close, which shows the consistency of the measurements. Repeatability of the wheel dynamometer across all the data points is  $<0.1\%$  FSO and that of the motor dynamometer is  $<0.08\%$  FSO. To minimize the error, the mean value of three experiments was used for obtaining the calibration curve. The least

square calibration line was obtained for each direction. A line from which the sum of the squares of the deviations of the data points (measured value vs input values) is minimized. The slope of the line indicates the sensitivity of the dynamometer for each direction. The maximum distance between the data points and the line corresponds to the linearity. Figure 6-17 and Figure 6-22 show the calibration curves for x, y, z directions, respectively. Calibration curves show the measured force value of the summated signal for each direction (converted to Newtons according to manufacturer’s individual sensor’s sensitivities) versus the input calibration force to the dynamometers using the weight blocks.



**Figure 6-16: Calibration setup for the dynamometers**

The force calibration formula for each direction considering the cross-talk among directions are presented in Equation 9 for the wheel dynamometer and in Equation 10 for the motor dynamometer.

$$\begin{aligned} F_x &= 0.9987F_{x,r} - 0.0093F_{y,r} + 0.0005F_{z,r} \\ F_y &= -0.0036F_{x,r} + 0.999F_{y,r} + 0.0004F_{z,r} \\ F_z &= +0.0021F_{x,r} + 0.0159F_{y,r} + 1.0168F_{z,r} \end{aligned} \quad (6-13)$$

$$\begin{aligned} F_{x,s} &= 0.9971F_{x,rs} - 0.0054F_{y,rs} + 0.0117F_{z,rs} \\ F_{y,s} &= +0.0005F_{x,rs} + 0.9931F_{y,rs} - 0.0037F_{z,rs} \\ F_{z,s} &= +0.0181F_{x,rs} + 0.0078F_{y,rs} + 1.0313F_{z,rs} \end{aligned} \quad (6-14)$$

Where subscript “r” and “rs” denote summated signal read by the wheel and motor dynamometers, respectively.

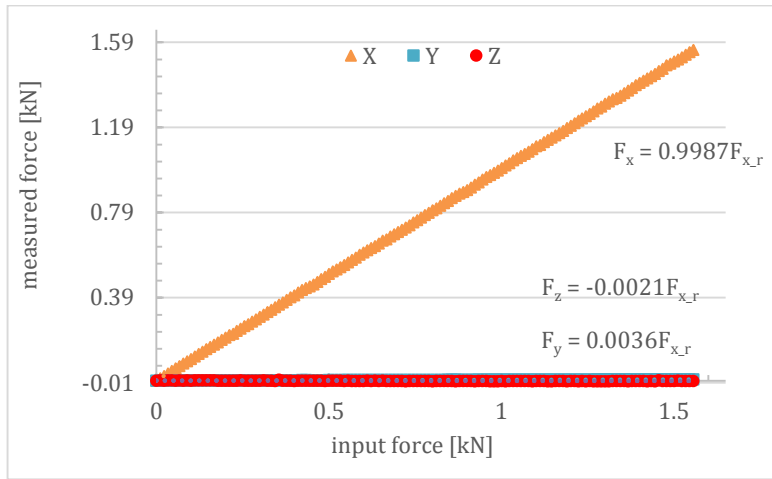


Figure 6-17: Quasi-static calibration and cross-sensitivity curves of the wheel dynamometer for input force in x-direction

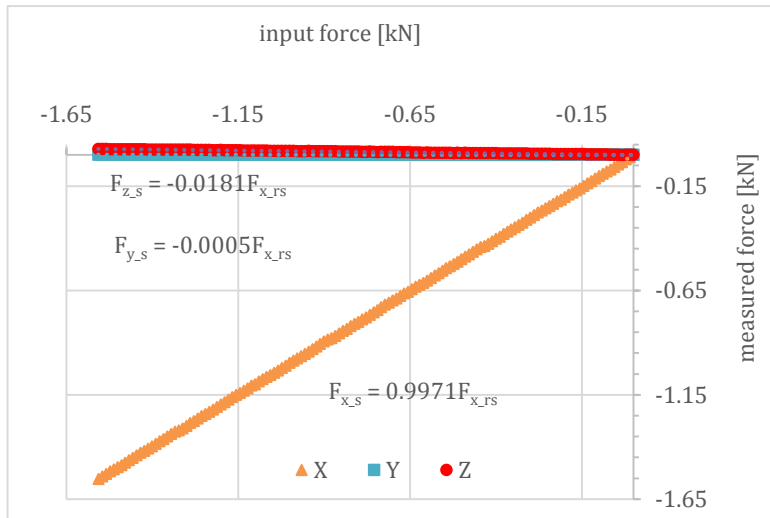


Figure 6-18: Quasi-static calibration and cross-sensitivity curves of the motor dynamometer for input force in x-direction

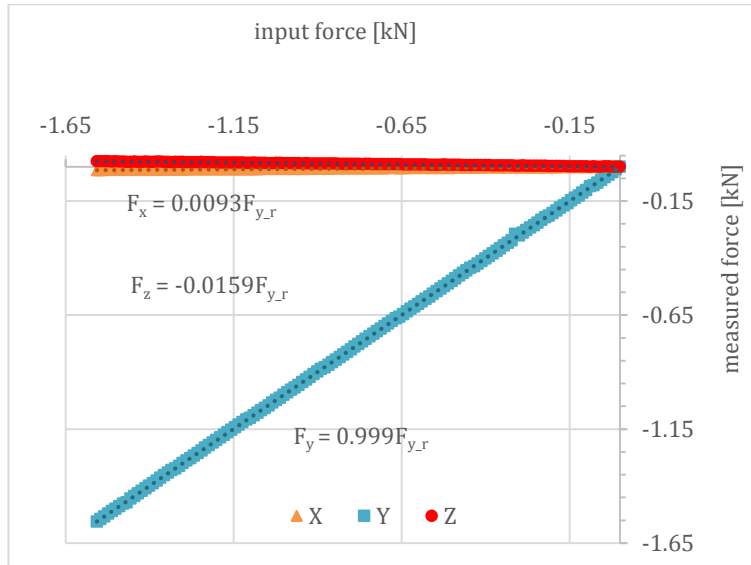


Figure 6-19: Quasi-static calibration and cross-sensitivity curves of the wheel dynamometer for input force in y-direction

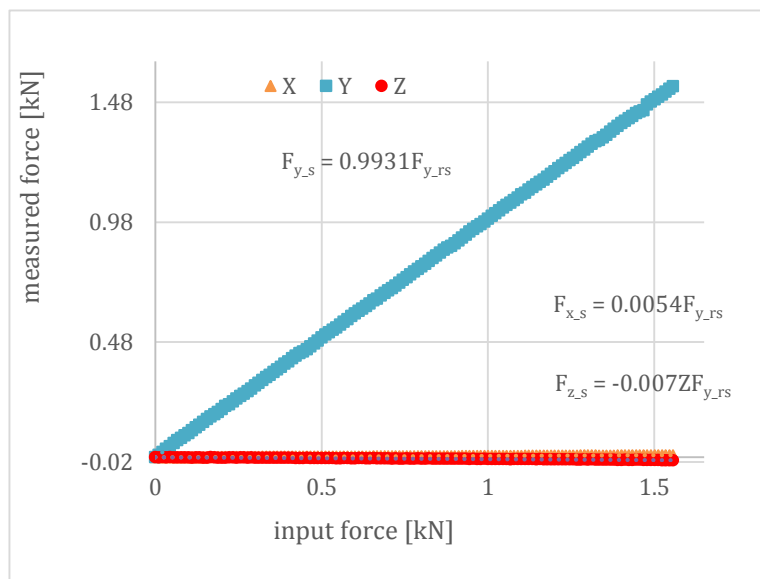
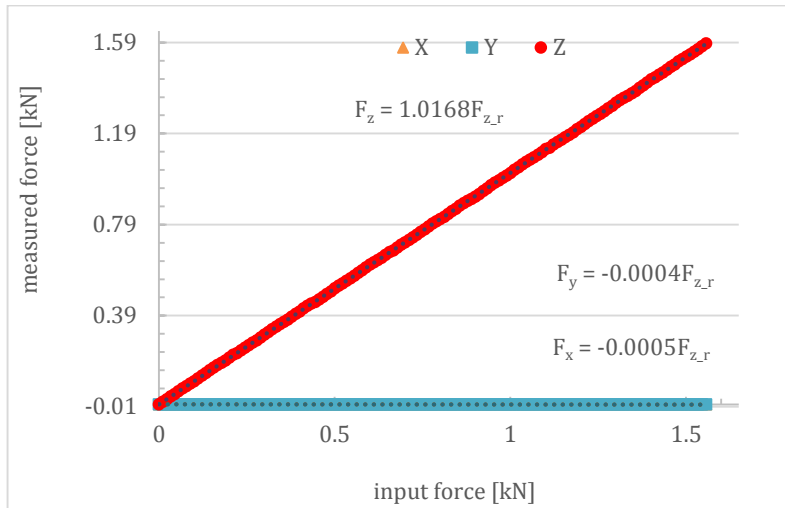
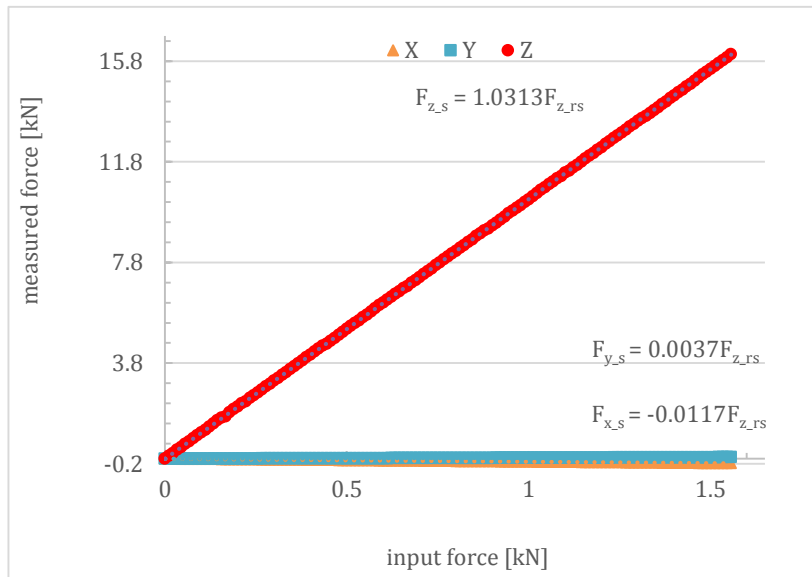


Figure 6-20: Quasi-static calibration and cross-sensitivity curves of the motor dynamometer for input force in y-direction



**Figure 6-21: Quasi-static calibration and cross-sensitivity curves of the wheel dynamometer for input force in z-direction**



**Figure 6-22: Quasi-static calibration and cross-sensitivity curves of the motor dynamometer for input force in z-direction**

The calibration results indicate that the linearity for the wheel dynamometer is <0.2% FSO and the motor dynamometer is less than 0.3% FSO. The calibration equations (Equations 9 and 10) suggest that the error between calibrated results and non-calibrated readings (individual sensors' readings) is less than 2% FSO. Therefore, the individual sensors' readings can be used for

estimating the moment components reacted at the dynamometers according to equations 2 to 4 with an error of less than  $\sim 2\%$  FSO.

Dynamic calibration was conducted using impact response of the dynamometers. The impact response of the dynamometers was obtained using a quartz impact force hammer (Kistler, Type 9724A). To this end, the base plate of the dynamometer was fixed to a rigid t-slotted base plate (2200 × 2500 × 250 mm) using four t-nuts and studs. This closely replicates the boundary conditions of the dynamometer in the rig, as the rig is assembled on top of the same t-slotted base plate. The force readings of the dynamometer for a hammer’s impact on the cover plates of the dynamometers were recorded. The frequency responses of the recorded impact response for three directions are shown in Figure 6-23 and Figure 6-24 for the wheel and motor dynamometers. The modal frequencies of the dynamometers are indicated in the frequency response functions.

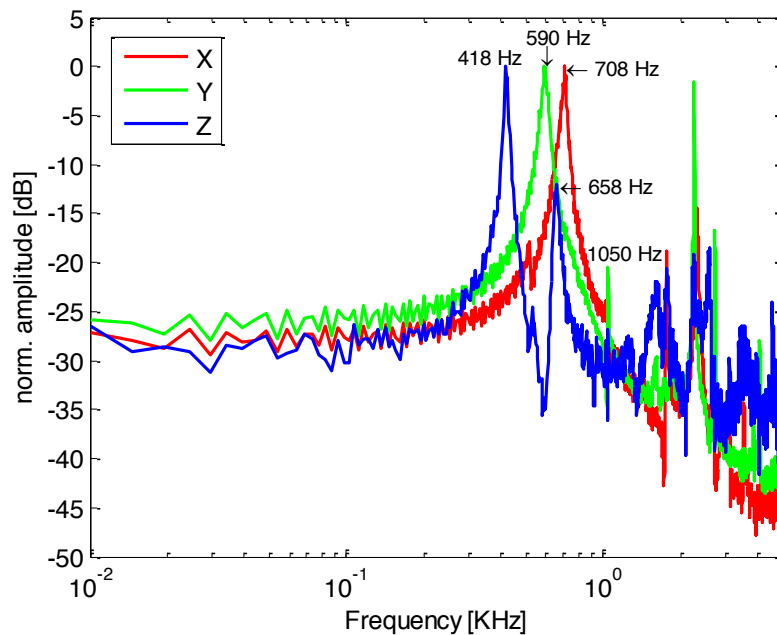


**Figure 6-23: Impact frequency response of the wheel dynamometer for an impact input in x,y,z-directions**

The results of the experimental modal analysis closely follow the natural frequencies of the FE model of the plates presented in Table 6-5 and Table 6-6. The stiffness values used in FE model may not exactly match the actual stiffnesses of the sensors. In addition, the boundary conditions

of the FE model are not exactly the same as that of the experiment. As a result, the minor discrepancies between the FE results and experiments are justifiable.

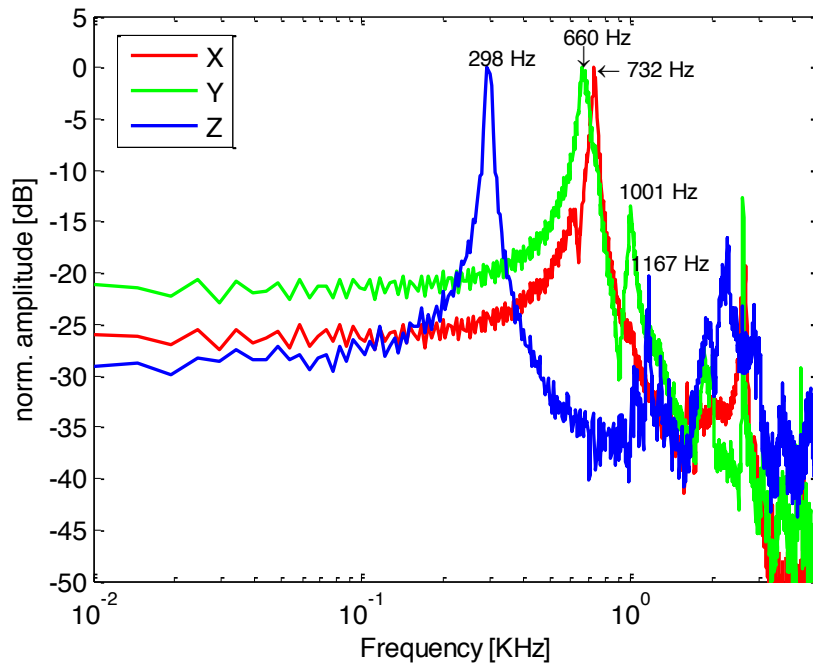


Figure 6-24: Impact frequency response of the motor dynamometer for an impact input in x,y,z-directions

### 6.1.7 Conclusions

A novel force measurement system using dynamometers for measuring the contact forces in a railroad testing facility is designed and developed. The dynamometers consist of piezo-electric load cells, which provide increased rigidity and improved dynamic range. The measurement system is capable of measuring all the six contact forces and moments. It is designed to measure forces up to 10 kN with less than  $\sim 0.1\%$  FSO accuracy for force components and less than  $\sim 2\%$  FSO for moment components.

The dynamometer is mounted in-line with the wheel-roller interface for minimizing the reaction moments of the creep forces. It sits in the load-path from the wheel-rail interface to the ground, ensuring that all the creep forces are reacted at the dynamometer. Proper arrangement of the highest quality load cells in the multi-component force platform leads to much higher resolutions

in force measurements. The designed configuration provides the rig with more accurate force measurements, functioning as a laboratory scale system in contrast to off-the-shelf products.

## 6.2 Contact Geometry Instrumentation

One of the research areas of contact mechanics is the normal contact problem. Both the contact geometry and normal pressure distribution are of great interest for contact mechanist to develop more accurate creep-creepage models as the contact patch dimensions and pressure distribution are inputs to the tangential contact theories. Reviewing the past and current roller rigs show that there is no known roller rig that is equipped with normal contact instrumentation. Additionally, there are just a few experimental studies on the normal contact using simple laboratory test setups, which are mostly based on static conditions [106] [107] [108] [109]. Poole [63], however, conducted a real time measurement of contact area through placing an array of 1 mm holes on top of a rail segment, and pumped compressed air through the holes. As the wheel travels on the rail, the blockage of the airflow determines the shape and size of the contact patch. The accuracy of this method is limited by the resolution of the hole-array and the speed of the traveling wheel. Placing the holes in the rail could also change the rail properties from the actual rail.

Reviewing the general literature on the experimental normal contact studies (not solely for wheel-rail interface) and consulting with industry experts, several techniques have been proposed to experiment the wheel-rail contact area. Pau et al. [110] categorize the methods, as follows:

**Impression Methods:** Insertion of thin film of carbon and ordinary white paper between the contacting elements, thus obtain a printed image of contact area. Other developments of this kind of method include the use of thin aluminium sheets, nitric acid etching and coloured paints removed with adhesive tape (a system known as 'Blue and Tape'). While most of the Impression techniques are useful in obtaining the extent of the real contact area, little or no information is supplied concerning contact pressure distribution. Although impression methods are not expensive, they can't be configured for real time measurements.

**Photoelasticity based method:** Photoelasticity is an experimental method to determine the stress distribution in a photoelastic materials, based on the principle that a light beam that impinges a surface can be variously refracted (or affected by total internal reflection if a prism is used),

depending on the stresses of the surface points. This could be used for contact area measurement, as well as tangential stress distribution. It, however, requires a photoelastic materials; hence it can't be used for railroad wheel-rail interface. Same is true for phase-contrast method and Nomarski interference technique. The former one requires a rough metallic surface and a flat glass coated with a metallic film on one side, and the latter one needs a rough aluminum surface with a flat silver-steel surface. These methods, however, could provide pressure distribution and might be configured for real time measurements.

Pressure sensitive media: Fuji Company, Tokyo, Japan supplies a pressure-sensitive film, called Prescale film, for measuring nominal contact area and contact pressure through a system of small microcapsules filled with liquid ( $2 \pm 25$  mm diameter) between two layers (two-sheet type). Pressure sensitive films, which are constrained by an upper limit for the maximum contact pressure measurable, can record contact information for a single measurement (not very suitable for real time measurements). Other examples include thin films of polyethyleneterephthalate (PET) and thin sensor (0.1mm thickness) by Tekscan Inc., Boston, MA. They are relatively cheap and can provide the pressure distribution.

Wave-based methods: The method works based on the fact that when two metallic surfaces are pressed against each other, the amount of energy (due to electromagnetic or ultrasonic waves) reflected by the contact interface tends to decrease with an increasing load. Correspondingly, the transmitted part increases. No quantitative law, however, has been formulated for the relation between reflected wave and applied pressure. Ultrasound reflection based methods are implemented as routine industrial non-destructive testing and can be configured for obtaining real-time graphical information about the state of contact.

Electrical and thermal based methods: These methods exploit electrical or thermal conduction to estimate the real contact area. They are limited, as electrical conduction is influenced by the presence of oxide layers on the surface, while thermal conduction is affected by the air gaps that always present at the contact interface.

As discussed there is no ideal method that can be used for railroad material and can measure contact area and tangential distribution in real time. Each method has its own advantages and disadvantages. Considering all the methods, a vision system for measuring the contact ellipse is

proposed. It can also detect the location of the contact patches in case there is more than one. Two high-resolution cameras look at the contact patch from two different angles (most likely perpendicular angles) to estimate major and minor axes of the contact ellipse. The design of the cradle is such that it can accommodate two high-resolution cameras looking at the contact (Figure 6-25). This method does not provide any information about the pressure distribution throughout the contact area. It, however, could be synchronized with other sensory measurement via Synqnet control network. As such, it can provide real time measurement of the contact area. The high-definition imaging, using advanced image-processing methods, need to be configured system, as the light diffraction, due to very close gap, could make erroneous results for measuring the exact location where wheel and roller meet.

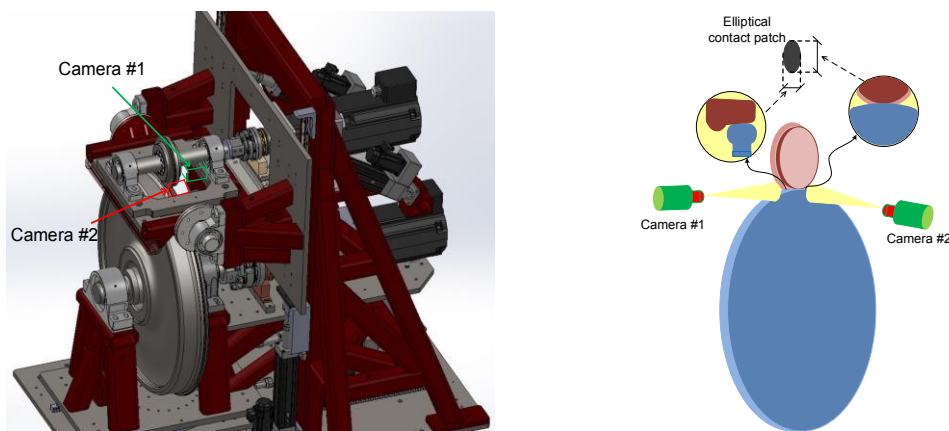


**Figure 6-25: The provisional design of the cradle for accommodating vision system (left) and schematic drawing of the proposed vision configuration for estimating the contact area (right)**

### 6.2.1 Additional Sensors

In addition to the contact geometry measuring system, a proper instrumentation system is proposed for measuring the relative displacement between the wheel and roller accurately. The proposed configuration for measuring these variables is shown in Figure 6-26. In this configuration, three laser sensors (proximity sensors) are configured such that the readings from the sensors are used to extract the relative displacement between the wheel and roller. The readings from sensors number 1 and 2 will be averaged to extract the lateral displacement of the roller. The ratio of difference between the readings from sensor # 1 and # 2 over the distance

between the sensors is used for calculating the angle of attack. Similarly, the reading from sensor #3 is used for calculating the cant angle.

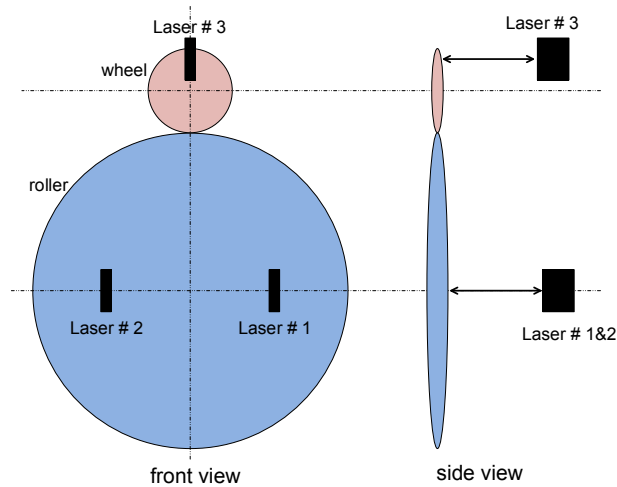


**Figure 6-26: The schematic drawing of the proposed configuration of laser sensors for measuring the relative displacements between the rotating bodies**

### 6.3 Control Architecture

A sophisticated powering scheme and control architecture is configured to actively drive all the components. It provides a unified command and feedback network between all the components with update rate of up to 48 kHz. The control architecture is developed based on the SynqNet data acquisition system offered by Kollmorgen (the motors supplier) highly compatible with the driving actuators. SynqNet motion control network is built over Ethernet link and provides a 100Mbps synchronous real-time connection between control nodes and axes [111]. It is configured in a ring topology between the host computer and control axes. Figure 6-27 shows the ring topology configured for the control scheme of the roller rig based on the SynqNet system. The ultra-high-performance QMP-SynqNet® card incorporates a 64-bit 1200MHz PowerPC processor for maximum axis count and speed. The controller offers servo update rates up to 48 kHz and can support up to 64 axes and 64 SynqNet nodes. As depicted in Figure 6-27 and Figure 6-28, the rig's control architecture includes a host computer that includes SynqNet platform (QMP-SynqNet-PMC card). The host computer, via Ethernet cable RJ45, connects to two S772 digital drives in series (the main servomotors drivers), then connects to 6 AKD drives

in series (the linear actuators drivers), then connects to SQIO-SQID cards for communicating with digital and analog (16-bit resolution) inputs and outputs. Finally, the SQIO-SQID cards connect back to the host computer. In order to have the best flexibility for communicating with input output signals, four Mixed Module I/O boards are stacked together that each provides 64 digital inputs, 64 digital outputs, 16 differential analog outputs, and 8 single ended analog inputs addressing 16 bit resolution.

The SyNqnet system uses a central motion processor to perform matrix computations based upon multiple inputs generating multiple outputs. MIMO (Multiple In Multiple Out) control systems use demand and feedback inputs, such as the actual torque and velocity, to compute new target data for output components such as drives and motors. SynqNet with a centralized processor, and minimized cable lengths, achieves fast cycle updates (max jitter < 1  $\mu$ s, and cycle time latency of  $\sim 25 \mu$ s) through the following methods [111]:

- SyNqnet has optimized programming that operates just above the hardware level with close coupling to controller and hardware design
- During network auto-setup – Discovery Mode – node distance is calculated by the controller to all nodes to reduce natural skew introduced over CAT5
- SyNqnet minimizes the data sent to components with a lightweight packet structure.
- During network auto-setup – Discovery Mode – node distance is calculated by the controller to all nodes to reduce natural skew introduced over CAT5 cable
- The Phase-locked loop technique is employed to generate stable frequencies and a constant ‘heartbeat’ to set master timing for guaranteed data delivery and synchronized communication to all nodes
- Flexible FPGA programming lets users modify background versus foreground task management to mitigate application requirements
- Robust software utilities to optimize timing and tuning of all nodes on a SynqNet network

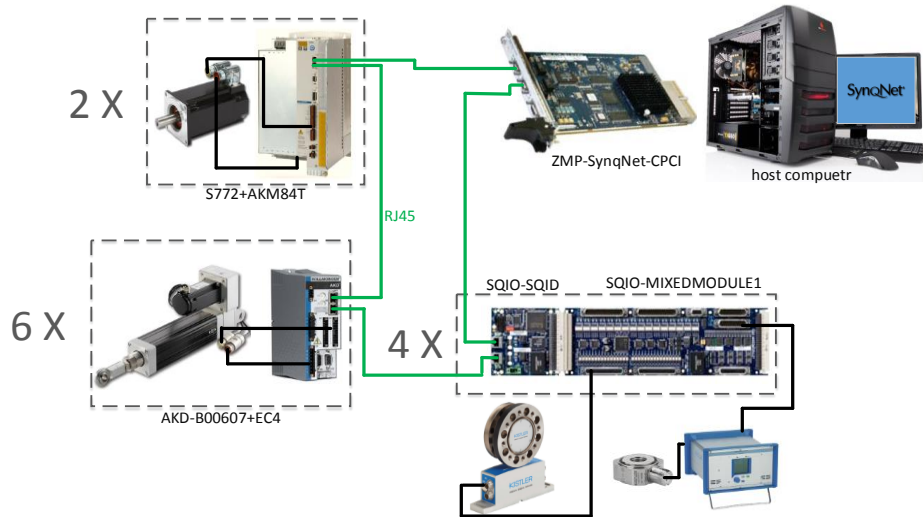


**Figure 6-27: Schematic diagram of the control architecture configured for the roller rig. The host computer that includes ZMP-SynqNet card connects to two S772 digital drives in series, then connects to 6 AKD drives in series, then connects to four SQIO-SQID cards in series, and finally connects back to the host computer.**

Another attractive aspect of the Synqnet system is its increased durability. The system is able to utilize a “Self-Healing,” model to activate parallel processes in the event of a node failure. The “Self-Healing” tolerance allows the system to sense if a node is disconnected and can shift that node’s process to a redundant node.

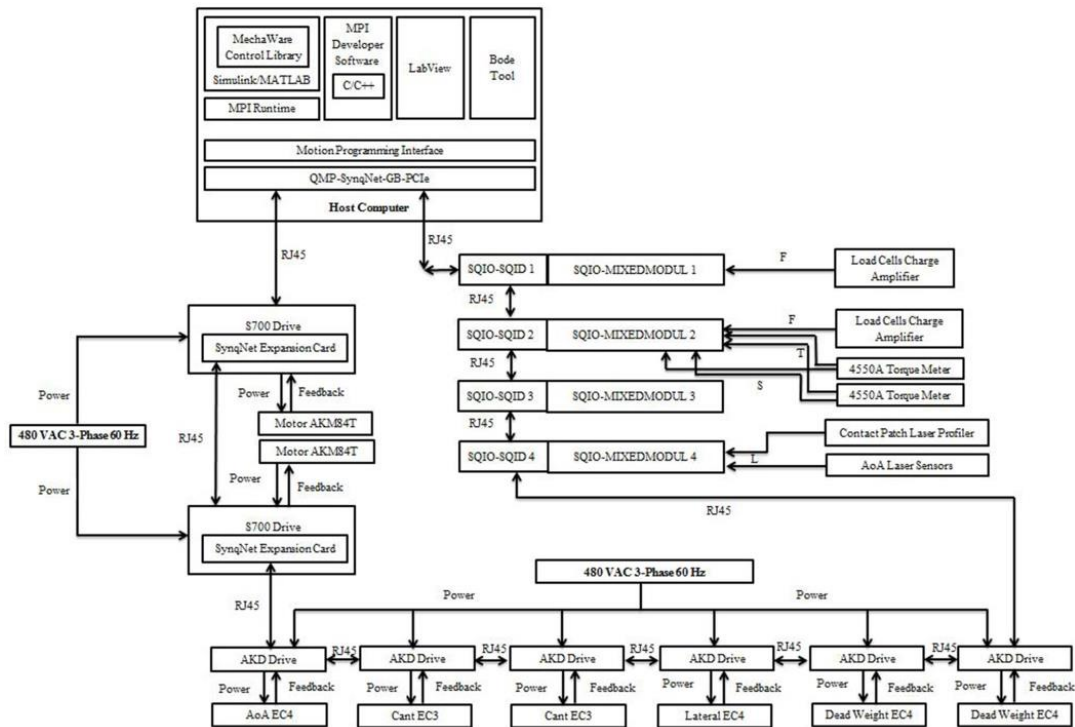


Figure 6-28: Block diagram of the control architecture of the rig

SynqNet supports various motion controllers such as Motion Programming Interface (MPI), MechaWare® and Bode Tool™ that could easily be linked to MATLAB, SIMULINK, C/C++, etc [83].

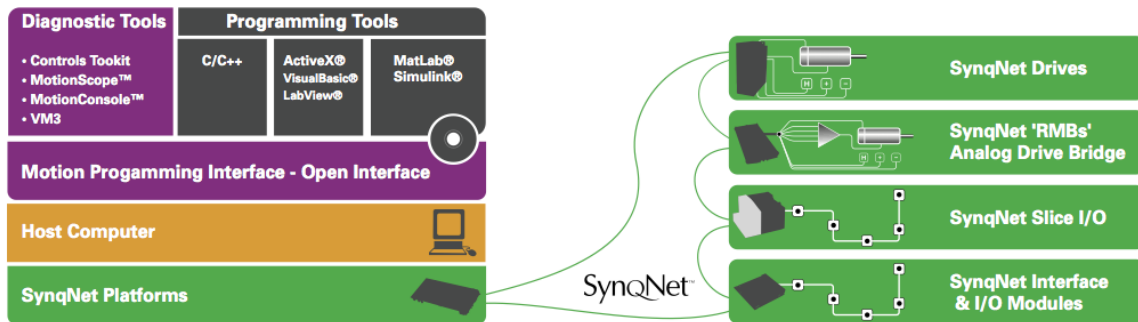


Figure 6-29: SynqNet supports various motion controllers [111]

The Motion Programming Interface (MPI) provides a library that defines a rich set of object-oriented, C/C++ language functions and data types. MPI allows engineers to integrate motion applications directly into machine software using familiar tools such as Microsoft Visual Studio.

The MPI library is built to run in most Windows environments and many real-time operating systems. It provides with the lowest latency command-to-motion execution, perfect for integration of real-time motion with vision or high-speed I/O.

MechaWare™ provides the ability to fine-tune performance and create custom solutions for complex controls challenges—in particular, issues of system resonance, vibration control and settling time. The MechaWare block library is used with MATLAB®/Simulink® to provide a graphical environment with full simulation capability, enabling engineers to easily program complex control system tasks and upload the code directly to any SynqNet® controller for immediate validation. MechaWare features include: a wide variety of Filters, State Observers, State Feedback, Coordinate Transformations, 64-bit (double precision) calculations with ZMP, complex gearing, following methods, gain switching, vibration control, sophisticated MIMO plant models, easily defined gantry control topology, and allows you to design your own custom control schemes. MotionConsole allows exercise motors, tune & configure all axes in your system. MotionScope allows full graphing and analysis of real-time motion data. Position, velocity, and numerous other critical motion parameters are displayed with the click of the mouse. Run all utilities locally or over a TCP/IP connection for remote diagnostics. Controls Toolkit allows for analyzing machine mechanical response, develop notch filters, and custom algorithms to tune and optimize machine performance. Controls Toolkit includes the BodeTool and FilterDesigner [111].

The powering scheme of the rig provides 150kVA power for the 200A load of the rig at 480VAC 3-phase. It guarantees least susceptibility to electromagnetic noise and assures safe operation for the rig and the personnel based on IEC and ISO standards. A control cabinet, shown in Figure 6-30, is configured for providing a unified user interface for control, safety, and power systems. It facilitates the cable management.

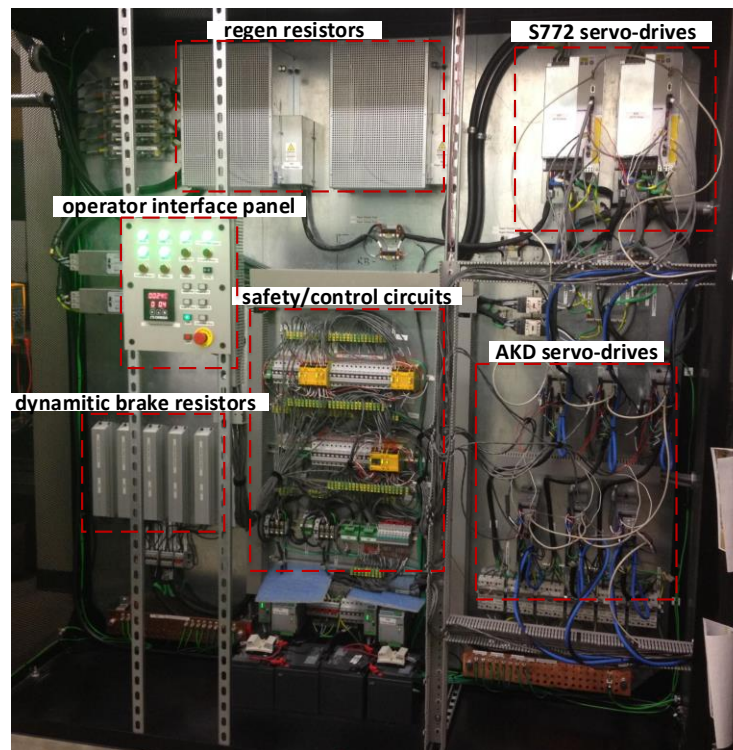


**Figure 6-30: The control cabinet of the rig including S700 drives, AKD drives, regenerative and dynamic brake resistors, safety/control circuits, etc. All the components are placed inside a Faraday cage and are controlled through operator interface panel.**

In order to have the best isolation between the control cabinet including the digital drives, and the rig, a dedicated electronics room, right next to the roller rig, is devoted for accommodating the control cabinet and all the safety, and powering elements. The room is equipped with an industrial cooling system for controlling the temperature and humidity of the electronics room.

## 7 Technical Survey of Contact Models

(This chapter was published in part in Vehicle System Dynamics journal [112]. Reproduced with permission.)

Rail vehicles are supported, steered, accelerated, and decelerated by contact forces acting in extremely small (around 1 cm<sup>2</sup>) wheel-rail contact areas. The behavior of these forces is quite complex. A broad interdisciplinary research is needed to understand, model and optimize the contact mechanics and dynamics problem. Many researchers have investigated the contact problem throughout the last century. Joost Kalker, in his prolific career, proposed different contact theories. Most notably, these are the FASTSIM algorithm for quickly evaluating the nonlinear creep-force law in vehicle dynamic simulations and the CONTACT program for the exact theory of rolling contact in 3D elastic half-spaces. In addition, other researchers (such as Polach, and Johnson) tried to tackle the contact problem and developed some contact models.

During past few decades, several review articles have been published on the contact mechanics problem. Each of these articles focuses on a different facet of the rolling contact problem and describes a different time period. Specifically, Sichani et al. [113] compares non-elliptical contact methods, including the most recent ones. Elkins [114] gives a broad overview of wheel-rail contact models developed up to 1991. Piotrowski and Chollet [115] review multipoint contact and non-Hertzian theories. Falomi et al. [116] summarize the methods for wheel-rail contact point determination. Knothe [117] gives a broad overview of contact models, including some very early models rarely mentioned elsewhere. Zaazaa and Schwab [118] focus specifically on Kalker's theories. Sugiyama and Suda [119] discuss the methods for detection of wheel-rail contact points, and so on.

The main objective of this chapter is to combine and classify multiple sources and give a comprehensive overview of the contact problem. It reviews the past and recent most influential works in the field and discusses the future developments. Most commonly used contact models and their recent advancements and derivatives are discussed in detail; all the simplifying assumptions for developing the models are reviewed, and the performance and functionality of the models are compared. Using software packages CONTACT and MATLAB, the performance

of tangential contact theories are compared. The chapter concludes with the open research areas in the theory of wheel-rail contact from an experimental point of view.

## 7.1 The law of Coulomb-D'Amontons

Assume a rigid wheel is rolling down a rigid rail, as shown in Figure 7-1. A normal force ( $F_n$ ) and a tangential force ( $F_t$ ), which is a vector in the plane of contact area act on the wheel. The translational velocity of the wheel is  $\mathbf{v}$  and its circumferential velocity at the contact is  $\mathbf{c}$ . The creepage, differential speed at the contact, is given by:

$$\mathbf{w} = \mathbf{v} + \mathbf{c} \quad (7-1)$$

The law of Coulomb-d'Amontons states a relation between normal and tangential forces as:

$$\begin{cases} F_t = -\frac{\mu F_n \mathbf{w}}{|\mathbf{w}|} & \mathbf{w} \neq 0 \\ |F_t| \leq \mu F_n & \text{otherwise} \end{cases} \quad (7-2)$$

Where  $\mu$  is the coefficient of friction. Although the hypothesis of rigidity of wheel and rail is too crude for modeling wheel-rail interaction, the Coulomb's law has been used, in a local sense, for developing contact models [120].

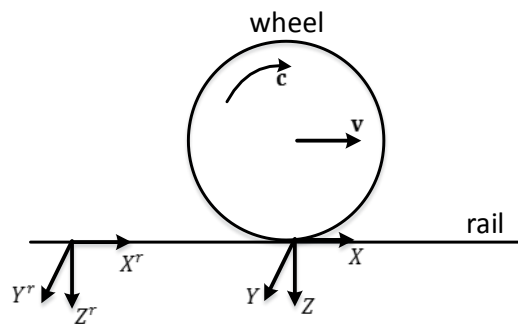


Figure 7-1: Schematic drawing of a wheel rolling over a rail showing the fixed and moving coordinate systems

## 7.2 General statement of Wheel-rail rolling contact problem

In order to define the wheel-rail contact problem, two coordinate systems are considered: A fixed reference coordinate system ( $X^r Y^r Z^r$ ) attached to the rail of which the  $X^r$ -axis is in the direction of wheel rolling on the rail,  $Z^r$ -axis points vertically downward, and  $Y^r$ -axis is obtained from right hand rule and a coordinate system ( $XYZ$ ) that moves with the contact patch over the rail with a rolling velocity vector of the wheel  $\mathbf{v}$ , as shown in Figure 7-1. So, we have:

$$X = X^r - Vt \quad (7-3)$$

Where  $t$  is the time, and  $V = |\mathbf{v}|$  is the magnitude of the rolling velocity. In the point of contact, the circumferential velocity of the wheel ( $\mathbf{c}$ ) is almost opposite to the rolling velocity ( $\mathbf{v}$ ). When the wheel is accelerating, braking, or steering, small slip occurs between the wheel and the rail. The rigid slip of the wheel over the rail, as defined in Equation (7-1), includes a translational term in the ( $X, Y$ )-plane of contact, and a rotation term around the  $Z$ -axis [121]:

$$\mathbf{w} = \mathbf{v} + \mathbf{c} = V[(v_x - \varphi y)\mathbf{i} + (v_y + \varphi x)\mathbf{j}] \quad (7-4)$$

Where  $\mathbf{i}, \mathbf{j}$  are unit vectors of  $X, Y$  axes, respectively.  $v_x, v_y$ , and  $\varphi$  are longitudinal, lateral, and spin creepage, respectively. The longitudinal creepage is connected with tractive and braking actions. The lateral creepage is connected with the angle of attack (the angle between the wheel plane and the plane of  $Y = 0$ ), and sideslip. The spin creepage is connected with the conicity of the wheel ( $\gamma$ ). The creepage definitions and formulations are discussed and detailed in Section 7.4.1.

The hypothesis of rigid wheel and rail results in a point contact, which does not allow investigation of adhesion and slip phenomena in the contact patch. So, although rigid wheel and rail hypothesis may be useful for finding the location of contact point, it cannot be used to investigate contact forces. Hence, wheel and rail need to be regarded, at the very least, as linearly elastic.

Due to elasticity of the wheel and the rail, the two bodies will deform under external loading and touch along a contact area instead of a contact point, as shown in Figure 7-2. The centers of the bodies are pressed toward each other, and the distance between the deformed surfaces is the summation of the deformations and undeformed locations, as given by:

$$D(x, y) = h(x, y) + u_z(x, y) - d \quad (7-5)$$

Where  $h(x, y) = |h^w(x, y)| + |h^r(x, y)|$  is the distance between the undeformed surfaces,  $d$  is the elastic approach, and  $u_z(x, y) = |u_z^w(x, y)| + |u_z^r(x, y)|$  is the normal elastic deformation of the bodies, as per Figure 7-2. In reality, the bodies cannot penetrate, and the normal pressure at the contact ( $p$ ) is compressive, so the normal contact problem can be formulated as:

$$\begin{cases} D(x, y) = 0, & p(x, y) > 0 & (x, y) \in U \text{ contact area} \\ D(x, y) > 0, & p(x, y) = 0 & (x, y) \in U_e \text{ exterior area} \end{cases} \quad (7-6)$$

The problem of investigating the geometry of the contact (shape, area, etc.), and formulating the normal pressure distribution inside the contact patch is called the normal contact problem.

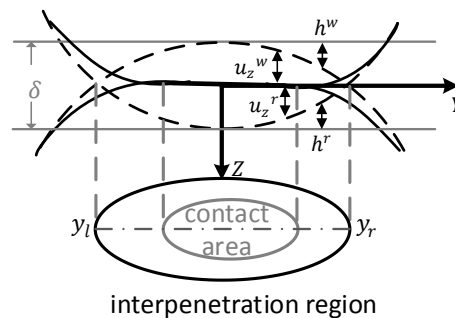


**Figure 7-2: Schematic drawing of the interface of two elastic bodies in contact showing deformed and undeformed states of the interface. The interpenetration region and the contact area are shown in the bottom (adapted from [122]).**

As a consequence of the compression and the elasticity, the displacement of a particle of wheel ( $\mathbf{u}^w$ ) is different from the displacement of a particle of the rail ( $\mathbf{u}^r$ ). The surface displacements of  $\mathbf{u}^w$  and  $\mathbf{u}^r$  are in the  $XYZ$ -coordinate system, which moves with the contact. In order to take the elastic deformation into account, the true slip ( $\mathbf{s}$ ) is defined as the summation of the rigid slip,

defined in Equation (7-4), and the material derivative of the relative displacement of the wheel and rail particles ( $\mathbf{u} = \mathbf{u}^w - \mathbf{u}^r$ ):

$$\mathbf{s} = \mathbf{w} + \dot{\mathbf{u}}(x, y, t) \quad (7-7)$$

The particles of wheel and rail flow through the XYZ-coordinate system with a velocity of  $\mathbf{c}$  (wheel) and a velocity of  $\mathbf{v}$  (rail), which are both approximated by  $(-V, 0)$ . Therefore:

$$\mathbf{s} = V[(v_x - \varphi y)\mathbf{i} + (v_y + \varphi x)\mathbf{j}] - V(\partial\mathbf{u}/\partial x) + (\partial\mathbf{u}/\partial t) \quad (7-8)$$

In case of steady-state contact problem,  $(\partial\mathbf{u}/\partial t)$  is zero.

According to the definition of true slip ( $\mathbf{s}$ ), the Coulomb's law (Equation (7-2) in a local sense, is refined as:

$$\begin{cases} \boldsymbol{\sigma}_t = -\frac{\mu p \mathbf{s}}{|\mathbf{s}|} & |\mathbf{s}| \neq 0, \text{ slip area} \\ |\boldsymbol{\sigma}_t| = |[\sigma_{tx} \quad \sigma_{ty}]^T| \leq \mu p & |\mathbf{s}| = 0, \text{ adhesion area} \end{cases} \quad (7-9)$$

Where  $p$  is the contact normal pressure, and  $\sigma_{tx}, \sigma_{ty}$  are the longitudinal and lateral creep forces per unit area (tangential stress), respectively. Therefore, the total longitudinal, lateral creep forces, and spin creep moment can be formulated as:

$$\begin{cases} F_x = \iint_{\text{contact area}} \sigma_{tx} dx dy \\ F_y = \iint_{\text{contact area}} \sigma_{ty} dx dy \\ M_\varphi = \iint_{\text{contact area}} (x\sigma_{ty} - y\sigma_{tx}) dx dy \end{cases} \quad (7-10)$$

The problem of studying the relationship between creepage  $(v_x, v_y, \varphi)$  and creep forces  $(T_x, T_y, M_\varphi)$ , or particularly tangential shear stress distribution over the contact patch area is called tangential contact problem.

The division of the contact problem into normal and tangential problems is justifiable as the friction forces transmitted (tangential stress distribution) between the wheel and rail usually has negligible influence on the size of the contact patch and pressure distribution. Kalker [70] discusses in detail the effect of geometry and elasticity symmetries between the contacting bodies on the coupling between normal and tangential problems. He concludes when the contacting bodies have the same elastic constants, which is usually the case for the wheel-rail contact, the tangential stresses have no influence on the normal pressure [70].

## 7.3 Normal Contact

### 7.3.1 Hertz's Theory

In 1880's, Hertz developed his influential work on contact mechanics, which calculated the contact area and the normal pressure distribution carried by it [71]. Although Hertzian theory rests on a number of rather restrictive assumptions, it is still widely used in studying wheel-rail contact mechanics and dynamics, and serves as a foundation for many tangent contact theories, both empirical and analytical [117] [123].

Hertz theory is developed based on the following key assumptions [123]:

- The kinematic equations and the materials elastic properties are linear.
- Wheel and rail material exhibit completely elastic behavior (no plastic deformation).
- Wheel and rail material is homogeneous and its properties are isotropic.
- The contact surfaces are perfectly smooth and there is no friction between them.
- Contact surfaces curvature is constant within the contact patch.
- Contact surfaces radii of curvature are much larger than the dimensions of the contact patch.

Under these assumptions, the contact area is an ellipse with a semi-ellipsoid normal pressure distribution. In the undeformed state, rail and wheel penetrate, as shown in Figure 7-3. The distance between two opposing points on wheel and rail is defined as  $D(x,y)$ ; the distance is negative where two bodies intersect and there exists contact between the bodies, and is positive otherwise. Hertz assumes that the distance  $D(x,y)$  is a quadratic expression [121]:

$$D(x,y) = Ax^2 + By^2 - d \quad (7-11)$$

With

$$A = \frac{1}{2} \left( \frac{1}{R_{wx}} + \frac{1}{R_{rx}} \right) \tag{7-12}$$

$$B = \frac{1}{2} \left( \frac{1}{R_{wy}} + \frac{1}{R_{ry}} \right) \tag{7-13}$$

Where  $R_{wx}$  and  $R_{wy}$  are longitudinal (X-axis) and lateral (Y-axis) radii of curvature of the wheel profile at the contact point. Similarly,  $R_{rx}$ , and  $R_{ry}$  are longitudinal and lateral radii of curvature of the rail profile at the contact point.  $d$  is the depth of penetration.

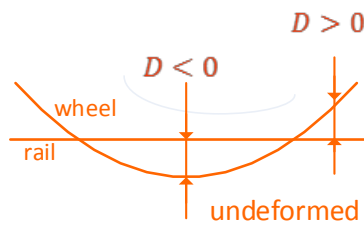


Figure 7-3: Wheel-rail interface for plane X=0 in the undeformed state

The sign of each radius is important, and it depends on the convexity or concavity of the curvature. Each radius is positive if the curvature center is inside the body. Most of the time, the longitudinal wheel radius and the lateral rail radius are positive (convex). The lateral wheel radius, however, at the contact point can be positive (convex) or negative (concave).

There are multiple formulations to the Hertzian problem. Two most commonly used approaches for wheel-rail contact applications are presented here:

Garg [124] defines the major ( $a$ ) and minor ( $b$ ) axes of the contact ellipse as:

$$a = m \left[ 3\pi N \frac{K_1 + K_2}{4K_3} \right]^{1/3} \tag{7-14}$$

$$b = n \left[ 3\pi N \frac{K_1 + K_2}{4K_3} \right]^{1/3} \tag{7-15}$$

Where  $N$  is the normal force at the contact and:

$$K_1 = \frac{1 - \nu_w^2}{\pi E_w}, \quad K_2 = \frac{1 - \nu_r^2}{\pi E_r}, \quad K_3 = \frac{1}{2} \left[ \frac{1}{R_{wx}} + \frac{1}{R_{wy}} + \frac{1}{R_{rx}} + \frac{1}{R_{ry}} \right] \quad (7-16)$$

Where subscripts  $w, r$  denotes wheel, and rail properties, respectively.

The coefficients  $m$ , and  $n$  in the above equations depend on the ratio of  $\frac{K_4}{K_3}$ , where  $K_4$  is defined as:

$$K_4 = \frac{1}{2} \left[ \left( \frac{1}{R_{wx}} + \frac{1}{R_{wy}} \right)^2 + \left( \frac{1}{R_{rx}} + \frac{1}{R_{ry}} \right)^2 + 2 \left( \frac{1}{R_{wx}} - \frac{1}{R_{wy}} \right) \left( \frac{1}{R_{rx}} + \frac{1}{R_{ry}} \right) \cos 2\theta \right]^{1/2} \quad (7-17)$$

Where  $\theta$  is the angle between the normal planes that contain the curvatures  $\frac{1}{R_{wx}}$  and  $\frac{1}{R_{rx}}$  (commonly known as cant angle). The coefficients  $m$ , and  $n$  are given in Table 7-1 as a function of  $\theta$ , which is defined as:

$$\theta = \cos^{-1} \left( \frac{K_4}{K_3} \right) \quad (7-18)$$

**Table 7-1: Coefficients  $m$ , and  $n$  for different values of  $\theta$  [124]**

$\theta$ (deg)	$m$	$n$	$\theta$ (deg)	$m$	$n$	$\theta$ (deg)	$m$	$n$
0.5	61.4	0.1018	10	6.604	0.3112	60	1.486	0.717
1.5	36.89	0.1314	20	3.813	0.4123	65	1.378	0.759
2	27.48	0.1522	30	2.731	0.493	70	1.284	0.802
3	22.26	0.1691	35	2.397	0.530	75	1.202	0.846
4	16.5	0.1964	40	2.136	0.567	80	1.128	0.893
6	13.31	0.2188	45	1.926	0.604	85	1.061	0.944
7	9.79	0.2552	50	1.754	0.641	90	1.000	1.000
8	7.86	0.285	55	1.611	0.678			

In addition to Garg's formulation, Ayasse and Chollet [123] present a different set of formulation to calculate the major and minor axes for the elliptical contact patch. In their formulation, the

wheel and rail are made of the same material, and the contact ellipse radii's exact values can be determined via:

$$a = m \left( \frac{3N(1 - \nu^2)}{2E(A + B)} \right)^{\frac{1}{3}} \quad (7-19)$$

$$b = n \left( \frac{3N(1 - \nu^2)}{2E(A + B)} \right)^{\frac{1}{3}} \quad (7-20)$$

In this case,  $a$  is the longitudinal semi-axis (along the direction of rolling), and  $b$  is the transverse semi-axis (caution must be used, since some authors use an opposite convention). The magnitudes of these major and minor axes will vary depending on the location of the wheel-rail contact point due to the fact that the wheel and the rail's transverse curvatures are non-constant.

The Hertzian coefficients  $m$  and  $n$  can be determined by interpolating from tabulated information (Table 7-1), or by calculating the elliptical integrals [125]:

$$m = \left( \frac{2g^2 \mathbf{E}(e)}{\pi} \right)^{\frac{1}{3}} \quad (7-21)$$

$$n = \left( \frac{2\mathbf{E}(e)}{\pi g_{ab}} \right)^{\frac{1}{3}} \quad (7-22)$$

Where:

$$g_{ab} = \frac{a}{b} \quad (7-23)$$

$$e = \left( 1 - \frac{1}{g_{ab}^2} \right) \quad (7-24)$$

and  $\mathbf{E}(e)$  is the complete elliptical integral of the second kind [125]:

$$\mathbf{E}(e) = \int_0^{\pi/2} \sqrt{1 + e^2 \sin^2(\varrho)} d\varrho \quad (7-25)$$

Hertzian theory assumes an semi-ellipsoid normal pressure distribution over the contact area exerted on both the wheel and rail, which is defined as:

$$p(x,y) = \frac{3N}{2\pi ab} \sqrt{1 - (x/a)^2 - (y/b)^2} \quad (7-26)$$

Where  $x$ , and  $y$  are the coordinates of the point inside the contact area in the  $XY$ -plane (Figure 7-4).

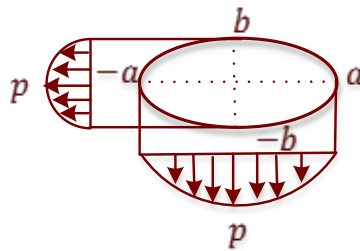


**Figure 7-4: Semi-ellipsoid normal pressure distribution**

The main limitations of Hertzian contact theory are the assumption of one-point contact, the assumption that ellipse radii are much smaller than the contact surfaces' radii of curvature, and the assumption that these curvatures are constant in the vicinity of the contact point. As a result, the dimensions of contact patch given by Hertzian theory are often a poor representation of the true contact shape, primarily due to non-constant surface curvatures [117] [70].

### 7.3.2 Non-Hertzian Models

The main limitations of Hertzian contact theory are the assumptions that there is one-point contact, the ellipse semi-axes are much smaller than the contact surfaces' radii of curvature, and that these curvatures are constant in the vicinity of the contact point (Figure 7-5). As a result, the dimensions of contact patch given by Hertzian theory are often a poor representation of the true contact shape, primarily due to non-constant surface curvatures and multiple contact zones [70,117]. The curvatures of both wheel and rail can significantly vary through the width of the contact patch, particularly for the case of worn wheels and rails in the flange throat contact.

A number of non-Hertzian and semi-Hertzian normal contact theories have been used to better describe wheel-rail normal contact [115,126]. Some of these theories are modifications of

Hertzian theory, and some are based on different principles. Normal contact theories can be classified in three main categories [115]:

- i. Kalker's non-Hertzian models
- ii. Approximate multi-Hertzian models
- iii. Approximate virtual penetration models

#### **7.3.2.1 Kalker's Non-Hertzian Models**

The most successful non-Hertzian model (as applied to wheel-rail geometry) is Kalker's exact three-dimensional rolling contact theory, which has been implemented in software CONTACT. This software, which numerically solves the normal and tangential contact problems, will be discussed later.

Like Hertzian model, Kalker's exact theory presents wheel and rail as elastic half-spaces with surface curvature radii much greater than the dimensions of the contact patch. The theory, however, is able to deal with non-elliptic and multi-contact patches cases very accurately. The theory is discussed in detail in Kalker's works [121,127]. This numerical method is considered to be very accurate for non-Hertzian, non-conformal thread contacts, i.e. cases of contact between wheel tread and rail head in which contact patch shape deviates from Hertzian shape, but the contact is not yet conformal [123,128].

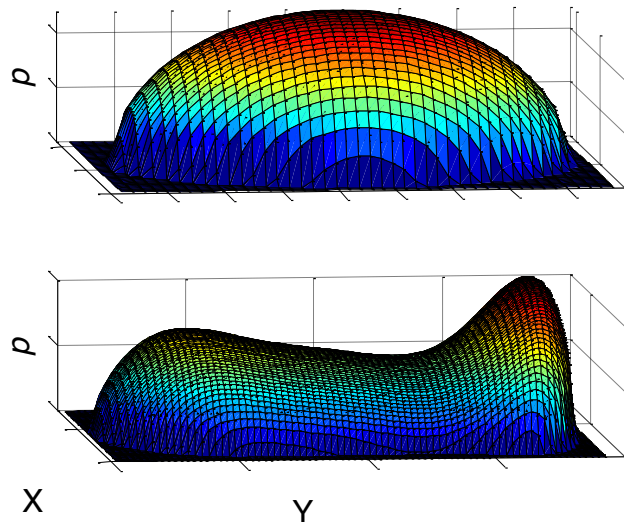


**Figure 7-5: Hertzian vs Non-Hertzian normal pressure distribution**

One of the common non-Hertzian cases is conformal contact such as contact between hollow wheel tread and rail head, or between flange root and gage corner. The modified version of Kalker’s exact theory, known as conformal contact theory or Li-Kalker theory [129,130], allows solving conformal contact cases. Vollebregt et al. [131] incorporated conformal contact solution into the CONTACT algorithm, and recent versions of CONTACT have the option of using the conformal contact theory. The conformal contact theories are discussed in more detail in “Other Advancements of Rolling Contact” section.

Since CONTACT is relatively computationally expensive for solving contact problem, it is not suitable for vehicle dynamics simulations that need online calculation of the contact for each time step (though some software packages use pre-calculated tables generated with CONTACT). Therefore, fast/approximate methods are introduced to solve the normal contact problem [115].

### 7.3.2.2 Approximate multi-Hertzian models

Approximate models based on presenting the interface between contacting bodies as a series of Hertzian ellipses and often representing an equivalent ellipse instead of multiple ellipses are known as multi-Hertzian models. Sauvage [115,132] proposed calculating the interpenetration of surfaces based on Hertzian theory, then subtracting this interpenetration from the initial profiles, and finally, calculating the new Hertzian interpenetration of these modified profiles (Figure 7-6).

The approach allows calculating the dimensions of multiple contact ellipses. Sauvage [115,132] also incorporated an innovation into his method for determining secondary ellipses in addition to the main ellipse; however, little information about this aspect of the method was published. Piotrowski and Chollet [115] proposed modifying this method to use Boussinesq deformation rather than Hertzian deformation in order to avoid false “secondary contacts” adjacent to the border of the first contact. This makes the deformation distance a bell-shaped curve rather than a semi-ellipsoid (Figure 7-6).

Sauvage’s method [132] for determining secondary contacts remained unexplained until Pascal et al. [133] developed their rigid multi-Hertzian method. They introduced the concept of “gutters” as the forbidden contact areas. Using the gutters’ edges information, they could locate local maxima in the rigid interpenetration curve; hence determining the secondary ellipses. This method avoids instabilities due to discontinuous contacts and develops smooth continuous contact forces during dynamical simulations.

Pascal et al. [134,135] used pre-computed knowledge of the necessary contact parameters (the contact angle, rolling radii, aspect ratio of ellipse, and wheelset roll angle) as a function of lateral shift of the wheelset for calculating the contact patches. Then, an equivalent ellipse was calculated such that the resultant contact forces are kept the same under the same conditions. Similarly, Ayasse et al. [136] proposed pre-calculated tables and an analytical formulation of the jump overlap as a function of the initial normal load for simplifying the multi-Hertzian contact calculations. Although the equivalent ellipse can be used for dynamic simulation of rail vehicles, it is not useful for studying complex phenomena such as wear prediction where surface stress analysis is required [115]. The pre-calculated tables or analytical formulations needed for these methods do not allow them to be used for applications where profiles vary along the track [115].

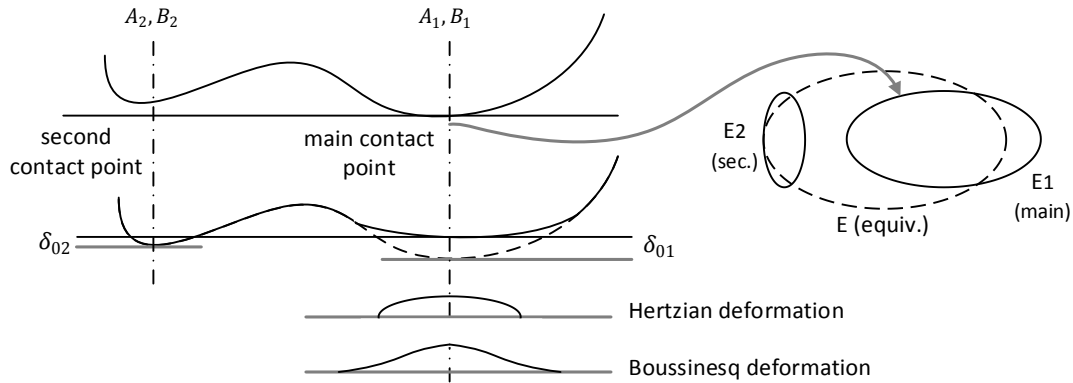


**Figure 7-6: Determination of multiple ellipses using Multi-Hertzian methods and representing them by an equivalent ellipse (adapted from [115])**

### 7.3.2.3 Approximate virtual penetration models

In addition to multi-Hertzian contact, another approximate method known as virtual penetration method has been used for solving the normal contact problem. In the concept of virtual penetration, the elastic deformations ( $u_z(x, y)$  in Equation (7-5) are neglected and it is assumed that bodies can rigidly penetrate into each other, as shown in Figure 7-2. The method assumes that the wheel and rail are two bodies of revolution (in case of flat rail, rail is a body of extrusion;  $A = 1/(2R_{wx})$ ). Since the wheel is body of revolution, a semi-elliptical normal stress distribution similar to Hertz theory assumed in the direction of rolling. That is why the method is also called semi-Hertzian. Thus, the distance between the penetrated bodies (similar to Equation (7-5)) is given by:

$$D(x, y) = Ax^2 + h(y) - d_0 \quad (7-27)$$

Where  $d_0$  is the virtual penetration at the first point of contact. It is suggested to be less than the elastic approach ( $d$ ), as Hashemi et al. [137] that the interpenetration region encircles the contact area when the influence function describing the normal deflection of bodies is unidirectional (Figure 7-2). Observations [138] showed that  $d_0 = d/2$  (half of the elastic approach taken as the virtual penetration) gives a good approximation of the contact area with the contour of the interpenetration region. Piotrowski et al. [122] and Linder [139] used a virtual penetration value of  $d_0 = 0.55d$  based on numerous tests and comparison of results with CONTACT program.

Equation (7-33) determines the contact area as the region where  $D(x, y) \leq 0$ . For the sake of calculations, positive values of  $D$  (exterior area) are taken as  $D = 0$ . The contact patch is symmetrical around the line  $x = 0$ , so the leading/trailing edges of the contact area (interpenetration region), as a function of lateral coordinate  $y$ , are:

$$x_l(y) = -x_t(y) = \sqrt{-D(0, y)/A} \quad (7-28)$$

According to the assumed semi-elliptical stress distribution, the normal pressure distribution is:

$$p(x, y) = \frac{p_0}{x_l(0)} \sqrt{x_l^2(y) - x^2} \quad (7-29)$$

Where  $p_0$  is the maximum pressure at the contact. Piotrowski et al. [122] used the deflection ( $d$ ) at the first point of the contact ( $x, y = 0, 0$ ) for calculating the maximum pressure ( $p_0$ ). According to the half-space assumption, the elastic deflection is equally shared by the contacting bodies [122]. Thus, the normal deflection, using the Boussinesq's function, is given by:

$$\frac{d}{2} = \frac{1 - \nu^2}{\pi E} \frac{p_0}{x_l(0)} \int_{y_l}^{y_r} \int_{x_t}^{x_l} \frac{\sqrt{x_l^2(y) - x^2}}{\sqrt{y^2 + x^2}} dx dy \quad (7-30)$$

Equation (7-30) gives the maximum pressure as a function of the given elastic approach. Then, the normal loading at the contact can be calculated by integrating of the pressure distribution (Equation (7-35)) throughout the interpenetration area. The comparison of the normal load results with those from CONTACT [122] showed a good agreement for a broad range of contact conditions including multi-point contact. Contact zone comparison, however, showed some differences especially for slender contact areas. So, Piotrowski et al. [122] proposed a method for refining the shape of the contact area by using the theory of Hertz. The length ( $Q$ ) and width ( $W$ ) of the interpenetration region are calculated as:

$$Q = \sqrt{4d_0/A}, \quad W = \sqrt{4d_0/B} \quad (7-31)$$

According to the ratio of  $Q/W$ , the ratio of  $A/B$  is redefined, and consequently a coefficient ( $\beta$ ) based on Hertzian table is introduced. Then, the corrected length and width of the contact area are proposed as:

$$Q_c = \sqrt{\beta QW}, \quad W_c = \sqrt{QW/\beta} \quad (7-32)$$

According to the corrected width of the interpenetration area, the separation distance in lateral direction ( $D'(0,y)$ ) is corrected (contracted or stretched) such that the first point of contact stays at its place.

Linder et al. [139,140] proposed similar procedure with different integration method for calculating the contact area and pressure (Figure 7-7). Ayasse et al. [141] proposed another semi-Hertzian model of contact known as STRIPES. The interpenetration region is discretized to strips parallel to the direction of rolling. On each strip the Hertzian conditions are considered locally. Local stresses are calculated on each strips; FASTSIM algorithm is adapted for obtaining tangential stresses. A curvature smoothing method is proposed accordingly. The accuracy of the method is compared with CONTACT program for different conditions [141,142]; results show that the method is reliable and fast for non-Hertzian cases and exact for Hertzian cases [142]. In general, the virtual penetration methods [122,141] have the advantage of accounting for the influence of curvature in the contact patch on local spin.

Sichani et al. [113] discussed and compared the virtual penetration methods in terms of contact patch prediction, contact pressure and traction distribution. Although the methods are faster than CONTACT, the results [113] show that the contact patch and pressure distribution predictions by them could deviate from CONTACT for some contact conditions. So, Sichani et al. [143] modified the virtual penetration method for taking the effect of elastic deformation into account. Two coefficients are introduced for approximating the deformation ( $h(x,y)$ ) from the undeformed distance ( $u_z(x,y)$ ) between the contacting bodies. The coefficients are estimated based on the assumption of Hertzian contact. The method is implemented in an algorithm called ANALYN, and the results show improved accuracy in predicting contact patch [143].

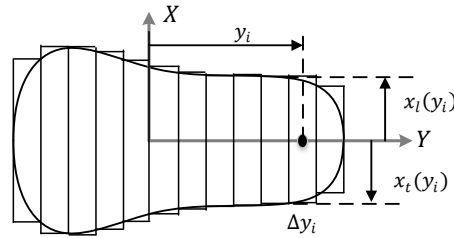


Figure 7-7: Discretization of the contact area by strips (adapted from [115])

## 7.4 Tangential Contact

### 7.4.1 Creepage definition and formulation

Prior to investigating the contact models, definition of creepage and its formulation is discussed. The relationship between the creepage, geometry, and kinematical variables of the wheel and rail is investigated.

The differential tangential speed at the interface between rail/roller and wheel causes the friction forces at the contact. This differential speed can be normalized based on the absolute velocities of contacting bodies. In railroad terminology, the differential speed is called creepage, and in a local sense, called slip. Correspondingly, the friction forces at the contact are called creep forces.

Ayasse and Chollet [123] formulized the general expressions for the creepage of two rolling bodies (Figure 7-8). Expressions are based on the projection of speed vectors on the coordinate system inline with the contact patch (XYZ):

$$v_x = \frac{\text{proj}(x)(\mathbf{c}_w - \mathbf{c}_r)}{\frac{1}{2}(\mathbf{c}_w + \mathbf{c}_r)} \quad (7-33)$$

$$v_y = \frac{\text{proj}(y)(\mathbf{c}_w - \mathbf{c}_r)}{\frac{1}{2}(\mathbf{c}_w + \mathbf{c}_r)} \quad (7-34)$$

$$\varphi = \frac{\text{proj}(z)(\boldsymbol{\Omega}_w - \boldsymbol{\Omega}_r)}{\frac{1}{2}(\mathbf{c}_w + \mathbf{c}_r)} \quad (7-35)$$

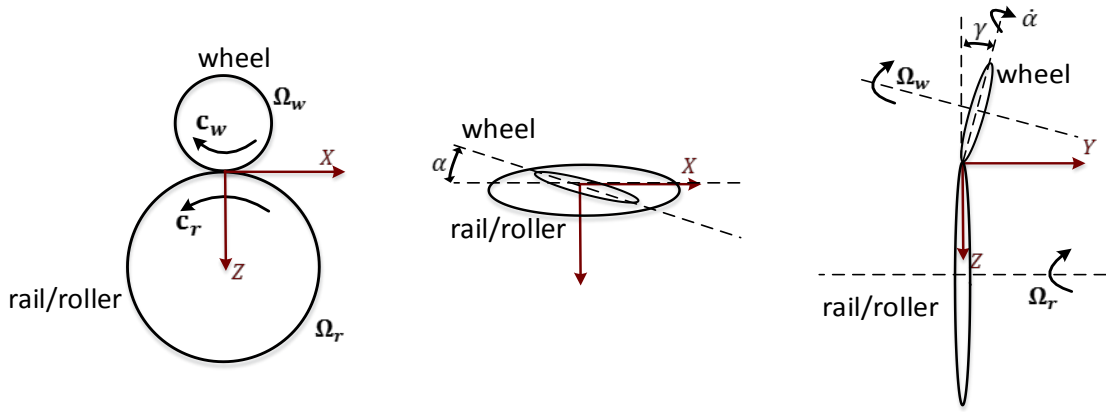


Figure 7-8: Schematic drawings for definition of creepage

Where subscripts  $w$  and  $r$  denotes wheel and rail properties, respectively. The quantity  $\mathbf{c}$  is the circumferential velocity vector at the contact, and  $\mathbf{\Omega}$  is the angular speed of two bodies.

Ayasse and Chollet used these general creepage expressions to develop their relationship with geometry and displacement of wheel and rail for the quasi-static conditions. For small creepages, the longitudinal creepage will be:

$$v_x^l = (-1)^l \frac{\Delta R}{R_0} = (-1)^l \frac{\gamma y}{R_0} \quad (7-36)$$

Where  $R_0$  is the mean rolling radius of the wheel,  $\gamma$  is the conicity of the wheel,  $y$  is the lateral shift of the wheel w.r.t the rail, and  $\Delta R$  is the change of the rolling radius due to the conicity of the wheel and its lateral shift. In the above formulation,  $l = 1$  is for left wheel-rail pair, and  $l = 2$  is for right wheel-rail.

Similarly, the lateral creepage can be as simple as the yaw angle (angle of attack,  $\alpha$ ):

$$v_y^l = -\alpha \quad (7-37)$$

For the spin creepage, the expression leads to:

$$\varphi^l = \frac{\sin \gamma}{R_0} \quad (7-38)$$

These quasi-static creepages can be generalized to dynamic formulation using the speed terms:

$$\begin{aligned}
 v_x^l &= (-1)^l \left( \frac{\Delta R}{R_0} + \frac{D_g}{2} \frac{\dot{\alpha}}{\dot{X}_w} \right) \\
 v_y^l &= \frac{\dot{Y}_w}{\dot{X}_w} - \alpha \\
 \varphi^l &= \frac{\sin \gamma}{R_0} - \frac{\dot{\alpha}}{\dot{X}_w} \cos \gamma
 \end{aligned} \tag{7-39}$$

Where  $\dot{\alpha}$ ,  $\dot{Y}_w$ , and  $\dot{X}_w$  are the relative speed of the wheelset in the rail reference system.  $D_g$  is the gauge value of the track.

Dynamic creepage formulations contain an elastic term and a damping term. For the lateral and spin creepages, damping terms have the opposite sign of elastic terms. The damping effects stabilize the wheelset for dynamic stability analysis. Moreover, the damping terms are inversely proportional to the forward velocity of the wheelset. Therefore, as the forward speed increases the damping terms decreases, hence the wheelset tends to become unstable.

Similar to Ayasse and Chollet expressions, Garg and Dukkipati [124] developed more general creepage formulations containing kinematics parameters of the wheelset, as well as considering the lateral radius of the rail.

$$\begin{aligned}
 v_x^l &= (-1)^l \left( \frac{\gamma y}{R_0} + \frac{D_c}{2} \left( \frac{1}{R_{ry}} + \frac{\dot{\alpha}}{\dot{X}_w} \right) \right) \\
 v_y^l &= \left( \frac{\dot{Y}_w}{\dot{X}_w} - \alpha + \frac{R_0 \dot{\vartheta}}{\dot{X}_w} \right) \cos(\vartheta + \gamma) \\
 \varphi^l &= (-1)^{l+1} \frac{\sin \gamma}{R_0} + \left( \frac{1}{R_{ry}} + \frac{\dot{\alpha}}{\dot{X}_w} \right) \cos(\vartheta + \gamma)
 \end{aligned} \tag{7-40}$$

Where  $R_{ry}$  is the lateral radius of the rail.  $\vartheta$  and  $\dot{\vartheta}$  are the relative rolling angle, and speed between the wheelset and the rail.

#### 7.4.2 Creep-Creepage relation models

Many scholars have investigated the rolling contact problem trying to propose a model defining the creep force at the contact as a function of creepage. Some of the proposed models just output

the net tangential forces, whereas some surface based models generate the shear stress distribution over the contact patch area. The models differ in terms of computational effort, accuracy, and so on. In addition to the analytical, numerical, or empirical models, the contact problem has been studied using finite element based methods, which are the most computationally expensive models. They, however, they may produce very accurate results [144].

In this section, the most commonly used creep-creepage models (non-FEM based) are studied. All the simplifying assumptions for developing the models are reviewed. In order to compare the performance and functionality of the models, the models are implemented in MATLAB. The investigated models are:

- Kalker's linear theory
- Johnson & Vermuelen theory
- Kalker's empirical theory
- Shen-Hedrik-Elkins models
- Ohyama's model
- Polach contact model
- FASTSIM algorithm
- CONTACT algorithm

#### 7.4.2.1 *Kalker's linear theory*

In the case of Hertzian contact, Kalker proposed a linear relationship between creepages and creep forces [145] [146]. This theory was based on the work originated by De Pater [147] [148]. Similar to Johnson's spin theory [149], Kalker's linear theory is a no-slip theory ( $\mathbf{s} = 0$ ). It means that it is assumed that the coefficient of friction is infinity. So, the slip does not occur throughout the contact [70].

Assuming rolling is in the direction of the principal axes of the contact ellipse, the creep forces and moment are defined as [150]:

$$\begin{aligned} T_x &= -Gabc_{11} v_x \\ T_y &= -Gabc_{22} v_y - G(ab)^{3/2}c_{23}\varphi \\ M_\varphi &= +G(ab)^{3/2}c_{23} v_y - G(ab)^2c_{33}\varphi \end{aligned} \tag{7-41}$$

Where  $G$  is the shear rigidity modulus of the contacting bodies.  $c_{ij}$  are the non-dimensional linear and spin creepage coefficients depending on Poisson’s ratio ( $\nu$ ), and the ratio of the contact axes ( $a/b$ ).

The formula of Hains and Ollerton [107] and subsequently Kalker’s linear theory [125] is remarkably in good agreement with the evidence for slender contact ellipse with the narrow side in the direction of rolling. However, these theories produce larger errors as the shape of contact differs, for instance for circular contact patch [151].

Linear theory does not consider saturation law for the creep forces. It means creep force increases linearly to infinity as the creepage increases to infinity. Many nonlinear models are proposed based on the linear Kalker theory introducing different saturation models [152] [123]. They behave similar to Kalker’s linear theory for small creepage (in the vicinity of zero creepage). However, depending on the saturation law, they gradually merge to the saturation line.

The Kalker linear theory derived for steady state condition and when true slip approaches zero (Equation (7-8)). According to Hertz theory, the contact area and normal pressure distribution are assumed to be elliptical. The traction distribution is assumed continuous at the leading edge of the contact where particles enter the contact area. The traction builds up within the contact area. In the two dimensional case, the traction distribution looks like Figure 7-9-left. As the coefficient of friction increases, the slip area decreases, and the traction becomes as in Figure 7-9-right [121]. As a result, at the trailing edge where particles leave the contact area, there is a discontinuity, and the condition of  $|\mathbf{F}_t| \leq \mu p$  is violated. In addition, the linear Kalker theory fails to handle large spin creepage accurately [118].

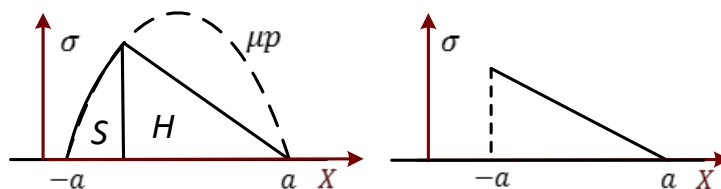


Figure 7-9: Traction distribution within contact area based on Kalker’s linear theory. Extreme condition when  $\mu$  is large (right) [121]

7.4.2.2 *Kalker's coefficients*

Using the Galin's theorem [148], Kalker calculated the creepage coefficients ( $c_{ij}$ ) for various values of Poisson ratio and contact patch geometry [70] [125]. The results are tabulated in Table 7-2.

**Table 7-2: Kalker's coefficients for various Poisson ratios and various contact ellipse aspect ratio (In this table  $\sigma$  represents Poisson ratio) [123]**

$g$	$C_{11}$			$C_{22}$			$C_{23} = -C_{32}$			$C_{33}$			
	$\sigma = 0$	1/4	1/2	$\sigma = 0$	1/4	1/2	$\sigma = 0$	1/4	1/2	$\sigma = 0$	1/4	1/2	
0.0	$\pi^2/4(1-\sigma)$			$\pi^2/4 = 2,47$			$\pi\sqrt{g}/3$	—	—	$\pi^2/16(1-\sigma)g$			
a/b	0.1	2.51	3.31	4.85	2.51	2.52	2.53	0.334	0.473	0.731	6.42	8.28	11.7
	0.2	2.59	3.37	4.81	2.59	2.63	2.66	0.483	0.603	0.809	3.46	4.27	5.66
	0.3	2.68	3.44	4.80	2.68	2.75	2.81	0.607	0.715	0.889	2.49	2.96	3.72
	0.4	2.78	3.53	4.82	2.78	2.88	2.98	0.720	0.823	0.977	2.02	2.32	2.77
	0.5	2.88	3.62	4.83	2.88	3.01	3.14	0.827	0.929	1.07	1.74	1.93	2.22
	0.6	2.98	3.72	4.91	2.98	3.14	3.31	0.930	1.03	1.18	1.56	1.68	1.86
	0.7	3.09	3.81	4.97	3.09	3.28	3.48	1.03	1.14	1.29	1.43	1.50	1.60
	0.8	3.19	3.91	5.05	3.19	3.41	3.65	1.13	1.25	1.40	1.34	1.37	1.42
	0.9	3.29	4.01	5.12	3.29	3.54	3.82	1.23	1.36	1.51	1.27	1.27	1.27
b/a	1.0	3.40	4.12	5.20	3.40	3.67	3.98	1.33	1.47	1.63	1.21	1.19	1.16
	0.9	3.51	4.22	5.30	3.51	3.81	4.16	1.44	1.59	1.77	1.16	1.11	1.06
	0.8	3.65	4.36	5.42	3.65	3.99	4.39	1.58	1.75	1.94	1.10	1.04	0.954
	0.7	3.82	4.54	5.58	3.82	4.21	4.67	1.76	1.95	2.18	1.05	0.965	0.852
	0.6	4.06	4.78	5.80	4.06	4.50	5.04	2.01	2.23	2.50	1.01	0.892	0.751
	0.5	4.37	5.10	6.11	4.37	4.90	5.56	2.35	2.62	2.96	0.958	0.819	0.650
	0.4	4.84	5.57	5.57	4.84	5.48	6.31	2.88	3.24	3.70	0.912	0.747	0.549
	0.3	5.57	6.34	7.34	5.57	6.40	7.51	3.79	4.32	5.01	0.868	0.674	0.446
	0.2	6.96	7.78	8.82	6.96	8.14	9.79	5.72	6.63	7.89	0.828	0.601	0.341
0.1	10.7	11.7	12.9	10.7	12.8	16.0	12.2	14.6	18.0	0.795	0.526	0.228	

Ayasse and Chollet [123] curve-fit polynomial expressions to the tabulated data for Poisson ratio of 0.27 (steel wheel and rail). The polynomial fit described as:

$$\begin{aligned}
 c_{11} &= 3.2893 + \frac{0.975}{\frac{b}{a}} - \frac{0.012}{\left(\frac{b}{a}\right)^2} \\
 c_{22} &= 2.4014 + \frac{1.3179}{\frac{b}{a}} - \frac{0.02}{\left(\frac{b}{a}\right)^2} \\
 c_{23} &= 0.4147 + \frac{1.0184}{\frac{b}{a}} + \frac{0.0565}{\left(\frac{b}{a}\right)^2} - \frac{0.0013}{\left(\frac{b}{a}\right)^3}
 \end{aligned}
 \tag{7-42}$$

**Table 7-3: Comparison table of proposed models for estimating  $c_{11}$  Kalker coefficient**

Fit model	Equation	SSE	R-square	RMSE
Polynomial	$a_0 + a_1v + a_2(b/a)$	1.27	0.9949	0.1533
Exponential	$a_0 + a_1e^v + a_2e^{b/a}$	64.12	0.7416	1.09
Power model A	$a_0\{v^{a_1} + (b/a)^{a_2}\}$	19.34	0.9221	0.5984
Power model B	$a_0 + v^{a_1} + (b/a)^{a_2}$	14.27	0.9425	0.5141
Linear logarithmic	$a_0 + a_1\log(v) + a_2\log(b/a)$	Diverged		
Gaussian	$a_0e^{-0.5\{((v-a_1)/a_2)^2 + ((b/a-a_3)/a_4)^2\}}$	30.17	0.8784	0.7617

In order to consider the dependency of the coefficients on the Poisson ratio, different model fits are investigated to estimate the Kalker’s coefficients. For different fit models, multiple error measurements are calculated and compared in Table 7-3. For each model, coefficients of  $a_i$  are calculated for the best fit. Error measurements are:

- Sum of Squares Due to Error (SSE): This statistic measures the total deviation of the response values from the fit surface created to match the response values, and is calculated as the summed square of residuals.
- R-Square: This statistic measures how successful the fit is in explaining the variation of the data. In another word, R-square is the square of the correlation between the response values and the predicted response values. It is also called the square of the multiple correlation coefficients and the coefficient of multiple determination

- Root Mean Squared Error (RMSE): This statistic is also known as the fit standard error and the standard error of the regression. It is an estimate of the standard deviation of the random component in the data.

**Table 7-4: Comparison table of proposed models for estimating  $c_{11}$  Kalker coefficient**

	Degree of $g$	Degree of $v$			
		1	2	3	4
SSE	1	1.3365	0.2537	0.3673	0.4941
	2	0.8144	<b>0.2098</b>	0.1641	0.1887
	3	0.7538	0.1419	0.1531	0.0964
	4	0.7606	0.0562	0.0618	0.0629
R-Square	1	0.9946	0.9990	0.9985	0.9980
	2	0.9967	<b>0.9992</b>	0.9993	0.9991
	3	0.9969	0.9994	0.9994	0.9996
	4	0.9969	0.9998	0.9998	0.9997
RSME	1	0.1573	0.0698	0.0857	0.1015
	2	0.1251	<b>0.0641</b>	0.0585	0.0648
	3	0.1228	0.0544	0.0571	0.0474
	4	0.1259	0.0353	0.0379	0.0380
Number of	1	3	5	7	9
	2	5	<b>6</b>	9	12
	3	7	9	10	14
	4	9	12	14	15

Error results show that polynomial model results in the best estimation error. Linear logarithmic fit-model could not converge for the  $c_{11}$  dataset. Other common fit models (power models A & B, and Gaussian) result in larger estimation error than polynomial fit-model.

Since the polynomial equation could best fit the data-set, different polynomial degrees (degree 1 to 4) for both the dependent variables ( $v, g = a/b$ ) are examined. The results are shown in Table 7-4. Based on the estimation error measurements, as well as simplicity of equation (number of coefficients), a polynomial fit-model of degree two for sigma ( $v$ ) and a polynomial of degree two for  $g$  is chosen for  $c_{11}$  Kalker’s coefficients (SSE $\sim$ 0.2, R-Sq.  $>$ 0.999, RSME $\sim$ 0.06, # coef.: 6).

So, the proposed polynomial equation for  $c_{11}$  is:

$$c_{11}(v, g) = 2.39 + 2.338v + 1.014g + 2.736v^2 - 0.0728vg - 0.0139g^2 \tag{7-43}$$

Result from Ayasse and Chollet model (Equation (7-42)) are compared to the result from the proposed polynomial fit-model (Equation (7-43)), shown in Figure 7-10.

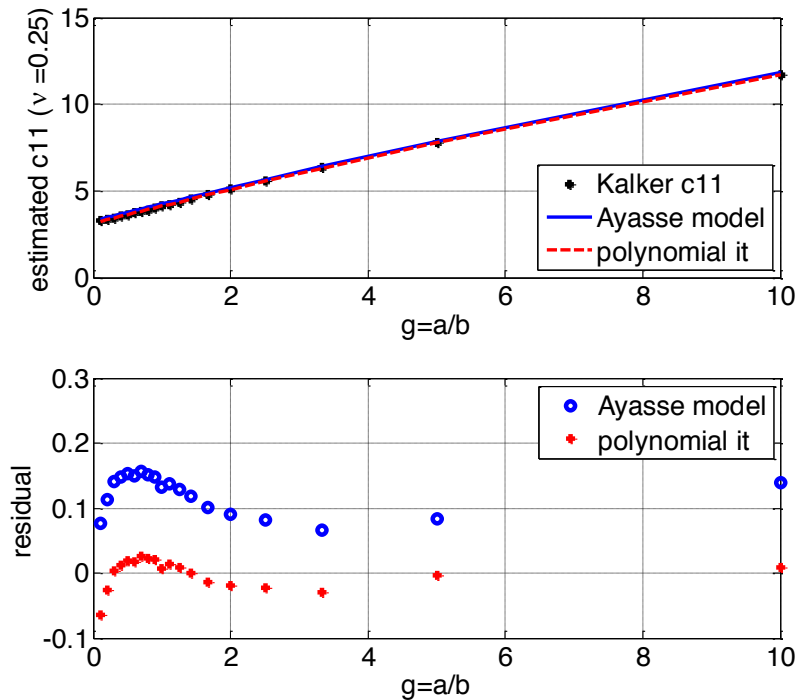


**Figure 7-10: Comparison between Ayasse model and proposed polynomial model for estimating  $c_{11}$  Kalker coefficient: Top plot shows estimated coefficients for both the models as a function of  $g$  for a constant Poisson ratio ( $\nu = 0.25$ ), and bottom plot presents their residual from tabulated values.**

As it is shown in the above figure, the proposed polynomial fit improves the estimation accuracy, as well as it takes the effect of Poisson ratio ( $\nu$ ) into account. Similarly, the same procedure is repeated for  $c_{22}$  and  $c_{23}$ , and  $c_{33}$ . The proposed polynomial fits for  $c_{22}$  is formulated as (SSE=0.12, R-Sq. =0.999, RSME=0.05, # coef.: 5):

$$c_{22}(v, g) = 2.353 - 0.0212v + 1.074g + 1.163vg - 0.0319g^2 \tag{7-44}$$

The proposed polynomial fits for  $c_{23}$  is formulated as (SSE=0.13, R-Sq. =0.999, RSME= $\sim$ 0.05, # coef.: 7 ):

$$c_{22}(v, g) = 0.2866 + 0.4467v + 1.049g + 0.038vg - 0.0177g^2 + 0.005g^3 + 0.1479g^2v \quad (7-45)$$

The proposed polynomial fits for  $c_{33}$  is formulated as (SSE=0.16, R-Sq. =0.999, RSME= $\sim$ 0.05, # coef.: 5 ):

$$c_{22}(v, g) = 0.7375 - 1.177v + 0.4506g + 1.076vg - 0.023g^2 \quad (7-46)$$

In this study, the above proposed formulations are used for calculating the Kalker's coefficients instead of the tabulated values.

#### 7.4.2.3 *Johnson & Vermuelen theory*

Johnson [149] proposed a rolling contact theory considering the finite slip. The theory dealt with finite friction neglecting the spin creepage. Vermuelen and Johnson [153] later generalized this work for quasi-identical bodies with elliptical contact area. The contact area was divided into two regions: adhesion area, and slip area.

It was assumed that the adhesion area is also elliptic shape with the same orientation of principal axes as the contact ellipse. The ratio of major to minor axes for the contact ellipse is the same as for the adhesion ellipse. Depending on the creepage, the position of the center of adhesion ellipse is determined.

Vermeulen and Johnson's theory is an approximate one, since for the shaded area in the Figure 5, the slip is in the same sense as the traction. Note that the slip should be in the opposite direction of slip as it is the case for the rest of slip area in the picture (Coulomb's law).

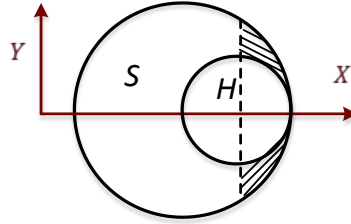


Figure 7-11: Slip and adhesion areas inside the contact patch defined in Vermuelen and Johnson theory [149]

Vermuelen and Johnson [153] analysis resulted in the total transmitted forces. The formulations for the Vermuelen and Johnson theory are:

$$F(F_x, F_y) = \begin{cases} \frac{\mu N}{\tau} \left[ \left(1 - \frac{1}{3}\tau\right)^3 - 1 \right] (\zeta \mathbf{i} + \eta \mathbf{j}) & \text{for } |\tau| < 3 \\ -\frac{\mu N}{\tau} (\zeta \mathbf{i} + \eta \mathbf{j}) & \text{for } |\tau| \geq 3 \end{cases} \quad (7-47)$$

Where  $\mathbf{i}$ , and  $\mathbf{j}$  are unit vectors in longitudinal, and lateral directions, respectively.  $T(T_x, T_y)$  is the resultant tangential force.  $\zeta$ , and  $\eta$  are normalized longitudinal and lateral creepages, defined as:

$$\zeta = \frac{\pi ab G v_x}{\mu N \phi}, \quad \eta = \frac{\pi ab G v_y}{\mu N \psi}, \quad \tau = \sqrt{\zeta^2 + \eta^2} \quad (7-48)$$

Where  $\phi$ , and  $\psi$  are normalized longitudinal and lateral coefficients, which are functions of  $B, C, D, g = \frac{a}{b}$ , and  $v$ .  $B, C$ , and  $D$  are complete elliptic integrals defined as:

$$\begin{aligned} B &= \int_0^{\pi/2} \cos^2 \varrho \left( \sqrt{1 - k^2 \sin^2 \varrho} \right)^{-1} d\varrho \\ C &= \int_0^{\pi/2} \sin^2 \varrho \left( \sqrt{1 - k^2 \sin^2 \varrho} \right)^{-1} d\varrho \quad \text{for } k \leq 1 \\ D &= \int_0^{\pi/2} \cos^2 \varrho \sin^2 \varrho \left( \sqrt{1 - k^2 \sin^2 \varrho} \right)^{-1} d\varrho \end{aligned} \quad (7-49)$$

Where  $k$  is defined as:

$$k = \begin{cases} \sqrt{1 - g^2} & \text{for } g < 1 \\ \sqrt{1 - \frac{1}{g^2}} & \text{for } g \geq 1 \end{cases} \quad (7-50)$$

The formulation for the normalized longitudinal, and lateral creepages is:

$$\begin{aligned} \phi &= B - v(D - C) & \text{for } g < 1 \\ \psi &= B - v g^2 C & \text{for } g < 1 \\ \phi &= [D - v(D - C)]/g & \text{for } g \geq 1 \\ \psi &= [D - vC]/g & \text{for } g \geq 1 \end{aligned} \quad (7-51)$$

Johnson and Vermuelen [154] have also proposed a simpler alternative formula as follows:

$$F(F_x, F_y) = \begin{cases} \frac{\mu N}{\tau_v} [1 - (1 - \tau_v)^3] (\tau_x \mathbf{i} + \tau_y \mathbf{j}) & \text{for } 0 \leq \tau_v \leq 1 \\ \frac{\mu N}{\tau_v} (\tau_x \mathbf{i} + \tau_y \mathbf{j}) & \text{for } \tau_v > 1 \end{cases} \quad (7-52)$$

Where:

$$\tau_x = \frac{\pi ab G v_x}{\mu N \phi}, \quad \tau_y = \frac{\pi ab G v_y}{\mu N \psi}, \quad \tau_v = \sqrt{\tau_x^2 + \tau_y^2} \quad (7-53)$$

The formula of Vermuelen and Johnson produces errors of up to 25%, and leads to a higher value for the total force than is warranted by the experiment [151].

#### 7.4.2.4 Normalized longitudinal and lateral coefficients

In Johnson and Vermuelen formulation,  $\phi$  and  $\psi$  are normalized longitudinal and lateral coefficients, which are functions of  $B$ ,  $C$ ,  $D$ ,  $g = \frac{a}{b}$ , and  $v$ . Kalker [151] calculated the values of  $\phi$ , and  $\psi$  for various values of  $g = \frac{a}{b}$ , and  $v$ . The results are tabulated in Table 7-5. Parameters  $B$ ,  $C$ , and  $D$  are complete elliptic integrals, which has been calculated and tabulated by Jahnke and Emde [155].

**Table 7-5: The values of  $\phi$ , and  $\psi$  as functions of Poisson ratio and contact ellipse aspect ratio ( $\sigma$  in this table represents Poisson ratio) [151]**

	$\phi = \psi_1$	$\phi$		$\psi_1$	
	$\sigma = 0$	$\sigma = \frac{1}{4}$	$\sigma = \frac{1}{2}$	$\sigma = \frac{1}{4}$	$\sigma = \frac{1}{2}$
<i>(a/b)</i>					
0.2	0.9686	0.7377	0.5068	0.9574	0.9461
0.4	0.9205	0.7151	0.5096	0.8958	0.8711
0.6	0.8719	0.6893	0.5066	0.8366	0.8012
0.8	0.8267	0.6633	0.5000	0.7834	0.7401
1.0	0.7854	0.6381	0.4908	0.7363	0.6872
<i>(b/a)</i>					
0.2	0.4095	0.3633	0.3171	0.3533	0.2971
0.4	0.5755	0.4933	0.4112	0.5138	0.4521
0.6	0.6740	0.5645	0.4549	0.6151	0.5562
0.8	0.7393	0.6086	0.4779	0.6852	0.6301
1.0	$\pi/4$	$(4 - 3\sigma)\pi/16$		$(4 - \sigma)\pi/16$	

Similar to Kalker’s coefficients, a polynomial fit-model is used to estimate the normalized longitudinal and lateral coefficients as a function of Poisson’s ratio, and ratio of axes of elliptical contact area. Kalker [151] shows that  $\phi$ , and  $\psi$  are linear functions of  $v$ . Out of various iterations for the degree of polynomials for Poisson’s ratio, and axes’ ratio, a polynomial equation with degrees of 1 in the  $v$  dimension and degrees of 4 in the  $g$  dimension would predicts the most accurate results:

$$\phi(v, g) = 1.02 - 1.031v - 0.2606g + 0.5856vg + 0.0198g^2 - 0.1616vg^2 + 0.009231g^3 + 0.01567vg^3 - 0.00153g^4 \tag{7-54}$$

$$\psi(v, g) = 1.028 + 0.004906v - 0.2992g - 0.2967vg + 0.06443g^2 + 0.1079vg^2 - 0.007991g^3 - 0.01155vg^3 + 0.0004245g^4 \tag{7-55}$$

#### 7.4.2.5 Kalker’s empirical theory

Kalker proposed an analytical expression for the total tangential forces at the contact [151]. Compared with the experimental results presented in Johnson’s work [153], as well as with numerical results of Kalker method [151] [156], the empirical model showed good agreement with the evidence [151]. Kalker’s empirical formula is given as [151]:

$$F(F_x, F_y) = \begin{cases} \mu N (f_1(\tau)\mathbf{e}_1 + f_2(\tau)\mathbf{e}_2) & \text{for } \tau < 1 \\ \mu N \mathbf{e}_2 & \text{for } \tau \geq 1 \end{cases} \quad (7-56)$$

Where

$$f_1(\tau) = \frac{3}{2}\tau \cos^{-1}\tau, \quad f_2(\tau) = 1 - \left(1 + \frac{1}{2}\tau^2\right)\sqrt{1 - \tau^2} \quad (7-57)$$

And

$$\mathbf{e}_1 = (\zeta\mathbf{i} + \eta\mathbf{j})/\tau, \quad \mathbf{e}_2 = (v_x\mathbf{i} + v_y\mathbf{j})/\tau \quad (7-58)$$

The remaining variables are defined in equations for Vermuelen and Johnson theory.

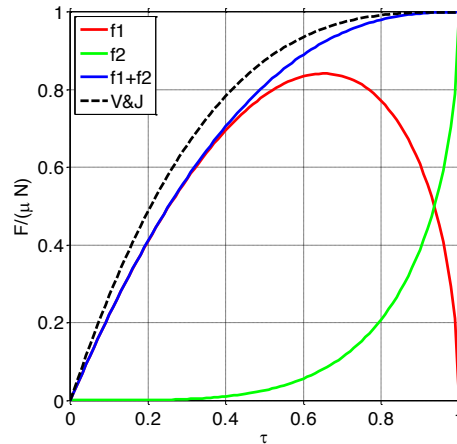


**Figure 7-12: Total tangential force comparison between Kalker's empirical model, and Vermuelen & Johnson model**

Kalker has compared the performance of his proposed empirical model with Vermuelen and Johnson formulation [151]. Results show that Kalker's empirical formula generates more accurate creep forces, although Vermuelen and Johnson formulation has the advantage of greater simplicity. It was seen that the experimental data points associated with  $\tau < 0.4$  lie on the empirical curve, however, as  $\tau$  increases for the values  $\tau > 0.4$ , the empirical model generates higher values than the experimental data points [151]. Figure 7-12 shows that Vermulen and

Johnson theory predicts higher creep forces compared with Kalker's empirical theory for the entire range of  $\tau$ .

#### 7.4.2.6 Shen-Hedrik-Elkins models

Shen, Hedrick, and Elkins [152] proposed a simple saturation creep force law for Kalker's linear creep force theory. The model tries to incorporate all the essential nonlinear behavior required to predict the lateral dynamic of railway systems. This model is a simplified approximate model based on Kalker's linear theory to compute the creep forces, and saturates the creep forces when necessary by an approximate method based on Johnson's nonlinear theory [149]. The model includes the effect of spin, as opposed to Vermuelen and Johnson model [153]. The proposed saturation law is based on the cubic saturation law introduced by Vermuelen and Johnson [153]. The formulation for the model is [152]:

$$\begin{aligned} F_{xNL} &= F_x \times \epsilon \\ F_{yNL} &= F_y \times \epsilon \end{aligned} \quad (7-59)$$

Where  $F_{xNL}$  and  $F_{yNL}$  are the nonlinear longitudinal and lateral creep forces,  $F_x$  and  $F_y$  are linear longitudinal and lateral forces from Kalker's linear theory (Equation (7-41)), and  $\epsilon$  is defined as:

$$\epsilon = \begin{cases} \frac{\mu N}{F_R} \left[ \left( \frac{F_R}{\mu N} \right) - \frac{1}{3} \left( \frac{F_R}{\mu N} \right)^2 + \frac{1}{27} \left( \frac{F_R}{\mu N} \right)^3 \right] & \text{for } F_R < 3\mu N \\ \frac{\mu N}{F_R} & \text{for } F_R > 3\mu N \end{cases} \quad (7-60)$$

Where  $F_R = \sqrt{F_x^2 + F_y^2}$  is the resultant linear creep force.

Shen et.al. [152] showed that the proposed model predicts more erroneous results as the spin creepage increases. However, the total force's error for a wide range of spin value is less than 18% compared with Kalker's exact model [152].

#### 7.4.2.7 Polach contact model

In 1990's, Polach proposed a fast algorithm and computer code for predicting the creep forces [157] [158]. The proposed method considers the contact geometry and creeages and spin conditions. It assumes elliptical contact area, and is based on the Hertzian normal stress

distribution. The computation time for the proposed method is much faster than well-known contact codes FASTSIM, and CONTACT (at least 10 times faster than FASTSIM). The computer code generates accurate results even for high spin values.

The proposed method assumes that elliptical contact area is divided into adhesion and slip areas. The solution assumes a linear growth of tangential stress ( $\sigma$ ) for the area of adhesion starting zero at the leading edge. In case the tangential stress reaches its maximum (Equation (7-61)) the relative motion between contacting bodies appears, and the tangential stress saturates with its maximum for the remaining area until the trailing edge of the contact (slip area), as depicted in Figure 7-13.

$$\sigma_{max} = \mu \cdot p \tag{7-61}$$

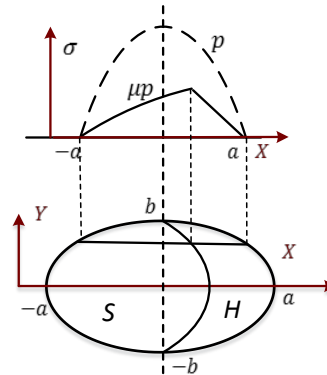


Figure 7-13: Normal and tangential stress distribution over the contact area for slip and adhesion areas [157]

By integrating these stresses in the contact area, the tangential contact forces will be determined:

$$\mathbf{F} = \iint_{(U:\text{contact area})} \sigma \, dx \, dy \tag{7-62}$$

Where  $U$  is the contact area including both adhesion and slip areas.  $\mathbf{F}$  is the resultant tangential force, so the longitudinal and lateral forces are calculated as:

$$F_i = \mathbf{F} \frac{v_i}{v}, \quad i = x, y, \quad v = \sqrt{v_x^2 + v_y^2} \tag{7-63}$$

Similar to Freibauer's method [159], a transformation of the tangential stress distribution ellipsoid to a hemisphere was used. Based on the transformed stress, Polach [157] calculated the tangential force as:

$$F = -\frac{2\mu N}{\pi} \left( \frac{\varepsilon}{1 + \varepsilon^2} + \arctan \varepsilon \right) \quad (7-64)$$

Where  $\varepsilon$  is the gradient of tangential stress in the area of adhesion, defined as:

$$\varepsilon = \frac{2}{3} \frac{H \cdot \pi \cdot a^2 \cdot b}{\mu N} v \quad (7-65)$$

where  $H$  is a proportionality constant characterizing the contact elasticity of the bodies.

To take the effect of spin creepage into consideration, Polach calculated the lateral force caused by spin separately. The moment effect of spin, as well as the moment effect of lateral creepage are neglected. The lateral creepage formulation is refined as:

$$v_{y\varphi} = \begin{cases} v_y + \varphi \cdot a & \text{for } |v_y + \varphi \cdot a| > |v_y| \\ v_y & \text{for } |v_y + \varphi \cdot a| \leq |v_y| \end{cases} \quad (7-66)$$

Therefore, the resulting lateral force ( $F_{yt}$ ) is the summation of lateral force from Equation (7-64), and lateral force due to spin ( $F_{y\varphi}$ ):

$$F_{yt} = F_y + F_{y\varphi} \quad (7-67)$$

Where  $F_{y\varphi}$  is calculated as:

$$F_{y\varphi} = -\frac{9}{16} a \cdot N \cdot \mu \cdot K_m \cdot \left[ 1 + 6.3 \left( 1 - e^{-\frac{a}{b}} \right) \right] \varphi / v_{y\varphi} \quad (7-68)$$

Where

$$K_m = |\varepsilon_\varphi| \left( \frac{\delta^3}{3} - \frac{\delta^2}{2} + \frac{1}{6} \right) - \frac{1}{3} \sqrt{(1 - \delta^2)^3}, \quad \delta = \frac{\varepsilon_\varphi^2 - 1}{\varepsilon_\varphi^2 + 1} \quad (7-69)$$

Where  $\varepsilon_\varphi$  is defined as:

$$\varepsilon_{\varphi} = \frac{2}{3} \frac{H_{\varphi} \cdot \pi \cdot a^2 \cdot b}{\mu N} \frac{v_{y\varphi}}{1 + 6.3 \left(1 - e^{-\frac{a}{b}}\right)} \quad (7-70)$$

The coefficient  $H$  and  $H_{\varphi}$  can be obtained experimentally or from Kalker's constants. In order to calculate  $H$  and  $H_{\varphi}$  from Kalker coefficients, Polach [157] introduced the following formulas:

$$H = \frac{3}{8} \frac{G}{a} \sqrt{\left(c_{11} \frac{v_x}{v}\right)^2 + \left(c_{22} \frac{v_y}{v}\right)^2}, \quad H_{\varphi} = \frac{4}{\pi} \frac{G \cdot \sqrt{b}}{\sqrt{a^3}} c_{23} \quad (7-71)$$

These independent expressions for the creep-creepage would produce more erroneous results, in the case of combined creepages (spin creepage is not negligible). Saturation laws could lead to non-uniform combined saturation of the shear stress over the contact area. Therefore, surface based models, which generate the shear stress distribution inside the contact area, are necessary.

#### 7.4.2.8 FASTSIM algorithm

Kalker [160] proposed a fast algorithm, and a computer code for calculating the creep forces from given creepages and spin. This theory is a generalization of strip theory introduced by Hains and Ollerton [107]. The strip theory was very successful in introducing the adhesion and slip areas inside the contact area, which were hitherto unknown. It, however, failed to represent three-dimensional rolling contact accurately.

In the simplified theory, Kalker assumed a simple traction-displacement constitutive law as:

$$\mathbf{u} = \mathbf{u}^w - \mathbf{u}^r = [L_x \sigma_{tx} \quad L_y \sigma_{ty}]^T \quad (7-72)$$

Where  $L_x$ , and  $L_y$  are the compliant parameters in the longitudinal and lateral directions, respectively. Substituting Equation (7-72) in Equation (7-8), for steady-state condition we will have:

$$\mathbf{s} = V[(v_x - \varphi y)\mathbf{i} + (v_y + \varphi x)\mathbf{j}] - V(\partial[L_x \sigma_{tx} \quad L_y \sigma_{ty}]^T / \partial x) \quad (7-73)$$

Separating the longitudinal and lateral equations, and dividing by compliant parameters, we will have:

$$\begin{cases} \frac{w_x}{VL_x} = \frac{v_x}{L_x} - \frac{\varphi y}{L_x} - \frac{\partial \sigma_{tx}}{\partial x} \\ \frac{w_{xy}}{VL_y} = \frac{v_y}{L_y} + \frac{\varphi x}{L_y} - \frac{\partial \sigma_{ty}}{\partial x} \end{cases} \quad (7-74)$$

Then, it approximated by:

$$\begin{cases} \frac{w_x}{VL} = \frac{v_x}{L_1} - \frac{\varphi y}{L_3} - \frac{\partial \sigma_{tx}}{\partial x} \\ \frac{w_{xy}}{VL} = \frac{v_y}{L_2} + \frac{\varphi x}{L_3} - \frac{\partial \sigma_{ty}}{\partial x} \end{cases} \quad (7-75)$$

In order to determine  $L_1$ ,  $L_2$ , and  $L_3$ , the exact linear theory of Kalker is employed. The linear theory sets that slip vanishes ( $\mathbf{s} = 0$ ), and the traction distribution is continuous for the leading edge of the contact where particles enter the contact area ( $[\sigma_{tx} \quad \sigma_{ty}]^T = \mathbf{0}$ ). Integrating Equation (7-75) gives:

$$\begin{cases} \sigma_{tx} = \left( \frac{v_x}{L_1} - \frac{\varphi y}{L_3} \right) (x - \bar{x}) + h_1(y) \\ \sigma_{ty} = \left( \frac{v_y}{L_2} \right) (x - \bar{x}) + \frac{\varphi y}{2L_3} (x^2 - \bar{x}^2) + h_2(y) \end{cases} \quad (7-76)$$

Where  $\bar{x}$  is the  $X$ -coordinate of the leading edge of the contact, which is given by:

$$\bar{x} = a\sqrt{1 - (y/b)^2} \quad (7-77)$$

And  $h_1(y)$ , and  $h_2(y)$  are two arbitrary functions. The arbitrary functions are set zero as the traction at the leading edge need to be zero. The traction distribution (Equation (7-76)) are integrated and compared with linear theory results (Equation (7-41)):

$$\begin{aligned} F_x &= \iint_{\text{contact area}} \sigma_{tx} dx dy \\ &= \int_{-b}^b dy \int_{-a}^a \sigma_{tx} dx = \frac{-8a^2 b v_x}{3L_1} = -Gabc_{11} v_x \end{aligned} \quad (7-78)$$

$$\begin{aligned}
 F_y &= \iint_{\text{contact area}} \sigma_{ty} dx dy = \int_{-b}^b dy \int_{-a}^a \sigma_{ty} dx = \frac{-8a^2 b v_y}{3L_2} - \frac{\pi a^3 b \varphi}{4L_3} \\
 &= -Gabc_{22} v_y - G(ab)^{3/2} c_{23} \varphi
 \end{aligned} \tag{7-79}$$

The comparison results generate the relationship between the compliant parameters and Kalker coefficients, given by:

$$L_1 = \frac{8a}{3Gc_{11}}, L_2 = \frac{8a}{3Gc_{22}}, L_3 = \frac{\pi a \sqrt{ab}}{4Gc_{23}} \tag{7-80}$$

So, the compliant coefficients depend on the material, geometric parameters of the contact area and Kalker coefficients.

Kalker turned the integration problem to a dimensionless problem, by transferring the elliptical shape of the contact to a unit circle. The dimensionless problem is formulated as:

$$\begin{aligned}
 x' &= \frac{x}{a}, \quad y' = \frac{y}{a}, \quad \sigma_{tx}' = \frac{\sigma_{tx}}{\mu p_0}, \quad \sigma_{ty}' = \frac{\sigma_{ty}}{\mu p_0}, \\
 p' &= p/p_0, \quad p_0 = \frac{N}{abN'}
 \end{aligned} \tag{7-81}$$

Similarly, for the normalized stress, we have:

$$v_x' = \frac{v_x a}{\mu p_0 L_1}, \quad v_y' = \frac{v_y a}{\mu p_0 L_2}, \quad \varphi_x' = \frac{ab\varphi}{\mu p_0 L_3}, \quad \varphi_y' = \frac{a^2\varphi}{\mu p_0 L_3}, \tag{7-82}$$

The contact area becomes:

$$U' = \{x', y' | x'^2 + y'^2 \leq 1\} \tag{7-83}$$

Therefore, based on the normalized slip ( $w' = \frac{wa}{\mu p_0 LV}$ ), we have:

$$\begin{cases} w_{x'}' = v_{x'}' - y'\varphi_{x'}' - \frac{\partial \sigma_{tx'}'}{\partial x'} \\ w_{y'}' = v_{y'}' + x'\varphi_{y'}' - \frac{\partial \sigma_{ty'}'}{\partial x'} \end{cases} \quad (7-84)$$

And the total force is given by:

$$(F_{x'}', F_{y'}', N') = \iint_{U'} (\sigma_{tx'}', \sigma_{ty'}', p') dx' dy' = \frac{1}{ab\mu p_0} (F_x, F_y, \mu N) \quad (7-85)$$

Kalker [160] published his fast algorithm called FASTSIM in 1982. In the algorithm, the elliptical contact area is divided into slices parallel to the direction of rolling with width  $\Delta y$ , and also each slice is divided to a certain number of sections with width  $\Delta x$ , as shown in Figure 7-14. Using numerical methods, the tangential stress in both longitudinal and lateral directions for each section is calculated, and multiplied by the slice area ( $\Delta x \Delta y$ ). Using numerical methods, the tangential stress in both longitudinal and lateral directions for each section is calculated and multiplied by the slice area ( $\Delta x \Delta y$ ). The integrated tractions for each slice are summed for the entire contact area to generate the total creep forces.

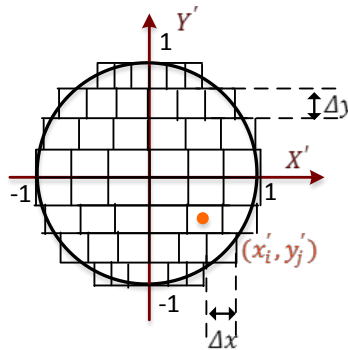
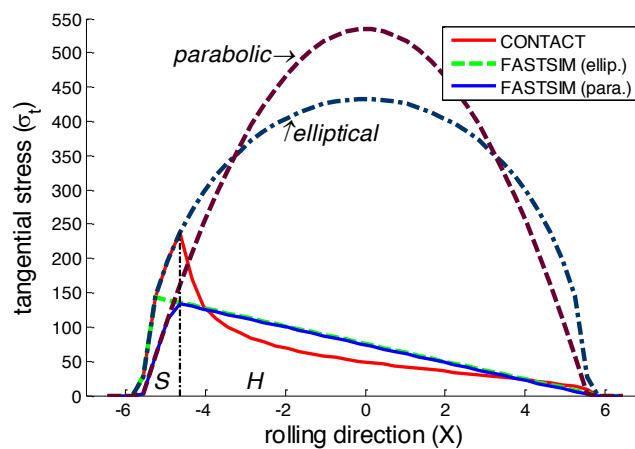


Figure 7-14: The area of contact slices and strips according to FASTSIM algorithm.

It is shown [121,139,142] that the parabolic traction bound results in more accurate prediction of adhesion-slip border than the elliptical traction bound compared with CONTACT results, as shown in Figure 7-15. Kalker [121] stated that he has chosen a parabolic traction bound for FASTSIM because of its better qualitative agreement with CONTACT. Vollebregt [161] compares the performance of FASTSIM algorithm with parabolic and elliptical traction bounds in

predicting slip and adhesion areas inside the contact patch with the result of CONTACT, and concludes that the parabolical traction bound gives results that compare better to those of the half-space approach. Figure 7-16 shows creep curve results of FASTSIM with parabolic and elliptical traction bounds compared with CONTACT result. The results show that FASTSIM with parabolic traction bound obtains better results for creep force estimation than FASTSIM with elliptical traction bound as compared with the result of CONTACT.



**Figure 7-15: Adhesion-slip border prediction by FASTSIM with parabolic and elliptical traction bounds compared with CONTACT.**

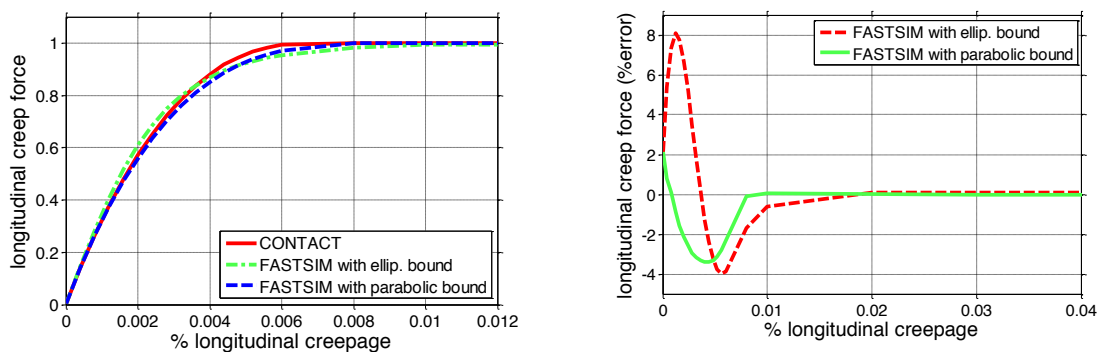


**Figure 7-16: Left) Creep curves comparison between FASTSIM with parabolic and elliptical traction bounds with CONTACT algorithm. Right) Creep force estimation error for FASTSIM with parabolic and elliptical traction bounds as compared with CONTACT algorithm**

Kalker refined his algorithm’s mesh around a point  $(x_0', y_0')$ , inside the contact area, where rigid slip vanishes [160]:

$$(x_0', y_0') = (-v_y' \varphi_y', v_x' \varphi_x') \tag{7-86}$$

The point is called the spin point, and the largest changes in the stress field occur near the spin point. Figure 7-17 shows the adhesion and slip areas for the case of pure spin  $((v_x', v_y') = \mathbf{0})$ . Kalker halved the width of sliced in the vicinity of the spin pole to account for the steep changes of stress.

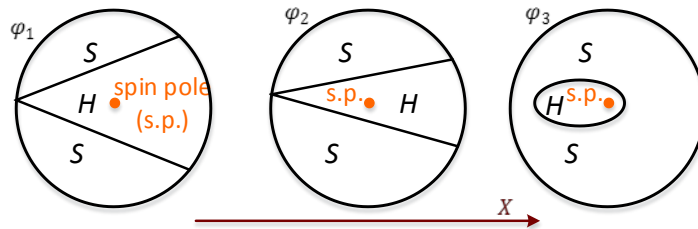


**Figure 7-17: The slip and adhesion areas for the case of pure spin creepage  $(\varphi_1 < \varphi_2 < \varphi_3)$  showing the area in the vicinity of spin pole is often marked by great stress changes [160]**

**7.4.2.9 CONTACT algorithm**

Kalker [162] developed his exact three-dimensional rolling theory in 1986 by generalizing the principal of virtual work for contact problem. The Kalker 3D rolling theory is based on the half space approximation, as the contact area is very small respect to the dimensions of the contacting bodies. The assumption is justified according to elasticity theory. The stresses due to surface loads die out away from the point of application proportional to the squared distance to the point of application. As a result, a few contact lengths away from the contact the stresses are negligible. In addition to half space approximation, Kalker solved his exact 3D contact problem for linearly elastic materials, and homogenous bodies. Inertial effects of the contact particles are neglected with respect to the contact stresses.

When two elastic bodies come into contact particles on the bodies will deform, as depicted in Figure 7-18. Two opposing points  $\mathbf{r}^w$  , and  $\mathbf{r}^r$  of wheel and rail that lie on the same normal vector

$(\mathbf{n}_n)$  to the contact will displace due to deformation by  $\mathbf{u}^w$ , and  $\mathbf{u}^r$ , respectively. The deformed locations are the summation of the deformations, and the undeformed locations, as given by:

$$\mathbf{e} = (\mathbf{r}^w + \mathbf{u}^w) - (\mathbf{r}^r + \mathbf{u}^r) \quad (7-87)$$

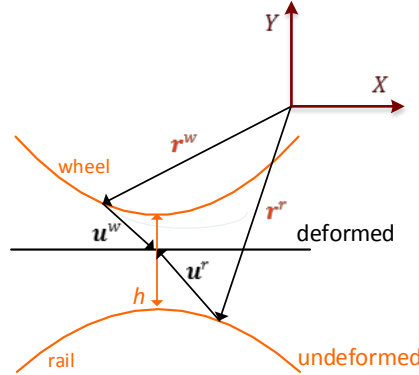


Figure 7-18: Two elastic bodies in contact: undeformed and deformed states

In general, the location  $\mathbf{r}^w + \mathbf{u}^w$  will not coincide with  $\mathbf{r}^r + \mathbf{u}^r$ . The normal component of the displacement difference will be:

$$e = h + u_n \quad (7-88)$$

Where  $h$  is the undeformed normal distance. It is physically impossible that the bodies penetrate in the deformed state;  $e \geq 0$ . The contact area will be determined by  $e = 0$ . Based on the above quantities, the normal and tangential problems are defined:

$$\text{Normal problem: } \begin{cases} \text{in } E: & e > 0, p = 0 \\ \text{in } U = H \cup S: & e = 0, p \geq 0 \end{cases} \quad (7-89)$$

$$\text{Tangential problem: } \begin{cases} \text{in } E: & \dot{\mathbf{w}} \text{ free}, p = 0 \\ \text{in } H: & \|\dot{\mathbf{w}}\| = 0, \|\sigma_t\| \leq \mu p \\ \text{in } C: & \|\dot{\mathbf{w}}\| > 0, \sigma_t = -\mu p \|\dot{\mathbf{w}}\| / \dot{\mathbf{w}} \end{cases} \quad (7-90)$$

Where  $E$ ,  $U$ ,  $H$ , and  $C$  are exterior area to the contact, contact area, adhesion area, and slip area, respectively. Rather than simple form of constitutive laws in Equation (7-72), for the exact rolling theory, based on the theory of elasticity, the constitutive law for traction-displacement relation is defined as:

$$\mathbf{u}(x, y, t) = \int_U \mathbf{A}((x, y), (x^*, y^*)) \mathbf{P}((x, y), (x^*, y^*)) dU \quad (7-91)$$

Where  $\mathbf{A}((x, y), (x^*, y^*))$  is the influence function determined analytically using Bosseiesq-Cerruti solution,  $\mathbf{P} = [\sigma_{tx} \quad \sigma_{ty} \quad p]$  is the stresses in the contact, and superscript \* stands for the previous time step in the numerical integration. The relation depends on the material behavior, and the geometries of the bodies.

$$\mathbf{u}(x, y, t) = \int_U \mathbf{A}((x, y), (x^*, y^*)) \mathbf{P}((x, y), (x^*, y^*)) dU \quad (7-92)$$

In order to numerically solve for the normal and tangential problems, a rectangular “potential contact area” is assumed. It is divided into rectangular elements of size  $\delta x \times \delta y$  for discretizing the problem. Then, for each element, it is determined whether it belongs to the adhesion (stick), slip or exterior areas.

A software package called CONTACT is developed based on the Kalker’s exact three dimensional rolling contact theory powered by VORtech [161]. It has a freely available basic version and a license-based extended premium version. The premium version contains all the basic version functionality plus several extended features:

- The extensions for solving conformal contact problems
- The extensions for an interfacial layer of roughness and contaminants
- The velocity dependent friction laws
- Fast and detailed calculation of the normal contact problem

The program CONTACT is a terminal-based program, with textual input from the keyboard or input-file and textual output to the terminal and several output- files. It works based on different modes of operation: online calculation of contact based on the input file or offline calculation of subsurface stresses from already calculated surface tractions. For each run, the specifications of the contact problem in determined by using control integers: whether it is a normal problem or tangential, whether penetration or total normal force in known, whether the friction coefficient is constant or velocity dependent, and etc. After configuring the contact problem, the program calculates the contact problem based on the given input values for parameters such as modulus of

elasticity, Poisson ratio, friction coefficient, potential contact area dimensions and its discretization, wheel and rail geometry, and etc. The program uses active set algorithms NORM and TANG and a specific nonlinear Gauss-Seidel approach called “ConvexGS” for solving the problem.

The program CONTACT is meant for [161]:

- 3D homogeneous bodies of (linearly) elastic and viscoelastic materials, which may be different for the two contacting bodies,
- with concentrated contact, i.e. where the resulting geometries are essentially flat in and near the contact zone, but not necessarily Hertzian,
- with dry (Coulomb) friction or boundary lubricated situations (third body layer, falling friction, friction memory effects),
- solving shifts as well as rolling, transient as well as steady state problems, with creepages and/or total forces prescribed,
- solving for the surface tractions first, but capable of computing the elastic field in the interiors of the bodies as well.

## 7.5 Experimental Validation of Contact Models

Andrews [106] conducted one of the earliest contact area studies using a pressure-sensitive medium by applying carbon paper between the contacting bodies. He compared the contact area of a locomotive wheel with the calculations of Hertzian theory under various wheel diameters and vertical loads. Reasonable agreement between experiments and Hertz theory was obtained, except for rough contact surfaces. Similar approaches based on impression and pressure-sensitive media have been employed for studying static measurements of railroad wheel-rail contact patch geometry [163,164].

Poole [63] conducted a real time measurement of contact area through placing an array of 1 mm holes on top of a rail segment, and pumped compressed air through the holes. As the wheel travels on the rail, the blockage of the airflow determines the shape and size of the contact patch. The accuracy of this method is limited by the resolution of the hole-array and the speed of the traveling wheel. Furthermore, placing the holes in the rail may alter its properties.

Pau et al. [109,165] proposed a method for estimating the size of wheel-rail contact patch using ultrasonic waves under static conditions. The method analyses the ultrasonic reflection from the contact interface (or the transmission through it) and yields direct information about the size and shape of the nominal contact area. The ultrasonic method has been developed further for studying the effect of surface roughness [64], conformal contact [110], and distribution of contact pressure [166]. Recently, Dwyer-Joyce et al. used this method to evaluate the contact patch in real time conditions [167] and to detect flange contact [168].

Poon [169] studied the traction distribution in rolling with spin using photoelasticity method. An apparatus consisting of two sets of hemispheres in rolling contact with each other was used for providing rolling with spin. A close agreement of the adhesion-slip boundaries was obtained between the measurements and Kalker's strip theory [150]. Using photoelasticity method, Ollerton et al. [107,170] had previously studied the contact stress distribution experimentally. Conducting experimental tests for obtaining the traction distribution of the actual wheel-rail contact is still challenging due to inaccessibility of the interface region.

A large number of experimental studies have addressed adhesion characteristics in railway applications [75,171]. Some have used experimental setups such as tribometers or roller rigs and some have conducted field tests. Logston et al. [172] conducted locomotive friction studies using EMD test car ET800. They investigated the effect of different parameters such as curvature, speed, and rail condition (dry, oil-covered, sand-covered, etc.) onto the creep curve. Similar fielded wheel-rail adhesion tests have been conducted using various locomotives [173,174,175,176]. Earlier efforts for experimental evaluation of creep force-creepage curve include Johnson's experimental work [149], Hobbs' [177] and Gilchrist's [178] studies at British Rail research department, Illingworth's [179] and Brickley's [180] experimental studies, etc. Most of the fielded wheel-rail adhesion experiments have been conducted for longitudinal creepage.

Magel et al. [181] with the aid of a rolling contact tribometer studied the relation of on-track measured creep curves with the theory. Doi et al. [182] investigated the creep force characteristics between wheel and rail using a novel tribometer applicable to rails. The device allows for setting yaw angle and normal loading. Harrison et al. [35] investigated multiple friction measurement devices including hand-pushed tribometer, rheometer, and Amsler machine; they evaluated the

data from these various devices for comparison of creep measurements [35]. Harrison [183] also developed a hand-operated tribometer capable of simulating low creepage regime. Although tribometers are applicable to fielded rails and very common for creep curve measurements, they suffer from contact patch distortion due to the size of the wheel and are not capable of replicating actual normal loading.

Zhang et al. [9,23], using a full-scale roller rig, studied the adhesion characteristics for various contact conditions (various speeds, axle-loads, contaminations). Other full-scale bogies have been employed for conducting creep test studies [184]. A full-scale rig is beneficial in terms of replicating the same conditions in the actual wheel-rail contact; it, however, could sacrifice the accuracy of the speed control, and force measurements due to the size of the equipment. The Sheffield University Rolling Sliding (SUROS) twin disc experimental device [50,51] has been used for conducting creep-creepage model and velocity dependent friction coefficient studies. The rig, however, is capable of producing solely longitudinal creepage. Same is true for other twin disc test machines [53,56,58,185,186]. Due to good controllability over the experiments, twin disks have been used for investigating the effect of various parameters on the wheel-rail contact mechanics; (i) normal loading, (ii) surface condition including roughness, contamination (sand, leaves, etc.), and friction modifiers (water, oil, etc.), (iii) velocity dependency of friction coefficient. Other roller rig configurations have also been used for investigating the creep force characteristics between roller and wheel at varying contact conditions [11,187].

As shown in Figure 7-19-Left, two main discrepancies between experimental results and theoretical curves have been reported for the creep-creepage curve [128,174,188]:

- i. There is a noticeable reduction in initial slope (low creepage values) of the measured creep curve compared with creep theories.
- ii. Beyond the peak point, the measured creep force decreases whereas theory predicts constant force. This reduction in traction at high creepages is responsible for wheel slip or wheel lock-up when excessive tractive or braking effort is applied.

The initial slope reduction phenomenon has been investigated by Bucher [189]. His results present the relationship between the reduction in the initial slope of the curve and surface roughness. In order to model a realistic rough surface, however, an extremely fine discretization is necessary, which demands for a special computer code [190]. Further advancements for

incorporating the slope reduction phenomenon into contact models are discussed in “Effect of contamination and surface roughness” section.

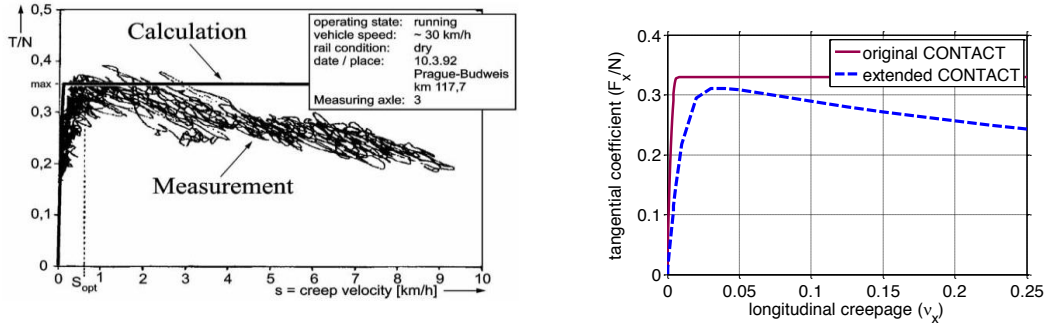


**Figure 7-19: Discrepancies between theoretical creep force calculations and measurements [174,191]. CONTACT program is extended to account for velocity dependent friction coefficient, surface roughness, and third body layer [161].**

Ertz [192] has investigated the falling friction phenomenon. He has shown the dependency of the reduction in the creep curve on the temperature rise at contact for high creepages. Heat dissipation and consequently temperature increases for high creepage values. He incorporated this effect into the temperature dependency of the coefficient of friction. Other theories on falling friction phenomenon and their implementation into contact theories are discussed in “Velocity-dependent friction coefficient” section.

### 7.5.1 Velocity dependent friction coefficient

Many scholars have reported that the friction coefficient is not constant, and it depends on the slip velocity [193] [9] [194]. As the slip velocity increases, the friction coefficient decreases. This phenomenon is known as falling friction. The falling friction could be a result of temperature rise due to friction loss [195] [196] [197] [198]. Kragelski et.al. [199] proposed a model for dependency of friction coefficient on slip velocity ( $\dot{s}$ ):

$$\mu = \mu_0[(1 - A_1)e^{-A_2s} + A_1] \tag{7-93}$$

Where  $\mu_0$  is the maximum friction coefficient,  $A_1$ , and  $A_2$  are two constants, which can be obtained by experiment. Typical model parameters are tabulated in Table 7-6.

**Table 7-6: Typical model parameters for different surface conditions of wheel-rail contact, adapted from [200]**

Model parameter	Wheel-rail condition	
	Dry	Wet
$k_A$	1.00	0.30
$k_s$	0.45	0.10
$\mu_0$	0.55	0.30
$A_1$	0.40	0.40
$A_2$	0.60	0.20

Rovira et.al. [51] proposed another exponential model that has more flexibility for defining the friction coefficient:

$$\mu = \mu_s(e^{-A_3s}) + \mu_d(1 - e^{-A_4s}) \quad (7-94)$$

Where  $\mu_s$ , and  $\mu_d$  is the static and dynamic friction coefficients,  $A_3$ , and  $A_4$  are two constants, which can be obtained by experiment. In addition, Croft et.al. [201] used a different velocity-dependent friction law, given by:

$$\mu = \mu_s \left[ \frac{50}{100 + |s|^2} + \frac{0.1}{0.2 + |s|} \right] \quad (7-95)$$

Vollebregt et.al. [202] introduced another friction law adapted from Croft's friction model, which does not approach zero for large slip velocities, as follows:

$$\mu = \mu_d + \mu_s \left[ \frac{0.2}{1 + |s/0.1|} + \frac{0.2}{1 + |s/\sqrt{0.1}|^2} \right] \quad (7-96)$$

Vollebregt [161] incorporated the velocity-dependent friction coefficient in the software CONTACT (premium version). Polach [200] studied the velocity-variant exponential friction law version of his contact model. Several researchers incorporated various friction laws in the FASTSIM algorithm [51,203,204].

The proposed variable friction coefficient models are implemented in various contact models to represent falling friction phenomenon in measured creep-creepage curves. Polach [205] studied the velocity-variant exponential friction law version of his contact model. Several researchers incorporated various friction laws in the FASTSIM algorithm [51,203,204]. Incorporation of slip velocity-dependent friction coefficient in the FASTSIM algorithm, where slip depends on the friction coefficient in the slide area, could lead to discontinuities in the traction distribution and slip velocity [206]. Researchers used various methods to address these discontinuities. Piotrowski [204], in his frictional power density analysis, iteratively calculates the friction coefficient for the first point inside the slip area, and uses the same value for the friction coefficient for the rest of the points in the slip area. Giemenez et al. [203] simplified the FASTSIM slip formulation for incorporating a piecewise linear friction law. They removed the slip derivative term in the slip calculation formulation to avoid mathematical instability for slip calculation. To prevent discontinuity in the traction distribution at the transition from adhesion to slip area, a reduced friction coefficient computed with a fictitious slip is used. Rovira [51] used the same method as Giemenez et al. [203] for incorporating exponential friction laws into FASTSIM method.

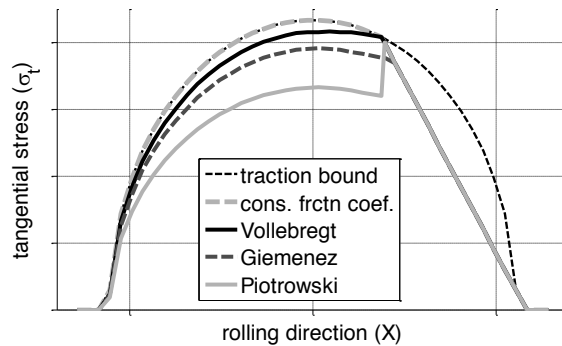


**Figure 7-20: Comparison of tangential stress distribution for a strip in the rolling direction under different methods implemented in the FASTSIM algorithm. Traction curves shown here are schematic.**

Vollebregt [206], however, introduced the concept of friction memory to stabilize the mathematical formulation of FASTSIM method with variable friction coefficient. His model is regularized by adjusting the friction coefficient gradually using previous state information. The actual friction coefficient ( $\mu_a(x)$ ) is defined as:

$$\mu_a(x) = \frac{-\max(\mathbf{s}(x), \mathbf{s}_{min})}{d_c(x)} (\mu_a(x) - \mu(\mathbf{s}(x))) \quad (7-97)$$

Where  $d_c(x)$  is the characteristic slip distance over which the friction coefficient relaxes to  $\mu(\mathbf{s}(x))$  with continuously sliding at velocity  $\mathbf{s}(x)$ .  $\mathbf{s}_{min}$  is a minimum value that allows adaptation of  $\mu_a$  in the adhesion area. The introduction of the friction memory regularizes the traction distribution and removes the kink at the traction distribution at the interface from adhesion to slip area. Vollebregt [161,202] also incorporated the velocity-dependent friction coefficient in the software CONTACT (Figure 7-19-right). The schematic comparison of the tangential stress distribution for a strip along the rolling direction under different modified FASTSIM algorithms (constant friction coefficient [160], Piotrowski's [204], Giemenes's [203], Vollebregt's [206]) is shown in Figure 7-20.

### 7.5.2 Effect of contamination and surface roughness

In addition to velocity dependency of friction coefficient, researchers have reported a reduction of initial slope for the Kalker's creep curve compared to experimental data [191] [207] [208] [35]. This could be due to surface roughness affected by contamination in the interface, which is modeled as a third body layer [209]. Experiments show that the third body layer could decrease the initial slope of the creep-creepage curve [207].

In order to incorporate the effect of contamination for compensation of initial slope reduction, various approaches has been studied. Fries [210] assumed a coefficient called percent Kalker for compensating the initial slope reduction. Polach [200] introduced two different reduction factors for adhesion area ( $k_A$ ) and slip area ( $k_s$ ). Correspondingly, the total tangential force formulation is refined as:

$$F = -\frac{2\mu N}{\pi} \left( \frac{k_A \varepsilon}{1 + (k_A \varepsilon)^2} + \arctan(k_s \varepsilon) \right), k_s \leq k_A \leq 1 \quad (7-98)$$

Where the total slope reduction factor is:  $k = \frac{k_s + k_A}{2}$ . The typical values for the coefficients are tabulated in Table 7-6. Rovira et.al. [51] incorporated the initial slope reduction effect into the FASTSIM algorithm with introducing an additional stiffness at the interface model due to contamination. Kalker assumed scrupulously clean and smooth surfaces at the interface for

modeling the contact. In reality the bodies are neither smooth nor scrupulously clean. FASTSIM algorithm assumes a simple constitutive law at the contact. Rovira et.al. [51] extended the assumption to take the effect of asperities and contamination into account. The compliant parameter for clean surfaces ( $L$ ) is broken to two compliant parameters for considering both the asperities ( $L_a$ ), and contamination effect ( $L_c$ ), as shown in Figure 7-21.

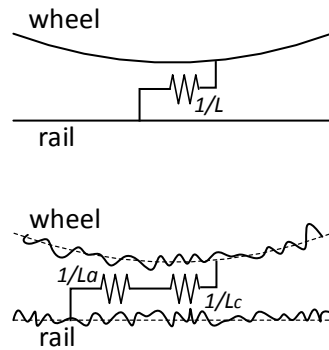


Figure 7-21: Schematic model of the tangential wheel-rail contact for (a) clean and smooth, ad (b) for rough and contaminated surfaces [51]

Vollebregt [209] incorporated the interfacial effect into CONTACT program with introducing a third layer at the interface and imposed its deflection and displacement to the wheel with respect rail displacement, as shown in

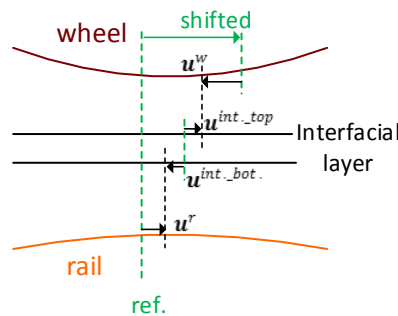


Figure 7-22: Schematic drawing of the interfacial layer modeling in CONTACT program [209]

Four surface points are considered, two the wheel and rail, and two on the intermediate layer touching the wheel and rail. The total displacement will be:

$$\mathbf{u}_t = \mathbf{u}_t^w - \mathbf{u}_t^r + \mathbf{u}'_{top} - \mathbf{u}'_{bottom} \quad (7-99)$$

Where  $\mathbf{u}_t^w$ , and  $\mathbf{u}_t^r$  are the total displacement of the wheel and rail, which are calculated using laws of linear elastic.  $\mathbf{u}'_{top} - \mathbf{u}'_{bottom}$  is the total displacement of the interfacial layer, and is described with:

$$\mathbf{u}'_{top} - \mathbf{u}'_{bottom} = \frac{\sigma_t h'}{G'} \quad (7-100)$$

Where  $h'$  and  $G'$  are the thickness and shear modulus of the third layer. The normal deflection of the third body is neglected.

Bucher et al. [191,207] investigated the effect of surface roughness on the wheel-rail interaction. They simplified the contacting bodies as two cylinders with rough surfaces; the results show significant variation between contact patch pressures and forces for different surface roughness parameters. Given sufficiently fine discretization of a rough surface, it can be shown that local normal stress can be as much as 10 times larger than Hertzian contact stress. Because of that, maximum possible local tangential stress ( $\mu p_{local}$ ) would be higher than what is expected for smooth surfaces, and the onset of slip would be delayed. At the same time, overall creep force per contact patch could be lower than with smooth surfaces; this explains the initial reduction in the creep curve slope in experimental data compared to Kalker's theories [211].

Researchers at the Virtual Vehicle Research Center, Graz, Austria have investigated the development of an extended creep model to take into consideration the influence of more phenomena on the creep characteristics. Tomberger et al. [212] developed a model that accounts for interfacial fluids, surface roughness and temperature parameters. Their model is based on FASTSIM method, however, it allows for locally varying coefficient of friction within the contact area. They assumed that the local friction coefficient is proportional to the real area of metallic contact, which depends on local contact temperature, microscopic roughness, and presence of interfacial fluids. The results showed a good qualitative agreement between the proposed model and measurements. In order to better explain the reduction in initial slope of the creep force-creepage curve, Meierhofer et al. [213] incorporated nonlinear properties of the third body layer into contact modeling. They assumed an additional layer fixed on the surface of the wheel whose

thickness is much less than the contact width. The third body layer assumed to be a homogenous and isotropic material with ideal elastic-plastic behavior. The elastic-plastic material deforms elastically below a certain shear stress called critical shear stress, and deforms plastically above the critical shear stress. They conducted a parametric study on the influence of nonlinear properties of the layer such as elastic and plastic shear moduli, critical shear stress, and layer thickness. The result showed that nonlinear parameters have considerable influence on the creep-creepage curve.

More recently, Six et al. [214] combined the two aforementioned approaches to develop an extended creep model that takes into account several tribological phenomena including temperature, roughness, interfacial fluid, and third body layer. Compared with ideal bi-linear elastic-plastic third body layer model presented in [213], they introduced a pressure and temperature third body layer model. To this end, the parameters describing the third body material, as shown in Figure 7-23, assumed to be a function of pressure ( $p$ ) and temperature ( $T$ ):

$$\begin{aligned}
 G'(p, T) &= G'_0 f_G^p(p) f_G^T(T) \\
 K'(p, T) &= K'_0 f_K^p(p) f_K^T(T) \\
 \sigma'_{t1}(p, T) &= \sigma'_{t10} f_{\sigma'_{t1}}^p(p) f_{\sigma'_{t1}}^T(T) \\
 \sigma'_{t2}(p, T) &= \sigma'_{t20} f_{\sigma'_{t2}}^p(p) f_{\sigma'_{t2}}^T(T)
 \end{aligned} \tag{7-101}$$

The functions  $f_i^p(p)$ , describing the pressure dependency of the elastic-plastic parameters, were determined by experimental tests conducted using a high pressure testing (HPT) rig by variation of normal loading. The temperature correction functions ( $f_i^T(T)$ ) are calculated using dissipated energy within the contact area due to the introduced creepages. The results show that the proposed model has increased the prediction quality of creep-creepage curves for different wheel-rail conditions as compared with measurement data.

Spiryagin et al. [215] extended the FASTSIM algorithm to accurately model the wheel-rail contact for large traction creep at low adhesion conditions. Variable contact flexibility with slip velocity-dependent friction coefficient is introduced into the FASTSIM code. The variable flexibility assumed to be proportional to the ratio of the slip area to the area of adhesion. Unlike the model by Meierhofer et al. [213], the nonlinear deformation and corresponding nonlinear tangential stress distribution for increased traction conditions are represented by a linear

deformation using a higher flexibility coefficient. The variable friction coefficient was assumed to be an exponential function of global slip velocity similar to Equation(7-101).

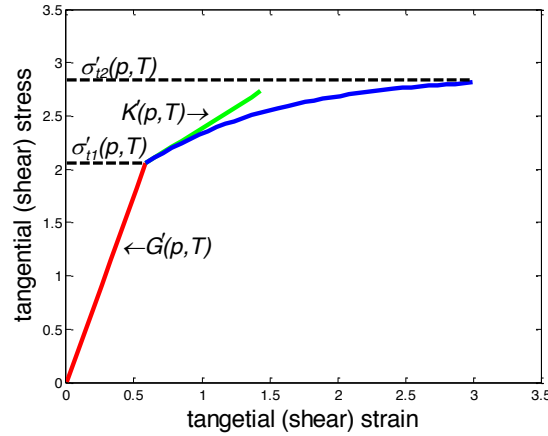


Figure 7-23: Elastic-plastic material properties of the third body layer (adapted from [214])

## 7.6 Results

In this section, the well-known creep-creepage models are compared. A difficulty in comparing different theories is due to their dependency on multiple parameters. The contact creep forces are function of contact geometry, creepages, material properties of the contacting bodies, and normal loading:

$$\begin{bmatrix} F_x & F_y & M_\phi \end{bmatrix} = \mathcal{F}(U, [v_x, v_y, \phi], v, G, \mu, N) \quad (7-102)$$

Dimensionless variables could help comparing the curves, as the effect of the related variables on the creep forces are combined using dimensionless analysis. For the simplified case of Hertzian contact, Equation (7-102) can be rewritten as:

$$\begin{bmatrix} \frac{F_x}{\mu N} & \frac{F_y}{\mu N} & \frac{M_\phi}{\mu N \sqrt{ab}} \end{bmatrix} = \mathcal{F}\left(\frac{a}{b}, [v_x, v_y, \sqrt{ab}\phi], v, \frac{Gab}{\mu N}\right) \quad (7-103)$$

Equations (7-43)-(7-46) show the dependency of Kalker coefficients ( $c_{ij}$ ) on the Poisson ratio and contact patch geometry. Using the calculated Kalker coefficients, the creep equation can be further simplified as:

$$\left[ \frac{F_x}{\mu N} \quad \frac{F_y}{\mu N} \quad \frac{M_\phi}{\mu N \sqrt{ab}} \right] = \mathcal{F} \left( \frac{Gabv_y c_{22}}{\mu N}, \frac{G(\sqrt{ab})^3 \phi c_{23}}{\mu N}, \frac{Gabv_x c_{11}}{\mu N} \right) \quad (7-104)$$

In general, the contact geometry is part of normal contact problem and should be generalized for non-Hertzian conditions. Friction coefficient is not constant and should be generalized as a function of slip velocity. Similarly, the effect of roughness and third body layer needs to be accounted for. Better-developed dimensionless formulation of the contact problem could lead to better and more efficient comparison of the contact models for different contact conditions.

Recently, Vollebregt et al. [216] conducted a statistical comparison of contact models, in order to compare their behavior in diverse circumstances. Using Vampire vehicle system dynamic package, a benchmark data set was obtained. Then, the accuracy of various models for different circumstances such as no spin creepage, typical, or close to derailment is compared with CONTACT results. The results show that FASTSIM and USETAB approaches predict more accurate results than Kalker's linear theory, Vermuelen's theory, Shen-Hedrick-Elkins' model, and Polach's model. USETAB is a pre-calculated table of creep forces by CONTACT program and interpolating the table in a look-up scheme [216].

The dimensionless representation of creep-creepage curve is used for comparison of the different tangential contact theories. The well-known creep-creepage models are implemented in MATLAB. Results for the exact theory of Kalker are obtained from basic version of CONTACT software. The wheel and rail properties and geometry parameters are tabulated in Table 7-7.

**Table 7-7: Wheel-rail contact parameters used in simulations**

Parameter	Value
Poisson ratio: $\nu$	0.27
modulus of rigidity: $G$	$8.2 \times 10^{10}$ [pa]
contact ellipse axes: $a, b$	6, 6 [mm]
normal loading: $N$	106.7 [kN]
friction coefficient:	0.33, 0.33, 0.11

$\mu_0, \mu_s, \mu_k$	
constant: $k_A, k_s$	$1, 0.4$
wheelset velocity: $V$	$16 [km/h]$
constant: $A_1, A_2, A_3, A_4$	$0.4, 0.6, 0.4, 0.6$

Figure 7-24 shows the results of different contact models for pure longitudinal creepage. The initial slope for all the curves is almost the same and very close to Kalker’s linear method except for the extended Polach method. After the initial linear behavior, curves merge to the saturation line with different rates and performance. Johnson and Vermeulen’s nonlinear curve behaves very similar to Shen, Hedrick, and Elkins’ heuristic nonlinear model. Polach method has a slower convergence rate than FASTSIM. CONTACT predicts the largest (except for Kalker’s linear) creep forces toward the saturation line. As it is explained before, Johnson and Vermuelen theory predicts higher creep forces compared with Kalker’s empirical theory.

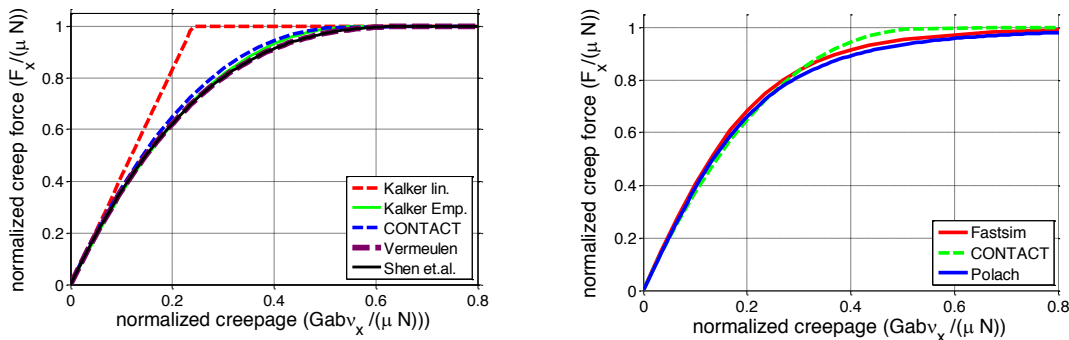


**Figure 7-24: Comparison of dimensionless longitudinal creep force-creepage curve for different contact models: Kalker’s linear theory, Kalker’s empirical theory, Vermeulen’s theory, Shen’s model, and CONTACT algorithm (Left), as well as FASTSIM algorithm, Polach’s, and CONTACT algorithm (Right).**

The effect of spin creepage on the creep-creepage curve is also studied in Figure 7-25. Some of the theories such as Johnson and Vermuelen, and Kalker’s empirical do not consider the effect of spin creepage; others take the effect of spin creepage into account, and this can influence the creep curve considerably. Figure 7-25-left shows lateral creep force results for combined longitudinal and spin creepages. Results show that FASTSIM predicts the closest creep forces to CONTACT results for combined creepages. Polach’s model, however, calculates the lowest creep

forces for the given combined creepages. Pure spin creepage curves are compared in Figure 7-25-right. Results show that for large creepages Shen’s model substantially overpredicts the creep forces, while Polach’s method underpredicts them. The results are consistent with the findings of statistical comparison of contact models [216]. Similar to the combined creepages case, FASTSIM predicts the closest creep forces to CONTACT’s results for pure spin creepages.

Figure 7-26 investigates the velocity dependent friction coefficient laws. The friction coefficient model of  $\mu_3$  approaches zero as creepage increases, whereas  $\mu_1, \mu_2$ , and  $\mu_4$  merge to a non-zero constant. Because of extra flexibility of  $\mu_2$  due to additional constants,  $\mu_2$  is the only law that could increase with increasing creepage for a certain set of constants ( $A_3 > A_4$ ). The friction laws are implemented in Polach model (Figure 7-26-right). Results show that different models could lead to considerable difference in the creep force for a given creepage value. Creep-creepage curve for all the proposed friction coefficient laws declines after it peaks. Results also show that the initial creep behavior for the different curves is very similar to constant friction coefficient curve.

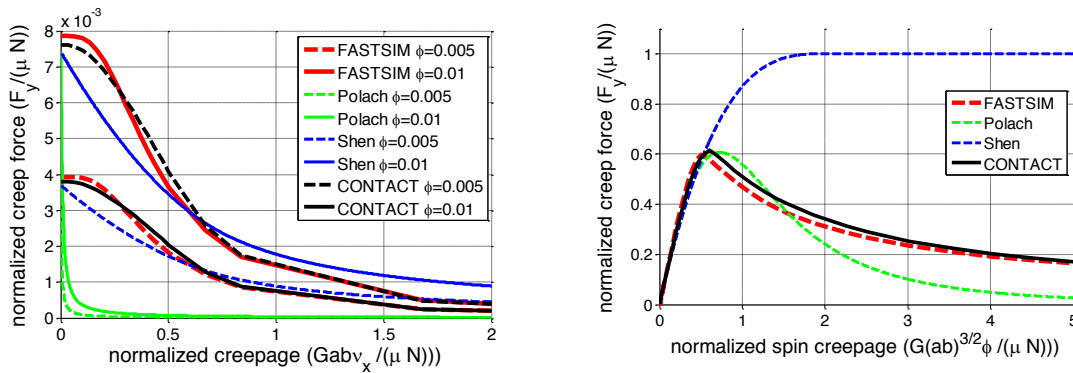


Figure 7-25: Comparison of lateral creep-creepage curve for combined longitudinal and spin creepage condition (left) and for pure spin creepage condition (right) for different contact theories.

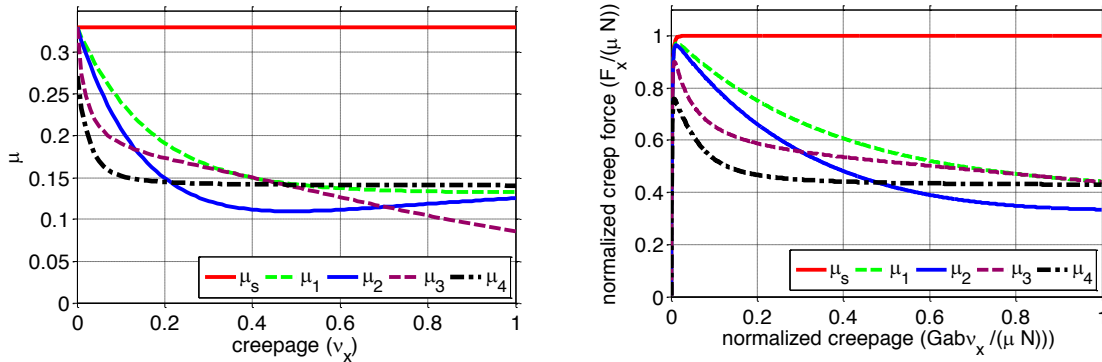


Figure 7-26: Comparison of various velocity dependent friction coefficient laws (left) and their implementation in Polach model (right)

## 7.7 Discussion and Conclusions

In this study, the contact mechanics theories of wheel-rail interaction for railway vehicles are reviewed. Commonly used normal and tangential contact mechanics theories, their restrictions, and simplifying assumptions are highlighted.

Hertz’s normal contact theory is the easiest to apply, but it is limited to interfaces with constant curvatures throughout the contact patch. Kalker’s exact three-dimensional theory is more accurate, yet computationally expensive. Approximate non-Hertzian and multi-Hertzian theories compromise between accuracy and computational efficiency of the two extremes. The use of conformal contact theories remains rare, although there are some promising developments.

In terms of tangential contact, the applications of Kalker’s linear theory are limited to small linear and spin creepages. Johnson and Vermeulen’s theory and Kalker’s empirical theory are valid for larger longitudinal and lateral creepages, but neglect the effects of spin creepage altogether. Shen-Hedrick-Elkins’ theory is based on linear theory, except for large creepages (saturation law). FASTSIM and Polach’s theories are widely used for determining the creep forces; Polach’s model is a simplified version of FASTSIM, which is itself a simplified model of Kalker’s three-dimensional exact theory. The latter is currently considered the “golden standard” for wheel-rail

contact evaluation, but is very computationally expensive; hence, it is not commonly used for fast calculation applications (such as multi-body dynamic simulations).

Tangential contact simulation results show that the contact models behave differently for the same interface conditions. For accurate creep force calculations, there are considerable differences between the models, as well as between the models and the experiments. The dependency of the friction coefficient on the slip velocity is not yet fully understood. Different models have been introduced to explain the phenomenon; various parameters are involved that need more exploration. The physics of the falling friction phenomenon and its dependency on the temperature, surface contamination, and other variables still need to be further developed. In addition, experiments show a noticeable reduction in the initial slope of the creep-creepage curve compared to the models. Some models (such as Polach's, FASTSIM, and CONTACT) are generalized to consider the slope reduction effect, but an accurate model for explaining the reduction is not yet determined.

Normal contact models need further exploration, as well. Faster and more accurate models for predicting contact geometry and pressure distribution that are verified with experimental studies are desired, especially for the case of conformal contact. Some contact phenomena, such as plastic flow of material, are still not well understood. Plastic flow of material could reduce the contact pressure and increase the size of the contact patch.

Due to inaccessibility of the interface region, few techniques have been developed for experimental investigation of both normal and tangential contact problems. The shape and size of the contact patch and the pressure distribution within the contact patch need further exploration. The existing experimental studies mostly conducted static measurements of the normal contact. To the best of the authors' knowledge, no experimental technique has been proposed to measure the tangential stress (traction) distribution at the actual wheel-rail interface. More accurate dynamic creepage and combined creepage experiments are needed to evaluate the performance of the existing contact models for various contact conditions. In summary, better-developed experimental methods and tools are still highly desirable.

Therefore, the field of wheel-rail contact mechanics is not a closed subject and warrants further theoretical and experimental research.

# 8 Multi-Body Dynamic Modeling and Contact Mechanics Simulations

(This chapter was published in part in proceedings of ASME 2016 Joint Rail Conference [217]. Reproduced with permission.)

This chapter develops a detailed multi-body dynamic model of the Virginia Tech Roller Rig (VTRR) using multi body simulation software package SIMPACK. In order to have a better understanding of the dynamics at the contact, dynamic behavior and interaction of various components and subsystems of the rig need to be understood. In addition, a MATLAB routine is configured for comparing the rig's experimental data with any desired contact model. It provides a benchmark for developing creep curves from raw experimental data of the rig and comparing them with existing creep curves.

## 8.1 Coupled Multi-Body dynamic Modeling

It is essential to make sure that the rig's measurements are only due to particular subject of study and not any intermittent source of disturbance. Any unwanted vibration at the contact needs to be compensated in the data measurements. To this end, a fully detailed model of the rig including all the components is developed in SIMPACK. The model has been used for conducting multiple simulations to evaluate the performance of different aspects of the rig.

### 8.1.1 SIMPACK

SIMPACK is a general-purpose multi-body dynamics simulation software that is used to help with analysis and design of mechanical and electro-mechanical systems. SIMPACK has a modular structure that enables it to generate models easily. SIMPACK is commonly used for different railway vehicles studies such as curving behavior, wheels-rail interface forces, passenger comfort, hunting stability, and other dynamic aspects important to rolling stock. In addition to the functionality of SIMPACK in the simulation of rail vehicles, SIMPACK drivetrain is suited for analysis and optimization of mechanical power transmission systems [218].

SIMPACK has a toolbox for wheel-rail contact that gives the user plenty of options to set the dynamic conditions between the two contacting bodies. Some of commonly used contact models can be selected to characterize the wheel-rail interface. The list of SIMPACK contact models is tabulated in Table 8-1. Depending on the selected contact model, the software allows tuning multiple coefficients to characterize the contact model. The wheel and rail profiles, coefficients of friction, Poisson ratio, modulus of elasticity, and among others need to be selected to fully characterize the contact model.

**Table 8-1: SIMPACK built-in contact theories**

<b>Contact theories</b>	
1	No friction (no tangential force)
2	Kalker's linear
3	Kalker's linear with saturation
4	Kalker's simplified theory (FASTSIM)
5	Vermeulen-Johnson theory
6	Polach method

### 8.1.2 Multibody Modeling

In order to study the interaction of components and subsystems, the designed roller rig is modeled using SIMPACK. The coupled multibody dynamic model represents all the major components of the rig. As shown in Figure 8-1, the model includes all the degrees of freedom and the unique electromechanical design of the rig. Like many other multibody dynamic simulation softwares, SIMPACK modeling works based on three main elements: (i) Bodies: defining inertia elements involved in the system (either as a rigid or flexible body). (ii) Joints and Constraints: defining the degrees of freedom in the system and the interactions between bodies, and (iii) Force Elements: introducing force elements in the system such as gearbox, bearing, coupling, actuator, contact model, and among others. The parameters for defining elements are extracted either from SolidWorks model of the rig (mainly for dimensions and inertia parameters), component catalogs, or consultation with vendors (for stiffness, damping, clearance, etc. for the force elements).

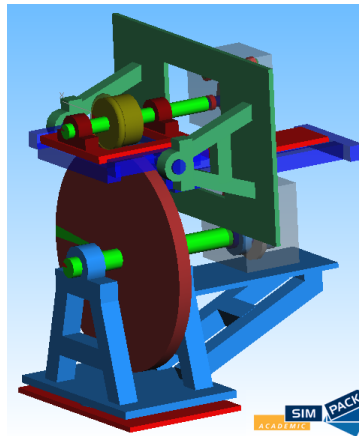


**Figure 8-1: Multi-body dynamic model of Virginia Tech roller rig implemented in SIMPACK software package**

#### **8.1.2.1 Bodies and Joints**

A list of bodies and joints implemented in the model is tabulated in Table 8-2. The model includes 52 degrees of freedom, not including the flexible bodies' DoFs. The model employs two discs, which are fixed to their shafts, functioning as wheel and roller. Two wheel profiles including  $\frac{1}{4}$ th scaled version of AAR-1B wide flange profile and a flat cylindrical profile have been used in the simulations. The scaled AAR1B profile is constructed based on 1500 points extracted from SOLIDWORKS model of the wheel. Similarly, a  $\frac{1}{4}$ th scaled version of 136-lb R is used as the roller profile based on 2000 points extracted from the SOLIDWORKS model of the roller. 136 Rail and AAR-1B wheel are most often used wheel and rail profiles for freight trains in the U.S. Figure 8-2 shows the wheel profiles and rail-head profile used for the roller rig. Similarly, other bodies of the rig including shafts, frames, positioning systems, etc. are modeled. The mass and inertia properties of the bodies are listed in Table 8-2. The inertia properties are extracted from SolidWorks model of the rig.

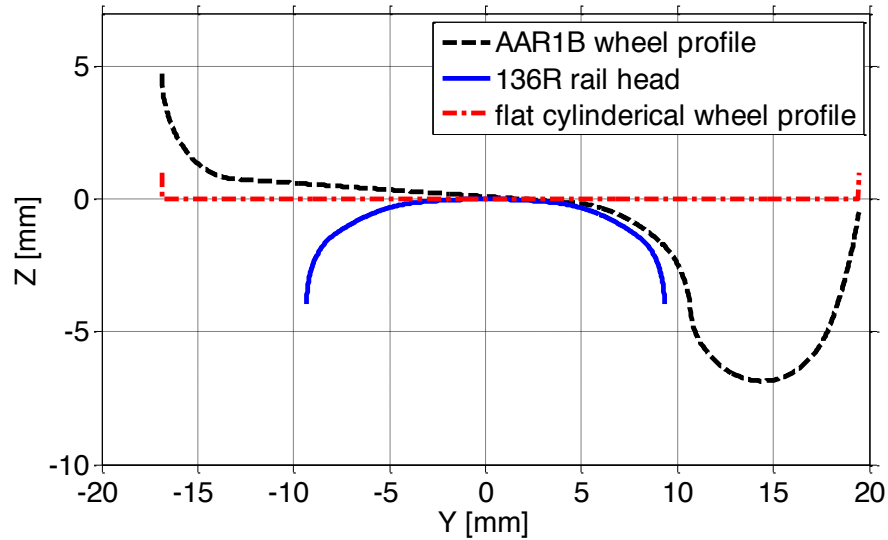


**Figure 8-2: AAR1B and flat cylindrical wheel profiles and 136R rail head profile used for the roller rig.**

The joints connecting the bodies accompanied with the force elements, implemented in the model, provide the same degrees of freedom as the actual rig. The wheel is fixed to the wheel shaft representing the keyless bushing connection with zero backlash. The wheel shaft is floating on the dynamometers and it is constrained with wheel bearing force elements representing pillow block bearings. The wheel bearing force elements provide the rotational motion of the wheel shaft. Similarly, wheel dynamometer is floating with respect to the cradle, and it is constrained via triaxial force elements representing the triaxial loadcells. The joint between the cradle and the vertical body is a 6 DOF, and the relative motion is constrained using cant bearing elements representing pillow block cant bearings. The cant bearing force elements provide the cant degree of freedom. The vertical body's motion relative to inertia system (ground) is constrained with linear bearing force elements providing the vertical degree of freedom for wheel relative to the roller. Similar joints and force elements are implemented in the roller driveline to provide the rotation of the roller, angle of attack and lateral degrees of freedom.

**Table 8-2: List of bodies and joints implemented in the roller rig’s SIMPACK model**

Body	Joint/ w.r.t	Mass [kg]	Inertia [kg.m <sup>2</sup> ]
Wheel	Fixed / wheel shaft	15.63	$\begin{bmatrix} 0.07 & 0 & 0 \\ \text{sym} & 0.133 & 0 \\ \text{sym} & \text{sym} & 0.07 \end{bmatrix}$
Wheel shaft	6 DOF/ Isys	21.37	$\begin{bmatrix} 0.62 & 0 & 0 \\ \text{sym} & 0.01 & 0 \\ \text{sym} & \text{sym} & 0.62 \end{bmatrix}$
Wheel Dynamometer	6 DOF/ Cradle	69	$\begin{bmatrix} 1.72 & 0 & 0 \\ \text{sym} & 1.52 & 0 \\ \text{sym} & \text{sym} & 3.23 \end{bmatrix}$
Cradle	6 DOF/ Vertical	267.4	$\begin{bmatrix} 62.3 & 0 & 0 \\ \text{sym} & 17.8 & 5.20 \\ \text{sym} & \text{sym} & 78.1 \end{bmatrix}$
Motor Dynamometer	6 DOF/ Cradle	39.2	$\begin{bmatrix} 1.35 & 0 & 0 \\ \text{sym} & 0.25 & 0 \\ \text{sym} & \text{sym} & 1.61 \end{bmatrix}$
Gearhead output	Rot (beta) / Motor Dynamometer	13.16	$\begin{bmatrix} 0.17 & 0 & 0 \\ \text{sym} & 0.0 & 0 \\ \text{sym} & \text{sym} & 0.17 \end{bmatrix}$
Gearhead Input	Rot (beta) / Motor Dynamometer	2.54	$\begin{bmatrix} 0.01 & 0 & 0 \\ \text{sym} & 0.0 & 0 \\ \text{sym} & \text{sym} & 0.01 \end{bmatrix}$
Vertical	6 DOF / Isys	280.5	$\begin{bmatrix} 17.8 & 0 & 0 \\ \text{sym} & 75.3 & -0.35 \\ \text{sym} & \text{sym} & 62.4 \end{bmatrix}$
Roller	Fixed / Roller Shaft	699.5	$\begin{bmatrix} 49.3 & 0 & 0 \\ \text{sym} & 96.6 & 0 \\ \text{sym} & \text{sym} & 49.3 \end{bmatrix}$
Roller Shaft	6 DOF / AoA frame	83.75	$\begin{bmatrix} 2.62 & 0 & 0 \\ \text{sym} & 0.25 & 0 \\ \text{sym} & \text{sym} & 2.62 \end{bmatrix}$
AoA frame	6 DOF / Lateral	483.8	$\begin{bmatrix} 104.7 & 0 & 0 \\ \text{sym} & 25.6 & -16.9 \\ \text{sym} & \text{sym} & 99.8 \end{bmatrix}$
Roller Gearhead output	Rot (beta) / AoA frame	23.96	$\begin{bmatrix} 0.15 & 0 & 0 \\ \text{sym} & 0.04 & 0 \\ \text{sym} & \text{sym} & 0.15 \end{bmatrix}$
Roller Gearhead Input	Rot (beta) / AoA Frame	8.62	$\begin{bmatrix} 0.05 & 0 & 0 \\ \text{sym} & 0.0 & 0 \\ \text{sym} & \text{sym} & 0.05 \end{bmatrix}$
Lateral	6 DOF / Isys	129.8	$\begin{bmatrix} 32.2 & 5.52 & 0 \\ \text{sym} & 4.67 & 0.02 \\ \text{sym} & \text{sym} & 36.9 \end{bmatrix}$

**8.1.2.2 Force Elements**

A list of force elements implemented in the roller rig’s model is presented in Table 8-3. The behavior and dynamics of the positioning systems, actuators, couplings, bearings, etc. are represented using appropriate force elements. The interaction between the wheel and roller is

modeled using SIMPACK wheel-rail force element. It allows selecting from Table 8-1 the theory with which contact forces are calculated. The parameters that are used in modeling the wheel-rail interaction are presented in Table 8-4.

**Table 8-3: List of force elements implemented in the roller rig’s SIMPACK model**

Force Element	From Body	To Body	Type
Wheel Rail Pair	Roller	Wheel	Wheel-rail interface
Wheel bearing	Wheel Dynamometer	Wheel shaft	Spring-damper parallel with viscous
Triaxial force sensors	Cradle	Wheel Dynamometer	Spring-damper parallel
Cant Bearing	Vertical	Cradle	Spring-damper parallel with viscous
Cant Actuator	Vertical	Cradle	Proportional actuator
Triaxial force sensors	Cradle	Motor Dynamometer	Spring-damper parallel
Wheel Gearbox	Wheel Input	Gearhead Wheel output	Gearbox torque
Wheel Coupling	Wheel output	Gearhead Wheel shaft	Spring-damper parallel with clearance
Vertical LM guides	Isys	Vertical	Spring-damper parallel with viscous
Dead Weight Actuator	Isys	Vertical	Force/Torque Expression
Roller bearing	AoA frame	Roller shaft	Spring-damper parallel with viscous
Roller Coupling	Roller output	gearhead Roller shaft	Spring-damper parallel with clearance
Roller gearhead	Roller Input	gearhead Roller output	Gearbox torque
Turntable	Lateral	AoA frame	Spring-damper parallel with viscous
AoA actuator	Lateral	AoA frame	Proportional actuator
Lateral Actuator	Isys	Lateral	Proportional actuator
Lateral LM guides	Isys	Lateral	Spring-damper parallel with viscous

Pillow block bearings are modeled using 3-dimensional parallel spring damper force elements that are located at the center of the shaft. Similarly, the linear bearings and cross roller ring in the system are represented by parallel spring-damper force elements. The stiffness and damping coefficients of the bearings are calculated from rigidity charts of the manufacturer manuals and are tabulated in Table 8-5.

Piezoelectric triaxial force elements are modeled as elastic elements with three-dimensional spring-damper characteristics. Since the stiffness of the elements are obtained from manufacturer’s manual, the deflection of the elements will be the same as the piezo-sensors, and they behave relatively the same. The stiffness and damping coefficients of the sensors are also tabulated in Table 8-5.

**Table 8-4: Wheel-rail/roller contact parameters**

<b>Parameter</b>	<b>Value</b>
Wheel diameter	9.47 [in]
Roller diameter	44.2 [in]
Wheel profile	1/4 <sup>th</sup> scaled AAR-1B
Rail profile	1/4 <sup>th</sup> scaled 136lb
Young’s Modulus	210 GPa
Poisson ratio	0.28
Friction coefficient	0.4

The wheel and roller driveline’s couplings are presented by elastic force elements that provide the minor misalignments. Four parallel spring-damper elements located at 90 degree with the adjacent element around a circle, which corresponds to the bolt pattern of the coupling, are implemented in the model. The stiffness and damping coefficients of the couplings are also tabulated in Table 8-5.

### 8.1.3 Simulations and results

After modeling the rig with SIMPACK, multiple simulation runs are conducted to evaluate the performance of the designed rig under various conditions. SIMPACK’s nonlinear numeric solver (SODASRT2) was used for simulations. The simulation was run for 5 seconds, at a sampling rate of 2000Hz.

**Table 8-5: Specifications of force elements implemented in the rig's multibody dynamic model**

<b>Force Element</b>	<b>Stiffness [<math>10^8</math> N/m]</b>	<b>Damping [<math>10^5</math> N.s/m]</b>
Wheel/cant/roller Bearing	radial: 1.9 & axial: 2	radial: 7.5 & axial: 1
Triaxial sensors	shear: 6 & axial: 22	radial: 6 & axial: 22
Wheel coupling	radial: 7 & axial: 100	radial: 5 & axial: 5
Roller coupling	radial: 16 & axial: 100	radial: 10 & axial: 10
LM guide	normal: 8.3 & lateral: 6.6	radial: 6 & axial: 6
Turntable	normal: 33.3 & lateral: 15.3	radial: 5 & axial: 5

The model was initially used to determine the maximum contact forces at the wheel-roller interface under extreme conditions. To this end, various speed profiles are fed to the wheel and roller to be followed. In addition, various displacement profiles are fed to different actuators of the rig to simulate various boundary conditions at the interface. Figure 8-3 shows a sample contact force result for complicated conditions at the contact including complex speed and displacement profiles. The results for the maximum loadings at the contact under extreme conditions are tabulated in Table 8-6. The results have been extensively used as the benchmark for maximum contact loadings during the design phase of the rig.

**Table 8-6: Predicted maximum contact loadings at the wheel-rail interface**

<b>Contact force direction</b>	<b>Value [kN]</b>
Normal	15
Lateral	+/- 6
Longitudinal	+/- 6

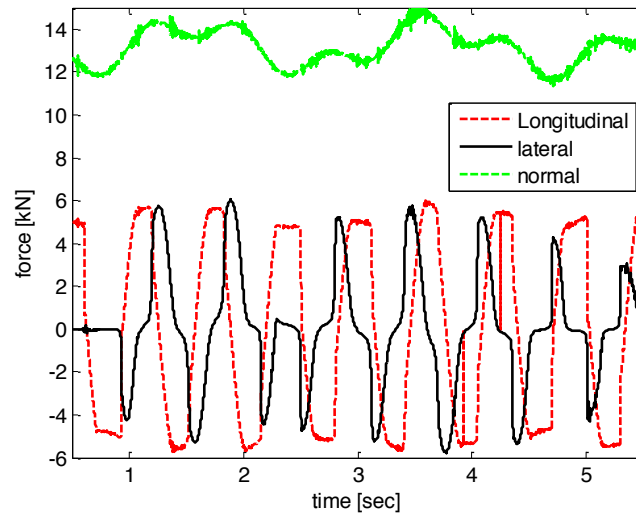


**Figure 8-3: Multi-body dynamic simulation sample results for estimating the maximum contact forces in longitudinal, lateral, and normal directions**

The multi-body dynamic model is also used for studying the performance of the proposed contact measurement system. A desired speed profile command was fed to the designed controller of the roller's driveline, and the wheel driveline was left to follow the roller's speed due to contact forces at the interface. At the same time, angle of attack and cant angle's actuators are fed to follow a desired displacement profile. This causes rapid changes in the contact forces (very dynamic forces), as well as quasi-static forces. The results are shown in Figure 8-4 to Figure 8-6.

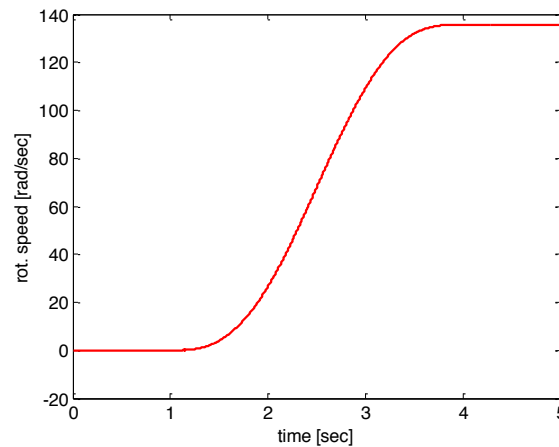


**Figure 8-4: Desired speed profile input for the roller shaft**

SIMPACK results show that the force readings from the motor dynamometer and hence the loading components through the drive shaft are considerable (upto 1/5th of the wheel dynamometers' readings). As a result, the readings from both the dynamometers is needed to estimate the contact forces, accurately. For the dynamic measurements, however, the results show that there is some difference between the estimated contact forces using the dynamometers' readings and the actual contact forces calculated by FASTSIM. Equation 8 shows that these differences are due to inertia terms of the wheel driveline's components. Apart from very sharp peaks (e.g. peaks at approximately 1.15 second in Figure 8-5), the inertia terms stay below 2% of the total contact forces. Nevertheless, the inertia terms could be measured and hence compensated in force estimation by implementing triaxial accelerometers on the driveline's components. Figure 8-5 shows that considering both the dynamometers' readings, as well as accelerometers' readings, the contact forces can be estimated very accurately for dynamic measurements.

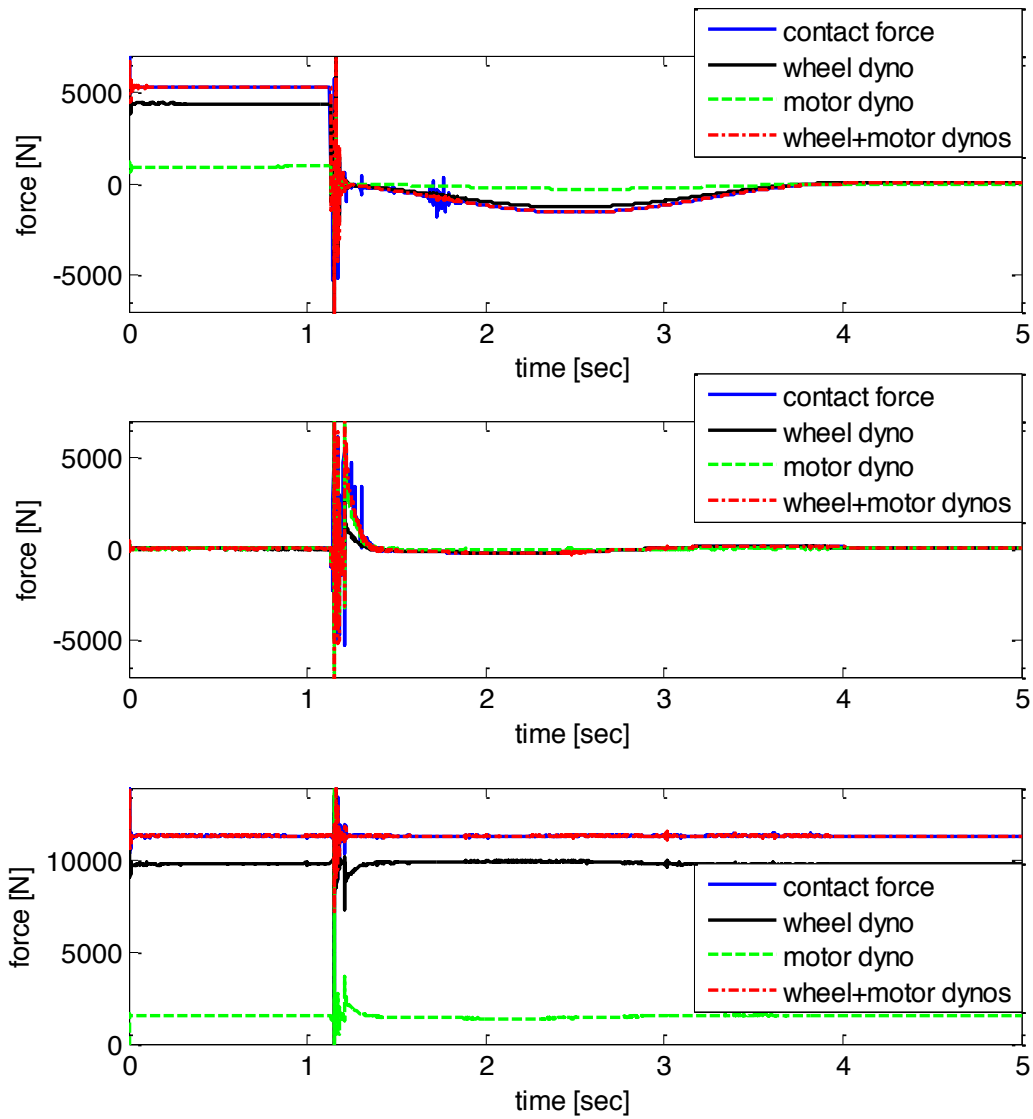


**Figure 8-5: Multi-body dynamic simulation results for estimating the contact forces in longitudinal (top), lateral (middle), and vertical (bottom) directions. Results show that individual force readings from either one of the wheel or motor dynamometers are not able to estimate the contact forces. However, the readings from both the dynamometers can estimate the contact forces accurately.**

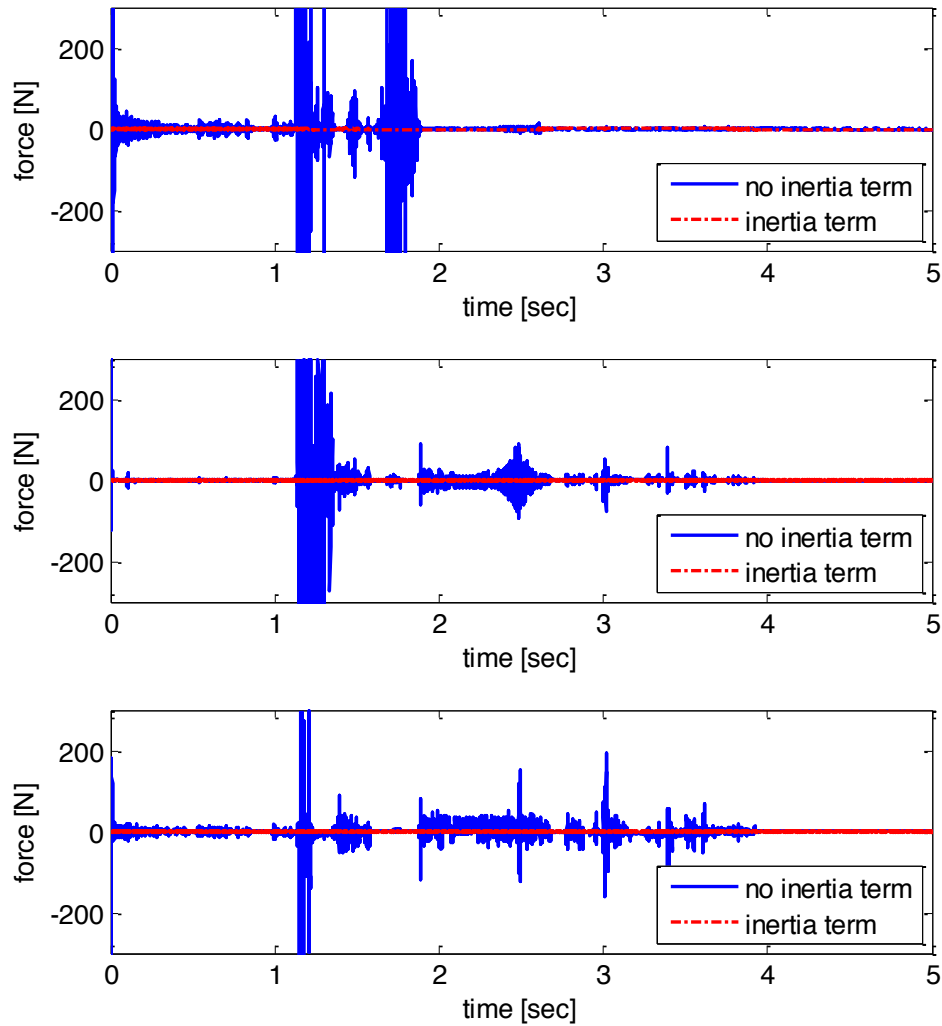


**Figure 8-6: Multi-body dynamic simulation results for the discrepancies between the estimated contact forces from dynamometers and actual contact forces with considering the inertia terms (using accelerometers' readings) and without considering the inertia terms in longitudinal (top), lateral (middle), and vertical (bottom) directions.**

The multibody dynamic model of the rig was also employed to obtain the modal frequencies and mode shapes of the system. To this end, the Eigenvalue solver of SIMPACK is used. The Eigenvalue solver linearizes the model and determines eigen-frequencies, natural damping,

undamped natural eigen-frequencies, and eigen-modes. The results are tabulated in Table 8-7. The solver predicts several critically damped or overdamped eigenmodes that are not listed in Table 8-7. For these modes that are indicated with frequency of zero and damping of unity, the software would not perform an oscillation but return asymptotically to the original position.

**Table 8-7: Results of the Eigenvalues analysis of the roller rig’s SIMPACK model**

<b>No.</b>	<b>Frequency (Hz)</b>	<b>Natural damping</b>	<b>Undamped frequency (Hz)</b>
1	67.5	0.184	68.6
2	66.3	0.573	80.9
3	95.7	0.176	97.2
4	114.2	0.479	130.1
5	130.9	0.023	130.9
6	171.1	0.561	206.8
7	170.1	0.653	224.8
8	177.0	0.824	312.8
9	190.2	0.800	317.4
10	324.1	0.211	331.6
11	323.8	0.391	351.9
12	252.7	0.701	354.5
13	445.8	0.615	565.7
14	507.4	0.606	637.9
15	181.5	0.978	874.4
16	336.4	0.967	1,325.7
17	744.6	0.945	2,281.5

The modal analysis predicts the first natural frequency of the rig to be approximately 70 Hz, providing a relatively high bandwidth for evaluating the dynamics at the wheel-rail interface. This also ensures the performance of the contact force measurement system, as the first modal frequency of the dynamometers lies well above the rig’s first natural frequency.

In order to evaluate the influence of flexibility of the shafts, the wheel shaft is modeled using SIMBEAM module. The SIMBEAM module provides three-dimensional flexible beam structures within SIMPACK that are either described by a modally reduced finite element approach or by a node-based non-linear finite difference approach. For the latter approach, a table of nodes and cross sections is defined. Then, a flexible beam element between two nodes using either Euler-Bernoulli or Timoshenko theories can be specified.

In the coupled multibody dynamic model, both wheel and roller shafts are modeled using Timoshenko elements. The eigenvalues simulation results show that the first natural frequency of both the shafts fall above 200 Hz frequency range. The results also indicate that flexible shafts have insignificant influence on the results for the performance of the contact force measurement system, although the model with flexible shafts runs much slower than the rigid model.

#### 8.1.4 Conclusions

The coupled multi-body dynamic model of the rig has been developed successfully using SIMPACK simulation software. It closely replicates all the major components of the rig and includes all the degrees of freedom. The model is used for conducting multiple simulations. The results of the contact forces at the wheel-roller interface has been extensively used for designing the rig.

The model is also used to evaluate the performance of the contact force measurement system designed for the rig. The multibody dynamic model's results show that the contact forces can be precisely estimated using the force measurement system.

The multibody dynamic model is employed for conducting noise, vibration, harshness (NVH) analysis of the rig. An Eigenvalue analysis provides the modal frequencies and mode shapes of the system. The modal analysis predicts the first natural frequency of the rig to be approximately 70 Hz, providing a relatively high bandwidth for evaluating the dynamics at the wheel-rail interface. Only dynamic that could have higher frequencies than the rig's bandwidth is wheel-rail squeal.

The detailed multi-body dynamic model could be employed for future analysis of the

experimental data. The multi-body vibration analysis could provide a comparison tool for future experimental vibration study of the rig, including vibration due to stick-slip dynamics at the contact. It also could be used for developing a compensation approach for removing any noise from the actual data measurement in order to get the maximum signal to noise ratio.

## 8.2 Contact Module; A MATLAB Routine

In order to compare the rig's experimental data with any desired contact model other than SIMPACK's built-in contact models (Table 8-1), a MATLAB routine is configured. It provides a benchmark for developing creep curves from raw experimental data of the rig and comparing them with existing creep curves. Commonly used contact models are implemented. In addition, the fast and approximate semi-Hertzian rolling contact model, called FaStrip, is advanced to consider the effect of angle of attack.

### 8.2.1 Flowchart

Figure 8-7 shows the flowchart of the contact module implemented in MATLAB. The flowchart is very similar to contact modules implemented in Multibody Simulation software. The inputs to the module include the contact conditions in terms of material properties, geometry, dimensions, kinematics, etc. Contact geometry subroutine calculates the number and location/coordinates of the contact points. Creepage calculation program calculates longitudinal, lateral, and spin creepages based on the kinematics and contact location. Based on the contact location, geometry of the contact and normal loading, normal contact module calculates the size of the contact area and the normal stress distribution. The tangential contact module calculates the contact forces and tangential stress distribution. Dynamometer module calculates the contact forces reacted at the dynamometer based on the contact forces (tangential and normal) and geometry of the rig.

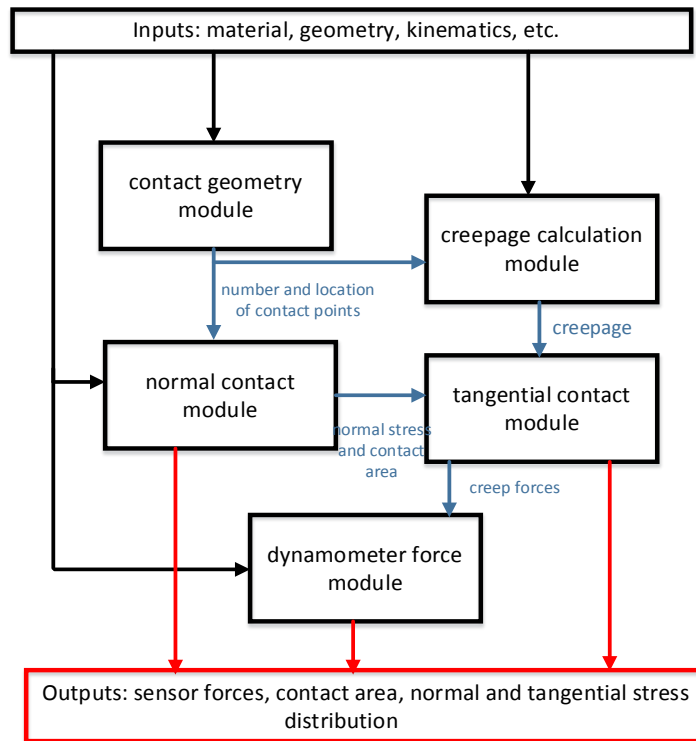
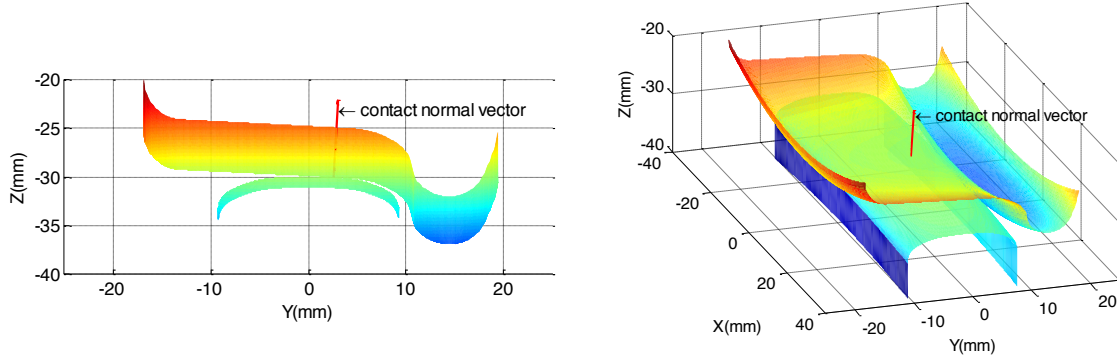
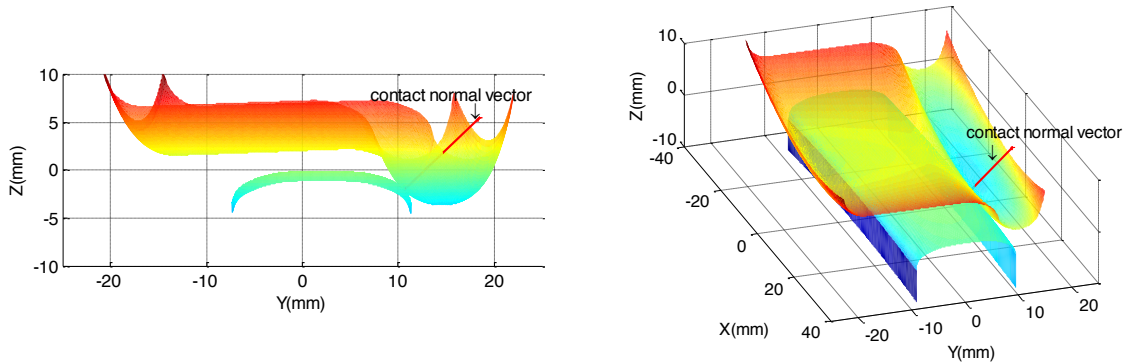


Figure 8-7: Flowchart for the contact module implemented in MATLAB

The contact geometry module assumes that the contact bodies are ideal rigid bodies and can penetrate into each other. Based on the contact condition in terms of wheel and roller profiles, lateral shift, angle of attack, and cant angle predicts the geometry of the contact including center of contact (contact location), normal vector at the contact point, number of contact points, and an estimation of the contact area for a given penetration value. Figure 8-8 and Figure 8-9 show two sample outputs of contact geometry module for two different rig's geometry conditions.



**Figure 8-8: Contact geometry subroutine calculates the location of the contact points based on given contact conditions (lateral shift=0, cant angle=0°, angle of attack=0°)**



**Figure 8-9: Contact geometry subroutine calculates the location of the contact points based on given contact conditions (lateral shift=2, cant angle=5°, angle of attack=3°)**

Equations (7-39) and (7-40) are generalized for the case of a single wheel-roller contact to obtain the creepage equations for the creepage calculation module, as given by:

$$\begin{aligned}
 v_x &= \left( \frac{\omega_r R_r - \omega_w R_w}{V_{ref}} + y_{con} \left( \frac{\dot{\alpha}}{V_{ref}} \right) \right) \\
 v_y &= \left( \frac{\dot{Y}_w}{V_{ref}} - \alpha + \frac{z_{con} \dot{\vartheta}}{V_{ref}} \right) \cos(\gamma) \\
 \varphi &= \frac{\omega_w \sin \vartheta}{V_{ref}} + \frac{\dot{\vartheta}}{V_{ref}} + \left( \frac{\dot{\alpha}}{V_{ref}} \right) \cos(\gamma)
 \end{aligned} \tag{8-1}$$

Where  $y_{con}$  and  $z_{con}$  are the coordinates of the contact location,  $\vartheta$  is the cant angle,  $\alpha$  is the angle of attack, and  $V_{ref}$  is the forward velocity of the vehicle, given by:

$$V_{ref} = \frac{\omega_r R_r + \omega_w R_w}{2} \quad (8-2)$$

Where  $\omega_r$  and  $\omega_w$  are the rotational speed of the roller and wheel, respectively.  $R_r$  and  $R_w$  are the rolling radius of the roller and wheel, respectively.

For the normal and tangential contact modules, some of the contact models do not provide the stress distribution such as Kalker's linear, Polach's, Johnson's, Shen's. These models predict the total contact/creep forces. These models and FASTSIM are based on the Hertzian theory so that contact patch is in elliptical shape. Two non-elliptical contact models are CONTACT and ANALYN+FaStrip method.

The dynamometer module calculates the total contact forces reacted at the dynamometer based on the contact forces (tangential creep forces, normal loading) and contact geometry, using Equations (6-8) and (6-9).

### 8.2.2 ANALYN+FaStrip Algorithm

As discussed in Chapter 7, due to limitations of Hertzian contact theory, the dimensions of contact patch given by Hertzian theory are often a poor representation of the true contact shape, primarily due to non-constant surface curvatures and multiple contact zones [70,117]. The curvatures of both wheel and rail can significantly vary through the width of the contact patch, particularly for the case of worn wheels and rails in the flange throat contact. Studies show that the contact patch is usually non elliptic. A number of non-Hertzian and semi-Hertzian normal contact theories have been used to better describe wheel-rail normal contact problem. These theories are discussed in detail in Chapter 7.

Since CONTACT is relatively computationally expensive for solving contact problem, it is not suitable for vehicle dynamics simulations that need online calculation of the contact for each time step. Therefore, fast/approximate methods are introduced to solve the normal contact problem [115]. Based on the concept of virtual penetration, several non-elliptic methods are introduced

such as Piotrowski et al. [122], Linder et al. [139,140], and Ayasse et al. [141]. Sichani et al. [113] discussed and compared these virtual penetration methods and concluded that the accuracy of the contact patch estimation and contact pressure distribution by these methods are case dependent and could deviate from CONTACT for some contact conditions. So, Sichani et al. [143] introduced his method by modifying the virtual penetration method for taking the effect of elastic deformation into account. The method is implemented in an algorithm called ANALYN, and the results show improved accuracy in predicting contact patch [143].

In this study, the ANALYN algorithm is implemented in MATLAB, and is improved to consider the effect of angle of attack (yaw angle). Semi-Hertzian models (virtual penetration methods) do not consider the effect of angle of attack (yaw angle) between wheel and rail. Non-zero angle of attack contact condition contradicts the assumption of Hertzian in rolling direction. However, since the maximum angle of attack for a wheelset in extreme condition (sharp curves) is less than 15 mrad, considering the angle of attack does not affect the semi-Hertzian assumption drastically.

In order to consider the effect of angle of attack on Virtual penetration methods, the rail profile is projected to the plane aligned with the wheel. Then, the lateral distance between the wheel and rail is calculated based on this altered rail profile. The pressure distribution is assumed elliptic in the rolling direction. The results show improved accuracy in the contact area prediction as well as creep force estimation. For the tangential contact, the FaStrip algorithm introduced by Sichani et al. is employed.

### 8.2.2.1 ANALYN Algorithm

Sichani et al. [143] generalized the concept of virtual penetration by considering the elastic deformations ( $u_z(x,y)$  in Equation (7-5)) in normal contact formulation. It is assumed that the wheel and rail are two bodies of revolution (in case of flat rail, rail is a body of extrusion;  $A = 1/(2R_{wx})$ ). Since the wheel is body of revolution, a semi-elliptical normal stress distribution similar to Hertz theory assumed in the direction of rolling. The separation (undeformed distance) is defined as:

$$h(x,y) = Ax^2 + h(y) \quad (8-3)$$

Sichani et al. [143] approximated surface deformation using the separation (undeformed distance), as given by:

$$u_z(x, y) = \alpha(y)Ax^2 + \beta(y)h(y) \quad (8-4)$$

Therefore, the distance between the contacting bodies (Equation (7-5)) will be

$$D(x, y) = (\alpha(y) + 1)Ax^2 + (\beta(y) + 1)h(y) - d \quad (8-5)$$

Where  $d$  is the elastic approach at the first point of contact and parameters  $\alpha$  and  $\beta$  are obtained by setting the semi-axes of the calculated contact ellipse using Equation (8-5), in a Hertzian contact, equal to the ones from Hertz solution [143], given by:

$$\alpha(y) = \frac{r(y)}{m^2(y)} \left( \frac{B(y)}{A(y)} + 1 \right) - 1 \quad (8-6)$$

$$\beta(y) = \frac{r(y)}{n^2(y)} \left( \frac{A(y)}{B(y)} + 1 \right) - 1 \quad (8-7)$$

Where  $A(y)$  and  $B(y)$  are the local curvatures at point  $(x=0, y)$ , and  $m(y)$ ,  $n(y)$ , and  $r(y)$  are non-dimensional Hertzian coefficients calculated using the local relative curvatures [143]. Sichani et al. define the contact patch boundary as:

$$|a(y)| = \sqrt{\frac{d - (\beta(y) + 1)h(y)}{(\alpha(y) + 1)A(y)}} \quad (8-8)$$

The pressure distribution is defined as:

$$p(x, y) = p_0(y) \sqrt{1 - \left( \frac{x}{|a(y)|} \right)^2} \quad (8-9)$$

Where the maximum pressure value  $p_0(y)$  is estimate using Hert solution, as:

$$p_0(y) = \frac{E}{1 - \nu^2} \frac{1}{n(y)r(y)} \frac{d - (\beta(y) + 1)h(y)}{|a(y)|} \quad (8-10)$$

The local curvatures for wheel and rail profiles are obtained by calculating the osculating circle for each point. The small non-positive curvatures within the potential contact area are corrected before being used in the method.

### 8.2.2.2 FaStrip Algorithm

Sichani et al. [219] combined strip theory and FASTSIM to develop a tangential contact model called FaStrip algorithm. The stress distribution within the adhesion area and adhesion-slip boundary is determined using strip theory, and stress distribution within the slip area is determined using the FASTSIM algorithm. The results show that FaStrip improves the accuracy of the estimated tangential stress distribution, as well as improves the creep force estimation compared with FASTSIM [219].

In their formulation, based on the strip theory, the contact area is divided to strips parallel to rolling direction, and the longitudinal and lateral shear stress distribution in the adhesion area is given by:

$$\begin{aligned} \sigma_{tx}(x, y) = & \frac{\mu p_0(y)}{a(y)} [\kappa(y) \sqrt{a^2(y) - x^2} \\ & - \kappa'(y) \sqrt{(a(y) - q(y))^2 - (x - q(y))^2}] \end{aligned} \quad (8-11)$$

$$\begin{aligned} \sigma_{ty}(x, y) = & \frac{\mu p_0}{a(y)} [\iota(y) \sqrt{a^2(y) - x^2} \\ & - \iota'(y) \sqrt{(a(y) - q(y))^2 - (x - q(y))^2}] \end{aligned} \quad (8-12)$$

Where  $\mu$  is the friction coefficient and  $p_0(y)$  is the maximum Hertzian pressure in the strip, defined in Equation (8-10). The parameter  $q(y)$  denotes the half-length of the slip area, and is calculated as:

$$q(y) = \frac{\sqrt{v_y'^2 + (1 - \varphi'^2)(v_x'^2 - \frac{\varphi'y}{a(y)})^2} + v_y'\varphi' a(y)}{1 - \varphi'^2} \frac{1}{1 - \nu} \quad (8-13)$$

Where

$$v_x' = -\frac{G}{2\mu p_0(y)} \frac{4(1 - \nu)}{\pi^2} c_{11} v_x \quad (8-14)$$

$$v_y' = -\frac{G}{2\mu p_0(y)} \frac{4(1 - \nu)}{\pi^2} c_{22} v_y \quad (8-15)$$

$$\varphi' = -\frac{G}{2\mu p_0(y)} \frac{3\sqrt{a(y)b(y)}}{\pi} c_{23} \varphi \quad (8-16)$$

The coefficients  $\kappa(y)$ ,  $\kappa'(y)$ ,  $\iota(y)$ , and  $\iota'(y)$  are defined as:

$$\kappa(y) = \kappa'(y) = \frac{v_x'^2 - \frac{\varphi'y}{a(y)}}{\sqrt{(v_y' + \frac{\varphi'd(y)}{a(y)})^2 + (v_x'^2 - \frac{\varphi'y}{a(y)})^2}} \quad (8-17)$$

$$\iota(y) = \frac{v_y' + \frac{\varphi'd(y)}{a(y)}}{\sqrt{(v_y' + \frac{\varphi'd(y)}{a(y)})^2 + (v_x'^2 - \frac{\varphi'y}{a(y)})^2}} \quad (8-18)$$

$$\iota'(y) = \frac{v_y' + \frac{\varphi'd(y)}{a(y)}}{\sqrt{(v_y' + \frac{\varphi'd(y)}{a(y)})^2 + (v_x'^2 - \frac{\varphi'y}{a(y)})^2}} - \varphi' \quad (8-19)$$

In the slip area ( $x < -a(y) + 2d(y)$ ), the tangential shear is determined using the FASTSIM algorithm. The longitudinal and lateral tangential stresses ( $\sigma_{tx_{FASTSIM}}(x, y)$  and  $\sigma_{ty_{FASTSIM}}(x, y)$ ) are determined using FASTSIM algorithm with a modified flexibility parameter as:

$$L_T = \frac{L_x|v_x| + L_y|v_y| + \sqrt{a(y)b(y)}|\varphi|L_\varphi}{\sqrt{v_x^2 + v_y^2 + a(y)b(y)\varphi^2}} \quad (8-20)$$

Then, the tangential stress distribution, using the elliptical normal pressure distribution defined in Equation (8-9), is defined as:

$$\sigma_{tx}(x, y) = \frac{\sigma_{tx_{FASTSIM}}(x, y)}{\sqrt{(\sigma_{tx_{FASTSIM}}(x, y))^2 + (\sigma_{ty_{FASTSIM}}(x, y))^2}} \mu p_0(y) \sqrt{1 - \left(\frac{x}{|a(y)|}\right)^2} \quad (8-21)$$

$$\sigma_{ty}(x, y) = \frac{\sigma_{ty_{FASTSIM}}(x, y)}{\sqrt{(\sigma_{tx_{FASTSIM}}(x, y))^2 + (\sigma_{ty_{FASTSIM}}(x, y))^2}} \mu p_0(y) \sqrt{1 - \left(\frac{x}{|a(y)|}\right)^2} \quad (8-22)$$

### 8.2.3 Results

In this section simulation results for the contact module implemented in MATLAB are presented. Figure 8-2 shows the wheel profiles and rail-head profile designed for the roller rig. These profiles are used for the simulations. Material properties and rig's geometry, inputs to the contact module, are listed in Table 8-8. Contact geometry, tangential stress distribution, and creep forces for different contact conditions are thoroughly discussed and compared.

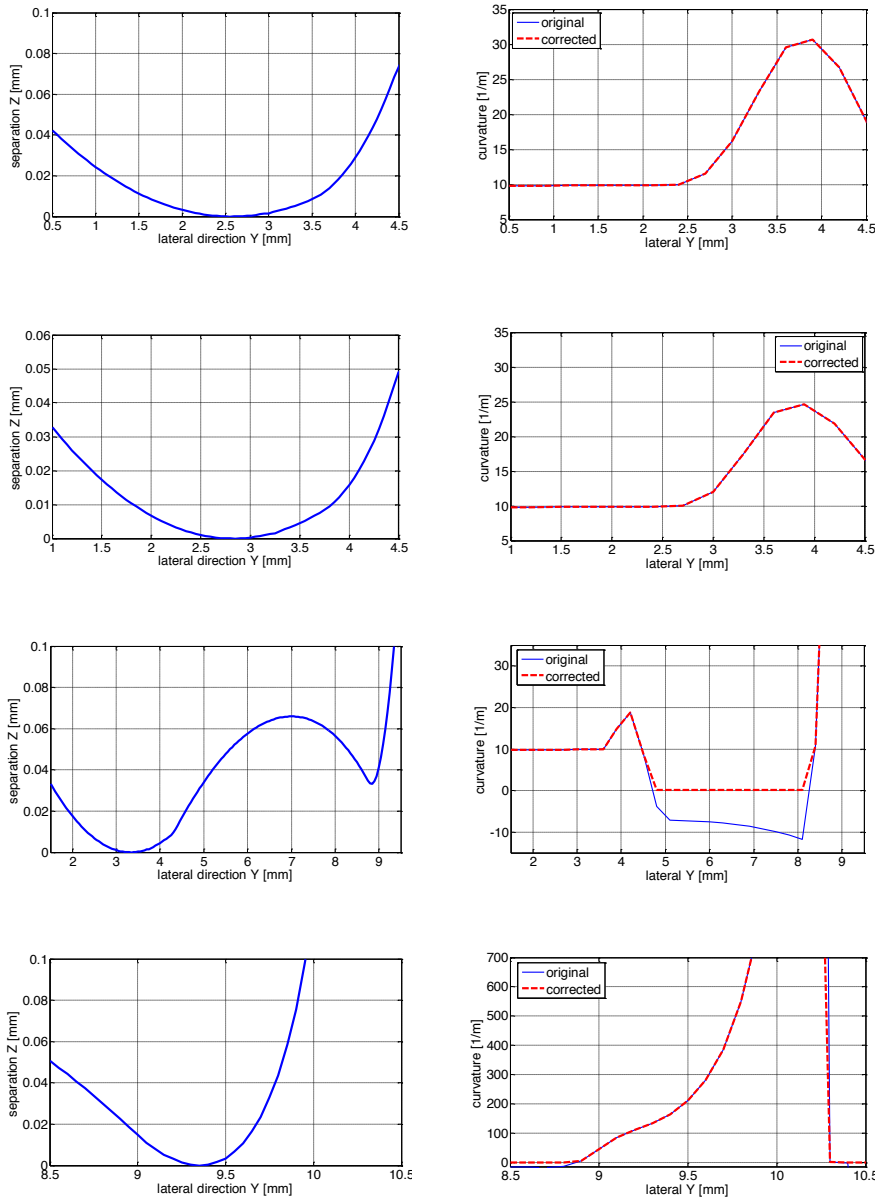
The effect of lateral displacement on contact geometry is investigated. To this end, the results of different models are compared for different lateral displacements. The results for the "Rigid" method are obtained using the contact geometry module (assuming contact bodies are ideal rigid bodies). The interpenetration value is selected as half of the elastic approach. The elastic approach is calculated using ANALYN algorithm using secant iterative method with normal force as input to the algorithm. Hertzian contact area is calculated based on the Hertz theory and radii of curvature at the point of contact (first point at which bodies touch).

**Table 8-8: Wheel-rail contact material properties and geometry parameters used in simulations**

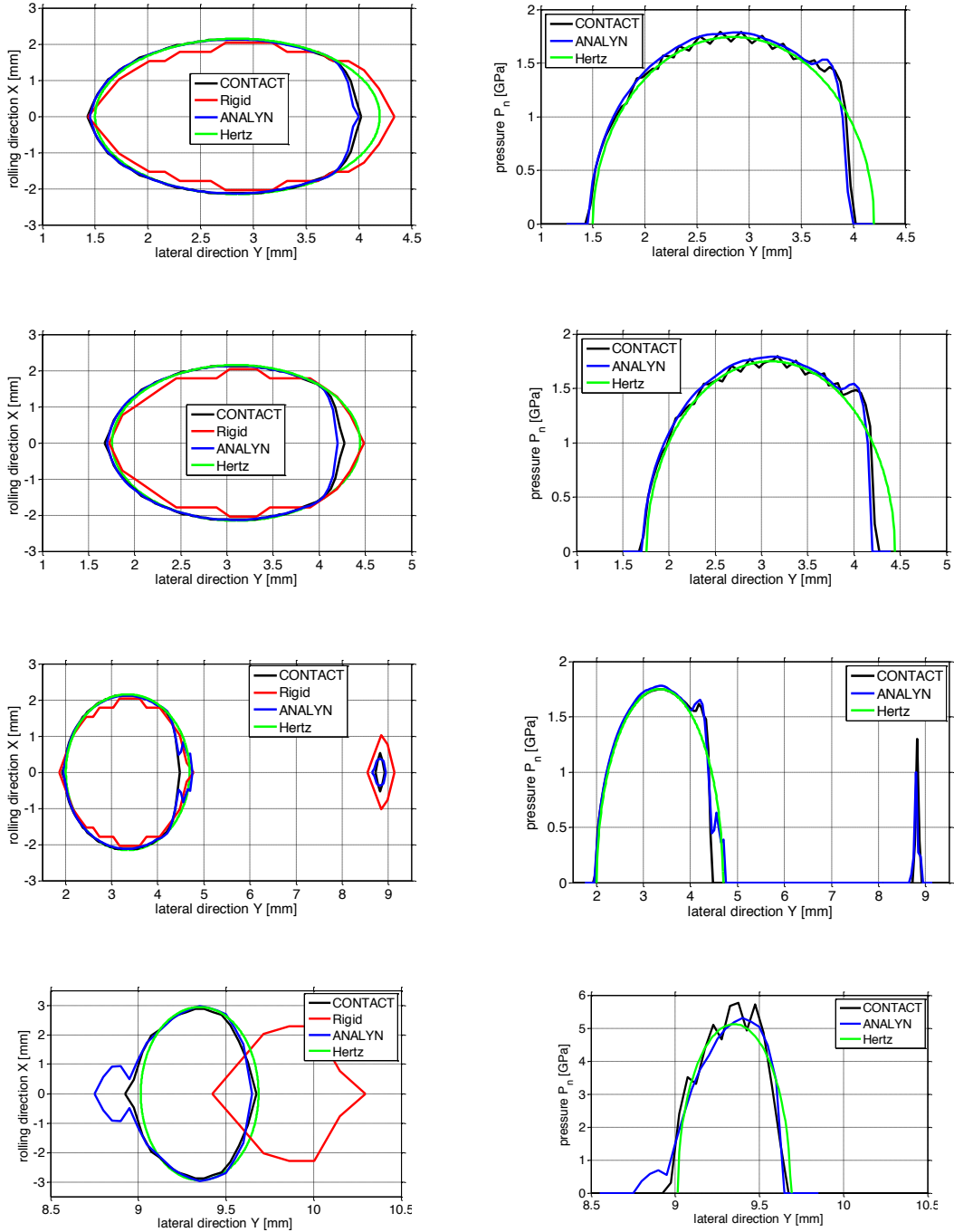
Parameter	Value
Poisson ratio: $\nu$	0.27
modulus of rigidity: $G$	$8.2 \times 10^{10}$ [pa]
Wheel radius	124.5 [mm]
Roller radius	561.3 [mm]
normal loading: $N$	10.6 [kN]
friction coefficient	0.33
Forward velocity: $V$	16 [km/h]

Figure 8-10 shows the separation curve between the bodies, as well as curvature and corrected curvature curves for different lateral displacement values. The curvature correction method comes into play for the case of  $y = 0.8$  where negative curvatures at the potential contact area are corrected. Accordingly, Figure 8-11 shows the contact area and normal pressure profile for the center strip aligned with  $x = 0$ . The results show that the contact area changes considerably as the lateral displacement changes. As the lateral displacement increases the contact geometry shifts from one point contact to two contact points and then shifts back to one point contact for flange contact. For the first two cases ( $y = 0$  and 0.4), the contact area does not deviate considerably from Hertzian contact. ANALYN generates the closest results to CONTACT algorithm for both the contact area and normal pressure. For the case of  $y = 0.8$ , two point contact happens and Hertz theory fails to detect the second contact point (second contact region). As shown in the results, ANALYN closely predicts both the contact regions and normal pressure contact. The side lobe predicted by ANALYN attached to the primary contact region ( $y = 4.5$ ) is due to very simple curvature correction method, and can be removed by implementing more complicated methods. In order to mitigate the computational expense of the algorithm a very simple curvature correction method is employed for this study. With increasing the lateral displacement, the contact switches back to a one point contact for a flange contact. The side lobe for the predicted

contact region by ANALYN can also be improved using a more complicated curvature correction method.



**Figure 8-10: Separation curve and corresponding curvature curve of wheel-roller contact for different lateral displacements; from top to bottom  $y = 0.0$ ,  $y = 0.4$ ,  $y = 0.8$ , and  $y = 1.2$  mm (cant angle= $0^\circ$ , angle of attack= $0^\circ$ )**



**Figure 8-11: Contact area and normal pressure distribution along line  $x = 0.0$  for wheel-roller contact for different lateral displacements; from top to bottom  $y = 0.0$ ,  $y = 0.4$ ,  $y = 0.8$ , and  $y = 1.2$  mm (cant angle=0°, angle of attack=0°)**

It must be noted that the ANALYN algorithm implemented in this study could be slightly different from original ANALYN algorithm [143], as the method for calculating the osculating circle and curvature correction method for negative curvature regions could be slightly different.

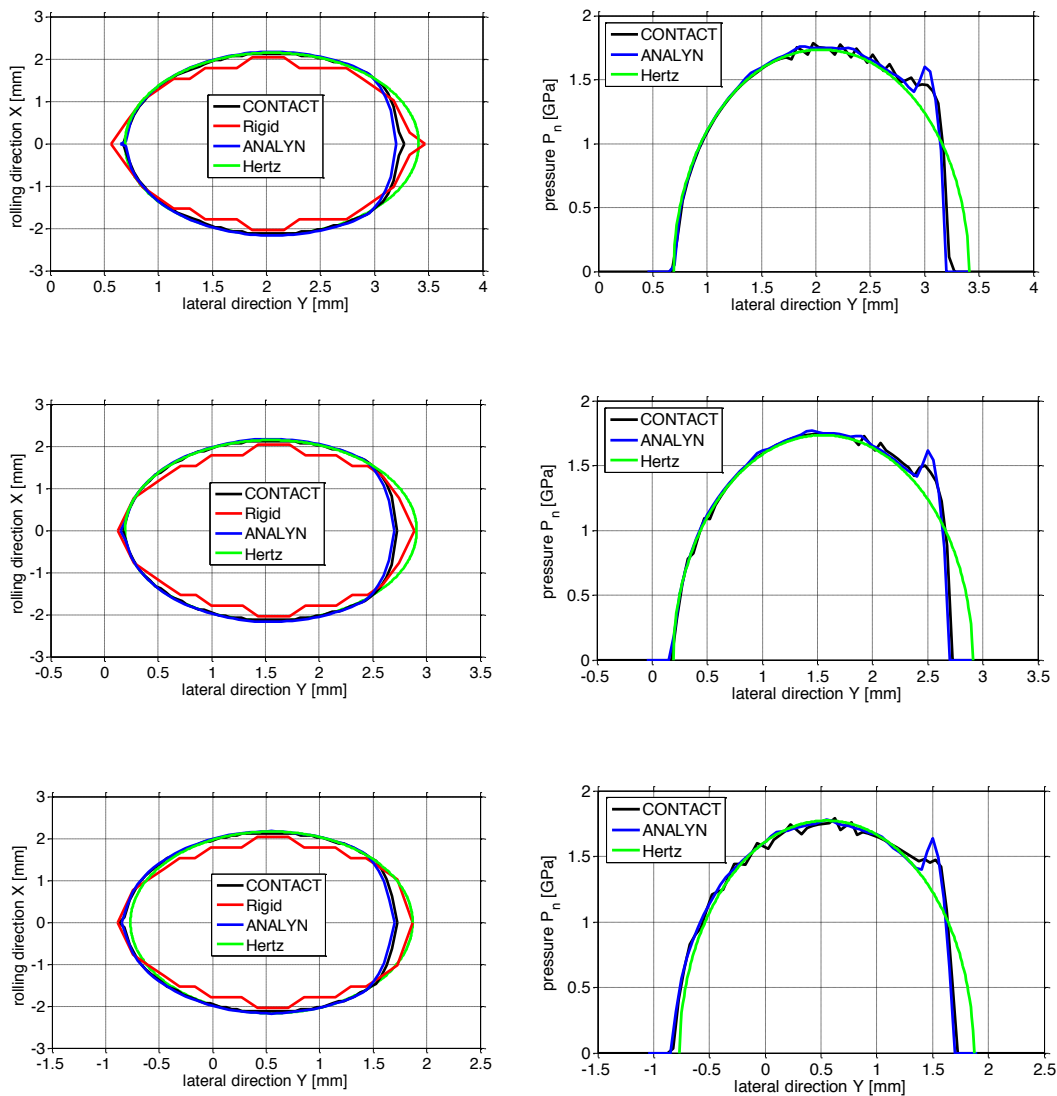


**Figure 8-12: Contact area and normal pressure distribution along line  $x = 0.0$  for wheel-roller contact for different lateral displacements; from top to bottom  $y = -0.5$ ,  $y = -1$ ,  $y = -2$ mm (cant angle= $0^\circ$ , angle of attack= $0^\circ$ )**

Similarly, Figure 8-12 shows the results of the contact area and normal pressure for negative lateral displacement values. Since the contact region remains on the conical shape of the wheel

for all these cases, the contact area and normal pressure distribution does not change as much. The contact location, however, changes with shifting the wheel to left with respect to the rail/roller.

For all the cases described in Figure 8-10 to Figure 8-12, the normal force is 10600 N. With increasing the normal loading, the contact region increases; hence the accuracy of non-Hertzian methods for predicting the contact area with respect to Hertz theory gets more conspicuous. As shown in Figure 8-13, for the increased normal loading ( $N=40600$ ), the second contact region that Hertz theory fails to predict, gets larger.

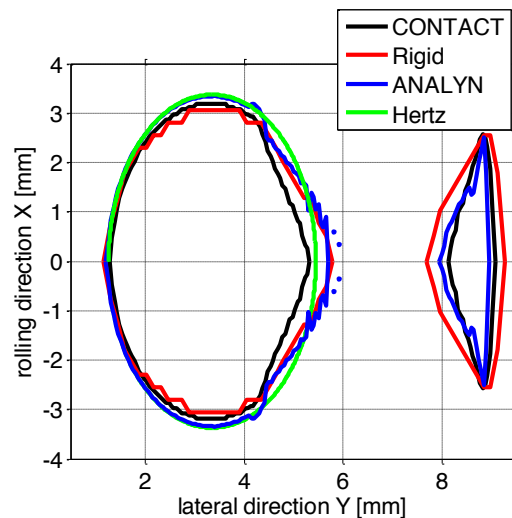


**Figure 8-13: Contact area predicted by different normal contact theories for increased normal loading condition at the interfaces (lateral shift=0.8, cant angle=0°, angle of attack=0°)**

In addition to the effect of lateral displacement on normal contact problem, the effect of cant angle on the contact geometry and normal pressure distribution is investigated. To this end, cant angle is changed, while the other geometry variables (lateral displacement, angle of attack) are kept constant. Figure 8-14 shows the geometry of wheel and roller profiles for different cant angles. As shown in Figure 8-14, cant angle has a noticeable effect on the contact location and normal contact vector.

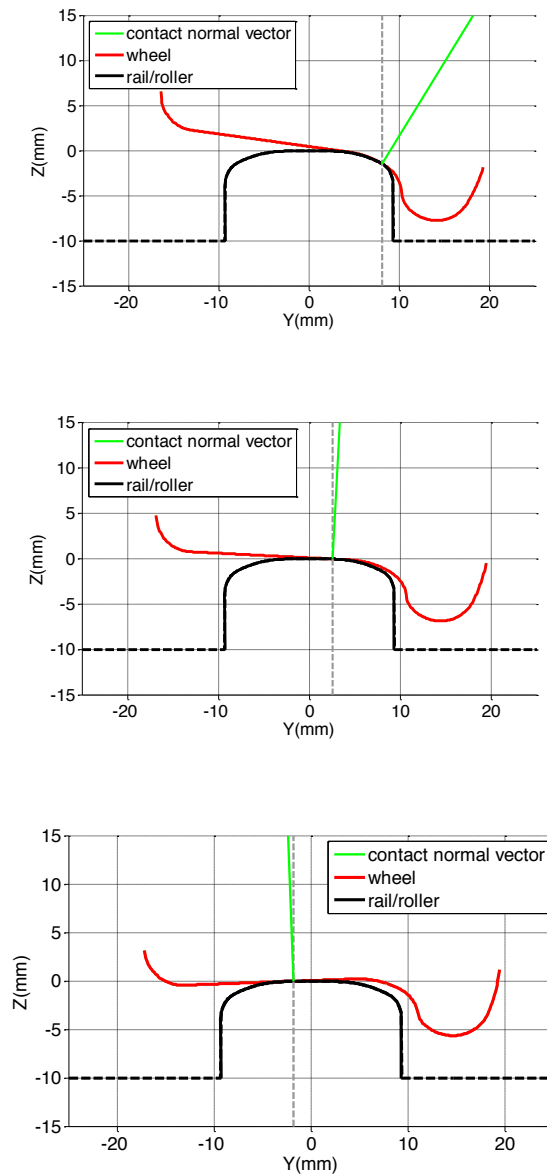


**Figure 8-14: Geometry of wheel-roller contact for different cant angles showing the contact point location and normal vector at the contact point; from top to bottom cant angle is  $-5^\circ$ ,  $0^\circ$ , and  $5^\circ$ , respectively (lateral shift=0mm, angle of attack= $0^\circ$ )**

Figure 8-15 shows the contact area and normal pressure curve for different cant angles. The results show that the contact area changes considerably as the cant angle changes. With a negative cant angle (cant angle= $-5^\circ$ ), a slender contact area with a side lobe occurs at the flange throat, while for a positive cant angle (cant angle= $5^\circ$ ) a wider contact area occurs at the conical part of the wheel. For the positive can angle, the contact area merges to a contact ellipse and normal contact distribution turns to an elliptical distribution.

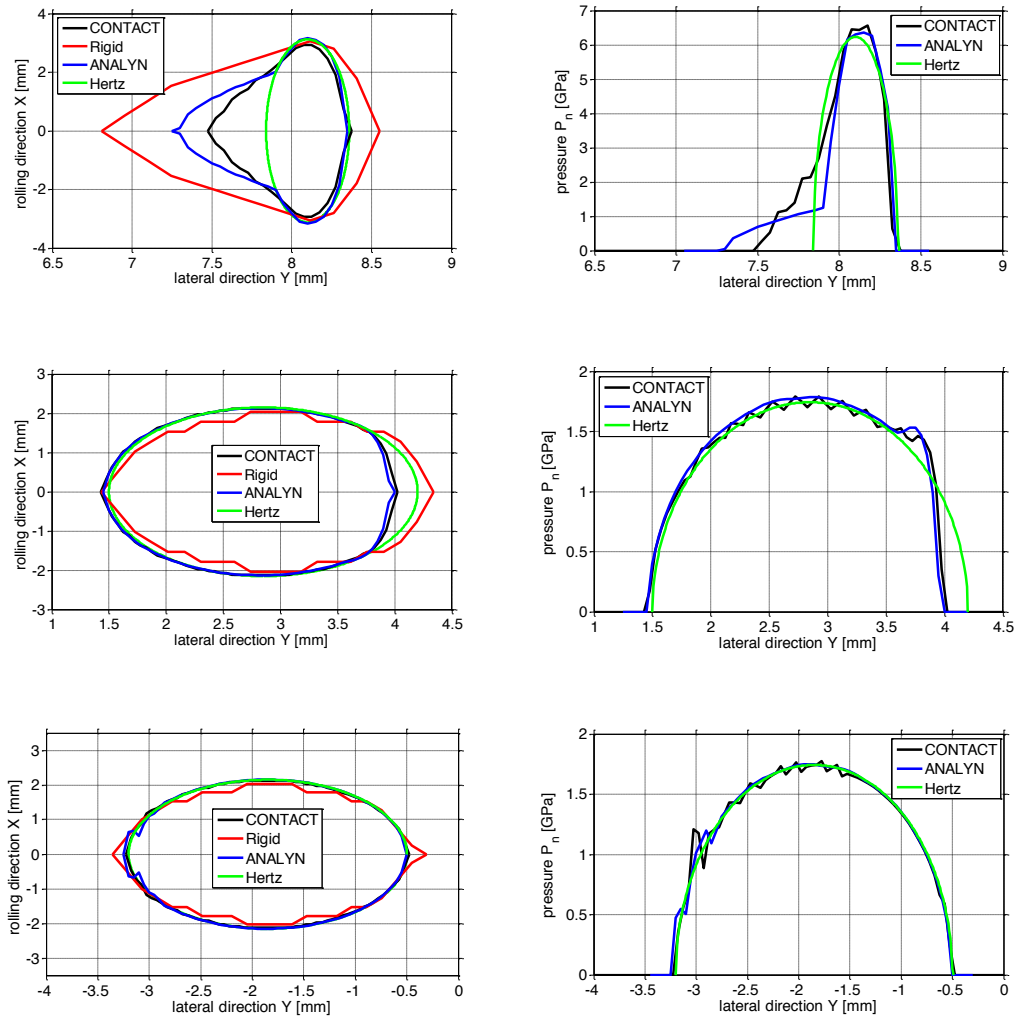


**Figure 8-15: Contact area and normal pressure distribution along line  $x = 0.0$  for wheel-roller contact for different cant angles; from top to bottom cant angle is  $-5^\circ$ ,  $0^\circ$ , and  $5^\circ$ , respectively (lateral shift=0mm, angle of attack= $0^\circ$ )**

The effect of lateral displacement and cant angle on the contact geometry is investigated. In order to investigate the effect of angle of attack or yaw angle, the ANALYN algorithm is generalized. The projected rail-head profile, aligned with wheel profile, is calculated for obtaining the separation curve between the contacting bodies. The contact is assumed to be Hertzian in the rolling direction. So, the contact is aligned with wheel, and consequently the pressure distribution and creep forces are aligned accordingly. The effect of angle of attack on the rolling direction's curvature needs to be considered. Since the change in rolling radius over the contact area is negligible compared with the nominal rolling radius, for simplicity of the algorithm, the change in rolling direction's curvature is neglected.

The simulation results for a train (using SIMPACK) and also consulting with rail professionals concluded that the angle of attack in real-life wheel-rail contact conditions is less than 1.5 degree even for the sharpest curves. In order to consider the angle of attack for CONTACT algorithm, premium version of CONTACT software is required. As a result, the geometry contact module, "rigid" method that has been shown is successful in estimating the contact area for different conditions, is used for comparing the results of generalized-ANALYN algorithm for predicting the area of contact. Results are shown in Figure 8-16 and Figure 8-17. The results show that the contact area, as well as the contact location slightly differ between zero and maximum angle of attack conditions.

Figure 8-16 shows the predicted contact area with and without considering the angle of attack. As shown in the figure, even for a large angle of attack of  $3^\circ$ , the contact area does not change considerably. Due to angle of attack, the contact point location, contact area, and contact alignment are slightly changed. Comparison of contact area predicted by generalized-ANALYN with the result of "rigid" method shows that the generalized-ANALYN is successful in considering the effect of angle of attack.

Figure 8-17 shows the predicted contact area with and without considering the angle of attack for a flange contact condition. As shown in the figure, the contact location changes considerably for a

1.5° change in angle of attack. Comparison of contact area predicted by generalized-ANALYN with the result of “rigid” method shows that the generalized-ANALYN is successful in considering the effect of angle of attack for flange contact condition as well.

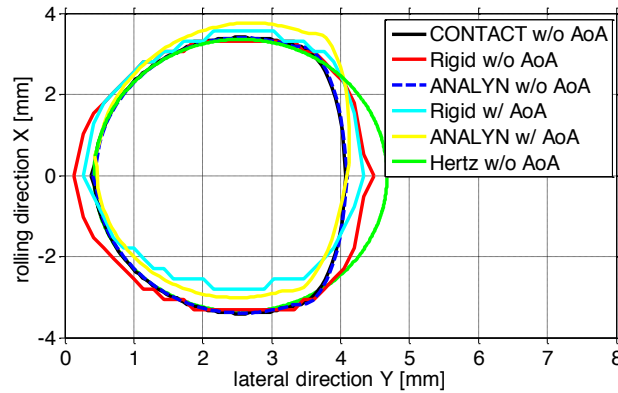


Figure 8-16: Contact area prediction with and without considering the angle of attack (lateral shift=0mm, cant angle=0°, angle of attack=3°, normal loading=40600N)

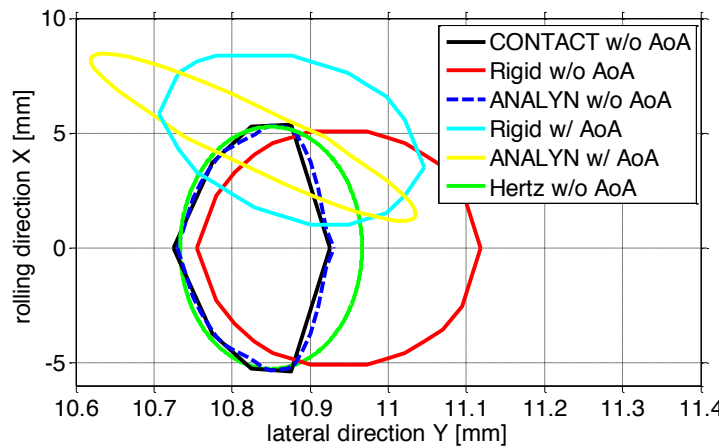
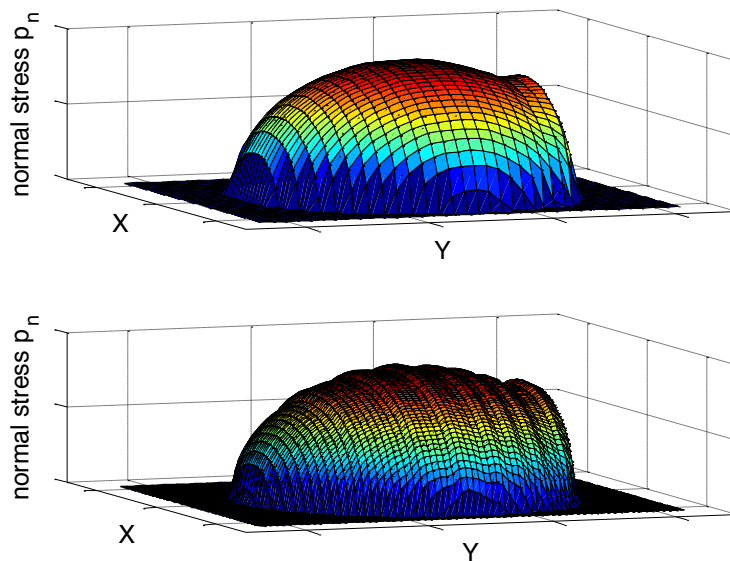


Figure 8-17: Contact area prediction with and without considering the angle of attack for a flange contact condition (lateral shift=2mm, cant angle=0°, angle of attack=1.5°, normal loading=10600N)

Figure 8-18 compares three-dimensional normal pressure distributions predicted by ANALYN and CONTACT algorithms for a given contact condition.

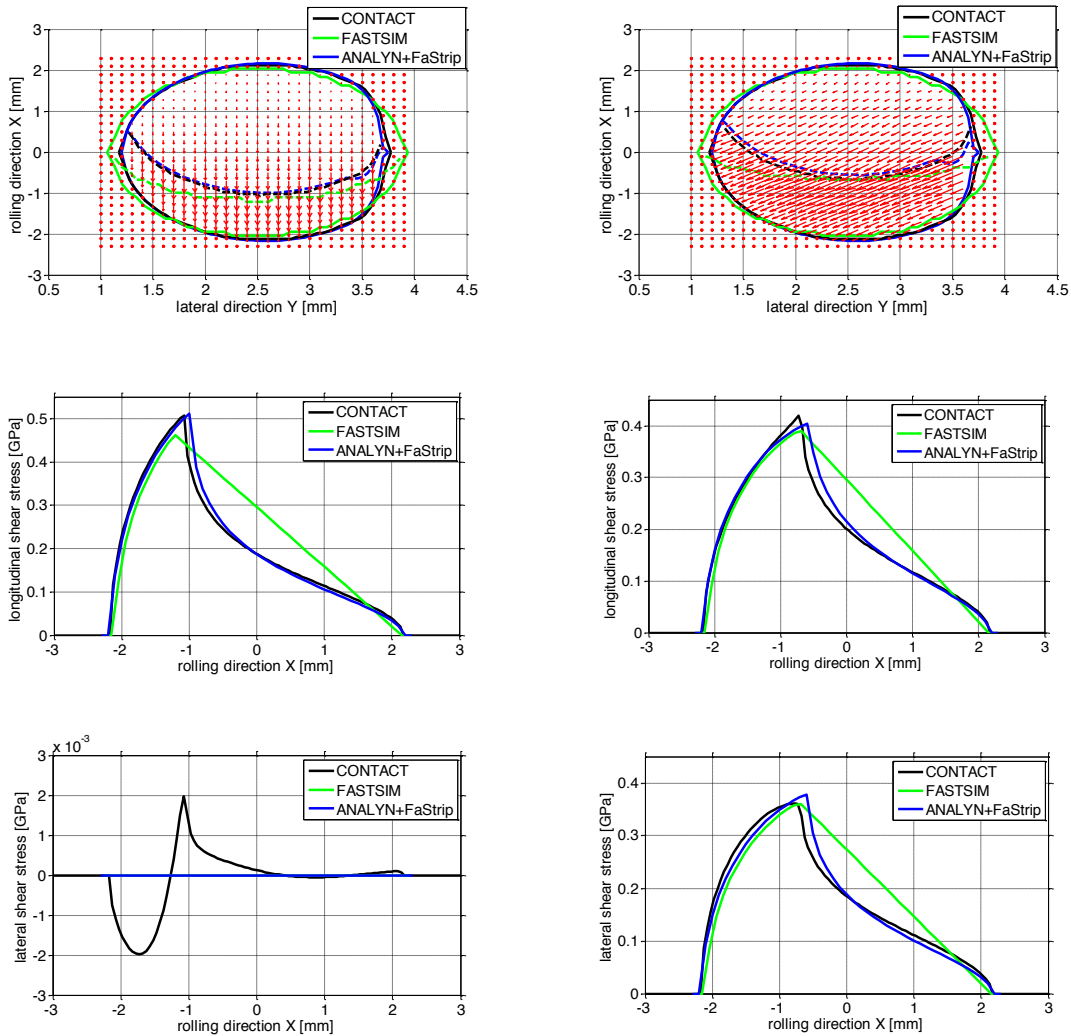


**Figure 8-18: Three-dimensional normal pressure distribution predicted by ANALYN (top) and CONTACT (bottom) algorithms (lateral shift=0mm, cant angle=0°, angle of attack=0°, normal loading=10600N)**

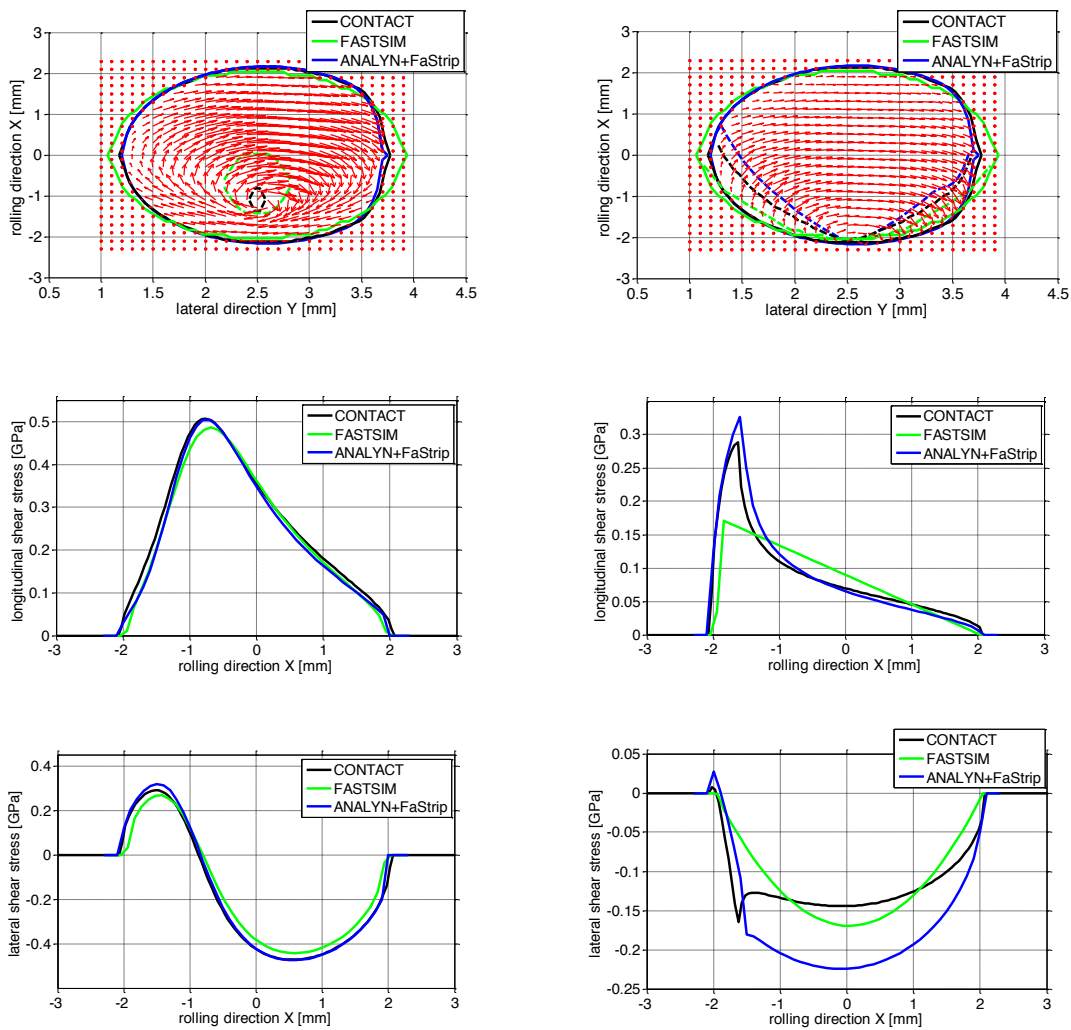
In addition to investigating the performance of different contact theories for contact area prediction, their performance in predicting the tangential (shear) stress distribution is also thoroughly investigated. To this end, CONTACT algorithm using CONTACT software, FASTSIM algorithm with elliptical contact area, and ANALYN-FaStrip algorithm are employed. Various creepage conditions at the wheel-roller interface are considered for geometry conditions of lateral shift=0mm, cant angle=0°, angle of attack=0°, normal loading=10600N. Stick-slip boundary (adhesion-slip border), longitudinal and lateral shear stress distribution are compared.

Figure 8-19 investigates the tangential contact problem for two creepage conditions at the contact; pure longitudinal creepage  $v_x = 0.2\%$  and combined lateral and longitudinal creepage  $v_x = v_y = 0.2\%$ . Results show that FaStrip algorithm closely replicate the stick-slip boundary predicted by CONTACT. Similarly, shear stress distributions are accurately predicted by FaStrip algorithm compared with CONTACT. CONTACT for pure longitudinal creepage predicts minor

lateral shear stress throughout the contact area, while both FaStrip and FASTSIM predicts zero lateral shear stress.



**Figure 8-19: Contact area and its division to adhesion and slip areas (top), longitudinal shear stress curve (middle), and lateral shear stress distribution (bottom) along rolling direction  $y = 2.5$  for pure longitudinal creepage condition;  $v_x = 0.2\%$  (left) and combined creepage condition  $v_x = v_y = 0.2\%$  (right).**



**Figure 8-20: Contact area and its division to adhesion and slip areas (top), longitudinal shear stress curve (middle), and lateral shear stress distribution (bottom) along rolling direction  $y = 3$  for pure spin creepage conditions;  $\varphi = -0.01$  (left) and  $\varphi = -0.001$  (right).**

Pure spin creepage condition is investigated in Figure 8-20. Results show that FaStrip is more successful in predicting the stick-slip boundary than FASTSIM compared with CONTACT. FaStrip, however, fails to predict the slip area accurate for increased spin creepage. The FaStrip algorithm relies on the assumption that the slip area is attached to the trailing edge of the contact area. As such, it fails to predict the slip area that falls in the middle of the contact area, as shown in Figure 8-20. Nevertheless, the shear stress distribution is predicted rather accurately by FaStrip algorithm.

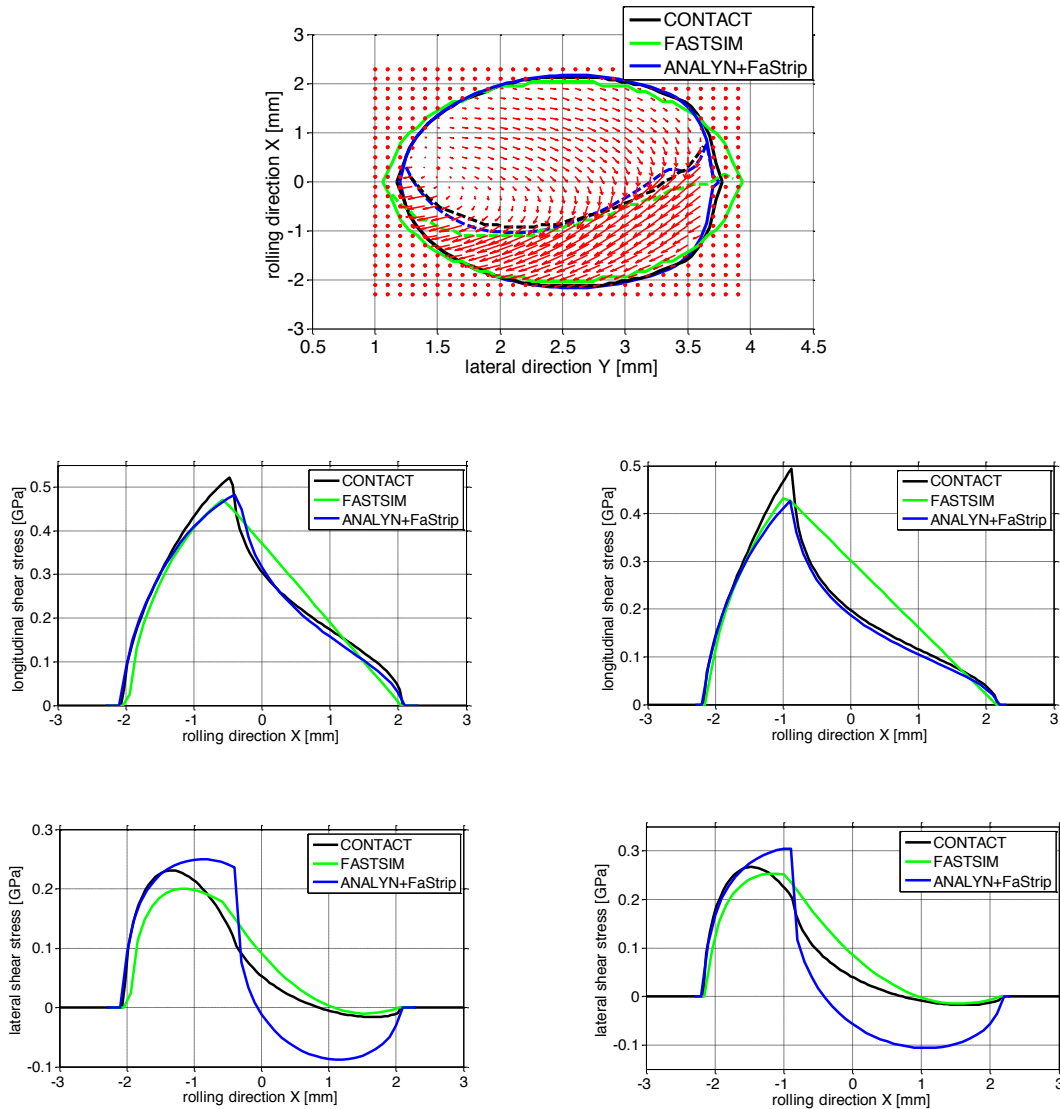


**Figure 8-21: Contact area and its division to adhesion and slip areas (top), longitudinal shear stress curve (middle), and lateral shear stress distribution (bottom) along rolling direction  $y = 3$  (left) and  $y = 2.5$  for combined creepage conditions;  $v_x = v_y = 0.2\%$  and  $\phi = -0.001$ .**

Combined creepage condition is investigated in Figure 8-21. Results show that FaStrip is more successful in predicting the stick-slip boundary than FASTSIM compared with CONTACT. Shear stress distributions along two lines along rolling direction ( $y = 3$  and  $y = 2.5$ ) are compared. Results show that FaStrip also accurately predicts the longitudinal shear stress distribution.

However, FASTSIM predicts more accurate lateral shear distribution than FaStrip compared with CONTACT. This is clearly reflected in lateral creep-creepgae curves shown in Figure 8-25.

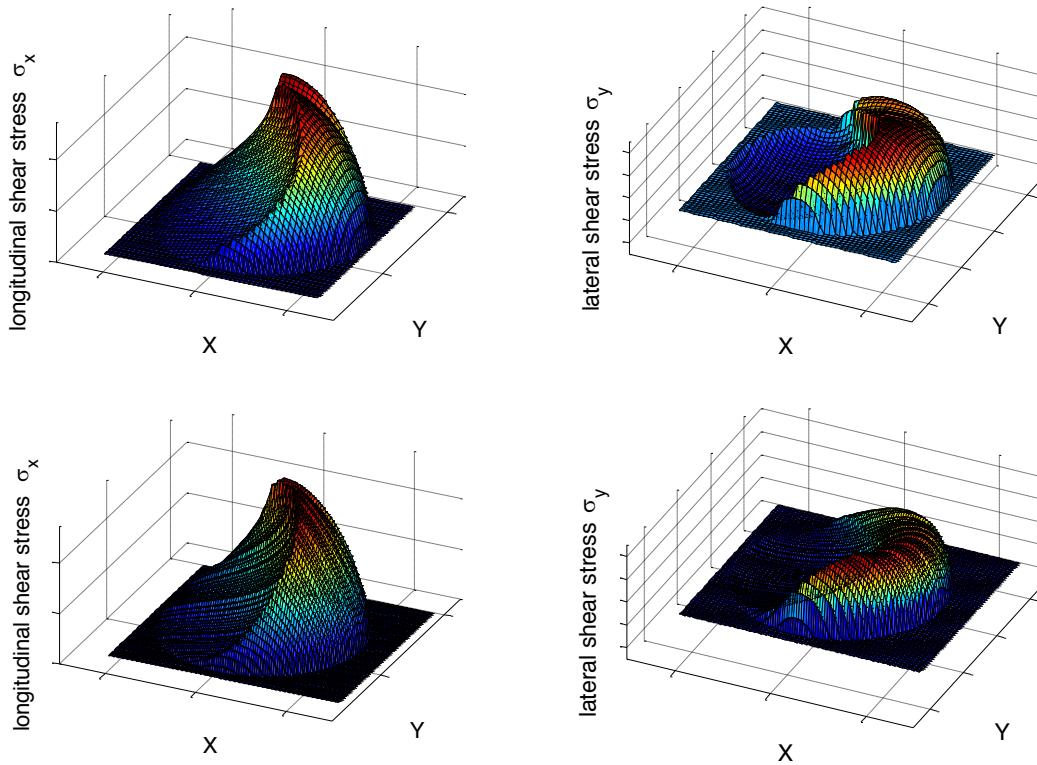


**Figure 8-22: Three-dimensional longitudinal (left) and lateral (right) shear stress distribution predicted by ANALYN-FaStrip (top) and CONTACT (bottom) algorithms for combined creepage conditions;  $v_x = v_y = 0.2\%$  and  $\varphi = -0.001$ .**

Figure 8-22 compares three-dimensional shear stress distribution throughout the contact area predicted by ANALYN-FaStrip and CONTACT algorithms for combined creepage condition at the contact. Results show that predicts more closely the longitudinal shear than lateral shear stress distribution compared with CONTACT results.

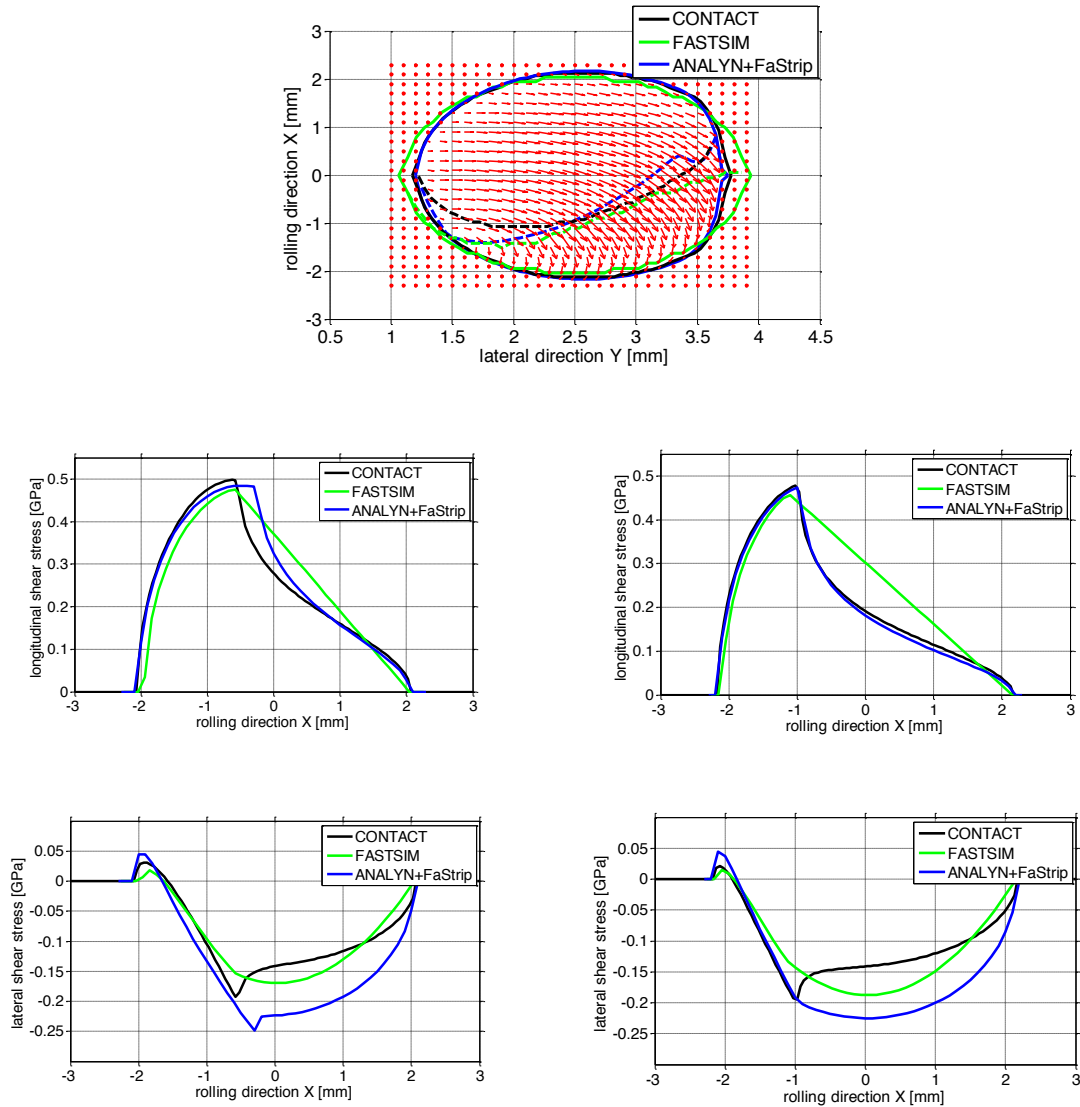


**Figure 8-23: Contact area and its division to adhesion and slip areas (top), longitudinal shear stress curve (middle), and lateral shear stress distribution (bottom) along rolling direction  $y = 3$  (left) and  $y = 2.5$  for combined creepage conditions;  $v_x = 0.2 \%$  and  $\phi = -0.001$ .**

The creep force-creepage curves predicted by different contact theories including CONTACT, FASTSIM, linear Kalker, empirical Kalker, Polach’s, and Johnson’s are thoroughly discussed and compared in chapter 7 (Figure 7-24 and Figure 7-26). The results show that FASTSIM predicts more accurate creep curves than the other theories compared with CONTACT results. As a result,

in this chapter, the creep curves predicted by ANALYN-FaStrip algorithm is compared with CONTACT and FASTSIM algorithms.

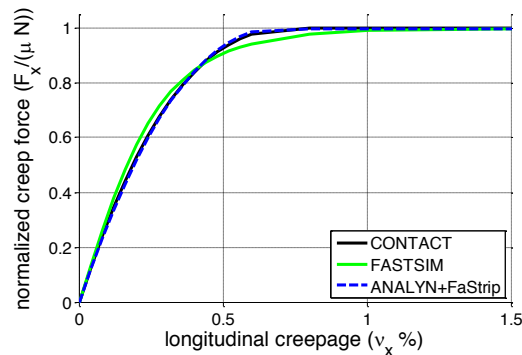


**Figure 8-24: Comparison of longitudinal creep force-creepage curve for different contact theories; CONTACT, FASTSIM, and FaStrip.**

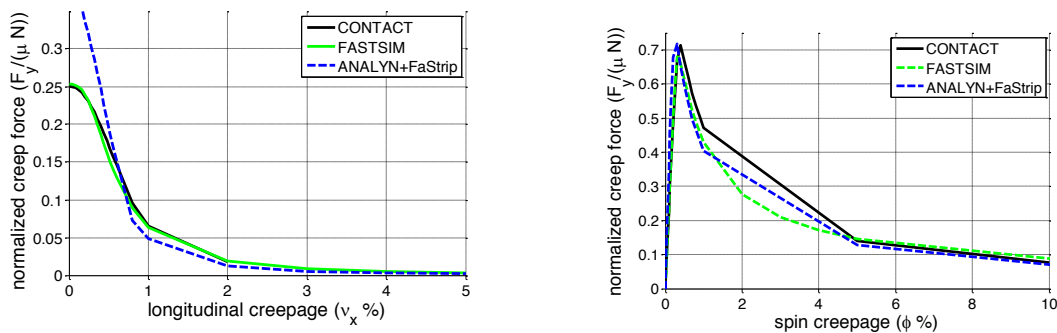


**Figure 8-25: Comparison of lateral creep force-creepage curve for combined longitudinal and spin ( $\phi = -0.001$ ) creepage (left) and pure spin creepage (right) conditions at the contact.**

Figure 8-24 compares the longitudinal creep force-creepage curves. It shows that FaStrip successfully replicates the creep curve predicted by CONTACT. Figure 8-25, however, shows that FASTSIM predicts rather more accurate lateral creep curves for combined and pure spin creepage conditions than FaStrip compared with CONTACT results.

### 8.2.4 Conclusions

A MATLAB routine is successfully implemented for comparing different contact theories. Hertzian theory and non-Hertzian theories are compared for estimating the contact area and

normal pressure distribution. ANALYN algorithm is generalized to consider the effect of angle of attack. Although the angle of attack does not change considerably in real-life conditions, the generalized-ANALYN shows promising results for predicting the orientation and area of contact.

The performance of different theories for tangential stress prediction is also discussed. Although FaStrip shows promising results for predicting the stick-slip boundary and shear stress distribution, it can be improved for considering conditions where slip area does not touch the trailing edge of the contact area. Considering the effect of interplay of strips (cross-influence of adjacent strips) could further improve the performance of FaStrip algorithm.

# 9 Summary and Conclusion

## 9.1 Summary

The research work presented in this study considered advancing the state of the art for wheel-rail contact mechanics and dynamics in railway systems. The current theoretical knowledge and experimental works have been thoroughly reviewed and discussed. A state of the art test facility with very flexible and robust design for precise evaluation of wheel-rail contact mechanics and dynamics is developed.

The wheel-rail contact mechanics and dynamics is one of the most complex aspects of railroading. Contact mechanics plays a crucial role in the behavior of railcars. Accurate determination of contact points and contact forces between wheel and rail play an important role in the dynamic study of rail vehicles. Full understanding of the physics behind the contact phenomenon provides a fundamental foundation for the vehicle performance study, both in terms of modeling the train dynamics and in terms of reducing operational costs in the long-term. While many researches have been conducted to deepen the understanding of the contact mechanics at the interface of wheel and rail, further studies are still highly desirable to shed more light on the understanding of the physics behind the contact phenomenon. Although there is a broad, high-level understanding of what happens at the wheel-rail interface, much of the science behind why it happens is lacking.

The survey of contact models presented in Chapter 7 showed that the existing contact models behave differently for the same interface conditions. For accurate creep force calculations, there are considerable differences between the models, as well as between the models and the experiments. The dependency of the friction coefficient on the slip velocity is not yet fully understood. Different models have been introduced to explain the phenomenon; various parameters are involved that need more exploration. The physics of the falling friction phenomenon and its dependency on the temperature, surface contamination, and other variables still need to be further developed. In addition, experiments show a noticeable reduction in the initial slope of the creep-creepage curve compared to the models. Some models are generalized to

consider the slope reduction effect, but an accurate model for explaining the reduction is not yet determined.

Normal contact models need further exploration, as well. Faster and more accurate models for predicting contact geometry and pressure distribution that are verified with experimental studies are desired, especially for the case of conformal contact. Some contact phenomena, such as plastic flow of material, are still not well understood. Plastic flow of material could reduce the contact pressure and increase the size of the contact patch.

Due to inaccessibility of the interface region, few techniques have been developed for experimental investigation of both normal and tangential contact problems. The shape and size of the contact patch and the pressure distribution within the contact patch need further exploration. The existing experimental studies mostly conducted static measurements of the normal contact. To the best of the authors' knowledge, no experimental technique has been proposed to measure the tangential stress (traction) distribution at the actual wheel-rail interface. More accurate dynamic creepage and combined creepage experiments are needed to evaluate the performance of the existing contact models for various contact conditions. In summary, better-developed experimental methods and tools are still highly desirable, since the field of wheel-rail contact mechanics is not a closed subject and warrants further theoretical and experimental research. Therefore, this study aimed to develop a roller rig primarily intended for accurate study and experimental research of the wheel-rail contact mechanics.

The Virginia Tech Roller Rig (VTRR) is designed to be a single-wheel test rig with a vertical plane roller (typical roller rig) configuration. As review study of design concepts for developing test facilities in Chapter 3 indicated that it is the least complex configuration that will allow for the precision control and sensing needed to improve upon contact models that are currently employed, as the rig is primarily intended for the contact mechanics and dynamics studies. Provision designs, however, are incorporated that makes the rig a viable platform for studying many other aspects of the rail vehicles.

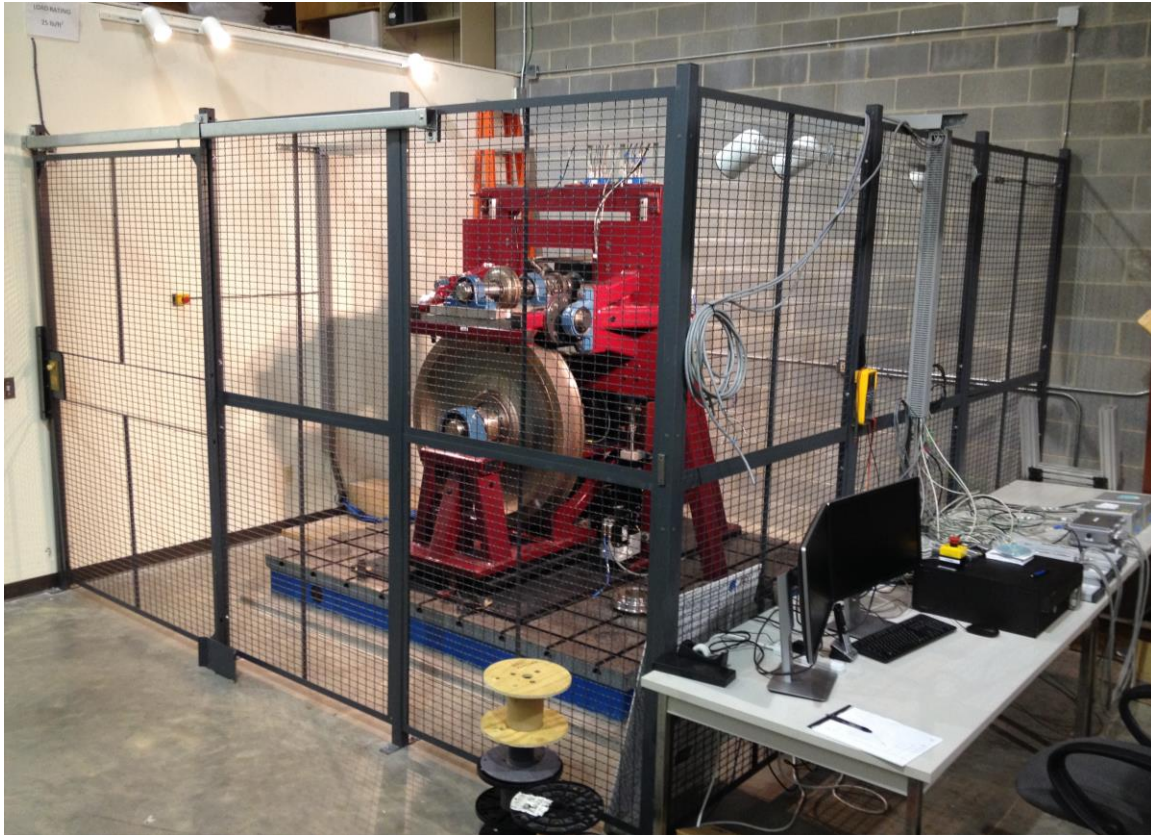


**Figure 9-1: Virginia Tech Roller Rig Testing Facility**

As shown in Figure 9-1, the rig is successfully designed, assembled together, and developed. Design analysis indicates that the rig can successfully meet the set requirements: additional accuracy in measurements, and better control on the design of experiments. Additionally, the evaluation of other roller rigs around the world indicates that the rig provides for capabilities not currently available in other rigs known to us, in terms of its controllability and measurements accuracy. Future plans set forth for the rig also prove that its design will lend its use for many studies to come with varying purposes.

The rig's stability and rigidity provides a great deal of confidence in conducting planned experiments and data measurements. Engineering approach to the hardware design and construction of the rig, as discussed in Chapter 4, guarantees that the dynamics and behavior of the testing facility is not influenced by external noise and vibration. Additional functionality of the rig lies in the ability to closely replicate boundary conditions of actual railway vehicles via

various positioning systems to actively control the relative angular and linear displacements between the two rotating wheels. These relative displacements are angle of attack (AoA), cant angle, lateral shift, and vertical displacement or normal loading.

Since the rig is primarily intended to study the contact mechanics, accuracy in controlling the differential speed (slip) at the wheel-roller interface accompanied with accuracy of contact force measurements are the most important key factors towards successful operation and achieving the goals of the rig. A highly compatible, and exclusive electro-mechanical system, as discussed in Chapter 5, provides a high level of precision in controlling the differential speed. In addition, a novel force measurement system capable of measuring the contact forces and moments with high level of precision is developed and tested, as discussed in Chapter 6. It outperforms off-the-shelf wheel hub transducers that are mostly designed for tire applications. One of the unique features of the rig is its unified communication protocol between actuators, drives, and data acquisition system eliminating data conversion between these units; hence facilitating online high-speed measurements and control. The state-of-the-art measurement and control network used in the rig, makes the sense-to-act process as fast as the sensors' update rate.

The design goals for the rig in the scope of this study were achieved in their entirety and future phase studies and developments of the rig look to be performed in a very seamless manner. A vision system for accurately looking at the interface between the wheel and rail for conducting contact geometry studies has been discussed and proposed for future phases of the rig's development. This high-definition imaging system is capable of precisely investigating the contact geometry using advanced image-processing methods and extracting measurements from every frame.

The test rig is capable of performing a full range of dynamic creepage studies, combined creepage studies, stick-slip dynamics at the interface, and among others that will allow the scientists and engineers to get a better understanding of the fundamental aspects of the wheel-rail contact physics. One of the features of the roller rig is the ability to perform Hardware-in-the-Loop (HiL) studies. This allows merging the rig with rail vehicle dynamic simulation models, to bring an unprecedented level of accuracy to the models. The rig also can be aligned with the needs of

railroad community for conducting future experiments and evaluating the effect of specific parameters under controlled environment.

While the current application of this research and design concepts is to a single wheel test rig, the contributions presented in this dissertation are applicable to number of different areas of research. The design concepts for subsystems implemented in the rig can be used for other applications beyond their immediate application towards a single wheel test rig. The novel force measurement system with relevant modifications could be used in other applications including measuring tire-road contact forces in automotive industry, measuring cutting forces in metal cutting devices, and potentially measuring real-life wheel-rail contact forces. Powertrain design analysis, kinematic analysis, and its implementation could also be applied to any other application requiring precision control of differential speed at the interface between two bodies such as paper machine devices. The frame design configuration allowing desired rigidity and strength in all directions, while providing enough accessibility to test specimen, as well as implementation of multiple positioning systems in a way that the center of rotation passes through one point can also have other applications beyond a single-wheel test rig.

## 9.2 Strengths and Limitations of the Rig

The potential contributions of the rig compared with the existing roller rigs around the world are summarized as:

- High level of precision in controlling the rotational speed of the contacting bodies and therefore accurate control of creepage
- High level of precision in measuring the contact forces and moments
- Capable of performing Hardware-in-the-Loop (HiL) simulations due to its unified communication protocol between actuators, drives, and data acquisition
- Providing accurate motion control of wheel-rail contact configuration; normal loading, cant angle, lateral shift, and angle of attack
- Providing a large diameter ratio between roller and wheel
- Providing the best vantage point to the interface for accurate study of contact geometry

The potential limitations of the rig are summarized as:

- Hunting Studies and suspension compliance studies are not possible
- Fielded components can't be used or require modifications for fitment
- Wear and RCF studies are limited
- Due to its scaled design, the contact condition differs from the actual wheel-rail contact condition
- Requires extensive calibration and tuning

### 9.3 Future Studies

The detailed multi-body dynamic model developed in Chapter 8 could be employed for future analysis of the experimental data. The multi-body vibration analysis could provide a comparison tool for future experimental vibration study of the rig, including vibration due to stick-slip dynamics at the contact. It also could be used for developing a compensation approach for removing any noise from the actual data measurement in order to get the maximum signal to noise ratio.

In addition to many experimental research studies that can be followed using the roller rig, the theoretical contact models, some are implemented and compared in Chapter 8, can be further investigated. The ANALYN algorithm could be better developed to consider the effect of angle of attack. Although FaStrip shows promising results for predicting the stick-slip border and shear stress distribution, it can be improved for considering conditions where slip area does not touch the trailing edge of the contact area. Considering the effect of interplay of strips (cross-influence of adjacent strips) could further improve the performance of FaStrip algorithm.

# 10References

- [1] S. Iwnicki, *Handbook of Railway Vehicle Dynamics*. Boca Raton, FL: Taylor & Francis Group, 2006.
- [2] A. Jaschinski, "On the Application of Similarity Laws to a Scaled Railway Bogie Model," TU Delft, Delft University of Technology, Thesis 1990.
- [3] H. Chollet, *Etude en Similitude Mechanique des Efforts Tangents au Contact Roue-Rail*, 1991.
- [4] T. Matsudaira, "Shimmy of Axle with Pair of Wheels (in Japanese)," *Journal of Railway Engineering Research*, pp. 16-26, November 1952.
- [5] T. Matsudaira, N. Matsui, S. Arai, and K. Yokose, "Problems on Hunting of Railway Vehicle on Test Stand," *Transactions of ASME Journal of Engineering in Industry*, vol. 91 ser. B, no. 3, pp. 879-885, 1969.
- [6] M.S. Kim, J.H. Park, and W.Y. You, "Construction of Active Steering System of the Scaled Railway Vehicle," *International Journal of Systems Applications, Engineering & Development*, vol. 2, no. 4, pp. 217-226, 2008.
- [7] D.R. Carling, "Locomotive Testing Stations," *Transactions of the Newcomen Society*, vol. 45, 1972.
- [8] R. Stock, D. Eadie, D. Elvidge, and K. Oldknow, "Influencing Rolling Contact Fatigue through Top of Rail Friction Modifier Application – a Full Scale Wheel–Rail Test Rig Study," *Wear*, vol. 271, pp. 134-142, 2011.
- [9] W. Zhang, J. Chen, X. Wu, and X. Jin, "Wheel/rail adhesion and analysis by using full scale roller rig," *Wear*, vol. 253, no. 1, pp. 82-88, 2002.
- [10] D. Eadie et al., "The effects of top of rail friction modifier on wear and rolling contact fatigue: Full-scale rail–wheel test rig evaluation, analysis and modeling," *Wear*, 265(9):1222-1230, 2008., vol. 265, no. 9, pp. 1222-1230, 2008.
- [11] A. Matsumoto et al., "Creep force characteristics between rail and wheel on scaled model," *Wear*,

vol. 253, no. 1, pp. 199-203, 2002.

- [12] S. Hsu et al., "Experimental and theoretical investigation of railway wheel squeal," in *Proceedings of the Institution of Mechanical Engineers, Part F: Journal of Rail and Rapid Transit*, vol. 221 (1), 2007, pp. 59-73.
- [13] H. Hahn and G. Sigl, "Simulation und experimentelle Verifikation des Radr/Schiene-Rollprufstands.," *Ingenieur Archiv*, vol. 57, pp. 329-348, 1987.
- [14] L.M. Sweet, A. Karmel, and S.R. Fairley, "Derailment Mechanics and Safety Criteria for Complete Railway Vehicle Trucks," in *Proceedings of 7th LAVSD Symposium*, Cambridge, UK, 1981.
- [15] C. Wallman and H. Åström, "Friction measurement methods and the correlation between road friction and traffic safety," Swedish National Road and Transport Research Institute, 2001.
- [16] S. Brennan and A. Alleyne, "The Illinois Roadway Simulator: A mechatronic testbed for vehicle dynamics and control," *IEEE/ASME Transactions on Mechatronics*, vol. 5, no. 4, pp. 349-359, 2000.
- [17] L. Mianzo, D. Fricke, and R. Chabaan, "Road profile control methods for laboratory vehicle road simulators," in *AUTOTESTCON'98 IEEE Systems Readiness Technology Conference*, 1998, pp. 222-228.
- [18] W. Zhang, H. Dai, Z. Shen, and J. Zeng, "Roller Rigs," in *Handbook of Railway Vehicle Dynamics.*, 2006.
- [19] A. Jaschinski, H. Chollet, S. Iwnicki, A. Wickens, and J. von Wurzen, "The Application of Roller Rigs to Railway Vehicle Dynamics," *Vehicle System Dynamics*, vol. 31, pp. 345-392, 1999.
- [20] L.M. Sweet, J.A. Sivak, and W.F. Putman, "Non-linear Wheelset Forces in Flange Contact.," *Journal of Dynamics Systems, Measurement and Control*, vol. 101, pp. 238-255, 1979.
- [21] A.H. Wickens and A.O. Gilchrist, *Railway Vehicle Dynamics - the Emergence of a Practical Theory.* , 1977.
- [22] M. Cox and H. Nicolin, "Untersuchung des Schwingungsverhaltens von Schienenfahrzeugen mit

Hilfe des Modellprufstands am Institut für Fordertechnik und Schienenfahrzeuge der RWTH Aachen," *Leichtbau der Verkehrsfahrzeuge*, vol. 23, no. 4, pp. 91-95, 1979.

- [23] X.S. Jin et al., "Adhesion experiment on a wheel/rail system and -its numerical analysis," *Proceedings of the Institution of Mechanical Engineers. Part J, Journal of engineering tribology*, vol. 218, no. 4, pp. 293-303, 2004.
- [24] M. Miyamoto, "JR rolling stock testing plant capable of testing at a speed of 500 km/h," *QR of RTRI*, vol. 32, no. 4, pp. 211-212, 1991.
- [25] R.H. Fries, Estimation of Transit Rail Vehicle Parameter from Roller Rig Tests; Ph.D. Dissertation, 1983.
- [26] N.K. Cooperrider, E.H. Law, R.H. Fries, and I. Haque, "State-of-the-Art-Car (SOAC), creep forces and dynamic response on the Roll Dynamics Unit," Arizona State University, Department of Mechanical and Aerospace Engineering, Report CR, 82037, 1982.
- [27] R.H. Fries, "Dynamic Response of a Transit Rail Vehicle on a Roller Rig, Vehicle Systems Dynamic," *International Journal of Vehicle Mechanics and Mobility*, vol. 12, no. 1-3, pp. 155-159, 1983.
- [28] D. Lubke, M. Mittermaier, L. Pfaffl, and F. Zollner, "Ein Rollprufstand zur Erforschung der Rad/Schiene-Technik," *ZEV Glasers Annalen*, vol. 100, no. 10, pp. 295-305, 1976.
- [29] K. Althammer and L. Pfaffl, "Versuchsanlage Rollprufstand," *Eisenbahntechnische Rundschau*, vol. 25, no. 11, pp. 663-676, 1976.
- [30] K. Althammer, "Planung, Bau und Betrieb des Rollprufstandes für das Rad/Schiene-Forschungsprogramm," *ZEV Glasers Annalen*, vol. 101, no. 8/9, pp. 312-323, 1977.
- [31] C.A.M. Smith and R.V. Dukkipati, "The NRC curved track simulator and its potential use," National Research Council Canada, 1988.
- [32] R.V. Dukkipati, "Lateral stability analysis of a railway truck on roller rig," *Mechanism and machine theory*, vol. 36, no. 2, pp. 189-204, 2001.

- [33] R.V. Dukkipati, "Modelling and simulation of the hunting of a three-piece railway truck on NRC curved track simulator," *vehicle system dynamics*, vol. 23, no. S1, pp. 105-115, 1994.
- [34] X. Lu, J. Cotter, and D. Eadie, "Laboratory study of the tribological properties of friction modifier thin films for friction control at the wheel/rail interface," *Wear*, vol. 259, no. 7, pp. 1262-1269, 2005.
- [35] H. Harrison, T. McCanney, and J. Cotter, "Recent developments in COF measurements at the rail/wheel interface," in *Proceedings of the 5th International Conference Contact Mechanics and Wear of Rail Wheel Systems*, Tokyo, Japan, 2000, pp. 30-35.
- [36] C. Ceppetelli. (2010) Centre for Surface Transportation Technology (CSTT), Ottawa, Ontario Canada. [Online]. [cstt.nrc.gc.ca](http://cstt.nrc.gc.ca)
- [37] J. Kalousek et al., "Tribological interrelationship of seasonal fluctuations of freight car wheel wear, contact fatigue shelling and composition brakeshoe consumption," *Wear*, vol. 191, no. 1, pp. 210-218, 1996.
- [38] J. Kalousek, "Development of a 1/8 Scale Dual Disc-On-Disc Rail/Wheel Wear Testing Facility," *Canadian Metallurgical Quarterly*, vol. 21, no. 1, pp. 67-72, 1982.
- [39] M. Jochim, Konstruktion eines Versuchsdrehgestells, 1984.
- [40] M. Jochim, Analyse der Dynamik eines Schienenfahrzeuges, 1987.
- [41] S.D. Iwnicki and Z.Y. Shen, "Collaborative railway roller rig project," in *Proceedings of SEFI World Conference on Engineering Education*, Portsmouth, 1992.
- [42] S.D. Iwnicki and A.H. Wickens, "Validation of a MATLAB Railway Vehicle Simulation Using a Scale Roller Rig," *Vehicle System Dynamics*, vol. 30, no. 3, pp. 257-270, 1998.
- [43] H. Chollet, "Essais en Similitude a l'Echelle 1/4 de Bogies de Wagons de la Famille Y25," 1988.
- [44] P. D. Allen, "Scale Testing," in *Handbook of Railway Vehicle Dynamics.*, 2006.
- [45] J. Kalivoda and P. Bauer, "Roller Rig Implementation of Active Wheelset Steering," in *Proceedings*

*of the First International Conference on Railway Technology: Research, Development and Maintenance. Stirling: Civil-Comp Press Ltd, vol. 1, 2012, pp. 1-13.*

[46] R. Conti et al., "A Numerical Model of a HIL Scaled Roller Rig for Simulation of Wheel–Rail Degraded Adhesion Condition," *Vehicle System Dynamics*, vol. 50, no. 5, pp. 775-804, 2012.

[47] B. Alotta, L. Pugi, M. Malvezzi, F. Bartolini, and F. Cangioli, "A Scaled Roller Test Rig for High-Speed Vehicles," *Vehicle System Dynamics*, vol. 48 (Supplement), pp. 3-18, 2010.

[48] B.G. Eom, B.B. Kang, and H.S. Lee, "Design of Small-Scaled Derailment Simulator for Investigating Bogie Dynamics," *International Journal of Railway*, vol. 4, no. 2, pp. 50-55, 2011.

[49] B.G. Eom, B.B. Kang, and H.S. Lee, "A study on running stability assessment methods for 1/5 small scaled bogie of saemaul using small-scaled derailment simulator," *International Journal of Precision Engineering and Manufacturing*, vol. 14, no. 4, p. 589=598, 2013.

[50] D. Fletcher and J. Beynon, "Development of a machine for closely controlled rolling contact fatigue and wear testing," *Journal of testing and evaluation*, vol. 28, no. 4, pp. 267-275, 2000.

[51] A. Rovira, A. Roda, Lewis, R., and M.B. Marshall, "Application of Fastsim with variable coefficient of friction using twin disc experimental measurements," *Wear*, vol. 274, 2012.

[52] E.A. Gallardo-Hernandez and R. Lewis, "Twin disc assessment of wheel/rail adhesion," *Wear*, vol. 265, no. 9, pp. 1309--1316, 2008.

[53] T. Ohyama, "Tribological studies on adhesion phenomena between wheel and rail at high speeds," *Wear*, vol. 144, no. 1, pp. 263--275, 1991.

[54] S. Kumar, M.F. Alzoubi, and N.A. Allsayyed, "Wheel/rail adhesion wear investigation using a quarter scale laboratory testing facility," *Railroad Conference, 1996., Proceedings of the 1996 ASME/IEEE Joint*, pp. 247--254, 1996.

[55] S. Kumar and P. Rao, "Wheel-Rail Contact Wear, Work, and Lateral Force for Zero Angle of Attack—A Laboratory Study," *Journal of dynamic systems, measurement, and control*, vol. 106, no. 4, pp. 319--326, 1984.

- [56] A. Kawamura et al., "Measurement of the tractive force and the new adhesion control by the newly developed tractive force measurement equipment," in *Proceedings of the Power Conversion Conference*, vol. 2, 2002, pp. 879-884.
- [57] K. Matsumoto et al., "Proposal of Wheel/Rail Contact Model for Friction Control," *Journal of Mechanical Science and Technology*, vol. 19, no. 1, pp. 437-443, 2005.
- [58] K. Matsumoto et al., "A Method to Apply Friction Modifier in Railway System," *JSME International Journal Series C*, vol. 47, no. 2, pp. 482--487, 2004.
- [59] Q.Y. Liu, B. Zhang, and Z.R. Zhou, "An Experimental Study of Rail Corrugation," *Wear*, vol. 255, pp. 1121-1126, 2005.
- [60] N. Bosso and N. Zampieri, "Real-time implementation of a traction control algorithm on a scaled roller rig," *Vehicle System Dynamics: International Journal of Vehicle Mechanics and Mobility*, vol. 51, no. 4, pp. 517-541, 2013.
- [61] N. Bosso, A. Gugliotta, and A. Som, "Dynamic identification of a 1: 5 scaled railway bogie on roller rig," in *Computers in Railways X. The Tenth International Conference*, 2006.
- [62] W.J. Wang, H.F. Zhang, H.Y. Wang, Q.Y. Liu, and M.H. Zhu, "Study on the Adhesion Behavior of Wheel/Rail under Oil, Water and Sanding Conditions," *Wear*, vol. 271, pp. 2693-2698, 2011.
- [63] W. Poole, "The measurement of the contact area between opaque objects under static and dynamic rolling conditions," in *Proceedings of the Conference on Contact Mechanics and Wear of Rail/Wheel Systems II*, 1986, pp. 59-72.
- [64] M. Pau, "Estimation of real contact area in a wheel-rail system by means of ultrasonic waves," *Tribology Int.*, vol. 36, no. 9, pp. 687-690, 2003.
- [65] F. Braghin, S. Bruni, and G. Diana, "Experimental and numerical investigation on the derailment of a railway wheelset with solid axle," *Vehicle System Dynamics*, vol. 44, no. 4, pp. 305-325, 2006.
- [66] N. Kim and T. Park, "A study on the dynamic performance of the 200km/h Korean tilting train by

- means of roller rig test," *Journal of Mechanical Science and Technology*, vol. 23, pp. 910-913, 2009.
- [67] O. Reynolds, "An experimental investigation of the circumstances which determine whether the motion of water shall be direct or sinuous, and the law of resistance in parallel channels," *Phil. Trans. R. Soc.*, vol. 174, pp. 935-953, 1883.
- [68] N. Bosso, A. Gugliotta, and A. Soma, "Comparison of different scaling techniques for the dynamics of a bogie on roller rig," *Vehicle System Dynamics Supplement*, vol. 37, pp. 514-530, 2002.
- [69] A. Keylin, "Analytical evaluation of the accuracy of roller rig data for studying creepage in rail vehicles," MS Thesis, Department of Mechanical Eng., Virginia Tech., 2012.
- [70] J.J. Kalker, *Three-Dimensional Elastic Bodies in Rolling Kontakt*. Boston, London,: Kluwer Academic Publishers, Dor- drecht, 1990.
- [71] H. Hertz, "Über die Berührung fester, elastischer Körper und über die Härte," *Verhandlungen des Vereins zur Bef*
- [72] A.D. De Pater, "The motion of a railway wheelset supported by a pair of rollers as compared with the motion of such a wheelset along a tangent track.," Delft University of Technology, Laboratory for Engineering Mechanics Report 1012, 1993.
- [73] N. Bosso, A. Gugliotta, and A. Som, "Dynamic behavior of a railway wheelset on a roller rig versus tangent track," *Shock and vibration*, vol. 11, no. 3, pp. 467--492, 2004.
- [74] U. Olofsson, Yi. Zhu, S. Abbasi, R. Lewis, and S. Lewis, "Tribology of the wheel-rail contact-aspects of wear, particle emission and adhesion," *Vehicle System Dynamics*, vol. 51, no. 7, pp. 1091-1120 , 2013.
- [75] S.Z. Meymand, M.J. Craft, and M. Ahmadian, "On the Application of Roller Rigs for Studying Rail Vehicle Systems," in *ASME 2013 Rail Transportation Division Fall Technical Conference*, Altoona, PA, 2013.
- [76] M. Kieninger, A. Rupp, and T. Gerlach, "Ein Neuer Radsensor zur Erfassung des multiaxialen Belastungsgeschehens an schienengebundenen Nahverkehrsfahrzeugen," *ZEV rail Glasers Annalen*, vol. 131, pp. 102-109, 2007.

- [77] S.Z. Meymand, M. Hosseini-pour, and M. Ahmadian, "The Development of a Roller Rig for Experimental Evaluation of Contact Mechanics for Railway Vehicles," in *ASME 2015 Joint Rail Conference*, San Jose, CA, 2015.
- [78] AirLoc Schrepfer-Ltd., "catalogue," Swiss Technology, Switzerland,.
- [79] J.D. Langdon, "Design and Adaptive Control of a Lab-based, Tire-coupled, Quarter-car Suspension Test Rig for the Accurate Re-creation of Vehicle Response," Virginia Tech, Blacksburg, Master thesis 2007.
- [80] THK-Ltd., "Linear Motion Systems – General catalog," Chicago, IL., Catalog No. 504E 2013.
- [81] M. Hosseini-pour, S.Z. Meymand, and Ahmadian M., "Vibration analysis of the driveline in a roller rig," in *ASME 2015 Joint Rail Conference*, San Jose, CA, 2015.
- [82] M. Hosseini-pour, S.Z. Meymand, M.J. Craft, and M. Ahmadian, "Modeling of a Roller Rig for Evaluation of Wheel/Rail Contact Mechanics," in *Joint Rail Conference*, 2014.
- [83] Kollmorgen Corporation, "Kollmorgen AKM Servomotor Seleccion Guide," Radford, VA, 2010.
- [84] Kollmorgen Corporation, "Digital Servo Amplifier S478.S772, Instruction MAnual," RADford, VA, 2013.
- [85] Mijno precision gearing, "BDB Catalog," France, 2013.
- [86] Thmoson Industries Inc., "True Planetary Gearheads, Instruction Mnual," Radford, VA, 2013.
- [87] SKF Group, "Roller bearings, Catalog," Houston, 2012.
- [88] Arema, "Manual for railway Engineering, Volume 1 Track," Lanham, MD,.
- [89] Fenner-Drives, "Keyless Locking Devices," Manheim, PA, 2013.
- [90] AAR, "Manuals of Standards and Recommended Practices and section G (Wheels and Axles) (M-107 Wheels, Carbon Steel)," 2011.

- [91] Kollmorgen Corporation, "Kollmorgen Linear Positioners Catalog," Radford, VA, 2009.
- [92] S.Z. Meymand and M. Ahmadian, "Design, development, and calibration of a force-moment measurement system for wheel–rail contact mechanics in roller rigs," *Measurement*, vol. 81, pp. 113-122, 2016.
- [93] W. Weiblen and T. Hofmann, "Evaluation of different designs of wheel force transducers," SAE Technical Paper, 980262 1998.
- [94] N.H. Cook, E.G. Loewen, and M.C. Shaw, "Machine-tool dynamometers," *American Machinist*, vol. 98, pp. 125-129, 1954.
- [95] S. Yıldız and F. Ünsaçar, "A dynamometer design for measurement the cutting forces on turning," *Measurement*, vol. 39, no. 1, pp. 80-89, 2006.
- [96] S. Yıldız, F. Ünsaçar, H. Sağlam, and H. Işık, "Design, development and testing of a four-component milling dynamometer for the measurement of cutting force and torque," *Mechanical Systems and Signal Processing*, vol. 21, no. 3, pp. 1499-1511, 2007.
- [97] C. Ferrero, "The measurement of parasitic components in national force standard machines," *Measurement*, vol. 8, no. 2, pp. 66-76, 1990.
- [98] L.P. Chao and K.T. Chen, "Shape optimal design and force sensitivity evaluation of six-axis force sensors," *Sensors and Actuators A: Physical*, vol. 63, no. 2, pp. 105-112, 1997.
- [99] J.D. Kim and D.S. Kim, "Development of a combined-type tool dynamometer with a piezo-film accelerometer for an ultra- precision lathe," *Journal of Materials Processing Technology*, vol. 71, no. 3, pp. 360-366, 1997.
- [100] S.A. Liu and H.L. Tzo, "A novel six-component force sensor of good measurement isotropy and sensitivities," *Sensors and Actuators A: Physical*, vol. 100, no. 2, pp. 223-230, 2002.
- [101] Y. Hara, S. Motonish, K. Yoshida, and N. Ikawa, "A new micro-cutting device with high stiffness and resolution," *Ann. CIRP* 39, pp. 375-378, 1990.

- [102] Kistler Group, "Technical Data Sheet: 3-component Quartz force sensor Type 9027C, 9028C, Type 9027C, 9028C, 9026C4," Winterthur Switzerland,.
- [103] Kistler group, "Instruction Manual: 3-component Quartz force sensor Type 9027C, 9028C, Type 9027C, 9028C, 9026C4," Winterthur Switzerland,.
- [104] Kistler group, "Technical Data Sheet: KiTorq Rotor-Torque Evaluation Unit (Stator) for a Torque Measuring Flange Type 4540A," Winterthur Switzerland,.
- [105] Kistler group, "Technical Data Sheet: Torsion Proof Multi-Disk Coupling Type 2305A for Torque Measurement Flange KiTorq Rotor Type 4550," Winterthur Switzerland,.
- [106] H.I. Andrews, "The contact between a locomotive driving wheel and the rail," *Wear*, vol. 2, no. 6, pp. 468-484, 1958.
- [107] D.J. Haines and E. Ollerton, "Contact stress distribution on elliptical contact surfaces subjected to radial and tangential forces," in *Proc. Int. Mech. Eng.*, vol. 177, 1963, pp. 95–114.
- [108] M.B. Marshall, R. Lewis, R.S. Dwyer-Joyce, U.I.f. Olofsson, and S. Bj, "Experimental characterization of wheel-rail contact patch evolution," *Journal of tribology*, vol. 128, no. 3, pp. 493-504, 2006.
- [109] M. Pau, F. Aymerich, and F. Ginesu, "Ultrasonic measurements of nominal contact area and contact pressure in a wheel-rail system," *Proceedings of the Institution of Mechanical Engineers, Part F: Journal of Rail and Rapid Transit*, vol. 214, no. 4, pp. 231-243, 2000.
- [110] M. Pau, A. Baldi, P. Orrù, and F. Ginesu, "Experimental investigation on contact between cylindrical conformal surfaces," *The Journal of Strain Analysis for Engineering Design*, vol. 39, no. 3, pp. 315-328, 218.
- [111] Kollmorgen corporation, "SynqNet Technology Overview Brochure," Sata Barbara, CA, 2007.
- [112] S.Z. Meymand, A. Keylin, and M. Ahmadian, "A Survey of Wheel-Rail Contact Models for Rail Vehicles," *Vehicle Systems Dynamics, In Press; DOI: 10.1080/00423114.2015.1137956*, 2016.

- [113] M. Sichani, R. Enblom, and M. Berg, "Comparison of non-elliptic contact models: Towards fast and accurate modeling of wheel-rail contact," in *9th International Conference on Contact mechanics and wear of rail/wheel systems (CM2012)*, Chengdu, China, 2012.
- [114] J.A. Elkins, "Prediction of wheel/rail contact models for vehicle system dynamics including multi-point contact," *Vehicle Systems Dynamics*, vol. 20, pp. 1-27, 1992.
- [115] J. Piotrowski and H. Chollet, "Wheel-Rail Contact Models for Vehicle System Dynamics including Multi-point Contact," *Vehicle System Dynamics*, vol. 43, no. 6-7, pp. 455-483, 2005.
- [116] S. Falomi, M. Malvezzi, E. Meli, and A. Rindi, "Determination of wheel-rail contact points: comparison between classical and neural network based procedures," *Meccanica*, vol. 44, pp. 661-686, 2009.
- [117] K. Knothe, "History of Wheel/Rail Contact Mechanics: From Redtenbacher to Kalker," *Vehicle System Dynamics*, pp. 9-26, 2008.
- [118] K.E. Zaaza and A.L. Schwab, "Review of Joost Kalker's Wheel-Rail Contact Theories and Their Implementation in Multibody Codes," in *the ASME 2009 International Design Engineering Technical Conferences & Computer and Information in Engineering Conference*, San Diego, California, USA, 2009.
- [119] H. Sugiyama and Y. Suda, "On the contact search algorithms for wheel/rail contact problems," *Journal of computational and nonlinear dynamics*, vol. 4, 2009.
- [120] J.J., Kalker, "The contact between wheel and rail," Reports of the Department of Mathematics and Informatics, Delft University of Technology, 82-27, 1982.
- [121] J.J., Kalker, "Survey of wheel—rail rolling contact theory," *Vehicle System Dynamics*, vol. 8, no. 4, pp. 317--358, 1979.
- [122] J. Piotrowski and W. Kik, "A simplified model of wheel/rail contact mechanics for non-Hertzian problems and its application in rail vehicle dynamic simulations," *Vehicle System Dynamics*, vol. 46, no. 1-2, pp. 27-48, 2008.

- [123] J.B. Ayasse and H. Chollet, "Wheel-Rail Contact," in *Handbook of Railway Vehicle Dynamics*.: CRC press, 2006.
- [124] V. Garg and R.V. Dukkipati, *Dynamics of railway vehicle systems*.: Elsevier, 1984.
- [125] J.J., Kalker, "On the rolling contact of two elastic bodies in the presence of dry friction," T.H. Delft, Thesis 1967.
- [126] J.J. Kalker, "A simplified theory for non-Hertzian contact," *Vehicle System Dynamics*, vol. 12, no. 1-3, pp. 43--45, 1983.
- [127] J.J. Kalker, "Wheel-Rail Rolling Contact Theory," *Wear*, no. 144, 1991.
- [128] K. Knothe, R. Wille, and B.W. Zastra, "Advanced Contact Mechanics - Road and Rail," *Vehicle System Dynamics*, vol. 35, no. 4-5, pp. 361--407, 2001.
- [129] L.Z. Li, "Wheel-Rail Rolling Contact and Its Application to Wear Simulation," Delft University, Delft, The Netherlands, PhD Thesis 2002.
- [130] L.Z. Li and J.J. Kalker, "The Computation of Wheel-Rail Conformal Contact," in *Proceedings of the 4th World Conference on Computational Mechanics*, Buenos Aires, Argentina, 1998.
- [131] E. Vollebregt and G. Segal, "Solving conformal wheel--rail rolling contact problems," *Vehicle System Dynamics*, vol. 52, pp. 455-468, 2014.
- [132] J.P. Pascal and G. Sauvage, "New method for reducing the multicontact wheel/rail problem to one equivalent contact patch," *Vehicle System Dynamics*, vol. 20, no. 1, pp. 475-489, 1992.
- [133] J.P. Pascal and F. Jourdan, "The "Rigid-Multi-Hertzian Method" as Applied to Conformal Contacts," in *ASME 2007 International Design Engineering Technical Conferences and Computers and Information in Engineering Conference*, San Diego, CA, 2007, pp. 1811-1825.
- [134] J.P. Pascal and G. Sauvage, "The available methods to calculate the wheel/rail forces in non Hertzian contact patches and rail damaging," *Vehicle System Dynamics*, vol. 22, no. 3-4, pp. 263--275, 1993.

- [135] J.P. Pascal, "About multi-hertzian-contact hypothesis and equivalent conicity in the case of S1002 and UIC60 analytical wheel/rail profiles," *Vehicle System Dynamics*, vol. 22, no. 2, pp. 57--78, 1993.
- [136] J.B. Ayasse, H. Chollet, and J.L. Maupu, "Paramètres caractéristiques du contact roueraill," *Recherche-Transports-Sécurité*, vol. 68, p. 88, 2000.
- [137] J. Hashemi and B. Paul, "Contact stresses on bodies with arbitrary geometry. Applications to wheels and rails.," Report to FRA-ORD, Washington, DC, 79/23 1979.
- [138] G. Vohla, "Werkzeuge zur realitätsnahen Simulation der Laufdynamik von Schienenfahrzeugen," ETH, Verlag Düsseldorf, PhD Thesis 1995.
- [139] Ch. Linder, "Verschleiß von Eisenbahnrädern mit Unrundheiten," ETH, Zurich, Dissertation Nr. 12342 1997.
- [140] Ch. Linder and H. Brauchli, "Prediction of wheel wear," in *Proceedings of the Second Mini Conference on Contact Mechanics and Wear of Rail/Wheel Systems*, Budapest, 1996, pp. 215-220.
- [141] J.B. Ayasse and H. Chollet, "Determination of the wheel rail contact patch in semi-Hertzian conditions," *Vehicle System Dynamics*, vol. 43, no. 3, pp. 161-172, 2005.
- [142] X. Quost et al., "Assessment of a semi-Hertzian method for determination of wheel--rail contact patch," *Vehicle System Dynamics*, vol. 44, no. 10, pp. 789-814, 2006.
- [143] M. Sichani, R. Enblom, and M. Berg, "A novel method to model wheel--rail normal contact in vehicle dynamics simulation," *Vehicle System Dynamics*, vol. 52, no. 12, pp. 1752--1764, 2014.
- [144] P. Wriggers and T.A. Laursen, *Computational contact mechanics*. Heidelberg: Springer, 2006, vol. 30167.
- [145] J.J. Kalker, "Survey of Wheel-Rail Rolling Contact Theory, State-of-the-Art Paper," *IUTAM-IAVSD Symposium, Berlin, Vehicle System Dynamics*, vol. 5, pp. 317-358, 1979.
- [146] J.J. Kalker, "Review of Wheel-Rail Rolling Contact Theories," *The General Problem of Rolling Contact*, L. Browne and N.T. Tsai (eds.), the 1989 ASME Winter, 1980.

- [147] J.J. Kalker and A.D. De Pater, "Survey of the Theory of Local Slip in the Elastic Contact Region with Dry Friction," *International Applied Mechanics*, vol. 7, no. 5, pp. 472-483, 1971.
- [148] A.D. De Pater, "On the reciprocal presence between two elastic bodies," *Rolling Contact Phenomena* edited by J. B. Bidwell, Elsevier Publishing Company, Amsterdam, 1962.
- [149] K.L. Johnson, "The effect of a tangential contact force upon the rolling motion of an elastic sphere upon a plane," *J. Appl. Mech.*, vol. 25, no. 339, 1925.
- [150] J.J. Kalker, "A Strip Theory for Rolling with Slip and Spin," in *Proc. Kon. Nederlandse Akademie van Wetenschappen, Amsterdam*, vol. B70, 1966, pp. 10-62.
- [151] J.J. Kalker, "The Tangential Force Transmitted by Two Elastic Bodies Rolling Over Each Other with Pure Creepage," *Wear*, vol. 11, pp. 421-430, 1968.
- [152] Z.Y. Shen, J.K. Hedrick, and J.A. Elkins, "A Comparison of Alternative Creep Force Models for Rail Vehicle Dynamic Analysis," *Vehicle System Dynamics: International Journal of Vehicle Mechanics and Mobility*, vol. 12, pp. 1-3, 2007.
- [153] P.J. Vermuelen and K.L. Johnson, "Contact of nonspherical Elastic Bodies Transmitting Tangential Forces," *J. appl. Mech*, vol. 86, pp. 338-340, 1964.
- [154] K.L. Johnson, *Contact Mechanics*. Cambridge: Cambridge University Press, 1987.
- [155] E. Jahnke and F. Emde, *Table of Functions*. Leipzig: 2nd Edn. Teubner Verlag, 1933.
- [156] J.J. Kalker, "Rolling with slip and spin in the presence of dry friction," *Wear*, vol. 9, pp. 20-38, 1966.
- [157] O. Polach, "A Fast Wheel-Rail Forces Calculation Computer Code," *Vehicle System Dynamics, Suppl. 33*, pp. 728-739, 1999.
- [158] O. Polach, "Solution of Wheel-Rail Contact Forces Suitable for Calculation of Rail Vehicle Dynamics," in *Proceedings of the Second Int. Conference on Railway Bogies*, Budapest, 1992, pp. 10-17.

- [159] L. Freibauer, "Adheze kola vozidla na dráze," in *Proc. of „VII. vědecká konference VŠDS*, vol. 3, 1983, pp. 214-219.
- [160] J.J. Kalker, "A Fast Algorithm for the Simplified Theory of Rolling Contact," *Vehicle System Dynamics*, vol. 11, pp. 1-13, 1982.
- [161] E. Vollebregt, "User guide for CONTACT, Vollebregt & Kalker's rolling and sliding contact model," Technical report TR09-03, version, 13, 2013.
- [162] J.J. Kalker, "The principle of virtual work and its dual for contact problems," *Ingenieur-Archiv*, vol. 56, no. 6, pp. 453--467, 1986.
- [163] I. Nitta, "Measurements of real contact areas using PET films (thickness, 0.9  $\mu\text{m}$ )," *Wear*, vol. 181, pp. 844--849, 1995.
- [164] H. Sugiyama et al., "Wheel/rail contact geometry on tight radius curved track: simulation and experimental validation," *Multibody System Dynamics*, vol. 25, no. 2, pp. 117--130, 2011.
- [165] F. Aymerich and M. Pau, "Assessment of nominal contact area parameters by means of ultrasonic waves," *Journal of tribology*, vol. 126, pp. 639--645, 2004.
- [166] M. Pau, F. Aymerich, and F. Ginesu, "Distribution of contact pressure in wheel--rail contact area," *Wear*, vol. 253, no. 1, pp. 265--274, 2002.
- [167] R. Dwyer-Joyce, C. Yao, J. Zhang, R. Lewis, and B. Drinkwater, "Feasibility Study for Real Time Measurement of Wheel-Rail Contact Using an Ultrasonic Array," *Journal of Tribology*, vol. 131, p. 041401, 2009.
- [168] R. Dwyer-Joyce, C. Yao, R. Lewis, and H. Brunskill, "An ultrasonic sensor for monitoring wheel flange/rail gauge corner contact," *Proceedings of the Institution of Mechanical Engineers, Part F: Journal of Rail and Rapid Transit*, vol. 227, pp. 188-195, 2011.
- [169] S.Y. Poon, "An experimental study of the shear traction distribution in rolling with spin," *Wear*, vol. 10, no. 1, pp. 61--69, 1967.

- [170] E. Ollerton, "Stresses in the Contact Zone," in *Proceedings of the Institution of Mechanical Engineers*, vol. 178, 1963, pp. 161-171.
- [171] A. Kostyukevich, "A survey of devices used for experimental investigation of frictional properties of wheel-rail contact," Electronic Archive of V.I. Dahl Institute, (In Russian), 2012.
- [172] C.F. Logston and G.S. Itami, "Locomotive friction-creep studies," *Journal of Manufacturing Science and Engineering*, vol. 102, no. 3, pp. 275--281, 1980.
- [173] B. Engel, H.P. Beck, and J. Alders, "Verschleißreduzierende Radschlupfregelung mit hoher Kraftschlussausnutzung," *Elektrische Bahnen*, vol. 96, pp. 201--209, 1998.
- [174] W. Lang and C. Roth, "Optimale Kraftschlussausnutzung bei Hochleistungs-Schienenfahrzeugen," *Eisenbahntechnische Rundschau*, vol. 42, pp. 61--66, 1993.
- [175] O. Polach, "Optimierung moderner Lok-Drehgestelle durch fahrzeug- dynamische Systemanalyse," *Eisenbahningenieur*, vol. 53, pp. 50-57, 2002.
- [176] O. Polach, "SBB 460 Adhäsionsversuche," SLM Winterthur, Technical Report No. 414 1992.
- [177] A. Hobbs, "A survey of creep," Brit. Rail Res. Dept., Derby, UK, Rept. DYN52 1967.
- [178] A. Gilchrist, "The effect of surface condition in rolling contact behaviour," Brit. Rail Res. Dept., Derby, UK, 1978.
- [179] R. Illingworth, "The mechanism of railway vehicle excitation by track irregularities," Oxford University, Doctoral Thesis 1975.
- [180] B. Brickle, "The steady state forces and moments on a railway wheel set including flange contact conditions," Loughborough University, Doct. Thesis 1973.
- [181] E. Magel and Y. Liu, "Study of friction—measurement analysis and practical implications for the wheel/rail contact," in *Proceedings of the 8th International Conference on Contact Mechanics and Wear of Rail/Wheel Systems*, Firenze, Italy, 2009, pp. 239--245.

- [182] H. Doi, T. Miyamoto, Y. Nishiyama, S. Ohe, and H. Kamachi, "A new experimental device to investigate creep forces between wheel and rail," *Wear*, vol. 271, pp. 40--46, 2011.
- [183] H. Harrison, "The development of a low creep regime, hand-operated tribometer," *Wear*, vol. 265, no. 9, pp. 1526--1531, 2008.
- [184] K. Nagase, "A study of adhesion between the rails and running wheels on main lines: results of investigations by slipping adhesion test bogie," *Proceedings of the Institution of Mechanical Engineers, Part F: Journal of Rail and Rapid Transit*, vol. 203, no. 1, pp. 33--43, 1989.
- [185] H. Chen, T. Ban, M. Ishida, and T. Nakahara, "Adhesion between rail/wheel under water lubricated contact," *Wear*, vol. 253, no. 1, pp. 75--81, 2002.
- [186] H. Chen et al., "Estimation of wheel/rail adhesion coefficient under wet condition with measured boundary friction coefficient and real contact area," *Wear*, vol. 271, no. 1, pp. 32--39, 2011.
- [187] A. Matsumoto, Y. Sato, M. Nakata, M. Tanimoto, and K. Qi, "Wheel-rail contact mechanics at full scale on the test stand," *Wear*, vol. 191, no. 1, pp. 101--106, 1996.
- [188] E. Vollebregt, "Numerical modelling of measured railway creep versus creep-force curves with CONTACT," *Wear*, vol. 314, no. 1, pp. 87-95, 2013.
- [189] F. Bucher, "The Contact between Micro-Rough Rails and Wheels," Logos Verlag, Berlin, 2002.
- [190] A. Lünenschloß, F. Bucher, and K. Knothe, "Normalkontakt zweier Körper mit rauen Oberflächen," *Fortschritt-Berichte VDI, Reihe 2*, vol. 596, 2002.
- [191] M. Ertz and F. Bucher, "Improved creep force model for wheel/rail contact considering roughness and temperature," *Vehicle Syst. Dyn. Suppl.*, vol. 37, pp. 314-325, 2002.
- [192] M. Ertz, "Temperatur, Materialbeanspruchung und Kraftschluss im Rad-Schiene-Kontakt," *Fortschritt-Berichte VDI, Reihe 12*, vol. 549, 2004.
- [193] P. Häse and S. Menth, "Kraftschluss bei Triebfahrzeugen – Modellbildung und Verifikation an Messdaten," *Elektrische Bahnen*, vol. 94, pp. 125–134, 1996.

- [194] O. Polach, "Rad-Schiene-Modelle in der Simulation der Fahrzeug- und Antriebsdynamik," *Elektrische Bahnen*, vol. 99, pp. 219-230, 2001.
- [195] J. Holland and F. Rick, "Einfluss der Kontakttemperatur auf den Kraftschlussbeiwert," *Tribologie und Schmierungstechnik*, vol. 44, pp. 73-78, 1997.
- [196] F. Rick, "Zur Erfassung der Geschwindigkeitsabhängigkeit des Kraftschlussbeiwertes eines hochbelasteten Rad-Schiene-Kontaktes," Thesis, Technical University Clausthal, Germany, 1998.
- [197] H. Schwarze, "Geschwindigkeitsabhängiger Kraftschluss hochbelasteter Rad-Schiene-Kontakte," *Elektrische Bahnen*, vol. 99, pp. 203-218, 2001.
- [198] K. Hou and J. Kalousek, "Thermal effect on adhesion in wheel/rail interface," in *Proceedings of the Fifth International Conference Contact Mechanics and Wear of Rail Wheel Systems*, Tokyo, Japan, 2000, pp. 239-244.
- [199] I.V. Kragelski, M.N. Dobycin, and V.S. Kombalov, *Friction and Wear: Calculation Methods*. Oxford: Pergamon Press, 1982.
- [200] O. Polach, "Creep forces in simulations of traction vehicles running on adhesion limit," *Wear*, vol. 258, pp. 992-1000, 2005.
- [201] B. Croft, C. Jones, and D. Thompson, "Velocity-dependent friction in a model of wheel-rail rolling contact and wear," *Vehicle System Dynamics*, vol. 49, no. 11, pp. 1791-1802, 2011.
- [202] E.A.H. Vollebregt and H.M. Schuttelaars, "Quasi-static analysis of two-dimensional rolling contact with slip-velocity dependent friction," *Journal of Sound and Vibration*, vol. 331, no. 9, pp. 2141-2155, 2012.
- [203] J.G. Gimenez, A. Alonso, and E. Gomez, "Introduction of a friction coefficient dependent on the slip in the FastSim algorithm," *Vehicle System Dynamics*, vol. 43, no. 4, pp. 233-244, 2005.
- [204] J. Piotrowski, "Kalker's algorithm FastSim solves tangential contact problems with slip-dependent friction and friction anisotropy," *Vehicle System Dynamics*, vol. 48, no. 7, pp. 869-889, 2010.

- [205] O. Polach, "Creep forces in simulations of traction vehicles running on adhesion limit," *Wear*, vol. 258, pp. 992-1000, 2005.
- [206] E. Vollebregt, "FASTSIM with Falling Friction and Friction Memory," *Noise and Vibration Mitigation for Rail Transportation Systems*, pp. 425-432, 2015.
- [207] F. Bucher, K. Knothe, and A. Theiler, "Normal and tangential contact problem of surfaces with measured roughness," *Wear*, vol. 253, pp. 204–218, 2002.
- [208] J.J., Kalker, "Über die Mechanik des Kontaktes zwischen Rad und "Schiene," *ZEV-Glasers Annalen*, vol. 102, pp. 214-218, 1978.
- [209] E.A.H. Vollebregt, "Numerical modelling of measured railway creep versus creep-force curves with CONTACT," *Wear*, vol. 314, no. 1, pp. 87-95, 2013.
- [210] R. Fries, C. Urban, N. Wilson, and M. Witte, "Modeling of friction modifier and lubricant characteristics for rail vehicle simulations," in *Proceedings of the 22nd International Symposium on Dynamics of Vehicles on Roads and Tracks, IAVSD*, Manchester, 2011.
- [211] A. Kostyukevich and I. Tsyganovsky, "A survey on wheel – rail frictional interaction models," Electronic Archive of V.I. Dahl Institute, (In Russian), 2012.
- [212] C. Tomberger, P. Dietmaier, W. Sextro, and K. Six, "Friction in wheel-rail contact: a model comprising interfacial fluids, surface roughness and temperature," *Wear*, vol. 271, no. 1, pp. 2-12, 2011.
- [213] A. Meierhofer, C. Hardwick, R. Lewis, K. Six, and P. Dietmaier, "Third body layer—experimental results and a model describing its influence on the traction coefficient}," *Wear*, vol. 314, no. 1, pp. 148-154, 2014.
- [214] K. Six, A. Meierhofer, G. Müller, and P. Dietmaier, "Physical processes in wheel-rail contact and its implications on vehicle-track interaction," *Vehicle System Dynamics*, vol. 53, no. 5, pp. 635-650, 2015.
- [215] M. Spiryagin, O. Polach, and C. Cole, "Creep force modelling for rail traction vehicles based on the

- Fastsim algorithm," *Vehicle System Dynamics*, vol. 51, no. 11, pp. 1765-1783, 2013.
- [216] E. Vollebregt, S. Iwnicki, and P. Shackleton, "Assessing the accuracy of different simplified frictional rolling contact algorithms," *Vehicle Systems Dynamics*, vol. 50, no. 1, pp. 1-17, 2012.
- [217] S.Z Meymand, M. Taheri, M. Hosseini-pour, and M. Ahmadian, "Vibration Analysis of a Coupled Multibody Dynamic Model of a Contact Mechanics Roller Rig," in *ASME 2016 Joint Rail Conference*, Columbia, SC, 2016.
- [218] SIMPACK GmbH, "SIMPACK Documentation," SIMPACK release 9.8, 2015.
- [219] M. Sichani, R. Enblom, and M. Berg, "An alternative to FASTSIM for tangential solution of the wheel-rail contact," in *24th International Symposium on Dynamics of Vehicles on Road and Tracks (IAVSD)*, Gratz, Austria, 2015.
- [220] H. Le The, "Normal- und Tangentialspannungsberechnung beim rollenden Kontakt für Rotationskörper mit nichtelliptischen Kontaktflächen," *Fortschritt-Berichte VDI*, vol. 12, 1987.
- [221] K. Knothe and H. Le The, "A Contribution to The Calculation of The Contact Stress Distribution Between Two Elastic Bodies of Revolution with Non-elliptical Contact Area," *Computers & Structures*, vol. 18, no. 6, 1984.
- [222] R. Enblom and M. Berg, "Impact of Non-elliptic Contact Modelling in Wheel Wear Simulation," *Wear*, vol. 265, no. 9-10, 2008.
- [223] A. Alonso and J. G. Giménez, "A New Method for The Solution of The Normal Contact Problem in The Dynamic Simulation of Railway Vehicles," *Vehicle System Dynamics*, no. 43(2), 2005.
- [224] T. Telliskivi, "Simulation of Wear in a Rolling-Sliding Contact by a Semi-Winkler Model and Archard's Wear Law," *Wear*, no. 256, 2004.
- [225] U. Olofsson and R. Lewis, "Tribology of the Wheel-Rail Contact," in *Handbook of Railway Vehicle Dynamics*, S. Iwnicki, Ed., 2006.
- [226] P. Hañse and S. Menth, "Kraftschluss bei Triebfahrzeugen – Modellbildung und Verifikation an

Messdaten," *Elektrische Bahnen*, vol. 94, pp. 125–134, 1996.

[227] W. Kik and J. Piotrowski, "A Fast Approximate Method to Calculate Normal Load at Contact between Wheel and Rail and Creep Forces during Rolling," in *Second Mini-Conference of Contact Mechanics and Wear of Rail/Wheel Systems*, Budapest, 1996.

[228] V. Yazykov, D. Pogorelov, and G. Mikhachenko, "Railway Vehicle Simulation Using Non-elliptical Wheel-Rail Contact Model," in *XXI ICTAM Proceedings*, Warsaw, Poland, 2004.

# Appendix A : Kinematic and Dynamic Analyses of a Differential Driveline

An alternative driveline to the independent drives for powering the rotational bodies in the system, and producing slip is a differential driveline. The differential driveline mainly works based on a differential gearbox (Figure 5-4). In this section, kinematic and dynamic analysis for a differential driveline is investigated. First, torque and force analyses for a differential gearbox are conducted using two methods: graphical method and free-body diagram. Results show that both methods calculate the same relations for torques and forces. Using the differential gearbox analysis results, the dynamic and kinematic analyses of the differential gearbox are thoroughly discussed.

The planetary differential gearbox, used in the differential driveline, consists of two sun gears, two planet gears, and one carriage. Two planets attaching to each other are in rolling contact with sun gears through a carriage (Figure A-1).

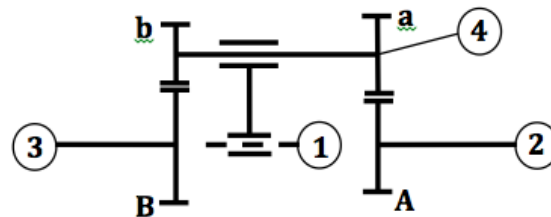


Figure A-1: Planetary differential gearbox

## A.1 Graphical Method

To analyze torques and forces in the differential gearbox, a graphical method is used. The graphical method, introduced by Kutzbach<sup>1</sup>, is based on the principle of kinematics that the

---

<sup>1</sup> KUTZBACH K. Mechanische Leistungsverzweigung. Ihre Gesetze und Anwendungen. *Maschfflenhau, Der Betrieb* 8,710-716 (1929)

instantaneous velocity of any point on a rigid body being in plane motion can be determined if the velocities of two other points on it are already known. A planet gear has three points which are of interest: its center, which is coincident with the center of arm pin, and its two pitch points, which are coincident with the pitch points of the central gears. Consequently, if the instantaneous velocities of these three points on the planet gear are known then the instantaneous velocity of one point on each planetary gear train element is also known. The tangential velocities are represented by vectors (Figure A-2). The endpoints of the vectors must lie in a straight line. If two vectors are given, the third one can be drawn easily. By projection of the vectors on some common radius one obtains straight lines, the lengths of which are proportional to the angular velocities of the planetary gearbox shafts. For differential gearbox used in the experimental rig, relation between arm and sun gear velocities is calculated as follows:

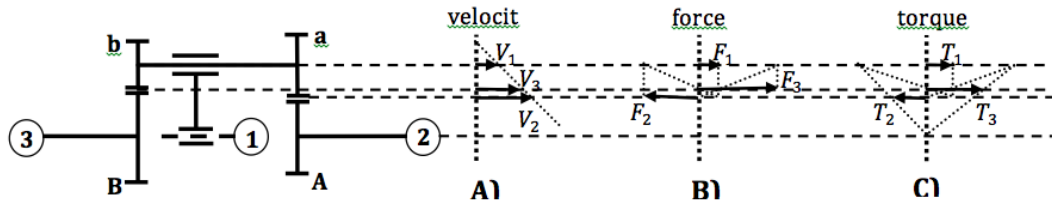


Figure A-2: Graphical method to analyze A) velocity B) force C) torque, in planetary gearbox

$$\begin{cases} v_1 = \omega_1 \times \left( \frac{a}{2p_2} + \frac{A}{2p_2} \right) = \omega_1 \times \left( \frac{b}{2p_3} + \frac{B}{2p_3} \right) \\ v_2 = \omega_2 \times \frac{A}{2p_2} \\ v_3 = \omega_3 \times \frac{B}{2p_3} \end{cases} \quad (\text{A-1})$$

Where  $p_3$  and  $p_2$  are gear pitch for left and right sun gears (Figure A-1), respectively.

$$\begin{aligned} \frac{v_1}{x} = \frac{v_3}{x + \frac{b}{2p_3}} &\Rightarrow \frac{v_1 \frac{b}{2p_3}}{v_3 - v_1} = \frac{v_1 \frac{a}{2p_2}}{v_2 - v_1} \Rightarrow \frac{b}{2p_3} \\ \frac{v_1}{x} = \frac{v_2}{x + \frac{a}{2p_2}} & \\ &= \frac{\omega_3 \frac{B}{2p_3} - \omega_1 \left( \frac{b}{2p_3} + \frac{B}{2p_3} \right)}{\omega_2 \frac{A}{2p_2} - \omega_1 \left( \frac{a}{2p_2} + \frac{A}{2p_2} \right)} \Rightarrow \frac{\omega_3 - \omega_1}{\omega_2 - \omega_1} = \frac{Ab}{Ba} = \rho \end{aligned} \quad (\text{A-2})$$

$$\Rightarrow \omega_3 = \rho \omega_2 + (1 - \rho) \omega_1$$

Graphical method is generalized for the analysis of the tangential forces and torques by Levai<sup>2</sup>. The method of drawing a force diagram is shown in Figure A-2. By taking first the force  $F_1$ , applied on the arm pin, one has to draw three lines in the directions shown by the arrows to get the force  $F_2$ , (Figure A-2). One can get the force  $F_3$ , in the same way. Force relations for the planetary differential gearbox are obtained as:

$$\left\{ \begin{array}{l} \frac{F_3}{F_1} = \frac{\frac{a}{2p_2}}{\frac{a}{2p_2} - \frac{b}{2p_3}} \\ \frac{F_2}{F_1} = \frac{\frac{b}{2p_3}}{\frac{a}{2p_2} - \frac{b}{2p_3}} \\ F_1 + F_2 = F_3 \end{array} \right. \quad (\text{A-3})$$

The torque diagram looks like the force diagram with the only difference that at the intersection, the third line must be dropped in the radial direction instead of vertically (Figure A-2). This results in the following torque relations for the differential gearbox:

$$\left\{ \begin{array}{l} \frac{T_3}{T_1} = \frac{\frac{a}{2p_2} \frac{B}{2p_3}}{\left(\frac{a}{2p_2} - \frac{b}{2p_3}\right) \left(\frac{b}{2p_3} + \frac{B}{2p_3}\right)} \\ \frac{T_2}{T_1} = \frac{\frac{b}{2p_3} \frac{A}{2p_2}}{\left(\frac{a}{2p_2} - \frac{b}{2p_3}\right) \left(\frac{a}{2p_2} + \frac{A}{2p_2}\right)} \\ T_1 + T_2 = T_3 \end{array} \right. \quad (\text{A-4})$$

---

<sup>2</sup> LEVAI, Z. Theorie des idealen einfachen Planetengetriebes. *VDI-Z.* 109,501 - 505 (1967)

## A.2 Free Body Diagram

In addition to the graphical method, free-body diagram is utilized to analyze forces and torques in the planetary differential gear box. To this end, the free body diagram for the assembly number 4 in Figure A-1 is considered. Free-body diagram represents interactive forces between sun gears and planet gears as well as force applied to the assembly by carriage (Figure A-3). Newton's second law is applied to the system to find relations between forces and torques as follows:

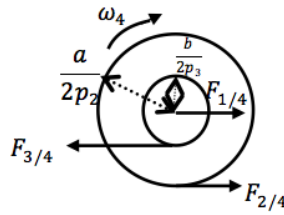


Figure A-3: Free-body diagram for assembly number 4

$$\left\{ \begin{array}{l} F_{2/4} \frac{a}{2p_2} = F_{3/4} \frac{b}{2p_3} \\ F_{1/4} - F_{2/4} + F_{3/4} = 0 \\ F_{1/4} \left( \frac{a}{2p_2} + \frac{A}{2p_2} \right) - F_{2/4} \left( \frac{A}{2p_2} \right) + F_{3/4} \left( \frac{B}{2p_3} \right) = 0 \end{array} \right. \quad (\text{A-5})$$

Hence, following relations will be obtained:

$$\left\{ \begin{array}{l} \frac{F_{3/4}}{F_{1/4}} = - \frac{\frac{a}{2p_2}}{\frac{a}{2p_2} - \frac{b}{2p_3}} \\ \frac{F_{2/4}}{F_{1/4}} = \frac{\frac{b}{2p_3}}{\frac{a}{2p_2} - \frac{b}{2p_3}} \\ \frac{F_{2/4}}{F_{3/4}} = \frac{\frac{b}{2p_3}}{\frac{a}{2p_2}} \end{array} \right. \quad (\text{A-6})$$

### A.3 Driveline Dynamics and Kinematics Analysis

Based on the above torque analyses, torque on one of the sun gears is always bigger than the other sun gear's torque. This results in two configuration for employing the differential gear box in the driveline: one is configured such that the bigger torque sun gear is connected to the input gearbox (reducer) and the alternative one is such that the bigger torque sun gear is connected to the wheel and the smaller torque sun gear is connected to the reducer (Figures A-4 and A-5). Therefore, motors M1 and M2 need to function differently for traction mode and braking mode. In another word, drive motor M1 needs to function as an electric motor for braking mode and to function as a generator for traction mode, however, creep control motor M2 needs to function as a generator for braking mode and to function as a electric motor for traction mode when the bigger torque sun gear is connected to the wheel. On the other hand, drive motor M1 needs to function as a electric motor for traction mode and to function as a generator for braking mode when the bigger torque sun gear is connected to the input gearbox (reducer). Free-body diagram and torque/power calculations for the first configuration are presented below. Similarly, same procedure should be repeated to analyze the second configuration:

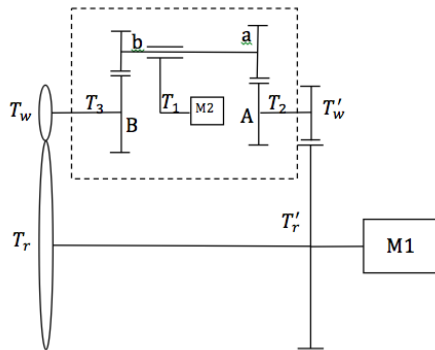


Figure A-4: Configuration representing the bigger torque sun gear is connected to input gearbox

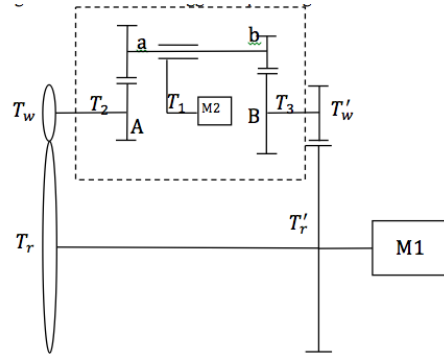


Figure A-5: Configuration representing the bigger torque sun gear is connected to wheel

### A.3.1 Kinematics Analysis

Experimental setup is designed to simulate tangential speed ( $V$  mph) for a real railcar. Based on the roller and wheel sizes, nominal angular velocities for the roller and wheel are:  $\omega_R$  and  $\omega_w = \frac{R_R}{R_w} \omega_R$ , respectively. To allow wheel speed to be precisely controlled between  $\omega_{3-min}$  (maximum negative creepage) and  $\omega_{3-max}$  (maximum positive creepage), while roller speed is at  $\omega_R$ , required casing speed (creep control motor speed) is calculated as:

$$\frac{\omega_3 - \omega_1}{\omega_2 - \omega_1} = \rho \xrightarrow{\omega_2 = \frac{r_R}{r_w} \omega_R \text{ rpm}} \frac{\omega_3 - \omega_1}{\frac{r_R}{r_w} \omega_R - \omega_1}$$

$$= \rho \Rightarrow \begin{cases} \omega_3 = \omega_{3-min} \Rightarrow \omega_{1-min} = \frac{\omega_{3-min} - \frac{r_R}{r_w} \omega_R \rho}{1 - \rho} \text{ rpm} \\ \omega_3 = \omega_{3-max} \Rightarrow \omega_{1-max} = \frac{\omega_{3-max} - \frac{r_R}{r_w} \omega_R \rho}{1 - \rho} \text{ rpm} \end{cases} \quad (\text{A-7})$$

### A.3.2 Dynamics Analysis

To analyze the governing dynamics of the system, free-body diagram for each shaft in Figure A-2 is sketched and Newton's second law is applied. It must be noted, the system is analyzed as it is operating in the steady state motion (all the velocities are constant). Note that the direction for the creep force at the contact between the wheel and roller is reversed for the braking mode compared to the traction mode. Dynamic analysis for the traction mode is conducted here (Similar approach

should be taken for the braking mode). Free body diagram of the each element of the system is considered for deriving the equilibrium equation:

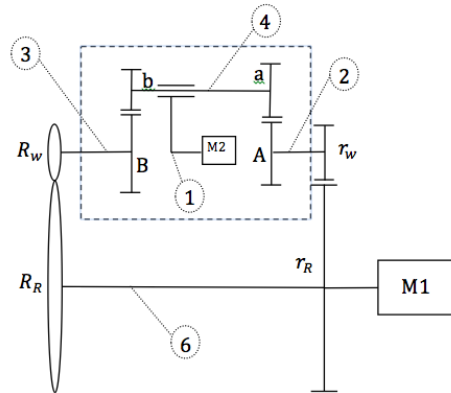


Figure A-6: Different shaft elements in the differential driveline

**Shaft 1:**

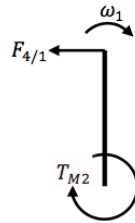


Figure A-7: Free-body diagram for carriage (shaft number 1)

$$T_{M2} = F_{4/1} \times \left( \frac{a}{2p_2} + \frac{A}{2p_2} \right) \tag{A-8}$$

**Shaft 2:**

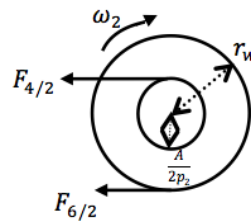
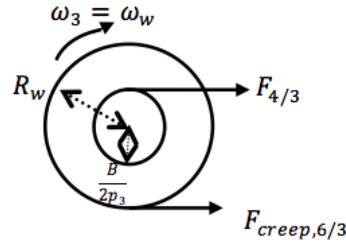


Figure A-8: Free-body diagram for shaft number 2

$$F_{4/2} \times \left( \frac{A}{2p_2} \right) = F_{6/2} \times r_w \tag{A-9}$$

**Shaft 3:**



**Figure A-9: Free-body diagram for shaft number 3**

$$F_{6/3} \times \left(\frac{B}{2p_3}\right) = F_{creep,6/3} \times R_w \quad (\text{A-10})$$

**Shaft 4:**

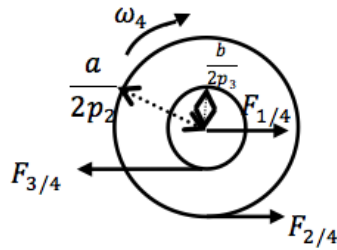


**Figure A-10: Free-body diagram for shaft number 4**

$$\left\{ \begin{array}{l} F_{2/4} \frac{a}{2p_2} = F_{3/4} \frac{b}{2p_3} \\ F_{1/4} + F_{2/4} - F_{3/4} = 0 \\ F_{1/4} \left(\frac{a}{2p_2} + \frac{A}{2p_2}\right) + F_{2/4} \left(\frac{A}{2p_2}\right) - F_{3/4} \left(\frac{B}{2p_3}\right) = 0 \end{array} \right. \quad (\text{A-11})$$

**Shaft 6:**

$$F_{creep,3/6} \times R_R = F_{2/6} \times r_R + T_{M1} \quad (\text{A-12})$$

Based on the equations developed from free-body diagrams, required torques for the drive motor M1 ( $T_{M1}$ ) and the creep control motor M2 ( $T_{M2}$ ) are obtained:

$$\begin{aligned}
 \text{Equation A-12} &\Rightarrow T_{M1} = -F_{2/6} \times r_R + F_{creep} \times R_R \\
 \xrightarrow{\text{equation A-9}} & T_{M1} = -F_{4/2} \times \left(\frac{A}{2p_2 r_w}\right) \times r_R + F_{creep,3/6} \times R_R \\
 \xrightarrow{\text{equation A-11}} & T_{M1} = -F_{3/4} \frac{2p_2}{a} \frac{b}{2p_3} \times \left(\frac{A}{2p_2 r_w}\right) \times r_R + F_{creep,3/6} \times R_R \\
 \xrightarrow{\text{equation A-10}} & T_{M1} = +F_{creep,6/3} \times R_w \frac{2p_3}{B} \frac{2p_2}{a} \frac{b}{2p_3} \times \left(\frac{A}{2p_2 r_w}\right) \times r_R + F_{creep,3/6} \times R_R \\
 &\Rightarrow T_{M1} = F_{creep,6/3} \times \rho \times \left(\frac{r_R}{r_w}\right) \times R_w + F_{creep,3/6} \times R_R \\
 &\Rightarrow T_{M1} = F_{creep,3/6} \times (R_R - \rho \times \left(\frac{r_R}{r_w}\right) \times R_w)
 \end{aligned} \tag{A-13}$$

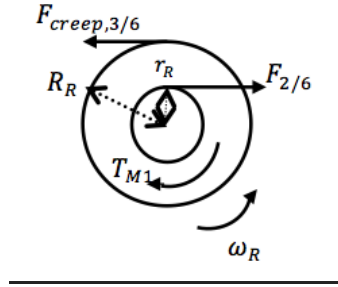


Figure A-11: Free-body diagram for roller axle (shaft number 6)

$$\begin{aligned}
 \text{Equation A-8} &\Rightarrow T_{M2} \\
 &= F_{4/1} \times \left(\frac{a}{2p_2} + \frac{A}{2p_2}\right) \\
 \xrightarrow{\text{equation A-11}} & T_{M2} = (F_{2/4} - F_{3/4}) \times \left(\frac{a}{2p_2} + \frac{A}{2p_2}\right) \\
 \xrightarrow{\text{equation A-11}} & T_{M2} = (F_{3/4} \frac{2p_2}{a} \frac{b}{2p_3} - F_{3/4}) \times \left(\frac{a}{2p_2} + \frac{A}{2p_2}\right) \\
 &\Rightarrow T_{M2} = (F_{3/4}) \left(\frac{2p_2}{a} \frac{b}{2p_3} - 1\right) \times \left(\frac{a}{2p_2} + \frac{A}{2p_2}\right) \\
 \xrightarrow{\text{equation A-10}} & T_{M2} = \left(-F_{creep,6/3} \times R_w \frac{2p_3}{B}\right) \left(\frac{2p_2}{a} \frac{b}{2p_3} - 1\right) \times \left(\frac{a}{2p_2} + \frac{A}{2p_2}\right) \\
 &\Rightarrow T_{M2} = \left(F_{creep,6/3} \times R_w \frac{2p_3}{B}\right) \left(-\frac{2p_2}{a} \frac{b}{2p_3} + 1\right) \times \left(\frac{a}{2p_2} + \frac{A}{2p_2}\right)
 \end{aligned} \tag{A-14}$$

### A.3.3 Creepage Calculation

Based on the kinematical analysis on the differential gearbox, we will have:

$$\omega_w = \omega_3 = \rho\omega_2 + (1 - \rho)\omega_1 \Rightarrow \omega_w = \rho\omega_R \frac{r_R}{r_w} + (1 - \rho)\omega_1 \Rightarrow \omega_R = \frac{1}{\rho} \omega_w \frac{r_w}{r_R} - \left(\frac{1 - \rho}{\rho}\right) \omega_1 \quad (\text{A-15})$$

Based on the definition of the creepage in terms of absolute linear velocities of the wheel, and rail/roller at the point of contact, we will have the following relation for the traction mode (similar relation can be derived for braking mode):

$$Creep = \frac{R_w \omega_w - R_R \omega_R}{(R_w \omega_w + R_R \omega_R)/2} = 1 - \frac{1}{\rho} \frac{R_R}{R_w} \frac{r_w}{r_R} + \frac{1 - \rho}{\rho} \frac{R_R}{R_w} \frac{r_w}{r_R} \frac{\omega_1}{\omega_w} \quad (\text{A-16})$$

### A.3.4 Power Calculation

Based on the torque and speed calculations, required power for the motors in the differential driveline is calculated (traction mode), as follows:

$$\begin{aligned} \text{Drive motor } M1 \text{ power: } P_{M1} &= -T_{M1} \times \omega_R \\ &= -F_{creep3,6} \times (R_R - \rho \times \left(\frac{r_R}{r_w}\right) \times R_w) \times \omega_R \end{aligned} \quad (\text{A-17})$$

$$\begin{aligned} \text{Creep control motor } M2 \text{ power: } P_{M2} &= T_{M2} \times \omega_1 \\ &= \left(F_{creep,6/3} \times R_w \frac{2p_3}{B}\right) \left(-\frac{2p_2}{a} \frac{b}{2p_3} + 1\right) \times \left(\frac{a}{2p_2} + \frac{A}{2p_2}\right) \times \omega_1 \end{aligned} \quad (\text{A-18})$$

$$\begin{aligned} \text{Power loss as heat in contact patch: } P_{hl} &= F_{creep} \times \Delta V \\ &= F_{creep} \times (R_w \omega_w - R_R \omega_R) \end{aligned} \quad (\text{A-19})$$

## A.4 Case Study

Based on specification for a differential gear box (SR42-3-15.42-108HTD8\*50-LT W/CLAMP REACTION HUB, Andantex Inc. NJ, USA) presented in Table A-1 and the desired specifications for size and speed of the roller rig which are presented in Table A-2, dynamical studies on the required power for the differential gearbox is performed.

**Table A-1: Specifications for the planetary differential gearbox**

gear	symbol	Number of teeth	Parameter (gear radius)	Normalized value
Sun gear 1	A	37	$\frac{A}{2p_2}$	214.6
Planet gear 1	a	26	$\frac{a}{2p_2}$	150.8
Sun gear 2	B	35	$\frac{B}{2p_3}$	220.5
Planet gear 2	b	23	$\frac{b}{2p_3}$	144.9

**Table A-2: Desired specifications for the case-study experimental rig**

parameter	symbol	value
Roller radius	$R_R$	25 inches
Wheel radius	$R_W$	5 inches
Roller to wheel radius ratio	$\frac{R_R}{R_W}$	5
Creep force	$F_{creep}$	5000 N
Nominal tangential speed	$V_{nom,R} = V_{nom,W}$	10 MPH

Studies show that the required power greatly depends on the gear ratio for the reducer gearbox. The required power for M1 and M2 based on the specifications listed in Table A-2 and maximum/minimum creepage values of +10 % and -10% is plotted versus reducer gear ratio per Figure A-12. The plot shows that there is an optimum point for the reducer gear ratio in terms of required power. The optimum point is related to the ratio of the roller to wheel diameter and the differential gear ratio as:

$$g_{opt, reducer} = \left(\frac{r_R}{r_W}\right) / \rho \quad (\text{A-20})$$

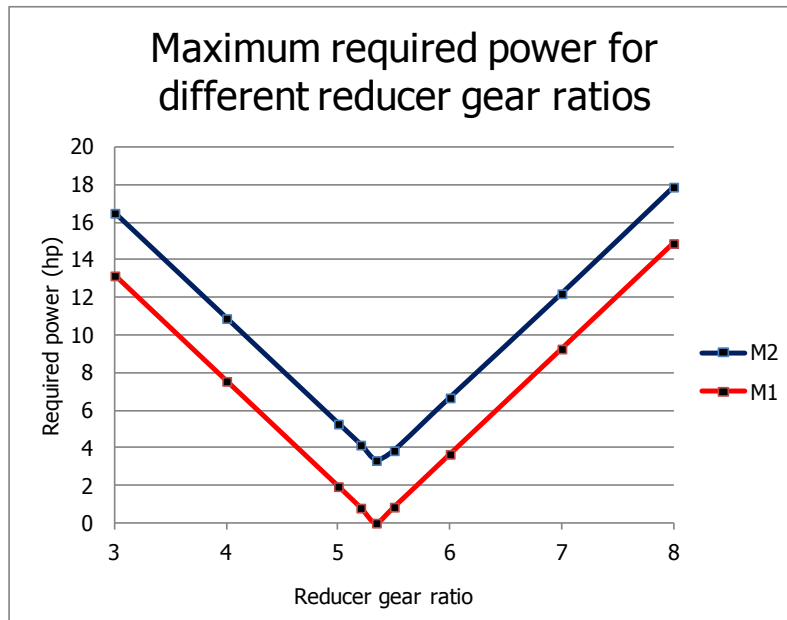


**Figure A-12: Maximum required power for the drive motors in the differential driveline versus the reducer gear ratio**

The result shows that designing a proper reducer gear ratio could result in decreasing the required power. Conversely, the required power could diverge from the optimum point as the reducer gear ratio differs from the optimum point. In addition, results show that the heat loss at the contact is constant for different reducer gear ratios (heat loss is equal to the difference between required power for M1 and M2). So, heat loss depends on the simulated speed and the creepage percentage.

Similarly, the required power for different simulated tangential speed is plotted (Figure A-13) for two reducer gear ratios ( $g=5$  and  $g=5/\rho$ ). Results show that the required power increases as the simulated speed increases. It must be noted that the heat loss increases as the simulated speed increases.

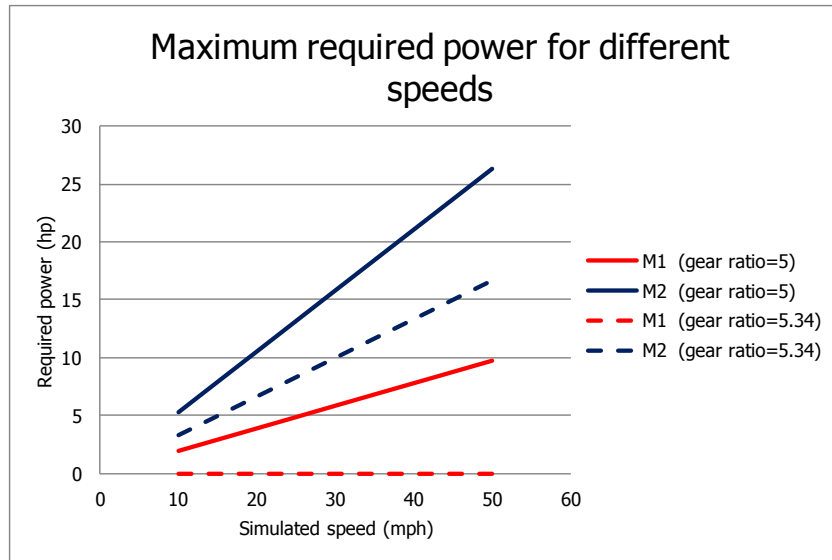


Figure A-13: Maximum required power for the drive motors in the differential driveline versus the simulated speed

These two cases for the reducer gear ratio are analyzed in depth below:

**Case 1 (reducer gear ratio is 5):**

Differential gearbox and reducer gear ratios are:

$$\rho = 0.9351 \text{ and } \frac{\tau_R}{\tau_w} = 5 \quad (\text{A-21})$$

So, we will have for the speed of creep control motor:

$$\begin{aligned}
 & \omega_R \\
 & = 67.2 \text{ rpm} \Rightarrow \omega_2 = \frac{r_R}{r_w} \omega_R = 336.1 \text{ rpm} \Rightarrow \text{equation 22} \\
 & \Rightarrow \left\{ \begin{array}{l} \omega_3 = 314 \text{ (-6.48\% creepage)} \Rightarrow \omega_1 = \frac{314 - 336.1\rho}{1 - \rho} \approx 0 \text{ rpm} \\ \omega_3 = 332.7 \text{ (-1\% creepage)} \Rightarrow \omega_1 = \frac{332.7 - 336.1\rho}{1 - \rho} = 284 \text{ rpm} \\ \omega_3 = 339.5 \text{ (1\% creepage)} \Rightarrow \omega_1 = \frac{339.5 - 336.1\rho}{1 - \rho} = 388 \text{ rpm} \\ \omega_3 = 373 \text{ (10\% creepage)} \Rightarrow \omega_1 = \frac{373 - 336.1\rho}{1 - \rho} = 912 \text{ rpm} \\ \omega_3 = 336.1 \text{ (0\% creepage)} \Rightarrow \omega_1 = \frac{336.1 - 336.1\rho}{1 - \rho} = 336.1 \text{ rpm} \end{array} \right. \quad (\text{A-22})
 \end{aligned}$$

Therefore, required power for the drive motor and creep control motor will be:

- Traction mode (1% creepage):

$$\left\{ \begin{array}{l} P_{M1} = T_{M1} \times \omega_R = -1.94 \text{ hp} \\ P_{M2} = T_{M2} \times \omega_1 = 2.24 \text{ hp} \\ P_{hl} = F_{creep} \times \Delta V = -0.3 \text{ hp} \end{array} \right. \Rightarrow P_{M1} + P_{M2} + P_{hl} = 0 \quad (\text{A-23})$$

- Traction mode (10% creepage):

$$\left\{ \begin{array}{l} P_{M1} = T_{M1} \times \omega_R = -1.94 \text{ hp} \\ P_{M2} = T_{M2} \times \omega_1 = 5.27 \text{ hp} \\ P_{hl} = F_{creep} \times \Delta V = -3.33 \text{ hp} \end{array} \right. \Rightarrow P_{M1} + P_{M2} + P_{hl} = 0 \quad (\text{A-24})$$

- Braking mode (-1% creepage):

$$\left\{ \begin{array}{l} P_{M1} = T_{M1} \times \omega_R = 1.94 \text{ hp} \\ P_{M2} = T_{M2} \times \omega_1 = -1.64 \text{ hp} \\ P_{hl} = F_{creep} \times \Delta V = -0.3 \text{ hp} \end{array} \right. \Rightarrow P_{M1} + P_{M2} + P_{hl} = 0 \quad (\text{A-25})$$

- Braking mode (-6.48% creepage):

$$\left\{ \begin{array}{l} P_{M1} = T_{M1} \times \omega_R = 1.94 \text{ hp} \\ P_{M2} = T_{M2} \times \omega_1 = 0.00 \text{ hp} \\ P_{hl} = F_{creep} \times \Delta V = -1.94 \text{ hp} \end{array} \right. \Rightarrow P_{M1} + P_{M2} + P_{hl} = 0 \quad (\text{A-26})$$

Therefore, in this case, two motors are needed to function as generator and electric motor. In traction mode, drive motor M1 functions as a generator, and creep control motor M2 functions as an electric motor. In Braking mode, however, drive motor M1 functions as an electric motor, and creep control motor M2 functions as a generator. Calculations show that the required power for the drive motor M1 is around 2 hp and for the creep control motor M2 is around 5.5 hp. Drive motor M1 sets the average speed of wheels and its speed does not need to be precisely controlled (just need to rotate in a constant speed). Creep control motor M2, however, sets the speed difference at the contact (sets creepage) and its speed needs to be precisely controlled.

**Case 2 (reducer gear ratio is  $5/\rho$ ):**

Differential gearbox and reducer gear ratios are:

$$\rho = 0.9351 \text{ and } \frac{r_R}{r_w} = 5/\rho \quad (\text{A-27})$$

Speed calculation for the creep control motor results in:

$$\begin{aligned} \omega_R &= 67.2 \text{ rpm} \Rightarrow \omega_2 = \frac{r_R}{r_w} \omega_R = 359.4 \text{ rpm} \Rightarrow \text{equation 22} \\ \Rightarrow \left\{ \begin{array}{l} \omega_3 = 302 \text{ (-10\% creepage)} \Rightarrow \omega_1 = \frac{327 - 359.4\rho}{1 - \rho} = -518 \text{ rpm} \\ \omega_3 = 332.7 \text{ (-1\% creepage)} \Rightarrow \omega_1 = \frac{332.7 - 359.4\rho}{1 - \rho} = -52 \text{ rpm} \\ \omega_3 = 339.5 \text{ (1\% creepage)} \Rightarrow \omega_1 = \frac{339.5 - 359.4\rho}{1 - \rho} = 52 \text{ rpm} \\ \omega_3 = 373.4 \text{ (10\% creepage)} \Rightarrow \omega_1 = \frac{373.4 - 359.4\rho}{1 - \rho} = 576 \text{ rpm} \\ \omega_3 = 336.1 \text{ (0\% creepage)} \Rightarrow \omega_1 = \frac{336.1 - 359.4\rho}{1 - \rho} = 0 \text{ rpm} \end{array} \right. \quad (\text{A-28}) \end{aligned}$$

Therefore, required power for the drive motor and creep control motor will be:

- Traction mode (1% creepage):

$$\begin{cases} P_{M1} = T_{M1} \times \omega_R = 0 \text{ hp} \\ P_{M2} = T_{M2} \times \omega_1 = 0.3 \text{ hp} \\ P_{hl} = F_{creep} \times \Delta V = -0.3 \text{ hp} \end{cases} \Rightarrow P_{M1} + P_{M2} + P_{hl} = 0 \quad (\text{A-29})$$

- Traction mode (10% creepage):

$$\begin{cases} P_{M1} = T_{M1} \times \omega_R = 0 \text{ hp} \\ P_{M2} = T_{M2} \times \omega_1 = 3.33 \text{ hp} \\ P_{hl} = F_{creep} \times \Delta V = -3.33 \text{ hp} \end{cases} \Rightarrow P_{M1} + P_{M2} + P_{hl} = 0 \quad (\text{A-30})$$

- Braking mode (-1% creepage):

$$\begin{cases} P_{M1} = T_{M1} \times \omega_R = 0 \text{ hp} \\ P_{M2} = T_{M2} \times \omega_1 = 0.3 \text{ hp} \\ P_{hl} = F_{creep} \times \Delta V = -0.3 \text{ hp} \end{cases} \Rightarrow P_{M1} + P_{M2} + P_{hl} = 0 \quad (\text{A-31})$$

- Braking mode (-10% creepage):

$$\begin{cases} P_{M1} = T_{M1} \times \omega_R = 0 \text{ hp} \\ P_{M2} = T_{M2} \times \omega_1 = 2.99 \text{ hp} \\ P_{hl} = F_{creep} \times \Delta V = -2.99 \text{ hp} \end{cases} \Rightarrow P_{M1} + P_{M2} + P_{hl} = 0 \quad (\text{A-32})$$

Therefore, in this case, creep control motor M2 needs to function as an electric motor all the time (in both traction and braking modes) with a maximum power required of 3.5 hp. This motor, however, needs to rotate in both directions to produce required positive and negative speeds for the traction and braking modes, respectively. On the other hand, drive motor M1 needs to rotated in the same direction as an electric motor all the time. The required power for M1 is at most 0.5 hp to start the system up (accelerate the system) and compensate for any loss (inefficiencies in the system like timing belt, reducer, etc.). This motor (M1) sets the average speed of wheels and its speed does not need to be precisely controlled (just need to rotate in a constant speed). Creep control motor M2, however, sets the speed difference at the contact (sets creepage) and its speed needs to be precisely controlled.

Additionally, variation analysis is used for calculating creepage resolution. In this regard, the variation calculus is conducted on the creepage relation for the braking mode:

$$\begin{aligned}
 Creep &= \frac{R_R \omega_R - R_W \omega_W}{R_R \omega_R} = \frac{\omega_R - \frac{R_W}{R_R} \omega_W}{\omega_R} = \frac{\omega_R - \frac{R_W}{R_R} (\rho \omega_R \frac{r_R}{r_W} + (1 - \rho) \omega_1)}{\omega_R} \\
 &= 1 - \rho \frac{r_R R_W}{r_W R_R} - (1 - \rho) \frac{\omega_1 R_W}{\omega_R R_R}
 \end{aligned} \tag{A-33}$$

$$\partial creep = -(1 - \rho) \frac{\partial \omega_1 \times \omega_R - \partial \omega_R \times \omega_1}{\omega_R^2} \left( \frac{R_W}{R_R} \right) \xrightarrow{\frac{R_W}{R_R} = \frac{1}{5}, \rho = 0.9351}$$

$$\begin{aligned}
 \partial creep &= -(1 - 0.9351) \frac{\partial \omega_1 \times \omega_R - \partial \omega_R \times \omega_1}{\omega_R^2} \left( \frac{1}{5} \right) \\
 &\approx 0.01298 \frac{|\partial \omega_1 \times \omega_R| + |\partial \omega_R \times \omega_1|}{\omega_R^2}
 \end{aligned} \tag{A-34}$$

Similarly the analysis can be repeated for the traction mode. The variation analysis shows that speed resolution of 0.5 RPM for both M1 and M2 results in 0.009 % creepage resolution.

# Appendix B : The MATLAB Code for the Contact Module

## The initialization code and main routine for running simulations

```
%% initialization

rr=44.2*25.4/2; % roller radius
rw=9.8*25.4/2; % wheel radius
N=10600; % normal loading
Gr=82*10^9; % roller modulus of rigidity
Gw=82*10^9; % wheel modulus of rigidity
nur=0.27; % roller poisson ratio
nuw=0.27; % wheel poisson ratio
x_res=0.1; % coordinate resolution in longitudinal direction
r_eq=1/((1/rr)+(1/rw)); % equivalent rolling radius

G=1/(0.5*((1/Gr)+(1/Gw)));
nu=G*(0.5*((nur/Gr)+(nuw/Gw)));
E=G*2*(1+nu);
% friction coefficient
mu_f=0.33;
% x_prof=1;
% prof_res=6;

delta_pent=.099/2; % estimated penetration
% positioning system configuration
y_shift=0; % lateral shift
AoA_angle=0; % angle of attack
cant_angle=0; % cant angle
ydot=0; % lateral shift rate
aoadot=0; % aoa rate
cantdot=0; % cant angle rate

% friction coefficient
mu_f=0.33;
% x_prof=1;
% prof_res=6;

[Fx,Fy,px_v,py_v,P,xx_1,y_con,d,a_vec,penet,x_y_contact]=main(r_eq,N,x_prof,prof_res,G,nu
,E,vx,vy,phi,x_res,mu_f,cant_angle,y_shift,delta_pent,AoA_angle);

function
[Fx,Fy,px_v,py_v,P,xx_1,y_con,z_1,d,a_vec,penet,x_y_contact]=main(r_eq,N,x_prof,prof_res,
G,nu,E,vx,vy,phi,x_res,mu_f,cant_angle,y_shift,delta_pent,AoA_angle)

% [YR1,RR1,YW1,WW1]=Wheel_rail_profile(x_prof,prof_res);
% YR1,RR1 roller profile peak point is zero--
% YW1,WW1 wheel profile min point is zero

% calculation the contact point location
[x_y_contact,g_sep,y_con,delta_azimuth,delta_elevation]=contact_finder_3d(YR1,RR1,YW1,WW1
,cant_angle,AoA_angle,y_shift,delta_pent);

% calculating the separation curve
figure,
[y_con,g_sep,y_contact]=contact_finder_2d(YR1,RR1,YW1,WW1,cant_angle,y_shift,delta_pent,A
oA_angle);
```

```

% calculating the lateral curvature
figure,
B=0.5*gradient(gradient(0.001*g_sep,0.001*y_con),0.001*y_con)./(1+(gradient(0.001*g_sep,0
.001*y_con).^2).^1.5);
plot(y_con,B,'b','LineWidth',2,'LineStyle','-')

for i=1:length(B)
    if B(i) <= .1
        B(i)=.1;
    end;
end
%B=smooth(B);
hold on
plot(y_con,B,'r','LineWidth',3,'LineStyle','--')
xlabel('Y [mm]','FontSize', 12)
ylabel('curvature [1/m]','FontSize', 12)
grid on
set(gca,'FontSize',12)
legend('original','corrected')
R=r_eq*ones(length(y_con),1);
[rt rte]=min(g_sep);
y_con_z=y_con - y_con(rte);
penet1=.1;
penet2=.05;
penet_err=.005;

% solving normal contact problem
[P,xx_1,a_vec,penet,y_con_2]=Secant_ANALYN_Mey(g_sep,y_con_z,R,B,E,nu,N,penet1,penet2,pen
et_err,x_res);
y_con_1=y_con_2*1000;
y_con_z_1=y_con_1+y_con(rte);
y_cent=y_con(rte);
% calculating the creepages
[vx
phi]=creepage_calculation(wr,ww,rr,rw,x_y_contact(1,2),ydot,x_y_contact(1,2)*tan(delta_el
evation*pi/180),aoa,oadot,cant,cantdot,delta_elevation);
vy

% solving the tangential contact problem
if (vx==0) && (vy==0) && (phi==0)
    fprintf('creepage is zero');
    px_v=zeros(size(P));
    py_v=zeros(size(P));
    Fx=0;
    Fy=0;
    d=zeros(length(a_vec),1);
else
    % a_ind=find(a_vec>0);
    % a_vec_z=a_vec(a_ind);
    % y_con_z=y_con(a_ind);
    [px_v
py_v
Fx
Fy]
d]=FaStrip_Mey_fig(g_sep,y_con_1,R,B,a_vec,xx_1,x_res,P,mu_f,vx,vy,phi,nu,G);
end;
xx_1=xx_1+x_y_contact(1,1);

```

## The code for solving rigid geometry contact module

```

function
[x_y_contact,g_sep,y_con,delta_azimuth,delta_elevation]=contact_finder_3d(YR1,RR1,YW1,WW1
,cant_angle,AoA_angle,y_shift,delta_pent)

% this fuction calculates the location of 3d contact point based on given cant
% angle, AoA angle and lateral shift
% cant_angle is in degree

```

```

% AoA_angle is in degree
% y_shift is lateral shift in mm
% delta_pent is penetration in mm

% YR1,RR1 roller profile peak point is zero--
% YW1,WW1 wheel profile min point is zero

% x_y_contact gives the (x and y) coordinates of the contact point
% g_sep is separation curve
% y_con is the y coordinate for separation curve
% delta_azimuth and delta_elevation are normal contact vector angles

ss=6.95469622; % wheel profile at taper line 6.95469622 for WW1 and 5 for WW2
Rw=9.47*25.4/2; %mm wheel radius
W_3=-Rw-ss+WW1; % origin on the wheel axle

xw_3=-141*.254:0.254:141*.254;
yw_3=YW1;
beta=zeros(length(yw_3),length(xw_3));
ZZ_W_3=zeros(length(yw_3),length(xw_3));
[XX_W_3,YY_W_3]=meshgrid(xw_3,yw_3);
% calculation of wheel segment

for i=1:length(xw_3)
for j=1:length(yw_3)
    beta(j,i)=asin(xw_3(i)/W_3(j)); % x=r*sin(theta)
    ZZ_W_3(j,i)=W_3(j)*cos(beta(j,i)); % Z=r*cos(theta)
end;
end;
ZZ_W_3=Rw+ss+ZZ_W_3;

theta_cant=cant_angle*pi/180; % in radian
alpha_AoA=AoA_angle*pi/180; % in radian

T_cant=[1 0 0;0 cos(theta_cant) -sin(theta_cant);0 sin(theta_cant) cos(theta_cant)]; %
rotation matrix around y axis (cant)
T_AoA=[cos(alpha_AoA) -sin(alpha_AoA) 0;sin(alpha_AoA) cos(alpha_AoA) 0;0 0 1]; %
rotation matrix around z axis (AoA)
T_tot=T_cant*T_AoA;

% calculation of rotated wheel
for j=1:length(xw_3)
for i=1:length(yw_3)
    P1=[XX_W_3(i,j) YY_W_3(i,j) ZZ_W_3(i,j)]*T_tot;
    X_Tw_3(i,j)=P1(1);
    Y_Tw_3(i,j)=P1(2);
    Z_Tw_3(i,j)=P1(3);
end;
end;

d_s=1; % resizing factor
% downsizing the matrix
SSw1=resizem(X_Tw_3,d_s);
SSw2=resizem(Y_Tw_3,d_s);
SSw3=resizem(Z_Tw_3,d_s);

% calculate the z coordinate of the rotated wheel surface for pre-determind
% meshgrid for comparing with shifted roller surface

q_x=length(xw_3);
q_y=length(yw_3);

for q=1:q_x
    X_Sw_3((q-1)*q_y+1:q*(q_y))=X_Tw_3(:,q);
    Y_Sw_3((q-1)*q_y+1:q*(q_y))=Y_Tw_3(:,q);

```

```

        Z_Sw_3((q-1)*q_y+1:q*(q_y))=Z_Tw_3(:,q);
end;

F_W=TriScatteredInterp(X_Sw_3',Y_Sw_3',Z_Sw_3');

for j=1:length(xw_3)
for i=1:length(yw_3)
    Z_TSw_3(i,j)=F_W(XX_W_3(i,j),YY_W_3(i,j));
end;
end;

%-----Roller-----

Rr=44.2*25.4/2; %mm Roller radius
R_3=+Rr+RR1; % origin on roller axle

xr_3=-137*0.25399909:0.25399909:137*0.25399909;
yr_3=YR1;
beta=zeros(length(yr_3),length(xr_3));
ZZ_R_3=zeros(length(yr_3),length(xr_3));
[XX_R_3,YY_R_3]=meshgrid(xr_3,yr_3);
% calculation of roller segment

for i=1:length(xr_3)
for j=1:length(yr_3)
    beta(j,i)=asin(xr_3(i)/R_3(j)); % x=r*sin(theta)
    ZZ_R_3(j,i)=R_3(j)*cos(beta(j,i)); % z=r*cos(theta)
end;
end;

ZZ_R_3=-Rr-30+ZZ_R_3;

%calculation of shifted roller

shif=y_shift;%y_shift;

X_Tr_3=XX_R_3;
Y_Tr_3=YY_R_3+shif;
Z_Tr_3=ZZ_R_3;

% downsizing the matrix
SSr1=resizem(X_Tr_3,d_s);
SSr2=resizem(Y_Tr_3,d_s);
SSr3=resizem(Z_Tr_3,d_s);

% calculate the z coordinate of the roller surface surface for pre determind
% meshgrid for comparing with rotated wheel

q_x_r=length(xr_3);
q_y_r=length(yr_3);

for q=1:q_x_r
    X_Sr_3((q-1)*q_y_r+1:q*(q_y_r))=X_Tr_3(:,q);
    Y_Sr_3((q-1)*q_y_r+1:q*(q_y_r))=Y_Tr_3(:,q);
    Z_Sr_3((q-1)*q_y_r+1:q*(q_y_r))=Z_Tr_3(:,q);
end;

F_R=TriScatteredInterp(X_Sr_3',Y_Sr_3',Z_Sr_3');

for j=1:length(xw_3)
for i=1:length(yw_3)
    Z_TSr_3(i,j)=F_R(XX_W_3(i,j),YY_W_3(i,j));
end;
end;

```

```

% calculation of minimum distance between shifted roller and rotated wheel

diff_3d=Z_TSw_3-Z_TSr_3;

[minval,ind] = min(diff_3d(:));
[I,J] = ind2sub([size(diff_3d,1) size(diff_3d,2)],ind);
figure,
h1=surf(SSw1,SSw2,SSw3-minval)

g_sep=diff_3d(I-floor(length(yw_3)/5):1:I+floor(length(yw_3)/5),J)-minval;
y_con=YY_W_3(I-floor(length(yw_3)/5):1:I+floor(length(yw_3)/5),1);

hold on
h2=surf(SSr1,SSr2,SSr3)
shading interp

hold on
x_contact = ones(1,26)*XX_W_3(I,J);
y_contact = ones(1,26)*YY_W_3(I,J);
z_line=-40:-15;
text(XX_W_3(I,J),YY_W_3(I,J)-4,-20, ' contact normal vector', 'FontSize',12)
text(XX_W_3(I,J),YY_W_3(I,J)+2.5,-25, ' \downarrow', 'FontSize',12)
axis equal
set(gca, 'FontSize',12)
%calculation of normal vector at the contact point

[c1,c2,c3]=surfnorm(XX_W_3,YY_W_3,Z_TSr_3-minval);
hold on
[c1,c2,c3]=surfnorm(XX_W_3,YY_W_3,Z_TSr_3);
quiver3(XX_W_3(I,J),YY_W_3(I,J),Z_TSr_3(I,J),c1(I,J),c2(I,J),c3(I,J),11, 'LineStyle','-','Color','r', 'LineWidth',2)

%calculation of azimuth elevation coordinates of normal vector

az_angle=atan(sqrt(c1(I,J)^2+c2(I,J)^2)/c3(I,J))*180/pi;

if (c2(I,J)<= 0 & c3(I,J)>=0 ) || (c2(I,J)>= 0 & c3(I,J)<=0 )
    az_angle=-az_angle;
end;

contact_angle=[atan(c2(I,J)/c1(I,J))*180/pi az_angle];
fprintf('\nazimuth angle of normal vector is (in degree): %f\n\n', contact_angle(1));
fprintf('\nelevation angle of normal vector is (in degree): %f\n\n', contact_angle(2));

delta_azimuth=contact_angle(1);
delta_elevation=contact_angle(2);
% calculation of contact area
delta_pen=delta_pent;
v_v=find(diff_3d<=minval+delta_pen);

contact_area_m=NaN*ones(size(XX_W_3));
for ii=1:length(v_v)
    contact_area_m(ind2sub([size(diff_3d,1) size(diff_3d,2)],v_v(ii)))=1; % -35 is
the height where contact area will be shown
end;
hold on

contact_area=.5*(length(v_v)-2)*(xw_3(2)-xw_3(1))*(yw_3(2)-yw_3(1));
fprintf('\ncontact area is (in mm^2): %f\n\n',contact_area);

%calculation of major and minor axes

T_AoA_1=[cos(-alpha_AoA) sin(-alpha_AoA) 0;-sin(-alpha_AoA) cos(-alpha_AoA) 0;0 0 1];
% rotation matrix around z axis (-AoA)

% calculation of major and minor axes of contact ellipse

```

```

for j=1:length(xw_3)
for i=1:length(yw_3)
    P1=[XX_W_3(i,j) YY_W_3(i,j) contact_area_m(i,j)]*T_AoA_1;
    X_T_c(i,j)=P1(1);
    Y_T_c(i,j)=P1(2);
    Z_T_c(i,j)=P1(3);
end;
end;

hold on

grid on
axis([-40 40 -25 25 -40 -20])
xlabel('X (mm)', 'FontSize', 12)
ylabel('Y (mm)', 'FontSize', 12)
zlabel('Z (mm)', 'FontSize', 12)

ma_mi_1=max(max(Y_T_c)-min(min(Y_T_c)));
ma_mi_2=max(max(X_T_c)-min(min(X_T_c)));

fprintf('\nmajor axis length is (in mm): %f\n\n', max(ma_mi_1,ma_mi_2));
fprintf('\nminor axis length is (in mm): %f\n\n', min(ma_mi_1,ma_mi_2));
fprintf('\nx coordinates of contact point is (in mm): %f\n\n', XX_W_3(I,J));
fprintf('\ny contact is in original coordinate**');
fprintf('\ny coordinates of contact point is (in mm): %f\n\n', YY_W_3(I,J));

figure,
surf(XX_W_3,YY_W_3,contact_area_m)
x_y_contact=[XX_W_3(I,J) YY_W_3(I,J)];

```

## The code for calculating the separation curve

```

function
[y_con,g_sep,y_contact]=contact_finder_2d(YR,R,YW,W,cant_angle,y_shift,delta_pent,AoA_angle)
% this function calculates the location of 2d contact point and separation curve based on
given cant
% angle, aoa angle and lateral shift
% cant_angle and AoA_angle are in degree
% y_shift is lateral shift in mm
% delta_pent is penetration in mm
% YR,R roller profile peak point is zero-
% YW,W wheel profile min point is zero

% y_contact gives the lateral (y) coordinate of the contact point
% g_sep is separation curve
% y_con is the y coordinate for separation curve

thet=-cant_angle*pi/180; % calculates the cant angle in radian
aoa=AoA_angle*pi/180; % calculates the cant angle in radian
A=[cos(thet) sin(thet);-sin(thet) cos(thet)]; % rotation matrix around y axis (cant
rotation)

% calculates the rotated wheel profile
for i=1:length(W)
    WY(:,i)=[YW(i) W(i)]*A;
end;

xx1=WY(1,:);
WW=WY(2,:);

% calculation of shifted roller profile
shif=floor(y_shift/.254); % YR resolution is .254

```

```

RR=R;%circshift(R',shif); % lateral shift of the roller
xx2=YR+shif*.254;

% minimum distance between wheel and roller

% interpolation of wheel and roller data points for predetermined points
xn=-30:.05:30;
FW = fixpt_interp1(xx1,WW,xn, 'double', 2^-8, 'double', 2^-14, 'Floor');
FR = fixpt_interp1(xx2,RR,xn, 'double', 2^-8, 'double', 2^-14, 'Floor');
[t,s]=min(FW-FR);
sep=FW-FR-t;

% effect of AoA: projecting the roller profile in-line with wheel profile
xx2_v=((xx2-xn(s))/cos(aoa))+xn(s);
FR_v = fixpt_interp1(xx2_v,RR,xn, 'double', 2^-8, 'double', 2^-14, 'Floor');
hold on
plot(xx1,WW-(t), 'LineStyle', '-', 'Color', 'g', 'LineWidth', 2.5)
hold on
plot(xx1,WW-(t), 'r', 'LineWidth', 3)
hold on
plot(xx2,RR, 'k', 'LineWidth', 3)
hold on
plot(xn,FR, '--k', 'LineWidth', 3)
line([xn(s) xn(s)], [-15 20], 'LineStyle', '--', 'Color', [.6 .6 .6], 'LineWidth', 2.5);
legend('contact normal vector', 'wheel', 'rail/roller')
c1=gradient(xn);
c2=gradient(FR);
quiver(xn(s), FR(s), -c2(s), c1(s), 1000, 'LineStyle', '-', 'Color', 'g', 'LineWidth', 2.5)

%method number 2
hold on
m=(FR(s+1)-FR(s-1))/(2*0.01);
y_s=FR(s)+(-1/m)*(xn-xn(s));
axis equal
axis([-25 25 -15 15])
grid on
xlabel('Y (mm)', 'FontSize', 18)
ylabel('Z (mm)', 'FontSize', 18)
set(gca, 'FontSize', 18)
set(gca, 'TickDir', 'out')
set(gca, 'Units', 'centimeters')
set(gca, 'Position', [2.5 2.9 17 10])
set(gcf, 'Units', 'centimeters', 'Position', [2.6 2.9 20 15])
set(gcf, 'PaperUnits', 'centimeters', 'PaperPosition', [2.6 2.9 20 15])

%calculation of angle between normal vector and z axis
contact_angle=atan(-c2(s)/c1(s))*180/pi;
fprintf('\ncontact angle is (in degree): %f\n\n', contact_angle);

% calculation of contact line
delta_pen=delta_pen_t;
p_ind=find(FW-FR<=t+delta_pen);
contact_length=xn(p_ind(end))-xn(p_ind(1));

fprintf('\ncontact length in y direction is (in mm): %f\n\n', contact_length);
fprintf('**y_contact is in shifted coordinate**');
fprintf('\ny coordinates of contact point is (in mm): %f\n\n', xn(s));
y_contact=xn(s);
y_con=xn(s-60:s+140);
g_sep_f=FW-FR_v-min(FW-FR_v);
g_sep=g_sep_f(s-60:s+140);

```

## The code for calculating Kalker's coefficients

## APPENDIX B

```

function [C1,C2,C3,C4,phi1,phi2]=Kalker_constant_fit (sigma,g)
% C1 Kalker's constant c11
% C2 Kalker's constant c22
% C3 Kalker's constant c23
% C4 Kalker's constant c33
% phi1 constant phi
% phi2 constant psi
% a longitudinal semiaxis of the contact ellipse
% b lateral semiaxis of the contact ellipse
% g ratio of b/a
% sigma poisson ratio
g=1/g;

p00 = 2.414 ; %(2.363, 2.465)
p10 = 2.153 ;%(1.798, 2.509)
p01 = 0.9035 ;%(0.8047, 1.002)
p20 = 4.652 ; %(3.992, 5.312)
p11 = -0.37 ; %(-0.7023, -0.03772)
p02 = 0.088; % (0.03134, 0.1447)
p21 = -1.282 ; %(-1.822, -0.7406)
p12 = 0.2058 ;%( 0.1397, 0.2719)
p03 = -0.02631 ; %(-0.0377, -0.01491)
p22 = 0.1001 ;%( 0.04522, 0.1549)
p13 = -0.01556 ; %(-0.01988, -0.01125)
p04 = 0.001676 ;%( 0.001004, 0.002349)

C1 =( p00 + p10*sigma + p01*g + p20*sigma^2 + p11*sigma*g + p02*g^2 + p21*sigma^2*g +
p12*sigma*g^2 + p03*g^3 + p22*sigma^2*g^2 + p13*sigma*g^3 + p04*g^4 );

p00 = 2.377;
p10 = 0.04177;
p01 = 1.037;
p20 = -.3133;
p11 = .9885;
p02 = -0.01527;
p21 = 0.657;
p12 = -0.05342;
p03 = -.003093;
p22 = 0.02579;
p13 = -0.001597;
p04 = 0.0002576;

C2 =( p00 + p10*sigma + p01*g + p20*sigma^2 + p11*sigma*g + p02*g^2 + p21*sigma^2*g +
p12*sigma*g^2 + p03*g^3 + p22*sigma^2*g^2 + p13*sigma*g^3 + p04*g^4 );

p00 = 0.2896;
p10 = 0.4107;
p01 = 1.026;
p20 = 0.348;
p11 = -0.1537;
p02 = 0.005547;
p21 = -0.008115;
p12 = 0.2061;
p03 = 0.0009288;
p22 = 0.0785;
p13 = -0.01195;
p04 = -0.00001687;

C3 =( p00 + p10*sigma + p01*g + p20*sigma^2 + p11*sigma*g + p02*g^2 + p21*sigma^2*g +
p12*sigma*g^2 + p03*g^3 + p22*sigma^2*g^2 + p13*sigma*g^3 + p04*g^4 );

p00 = 0.7255;

```

```

p10 = -0.865;
p01 = 0.4623;
p20 = -0.6009;
p11 = 0.7381;
p02 = 0.02736;
p21 = 0.6099;
p12 = -0.02149;
p03 = -.000259;
p22 = 0.07071;
p13 = 0.00009034;
p04 = 0.00009268;

g=1/g;
C4 = ( p00 + p10*sigma + p01*g + p20*sigma^2 + p11*sigma*g + p02*g^2 + p21*sigma^2*g +
p12*sigma*g^2 + p03*g^3 + p22*sigma^2*g^2 + p13*sigma*g^3 + p04*g^4 );

g_ek=g;

p00=0.1716;
p10=-.01456;
p01=1.446;
p11=-.9549;
p02=-1.369;
p12=0.4894;
p03=0.6891;
p13=-.1224;
p04=-.1666;
p14=0.01109;
p05=.01465;

phi1= p00 + p10*sigma + p01*g_ek + p11*sigma*g_ek + p02*g_ek^2 + p12*sigma*g_ek^2 +
p03*g_ek^3 + p13*sigma*g_ek^3 + p04*g_ek^4 + p14*sigma*g_ek^4 + p05*g_ek^5;

p00=0.1774;
p10=-.2091;
p01=1.409;
p11=-.152;
p02=-1.298;
p12=0.2357;
p03=0.6358;
p13=-.08622;
p04=-.1504;
p14=0.009294;
p05=.01303;

phi2= p00 + p10*sigma + p01*g_ek + p11*sigma*g_ek + p02*g_ek^2 + p12*sigma*g_ek^2 +
p03*g_ek^3 + p13*sigma*g_ek^3 + p04*g_ek^4 + p14*sigma*g_ek^4 + p05*g_ek^5;

```

## The code for solving normal contact problem based on ANALYN algorithm

```

function
[P,xx_1,a_vec,penet,y_con_1]=Secant_ANALYN_Mey(g,y,R,B,E,nu,N,penet1,penet2,penet_err,x_res)
% g: separation curve; y: separation curve lateral coordinate in mm
% R and B; longitudinal and lateral curvatures in mm
% E, nu: modulus of elasticity and poisson ratio
% N normal loading at the contact
% penet1,penet2: two initial guess for penetration value
% penet_err: penetration'e error tolerance
% x_res: resolution for longitudinal coordinate

```

```

% P: normal pressure distribution in Pa
% xx_1: longitudinal coordinate
% a_vec: vector of contact area expansion in longitudinal direction in mm
% penet: vector of penetration iterations
% y_con_1 refined y coordinate of the contact area

penet_i(1)=penet1;
penet_i(2)=penet2;
[N_c(1),P,xx_1,a_vec,y_con_1]=ANALYN_Mey(g,y,R,B,E,nu,penet1,x_res);
[N_c(2),P,xx_1,a_vec,y_con_1]=ANALYN_Mey(g,y,R,B,E,nu,penet2,x_res);

% secant iteration for solving for penetration less than error tolerance
for i=1:1000;
    penet_i(i+2) = ((penet_i(i)*(N_c(i+1)-N)-(penet_i(i+1)*(N_c(i)-N)))/(N_c(i+1)-
N_c(i))
    clear P xx_1 a_vec y_con_1
    [N_c(i+2),P,xx_1,a_vec,y_con_1]=ANALYN_Mey(g,y,R,B,E,nu,penet_i(i+2),x_res);

    error_del=penet_i(i+2)-penet_i(i+1);
    if abs(error_del) < penet_err
        break
    end;
end;
penet=penet_i;

function [N,P,xx_1,a_vec,y_con_1]=ANALYN_Mey(g,y,R,B,E,nu,penet,x_res)

% normal contact solution based on ANALYN algorithm when penetration is
% input

g=0.001*g;
y=0.001*y;
R=0.001*R;
penet=penet*0.001;
x_res=0.001*x_res;
nn=length(y);
yy1=y(2)-y(1);
A=(1./(2.*R));

% finding the contact area in lateral direction
for i=1:length(g)
    sep(i)=(penet-((1+beta(A(i),B(i))).*g(i)));
end;

y_ind=find(sep>=0);

yy_ind=(y_ind(1)-5):1:(y_ind(end)+5);
y_con_1=y(yy_ind);
xx=-.04:x_res:.04;
mm=length(xx);
mm_2=floor(mm/2);
p_contact=zeros(mm,length(yy_ind));
a_vec=zeros(length(yy_ind),1);
% solving for calculating the contact area in longitudinal direction
% and pressure distribution
for i=1:length(y_ind)
    iind=y_ind(i);
    cvb=alpha(A(iind),B(iind));
    a_con(i)=(1/1)*sqrt(sep(iind)/((1+cvb)*(A(iind))));%(1.1/(1.5))
    a_vec(iind-yy_ind(1)+1)=a_con(i);
    p_max(i)=(E/((1-
nu^2)*pi))*1/(n_hertz(A(iind),B(iind))*r_hertz(A(iind),B(iind)))*(sep(iind)/abs(a_con(i)
)));
    x_con=0:x_res:a_con(i);
    for j=1:length(x_con)

```

```

    p_contact(mm_2+1+(j-1),iind-yy_ind(1)+1)=p_max(i)*sqrt(1-(x_con(j)/a_con(i))^2);
    p_contact(mm_2+1-(j-1),iind-yy_ind(1)+1)=p_max(i)*sqrt(1-(x_con(j)/a_con(i))^2);
end;

% removing the extra zeros from p_contact
a_max=max(a_con(:));
mm_max=floor(1.1*floor(a_max/x_res));
xx_1=xx(-mm_max+mm_2+1:1:mm_max+mm_2+1);
p_contact_1=p_contact(-mm_max+mm_2+1:1:mm_max+mm_2+1,:);
P=p_contact_1;
a_vec=1000*a_vec;
xx_1=xx_1*1000;
% calculating the norma loading
N1=sum(sum(p_contact_1)*x_res*(y_con_1(2)-y_con_1(1)));
N2=trapz(y_con_1,trapz(xx_1*.001,P,1),2);
N=(N1+N2)/2;

```

## The code for calculating the creepages

```

function [vx vy phi]
=creepage_calculation(wr,ww,rr,rw,yy_cen,ydot,zz_cen,aoa,aoadot,cant,cantdot,delta)
% wr ww: rotational speed of roller and wheel in rad/s
% ydot: rate of lateral displacement change in mm/s
% rr rw: roller and wheel radii in mm
% angles and rate of change are in degree
% zz_cen yy_cen: coordinates of contact point location in mm
% delta: contact angle
% aoa, aoadot; Angle of attack and its rate of change
% cant,cantdot: cant angle and its rate of change

rw=rw*.001;
rr=rr*0.001;
yy_cen=yy_cen*0.001;
zz_cen=zz_cen*0.001;
ydot=0.001*ydot;
aoa=aoa*pi/180;
aoadot=aoadot*pi/180;
cant=cant*pi/180;
cantdot=cantdot*pi/180;
delta=delta*pi/180;

%calculating forward/reference velocity
v_ref=((rw*ww)+(rr*wr))/2;

vx= ((rw*ww)-(rr*wr)*cos(aoa)+aoadot*yy_cen)/v_ref;
vy=(ydot+aoa+zz_cen*cantdot)/v_ref;
phi=(aoadot*cos(delta)+cantdot+ww*sin(delta-cant))/v_ref;

```

## The code for solving tangential contact problem based on FaStrip algorithm

```

function [px_v py_v Fx Fy d]
=FaStrip_Mey_fig(g_sep,y_con,R,B,a_vec,xx_1,x_res,P,mu_f,vx,vy,phi,nu,G)

% g_sep: separation curve; y_con: separation curve lateral coordinate in mm
% R and B; longitudinal and lateral curvatures in mm
% P: normal pressure distribution in Pa

```

```

% xx_1: longitudinal coordinate
% a_vec: vector of contact area expansion in longitudinal direction in mm
% G, nu: modulus of rigidity and poisson ratio
% x_res: resolution for longitudinal coordinate
% vx: longitudinal creepage
% vy: lateral creepage
% phi: spin creepage

% px_v and py_v: longitudinal and lateral shear stress distribution
% Fx and Fy: longitudinal and lateral creep forces
% d represents stick-slip boundary (half length of slip area)

g_sep=0.001*g_sep;
y_con=0.001*y_con;
R=0.001*R;
a_vec=0.001*a_vec;
xx_1=0.001*xx_1;
x_res=0.001*x_res;
p_size=size(P);
p00=P(floor(p_size(1,1)/2)+1,:);
px_v=zeros(length(xx_1),length(y_con));
py_v=zeros(length(xx_1),length(y_con));
A=(1./(2.*R));

for i=1:length(y_con)
    if a_vec(i)>= x_res

        b(i)=a_vec(i)*n_hertz(A(i),B(i))/m_hertz(A(i),B(i));
        g=b(i)/a_vec(i);
        [C1,C2,C3,C4,phi1,phi2]=Kalker_constant_fit (nu,g);
        p0=p00(i);
        [px_f,py_f,
d(i)]=strip_FaStrip_fig(y_con(i),a_vec(i),x_res,p0,mu_f,vx,vy,phi,nu,G,C1,C2,C3,g);
        xx_con=0:x_res:a_vec(i);
        x_con=[-1*xx_con(end:-1:2),xx_con];

        % If there is slip and adhesion areas; FASTSIM is used for slip
        % area
        if d(i) < a_vec(i)
            slip_ind=find( x_con <-a_vec(i)+2*d(i));

[pxx,pyy]=Fastsim_FaStrip_fig(vx,vy,phi,C1,C2,C3,p0,mu_f,a_vec(i),b(i),d(i),G,x_con,y_con
(i),x_res);

            for j=1:length(slip_ind)

                p0_1=mu_f*p00(i)*sqrt((1)^2-(x_con/a_vec(i)).^2);

px_f(slip_ind(j))=pxx(slip_ind(j))*p0_1(slip_ind(j))/sqrt(pxx(slip_ind(j))^2+pyy(slip_ind
(j))^2);

py_f(slip_ind(j))=pyy(slip_ind(j))*p0_1(slip_ind(j))/sqrt(pxx(slip_ind(j))^2+pyy(slip_ind
(j))^2);

                if (pxx(slip_ind(j))==0) & (pyy(slip_ind(j))==0)
                    px_f(slip_ind(j))=0;
                    py_f(slip_ind(j))=0;
                end;

            end;
            clear p0_1

            % if there is only slip area
            elseif d(i)==a_vec(i)

```

```
[pxx,pyy]=Fastsim_FaStrip_fig(vx,vy,phi,C1,C2,C3,p0,mu_f,a_vec(i),b(i),d(i),G,x_con,y_con
(i),x_res);
    for j=1:length(pxx)
        %p0_1=mu_f*p00(i)*sqrt((1000*a_vec(i)^2-(1000*x_con).^2)/a_vec(i));
        p0_1=mu_f*p00(i)*sqrt((1)^2-(x_con/a_vec(i)).^2);
        px_f(j)=pxx(j)*p0_1(j)/sqrt(pxx(j)^2+pyy(j)^2);
        py_f(j)=pyy(j)*p0_1(j)/sqrt(pxx(j)^2+pyy(j)^2);
        if (pxx(j)==0) & (pyy(j)==0)
            px_f(j)=0;
            py_f(j)=0;
        end;
    end;
    clear p0_1
end;
px_v(floor(length(xx_1)/2)-floor(length(x_con)/2)+1:1:floor(length(xx_1)/2)-
floor(length(x_con)/2)+length(px_f),i)=px_f;
py_v(floor(length(xx_1)/2)-floor(length(x_con)/2)+1:1:floor(length(xx_1)/2)-
floor(length(x_con)/2)+length(py_f),i)=py_f;
else
end;

end;
Fx=sum(px_v(:))*(y_con(2)-y_con(1))*x_res;
Fy=sum(py_v(:))*(y_con(2)-y_con(1))*x_res;

function [px py x d]=strip_FaStrip_fig(y,a,x_res,p0,mu_f,vx,vy,phi,nu,G,C1,C2,C3,g)

% y: lateral coordinate in m
% x_res: resolution for longitudinal coordinate in m
% p0: maximum normal pressure in Pa
% mu_f: friction coefficient
% a: contact area semi-axis in longitudinal direction in m
% G, nu: modulus of rigidity and poisson ratio
% vx: longitudinal creepage
% vy: lateral creepage
% phi: spin creepage
% Ci: Kalker's coefficients
% g=a/b contact aspect ratio

% px and py: longitudinal and lateral shear stress distribution
% x: longitudinal coordinate in m
% d represents stick-slip boundary (half length of slip area)

cx=4*(1-nu)*C1/pi^2;
cy=4*(1-nu)*C2/pi^2;
cphi=3*sqrt(1/g)*C3/pi;

kisi=-G*vx/(2*mu_f*p0);
eta=-1*G*vy/(2*mu_f*p0);
psi=-G*phi*a/(2*mu_f*p0);

kisi=kisi*cx;
eta=eta*cy;
psi=psi*cphi;
a1=a;
if (y==0) & (vx==0) & (vy==0)
    y=10^-8;
end;

d=(sqrt(eta^2+((1-psi^2)*(kisi-(psi*y)/a1)^2))+eta*psi)*a/((1-psi^2)*(1-nu));
if (isreal(d)==0) | (d>a) | d<0
    if phi > 5*10^-2
        kisi=-G*vx/(2*mu_f*p0);
        eta=-1*G*vy/(2*mu_f*p0);
```

```

        %psi=-G*phi*a/(2*mu_f*p0);
        d=(sqrt(eta^2+(1-psi^2)*(kisi-(psi*y)/a1)^2))+eta*psi*a/((1-psi^2)*(1-nu));
    end;
    if (isreal(d)==0) | (d>a) | d<0
        d=a;
    end;
end;

kapa=(kisi-(psi*y)/a1)/sqrt((kisi-(psi*y)/a1)^2+(eta+(psi*d)/a1)^2);
lambda=(eta+(psi*d)/a1)/sqrt((kisi-(psi*y)/a1)^2+(eta+(psi*d)/a1)^2);
lambda_prime=(eta+(psi*d)/a1)/sqrt((kisi-(psi*y)/a1)^2+(eta+(psi*d)/a1)^2-psi);

if isnan(kapa)==1
    kapa=0;
end;
if isnan(lambda) == 1
    lambda=0;
end;
if isnan(lambda_prime)==1
    lambda_prime=0;
end;

xx_cn=0:x_res:a;
x=[-1*xx_cn(end:-1:2),xx_cn];
for i=1:length(x)
    px(i)=(mu_f*p0/a)*real(kapa*sqrt(a^2-x(i)^2)-kapa*sqrt((a-d)^2-(x(i)-d)^2));
    py(i)=(mu_f*p0/a)*real(lambda*sqrt(a^2-x(i)^2)-lambda_prime*sqrt((a-d)^2-(x(i)-d)^2));
end;

function [pxx,pyy]=Fastsim_FaStrip_fig(vx,vy,phi,C1,C2,C3,p0,mu_f,a,b,d,G,x_con,Y,x_res)

% vx: longitudinal creepage
% vy: lateral creepage
% phi: spin creepage
% Ci: Kalker's coefficients
% Y: lateral coordinate in m
% x_res: resolution for longitudinal coordinate in m
% p0: maximum normal pressure in Pa
% mu_f: friction coefficient
% a,b: contact area semi-axis in longitudinal and lateral directions in m
% G, nu: modulus of rigidity and poisson ratio
% d represents stick-slip boundary (half length of slip area)
% g=a/b contact aspect ratio

% pxx and pyy: longitudinal and lateral shear stress distribution

L1=8*a/3/C1/G;L2a=8*a/3/C2/G;L2b=pi*a*sqrt(a/b)/4/C3/G;
if (a <= d) %&& (phi~=0)

    Lt=(abs(vx)*L1+abs(vy)*L2a+sqrt(a*b)*abs(phi)*L2b)/sqrt(vx^2+vy^2+a*b*phi^2);
    Lx=Lt;Ly=Lt;L2x=Lt;L2y=Lt;
else
    Ltx=(abs(vx)*L1+sqrt(a*b)*abs(phi)*L2b)/sqrt(vx^2+a*b*phi^2);
    Lty=(abs(vy)*L2a+sqrt(a*b)*abs(phi)*L2b)/sqrt(vy^2+a*b*phi^2);
    Lx=Ltx;Ly=Lty;L2x=Ltx;L2y=Lty;
end;
z0=p0;
n1=a*v_x/mu_f/z0/Lx;
n2=a*v_y/mu_f/z0/Ly;
fin1=a*b*phi/mu_f/z0/L2x;
fin2=a*a*phi/mu_f/z0/L2y;
if isnan(n1)==1
    n1=0;
    fin1=0;
end;
end;

```

```

if isnan(n2)==1
    n2=0;
    fin2=0;
end;
px=0;py=0;
x_res=x_res/a;
Y=Y/b;
x_con=x_con/a;

SX=n1-Y*fin1;
pxx(1)=px;
pyy(1)=py;
for i=2:length(x_con)
    SY=n2+fin2*(x_con(end+1-i));
    px=px-SX*x_res;
    py=py-SY*x_res;
    pxx(i)=px;
    pyy(i)=py;
    Z=(1-(x_con(end+1-i))^2);
    p=sqrt(px^2+py^2)/Z;
    if p>1
        px=px/p;
        py=py/p;
        pxx(i)=px;
        pyy(i)=py;
    end
end
end
pxx=pxx(end:-1:1);
pyy=pyy(end:-1:1);

```

## The code for calculating Hertz theory's coefficients

```

function alpha=alpha(A,B)
% A,B: longitudinal and lateral curvatures
% alpha: alpha coefficient in ANALYN algorithm

alpha=(r_hertz(A,B)/(m_hertz(A,B))^2)*(1+(B/A))-1;

function beta=beta(A,B)
% A,B: longitudinal and lateral curvatures
% beta: beta coefficient in ANALYN algorithm

beta=((r_hertz(A,B)/((n_hertz(A,B))^2))*(1+(A/B)))-1;

function m_hertz=m_hertz(A,B)
% A,B: longitudinal and lateral curvatures
% m_hertz: m coefficient in Hertz theory

% calculating variable theta
if A<=B
    theta1=acos(abs(B-A)/(B+A));
    theta1=theta1*180/pi;
elseif A>B
    theta1=acos(-abs(B-A)/(B+A));
    theta1=theta1*180/pi;
end;

% giiven tabulated data
xdata=[0 5 10 30 60 90 120 150 170 175 180];
ydata=[10^8 11.238 6.612 2.731 1.486 1 0.7171 0.4931 0.311 0.2381 0];

%interpolation of the tabulated data
m_hertz=interp1(xdata,ydata,theta1,'pchip');

function g_hertz=g_hertz(A,B)

```

```

% A,B: longitudinal and lateral curvatures
% g_hertz: g=n/m coefficient in Hertz theory (ratio of n over m)

% calculating variable theta
if A<=B
thetal=acos(abs(B-A)/(B+A));
thetal=thetal*180/pi;
elseif A>B
thetal=acos(-abs(B-A)/(B+A));
thetal=thetal*180/pi;
end;

% giiven tabulated data
xdata=[0 5 10 30 60 90 120 150 170 175 180];
ydata=[0 0.0212 0.047 0.1806 0.4826 1 2.0720 5.5380 21.26 47.2 10^8];

%interpolation of the tabulated data
g_hertz=interp1(xdata,ydata,thetal,'pchip');

function r_hertz=r_hertz(A,B)
% A,B: longitudinal and lateral curvatures
% r_hertz: r coefficient in Hertz theory

% calculating variable theta
if A<=B
thetal=acos(abs(B-A)/(B+A));
thetal=thetal*180/pi;
elseif A>B
thetal=acos(-abs(B-A)/(B+A));
thetal=thetal*180/pi;
end;

% giiven tabulated data
xdata=[0 5 10 30 60 90 120 150 170 175 180];
ydata=[0 0.2969 0.428 0.7263 0.9376 1 0.9376 0.7263 0.428 0.2969 0];

%interpolation of the tabulated data
r_hertz=interp1(xdata,ydata,thetal,'pchip');

function n_hertz=n_hertz(A,B)
% A,B: longitudinal and lateral curvatures
% n_hertz: n coefficient in Hertz theory

n_hertz=g_hertz(A,B)*m_hertz(A,B);

```